DEVELOPMENT OF IMMERSED BOUNDARY-PHASE FIELD-LATTICE BOLTZMANN METHOD FOR SOLID-MULTIPHASE FLOW INTERACTIONS

SHAO JIANGYAN

A THESIS SUBMITTED

FOR THE DEGREE OF DOCTOR OF PHILOSOPHY

DEPARTMENT OF MECHANICAL ENGINEERING

NATIONAL UNIVERSITY OF SINGAPORE

2013

Declaration

I hereby declare that this thesis is my original work and it has been written by me in its entirety. I have duly acknowledged all the sources of information which have been used in the thesis.

This thesis has also not been submitted for any degree in any university previously.

SHAO Jiangyan

2013

Acknowledgements

First and foremost, I would like to express my deepest gratitude to my supervisors, Professor Shu Chang and Professor Chew Yong Tian, for their invaluable guidance, great patience and continuous support throughout my Ph.D. study.

In addition, I would also like to express my sincere appreciation to the National University of Singapore for providing me various essential assistances to complete this work, including research scholarship, abundant library resources and the advanced computing facilities as well as a good study environment. The assistance and help from NUS staff, my colleagues and friends are also highly appreciated.

Finally, I would like to thank my family for their endless love, encouragement and understanding.

SHAO Jiangyan

Table of Contents

Summary

Throughout fluid dynamics history, the fundamental importance and wide application bring the study of solid-fluid interaction a sustained academic and industrial interest. Among solid-fluid interactions, numerical simulation of solid-multiphase flow interaction might still be one of the most challenging topics in Computational Fluid Dynamics (CFD). The difficulties arise from the necessity of treating two distinct types of interfaces, fluid-fluid interface and solid boundary, simultaneously. To simulate such a problem, a multiphase flow solver and implementation of boundary conditions on a solid boundary are necessary. This work is devoted to study numerical methods in these two respects respectively and also establish a unified framework for simulation of solid-multiphase flow interactions.

In respect of multiphase flow solver, this work develops a stencil adaptive phase-field lattice Boltzmann method (LBM) for two dimensional incompressible multiphase flows. It utilizes two types of symmetric stencils which can be combined to form a similar structure to D2Q9 lattice model in LBM. This feature allows the present method to maintain the simplicity of original LBM. Numerical experiments demonstrate that the developed method enables a high resolution for interfacial dynamics with greater grid distribution flexibility and considerable saving in computational effort. Additionally, a free energy-based phase-field LBM is also developed for simulation of multiphase flow with density contrast. The present method is to improve the Z-S-C model (Zheng et al. 2006) for correct consideration of density contrast in the momentum equation. To achieve this aim, we start from a LBE of which the particle distribution function is used to measure the local density. To ensure simulation stability, a transformation was introduced to change the particle distribution function for the local

density and momentum into that for the mean density and momentum. As a result, the present model enjoys the good property of using the particle distribution function for mean density and momentum as in Z-S-C model. On the other hand, it can correctly consider the effect of density contrast in the momentum equation. Numerical examples demonstrate that the present model can correctly simulate multiphase flows with density contrast, and has an obvious improvement over the Z-S-C model in terms of solution accuracy.

The other major concern is implementation of boundary conditions such as Dirichlet and Neumann boundary conditions. Among methods to achieve this aim, Immersed Boundary Method (IBM) has gained growing popularity for its efficiency and robustness. Nevertheless, most previous works are restricted to Dirichlet boundary condition. To overcome this limitation, we take the first endeavour to develop an IBM for Neumann boundary condition in this work. The primary concept of the current method is to utilize the physical mechanism and interpret Neumann boundary condition as contribution of flux from the surface to its relevant physical parameters in a control volume. The developed IBM for Neumann boundary conditions can also be consistently applied with IBM for Dirichlet boundary conditions. In this way, both solid-single phase and multiphase flow interactions can be successfully simulated through IBM in the present work. This work releases IBM from the long existing restriction and opens the possibility of IBM simulation for ubiquitous fluid-solid interactions involving Neumann boundary conditions.

Last but not least, the application of immersed boundary phase-field LBM for simulation of solid-multiphase flow interactions is also demonstrated. Two types of interfaces, fluid-fluid interface and solid boundaries are successfully implemented simultaneously through the

developed framework. The equilibrium results and dynamic processes of solid-multiphase flow interactions are compared with results in the literature. Additionally, its capacity to be adapted to geometrical and/or chemical patterned surface is also demonstrated.

List of Tables

List of Figures

Nomenclature

Roman Letters

C_d	Drag coefficient
C_l	Lift coefficient
Ca	Capillary number
Cn	Cahn number
$\boldsymbol{e}_\alpha$	Lattice velocity vector
$Eö$	Eötvös number
$\boldsymbol{F}_b$	Body force
f_α	Density distribution function
f_α^{eq}	Equilibrium density distribution function
f_H^{-1}	Inverse of the Hoffman function
h_m	Characteristic length of a stencil
M	Mobility
Mo	Morton number

Oh	Ohnesorge number
p	Pressure
$\boldsymbol{q}$	Flux vector
Re	Reynolds number
t	Time
$\boldsymbol{U}, \boldsymbol{U}_B, \boldsymbol{u}, \boldsymbol{u}^*$	Velocity vector
$\delta\boldsymbol{u}, \delta\boldsymbol{u}_B$	Velocity correction vector
w	Interface width
w_α	Lattice model coefficients
We	Weber number
$\boldsymbol{X}_B$, $\boldsymbol{x}$	Coordinate vector
x, y, z	Coordinate

Greek Letters

α	Lattice velocity direction
ε	Small expansion parameter
θ	Contact angle

θ_{eq}	Equilibrium contact angle
κ	Coefficients in free energy function
μ	Dynamic viscosity
μ_{ϕ}	Chemical potential
ρ	Density
σ	Surface tension
τ	Relaxation parameter
υ	Kinematic viscosity
ϕ	Phase concentration
ϕ_{Bulk}	Phase concentration in bulk region
ϕ_{s}	Phase concentration on solid surface
$\Psi(\phi)$	Bulk fee energy
Ω_{α}	Collision operator
$\tilde{\omega}$	Wetting potential
$\Im$	Free energy function

Abbreviations

CFD	Computational Fluid Dynamics
2D	Two-Dimensional
3D	Three-Dimensional
LBM	Lattice Boltzmann Method
LBE	Lattice Boltzmann Equation
IBM	Immersed Boundary Method
IIM	Immersed Interface Method
N-S	Navier-Stokes
C-H	Cahn-Hilliard
AMR	Adaptive Mesh Refinement
VOF	Volume Of Fluid
LS	Level Set
SLIC	Simple Line Interface Calculation
PLIC	Piecewise Linear Interface Construction
SOLA	Subtractive Optimally Localized Averages

Chapter 1

Introduction

1.1 Background

Interaction of multiphase flow with solid is ubiquitous in both nature and industry. It is a crucial element of numerous phenomena such as spreading of two immiscible media, oil-water in porous media and solid impact on liquid surface. There are abundant theoretical and experimental works devoted to investigate the accompanying phenomena since one of the first systematic studies by Worthington (1908). Nonetheless, inherent complexity of interfacial dynamics poses a great challenge in theoretical prediction and experimental measurement (Prosperetti and Tryggvason 2003). In this regards, numerical simulation is instrumental in gaining better understanding of the phenomena by providing details that elaborate the solid-multiphase flow interaction in depth. To simulate solid-multiphase flow interactions, there are two essential elements: Firstly, a multiphase flow solver is necessary; Secondly, implementation of boundary conditions on a solid object is also indispensable. Although research in these two areas has advanced continuously in last few decades, there are still many challenging issues in computational fluid dynamics (CFD) to be solved.

Firstly, to perform direct numerical simulation of a multiphase flow system, interface track/capture schemes are needed to couple with a flow field solver. Based on different interpretations of the interface, there are various interface tracking/capture schemes developed. Among them, phase-field method (Anderson et al. 1998, Jacqmin 1999) becomes increasingly popular for its sound physical background and capability to capture an interface

with large deformation. The phase-field method is previously used together with Navier-Stokes (N-S) solver (Antanovskii 1995) (a macroscopic description of hydrodynamics and established on continuity assumption). Later, it is also coupled with lattice Boltzmann method (LBM, which is based on mesoscopic kinetic equation and serves as an alternative for flow field simulation). LBM has attracted particular attention in the last two decades (Aidun and Clausen 2010). Its popularity is mainly attributed to computational efficiency, easy parallel computation and simple implementation of boundary conditions on complex geometries. Owing to these advantages, the phase-field LBM has been applied to simulate various multiphase flow problems. However, as a diffuse interface method (in which the phases' interface has a finite thickness), the phase-field LBM faces the challenge of balancing accuracy and computational efficiency. To solve this problem, it is a good choice to apply adaptive mesh refinement (AMR) with phase-field LBM. Another challenge for phase-field LBM is simulation of multiphase flow with density contrast. The phase-field LBM is originally developed for density matched problems and it is nontrivial to adapt it to cases with density contrast. This is an important issue concerning the fact that most practical problems involve density and viscosity contrast. Therefore, to simulate more practical problems, there is also a necessity to develop a phase-field LBM for simulation of multiphase flows with density contrast.

Secondly, to simulate the solid interaction with single phase/multiphase flows, implementation of boundary conditions such as Dirichlet (value of physical parameters is given) and Neumann (value of derivatives along the normal direction is given) boundary conditions is an indispensable task. In respect of underlying mesh used, the methods to implement boundary conditions can be classified as: (1) body conformal methods and (2) non-body conformal methods. The most straightforward way to implement boundary

conditions might be using body conformal grid. However, it is usually difficult to generate a good quality body-fitted grid (Mittal and Iaccarino 2005). To overcome this difficulty, non-body conformal methods can be employed. A prominent advantage of non-body conformal methods is that they significantly simplify the grid generation process through decoupling solution of governing equations and implementation of boundary conditions. Based on the techniques to enforce boundary conditions, the non-body conformal methods can be further classified into: (1) sharp interface approaches and (2) diffuse interface approaches. In these two categories, the diffuse interface approaches enable more robust simulation and simpler procedure with partial loss of accuracy. The most celebrated method in this category might be immersed boundary method (IBM) developed by Peskin (1972). It has been widely applied to simulate fluid interaction with stationary/moving complex geometries (Mittal and Iaccarino 2005). Notwithstanding, IBM has fallen short in an important aspect so far. Albeit tremendous prominent efforts have been dedicated to refine IBM, most are restricted to the Dirichlet boundary condition. To the best of our knowledge, few works that implement the Neumann boundary condition through IBM can be found in the literature. This remarkably limits the application of IBM in CFD since physical phenomena with relevant Neumann boundary conditions are extremely common. One of the instances is solid-multiphase flow interactions. This indicates that there is a practical demand to develop an efficient IBM for Neumann boundary condition. Thus, to enable IBM to simulate more general solid flow interaction problems, it is essential to develop IBM that can be applied to both Dirichlet and Neumann boundary conditions.

In the following of this Chapter, a review of multiphase flow modeling will be presented in the first place. Considering the interest of this thesis, special attention will be paid to the phase-field method and lattice Boltzmann method. Secondly, implementation of boundary

conditions for solid, especially using the immersed boundary methods, will also be introduced. Lastly, objectives and organization of this thesis will be presented at the end of the Chapter.

1.2 Modeling of Multiphase Flow

Thanks to the rapid development of algorithms and computational power, direct numerical simulation of multiphase flows has undergone remarkable progress in the last decades. Various methods for multiphase flow simulation have been proposed based on different physical interpretations. This section aims to provide a literature review on the numerical methods for multiphase flow simulation. The review will mainly focus on the phase-field method and lattice Boltzmann method considering the scope of this thesis.

1.2.1 Navier-Stokes solvers for multiphase flow simulation

In direct numerical simulation of multiphase flows, the flow field is conventionally obtained by solving the celebrated Navier-Stokes equations, while the phase interface can be either tracked or captured through different methods. With respect to the grid on which the interface is tracked/captured, there are two classes of methods: (1) Moving grid methods and (2) Fixed grid methods (Scardovelli and Zaleski 1999). In the moving grid methods, phases' interface is explicitly treated as a grid boundary and boundary conditions must be applied on it. Methods in this category like interface fitted method (Ryskin and Leal 1984a, Ryskin and Leal 1984b, Ryskin and Leal 1984c) use a set of interface fitted grid that can only be occupied by one fluid. Later, this method has also been extended to account for both phases using two subdomains of grid and applied to simulate drop motion in quiescent liquid (Dandy

and Leal 1989). More recent application of interface fitted grid method can be found in the work of Magnaudet et al. (1995) and Cuenot et al. (1997). Additionally, other moving grid methods include boundary integral method (Toose et al. 1995, Cristini et al. 1998) and boundary element method (Khayat 2000). A common feature of moving grid methods is that re-generation of grid according to interface change is required. This procedure entails considerable computational cost and may also introduce interpolation error. In addition, it is also intractable for this class of methods to treat interface intersection and topology change. Owing to these characteristics, moving grid methods are commonly applied to simulate bubble dynamics in which phases' interface has relatively small deformation. Compared with the moving grid methods, fixed grid methods have grown in popularity due to their computational efficiency and flexibility. In this category, phases' interface can evolve on an (fixed or dynamically adapted) underlying Eulerian grid and this concept can be dated back to 1960s (Harlow and Welch 1965). Depending on the way to identify phases' interface, the fixed grid methods can be further categorized into: Lagrangian approaches and Eulerian approaches. In Lagrangian approaches such as marker-and-cell method (Harlow and Welch 1965, Harlow and Shannon 1967) and front-tracking method (Unverdi and Tryggvason 1992, Tryggvason et al. 2001, Muradoglu and Tryggvason 2008, Muradoglu and Tasoglu 2010), a set of explicit moving Lagrangian points is introduced to track interface motion. Compared with the previously introduced moving grid methods, computational load can be partially reduced in fixed grid-Lagrangian approaches. However, these approaches are still computationally expensive because artificial treatments such as adding or removing Lagrangian points are compulsory when interface undergoes large deformation. Moreover, the artificial treatments involved may also undermine conservation law. In addition to Lagrangian approaches, the other kind of approaches, Eulerian approaches have attracted much interest recently owing to their convenient description of interface topology.

Commonly applied Eulerian approaches include volume of fluid method (VOF) (Hirt and Nichols 1981, Lafaurie et al. 1994, Scardovelli and Zaleski 1999), Level set (LS) method (Osher and Sethian 1988, Sussman et al. 1994, Sethian and Smereka 2003) and phase-field method (Jacqmin 1999, Jacqmin 2000, Ding et al. 2007).

In VOF, volume fraction of one phase is used to identify different phases. The interface is captured by piecewise linear segments based on the volume fraction in the flow field. After the interface is identified, it is then advected by the velocity field. The most challenging theoretical and also practical problem in VOF might be the "reverse problem", that is, construction of interface according to the known volume fraction. This issue is crucial because it is a foundation to evaluate interface curvature, normal direction and surface tension. The difficulty arises from the fact that, with a given volume fraction, almost infinite types of interface shape are available to be selected and the selection process highly depends on artificial criteria. In fact, VOF has undergone continuous advancement in dynamic interface reconstruction (Scardovelli and Zaleski 1999). The early first-order interface reconstruction methods include Simple Line Interface Calculation (SLIC) and Subtractive Optimally Localized Averages (SOLA). Thereafter, more sophisticated methods such as the widely used Piecewise Linear Interface Construction (PLIC) methods (Ashgriz and Poo 1991, Lopez et al. 2005) have also been proposed. Moreover, with respect to solid-multiphase flow interaction, several methods have been proposed to treat the three-phase contact line (Pasandideh-Fard et al. 1996, Renardy et al. 2001, Sikalo et al. 2005). Generally speaking, extra effort must be paid to determine the volume fraction on solid boundary. Moreover, a slip model is required to relieve contact line singularity (which is caused by imposition of the no-slip boundary condition for viscous fluid). Another popular method for multiphase flow simulation is the level set method (Osher and Sethian 1988, Osher and Fedkiw 2001). In this

method, a signed distance function is used to identify different phases. With interface re-initialized (in which artificial manipulations are also required) based on distance function, interface outward normal and interfacial force can be evaluated. Although LS method and VOF use different variables to identify interface, both parameters are actually advected by velocity field according to similar equations. Moreover, considering the three-phase contact problems, LS also adopts similar approach with VOF. To be specific, the normal direction of interface can be determined by contact angle, while slip model is used to resolve contact line singularity.

Apart from VOF and LS method, another approach named phase-field method has gained increasing popularity recently. In the phase-field method (Anderson et al. 1998, Jacqmin 1999), order parameter (phase's concentration) is introduced to characterize different phases. Moreover, the interface is manipulated as a region with finite thickness where the physical parameters vary rapidly and smoothly. This concept originates from physical insight gained by Maxwell (1952) and Gibbs (1878) as well as the following "interface gradient theory" by Rayleigh (1892) and van der Waals (1893). Unlike VOF/LS method which is established on mechanical balance of surface forces, the phase-field method is based on theory of fluid free energy (which can be expressed as a function of order parameter). For a multiphase system with two immiscible fluids, total free energy has contribution from two parts. One is the bulk free energy and the other is gradient energy term contributed by phases' interface. In this framework, interfacial force can be variationally derived from the defined free energy field. Through this way, phase-field method provides a systematic and thermodynamic consistent description of a variety of multiphase flow phenomena including solidification, spinodal decomposition and moving contact line problems (Anderson et al. 1998). Another difference between VOF/LS method and phase-field method lies in the governing equation for interface

evolution. As introduced previously, the governing equation for interface in VOF/LS is an advection function. Without diffusion terms, sophisticated numerical discretization schemes might be required to ensure stability. On the other hand, the advection-diffusion Cahn-Hilliard equation is used in phase-field model for interface evolution. With a physical diffusion term in Cahn-Hilliard equation, it allows easier numerical treatment. Moreover, it is also noted that although VOF/LS method solves the advection equation in the whole field, only one contour curve of the solution function is used (volume fraction in VOF or distance function in LS method). In contrast, the solution function in the phase-field method usually has a physical meaning so that it can be directly coupled with the governing equations of flow field. In other words, the solution function in the whole field rather than a single contour curve is used in the phase-field method. Furthermore, the phase-field method also enjoys higher computational efficiency because it allows the interface to freely propagate on a fixed grid without any arbitrary inventions such as construction/re-initialization that are needed in VOF/LS method. Last but not least, phase-field method has specific advantages over VOF and LS method in respect of solid-multiphase flow simulation. Attributed to thermal consistency of phase-field method, solid-multiphase interaction can be readily modeled by adding a surface energy term in free energy function. Additionally, due to the diffusion mechanism involved in phase-field framework, the contact line singularity can be naturally resolved. Here, it must be stressed that although these interface track/capture schemes are originally coupled with N-S solver, the principle of these schemes is independent of flow field solvers.

1.2.2 Lattice Boltzmann methods for multiphase flow simulation

The preceding subsection reviewed multiphase flow models that are traditionally coupled with the N-S solvers. In recent years, another flow field solver, the lattice Boltzmann method has undergone rapid development and been applied in a variety of fluid problems (Chen and Doolen 1998, Nourgaliev et al. 2003, Aidun and Clausen 2010). Different from N-S equations which are derived from applying physical conservation laws to a control volume, the LBM originates from kinetic theory. In LBM, the dependent parameters are the density distribution functions and macroscopic hydrodynamic properties that are recovered from the averaged properties. Moreover, convection of fluid is represented by a streaming process while nonlinear diffusion is revealed in the collision process. The major advantages of LBM include simple formulation, easy implementation of boundary condition on complex geometries and suitable for parallel computation. A detailed examination of these features shows that LBM has potential to be an efficient tool for multiphase flow problems with complex geometries (Nourgaliev et al. 2003). In fact, many multiphase flow simulations have been accomplished using LBM. Generally speaking, there are four types of LBMs for interfacial dynamics. They are color-fluid model of Gunstensen and collaborators (1991), inter-particle-potential model of Shan and Chen (1993, 1994), mean-field model of He et al. (1999) and phase-field LBM of Swift et al. (1995, 1996). All these LBMs can be viewed as diffuse interface methods. In the color-fluid model, the red and blue particle distribution functions are used to represent two different fluids. More recent development can be found in the work of Lishchuk et al. (2003) and Reis and Phillips (2007). The inter-particle-potential model incorporates surface tension as a potential force through modification of collision term in lattice Boltzmann equation (LBE). However, as pointed out by Shan and Chen (1993, 1994), the modified collision process may not conserve the local net momentum. As a consequence, the numerical fluctuations such as spurious velocities (Guo et al. 2011) (caused

by force imbalance due to numerical errors) will appear near the interface. The mean-field model has been successfully applied to binary fluids as well as multiphase problems with viscosity and density contrast (Lee and Lin 2005). Nevertheless, it is not clear whether the Cahn-Hilliard equation is accurately recovered by this model. The phase-field LBM is originally developed by Swift for both liquid-vapor and binary fluid system (Swift et al. 1995, Swift et al. 1996). In the phase-field LBM, one set of LBE is used to simulate evolution of flow field. Concurrently, the other set of LBE is designed to recover Cahn-Hilliard equation for interface capturing (Zheng et al. 2005). Like the phase-field N-S solver, the phase-field LBM also enjoys advantages such as thermal consistency, ease of handling drastic topology change and natural resolution of contact line singularity. Owing to these advantages, the phase-field LBM is adopted in this work for multiphase flow simulation.

1.2.3 Challenges faced by phase-field LBM

The phase-field LBM has been successfully applied to simulate various multiphase flow problems (Inamuro et al. 2004, Zheng et al. 2005, Huang et al. 2008, Sbragaglia and Shan 2011). On the other hand, it also faces challenges to be overcome. Firstly, as a diffuse interface method, the phase-field LBM faces the challenge to balance high resolution of interface and computational load entailed. Secondly, many numerical works done by phase-field LBM do not account for density difference and it is nontrivial to take density contrast into consideration. This is a great concern because many practical problems involve density and viscosity contrast. The following subsections will introduce these two issues in more detail.

1.2.3.1 Accuracy and efficiency balance in phase-field LBM

A major challenge faced by the phase-field method is to obtain high resolution within affordable computational loads. It is known that the interface has a finite thickness in phase-field method. When the method is applied to simulate hydrodynamic phenomena, the underlying assumption is that thickness of interface is small relative to length scale of the problem studied. Namely, the sharp interface limit (Yue et al. 2010) should be approached. One straightforward way is to use fine grid. In multiphase flow problems, the position and structure of interface usually cannot be predicted in advance. Therefore, a non-uniform grid with pre-set finest region is not helpful in this situation. Additionally, if uniform grid is employed, the whole computational domain must be refined to keep a sharp interface. Such an approach will entail remarkable computational load. In this condition, Adaptive Mesh Refinement (AMR) technique is a natural choice to balance accuracy and efficiency. In fact, great effort has been devoted to incorporate AMR in the conventional CFD solvers, in which tree-structured grid might be the most frequently used grid (Burman et al. 2004, Anderson et al. 2005, Sussman 2005, Zheng et al. 2005, Ceniceros et al. 2010). In lattice Boltzmann framework, attempts have also been made to refine mesh locally. Based on multi-block algorithm, solution adaptive mesh refinement technique was first introduced in LBM by Crouse et al. (2003) and Toolke et al. (2006). More recently, this technique was combined with potential model to simulate bubbly flows by Yu and Fan (2009). In their work, time step and relaxation parameters are changed with local grid spacing. Consequently, interpolation must be applied in both space and time. In this manner, the conservation laws cannot be easily imposed. Moreover, variation of the relaxation parameters makes additional manipulation of collision term necessary. In addition to the multi-block-based AMR, Rohde et al. (2008) proposed an adaptive finite volume LBM. In this method, the conservation laws can be easily satisfied (Rohde et al. 2008). Nevertheless, simplicity of LBM is partially lost.

It can be seen that several versions of adaptive LBM developed so far either involve complex interpolation or partially lose the simplicity of LBM. One reason for complexities in adaptive LBMs is that the grid structure developed for N-S solvers is used in LBM framework. Although the tree-structured grid has been proven to be very efficient for N-S solvers, it may not be suitable for LBM. In LBM, the simulation is carried out on lattice models, of which the structures are not consistent with tree-structured grid. To solve this problem, a novel stencil adaptive (Ding and Shu 2006) LBM was proposed by Wu and Shu (2011) recently. In this algorithm, two different types of stencils, named orthogonal (denoted as "+") and diagonal (denoted as "×") structures ("+" is used to represent a configuration of 5-points symmetric stencil, where mesh points are distributed along the horizontal and vertical lines. While, the other stencil configuration is represented by "×", where mesh points are distributed along diagonal lines), appear alternatively during the mesh refinement process. It is interesting to note that combination of these two types of stencils has the same configuration as D2Q9 (2 dimensions with 9 discrete lattice velocity directions) lattice velocity model. Attributed to the consistency between grid structure and lattice model, an identical lattice relaxation parameter can be used (Wu and Shu 2011). Moreover, complex interpolation of physical variables and modification of collision term can be avoided. Detailed analysis of convergence and efficiency of stencil adaptive LBM for single phase flow can be found in the work of Wu and Shu (2011). In order to take advantage of the phase-field LBM and obtain high resolution at the same time, it is a good choice to develop a stencil adaptive phase-field LBM for multiphase flow simulation.

1.2.3.2 LBM for multiphase flow with density contrast

Besides accuracy and efficiency balance, another major issue for phase-field LBM is simulation of multiphase flows with density contrast. In the last decade, the phase-field LBM has been successfully applied to simulate a wide range of multiphase flow phenomena (Aidun and Clausen 2010). Nevertheless, the pioneering phase-field models are only feasible for multiphase flows with small density contrast and it is nontrivial to adapt them to the multiphase flows subject to even moderate density variation. The difficulty is mainly caused by the sharp variation of density across the interface. Hence, proper treatment of high density gradient across the interface is critical to ensure stability of simulation (Lee and Lin 2005). Besides the above issue that also exists in conventional N-S solvers (Ding et al. 2007), LBM encounters additional constraints in the simulation of multiphase flow with density contrast. These constraints are associated with intrinsic properties of LBM. It is well known that LBM has two basic processes. They are streaming and collision processes. From Chapman-Enskog expansion analysis, it is found that the streaming process is to recover the convection and pressure gradient terms of N-S equation while the collision process is to recover the viscous term of N-S equation. The pressure and density are linked by the equation of state, $p = \rho c_s^2$, where c_s is the speed of sound. In the lattice Boltzmann framework, c_s is a constant for a selected lattice velocity model. For this case, the pressure variation directly depends on the density variation. This application has no problem for incompressible single phase flows as both pressure and density change very little in the flow field. However, when it is applied to the multiphase flow with density contrast, it may lead to unphysical solution. Physically, it is known that the fluid-fluid interface is a contact discontinuity, where the density is discontinuous but the pressure and velocity are continuous across the interface. When $p = \rho c_s^2$ is directly applied for multiphase flow simulation, it implies that pressure is also

discontinuous across the interface. This is physically incorrect. As the streaming process of LBM can only recover ρc_s^2 for the pressure term, we can introduce a forcing term of $\nabla(p-\rho c_s^2)$ in LBE in order to simulate multiphase flows with density contrast by LBM. This technique has been used by many researchers such as He et al. (1999) and Lee and Lin (2005). Another constraint is related to numerical instability of LBM computation. Although LBM is a weak compressible method (Uriel et al. 1987, Guo et al. 2000), it is usually limited for application to incompressible flows. In LBM, the particle distribution function is used to measure the density and momentum. Thus, the variation of particle distribution function is closely related to the variation of density. For the incompressible single phase flow, the density variation in the flow field is very little, so does the variation of particle distribution function. This property ensures very stable computation of LBM for the single phase flow. On the other hand, when the multiphase flow with density contrast is considered, the density will have a large variation across the interface. For this case, the particle distribution function will also encounter a large variation, which may cause a severe instability of LBM computation. To remove this difficulty, some efforts have been made. An interesting work was given by He et al. (1999), who introduced an incompressible transformation to change the particle distribution function for density and momentum into that for pressure and momentum. As pressure is smooth in the whole flow field, the high variation of particle distribution function is avoided. Later, Lee and Lin (2005) (for simplicity, it is called L-L model in this thesis) also adopted the same incompressible transformation but went further to propose a series of stable discretization schemes to enhance numerical stability. The stabilization schemes include the use of stress form of surface tension force for the pressure and momentum LBE and the potential form of surface tension force for the order parameter LBE, the second-order biased/mixed difference approximation in the pre-streaming collision

step and the central difference approximation in the post-streaming collision step. Recently, Zheng et al. (2006) also presented a model (for simplicity, it is termed Z-S-C model in this thesis) to avoid high variation of particle distribution function. Like the work of He et al. (1999) and Lee and Lin (2005), Z-S-C model also uses two sets of LBEs. One set of LBE is used for interface capturing, which can recover the Cahn-Hilliard (C-H) equation (Cahn and Hilliard 1958) with the second order of accuracy (Zheng et al. 2005). The other set of LBE is utilized for simulation of flow field, where the particle distribution function is used to measure the mean density and momentum. For any multiphase flow problem, the mean density changes very little in the whole flow field. So, the variation of particle distribution function in the Z-S-C model is very small. This good property makes its numerical computation very stable and efficient (Zheng et al. 2006). On the other hand, we have to indicate that since the particle distribution function is directly used to measure the mean density, the effect of local density variation cannot be properly considered in the momentum equation when the multiphase flow with density contrast is solved. In order to keep the good stability condition and high computational efficiency of the Z-S-C model, an improved model for correct consideration of density contrast will be developed in this work.

1.3 Modeling of Solid-Fluid Interactions

The preceding section reviewed modeling of multiphase flow. This section will introduce the other essential element in modeling of solid-multiphase flow interactions, that is, implementation of solid boundary conditions.

In fluid mechanics, problems involving interactions between fluids and structures are ubiquitous. To simulate such problems, implementation of boundary conditions such as

Dirichlet and Neumann boundary conditions is inevitable. A conceptual straightforward way is to use a body-conformal method. In the body-conformal method, grid is generated to fit solid shape. Subsequently, governing equations are naturally discretized involving solid geometrical information and boundary conditions can also be readily imposed. In this way, an accurate solution can be yielded (Mittal and Iaccarino 2005). Nevertheless, it is sometimes impractical to generate a body-conformal grid especially when a complex geometry or a moving boundary is present in the flow field. In contrast with body-conformal method, a more feasible and robust way is to employ non-body-conformal methods (Peskin 1972, LeVeque and Li 1994, Fedkiw et al. 1999, Lee and Leveque 2003, Mittal and Iaccarino 2005, Le et al. 2006). In non-body-conformal methods, governing equations can be solved on a fixed Cartesian (Eulerian) grid, while influence of boundary is depicted by adding a forcing or source term into the governing equations. Depending on the way to treat forcing terms, the non-body conformal methods can be further divided into: sharp interface methods and diffuse interface methods. A representative method in the first category is the Immersed Interface Method (IIM) developed by LeVeque and Li (1994). A typical feature of IIM is that the jump conditions of physical parameters are applied across the interface. Such a treatment enables IIM to achieve second order accuracy but also entails complex implementation. The application of IIM has later been extended to three-dimensional (3D) simulation (Xu and Wang 2008, Xu 2011), moving boundary problems (Li and Lai 2001, Xu and Wang 2006), and also problems involving elastic membranes (Lee and Leveque 2003).

In contrast with sharp interface methods, the diffuse interface methods manipulate the effect of immersed boundary as a diffusive body force. When a jump condition is applied in shape interface methods, it is usually necessary to distinguish whether a fluid node is inside or outside of boundary and to reconstruct information according to interface's normal direction.

However, in the diffuse interface methods, these procedures are unnecessary. This can greatly simplify simulation procedure and enable a much more robust simulation for 3D and moving boundary problems. The most well-known diffuse interface methods might be Immersed Boundary Method (IBM) developed by Peskin (1972). Since his pioneering work, IBM has undergone continuous development in accurate evaluation of forcing terms. In Peskin's original work (Peskin 1972), solid boundary is treated as being elastic. A restoring force is first evaluated on the boundary and then distributed back to the flow field through discrete delta function. The relationship between the restoring force (generated by distortion of boundary) and body deformation is governed by the Hooke's law, in which a user-defined coefficient is involved. To avoid usage of arbitrary coefficient, a direct forcing method was introduced by Mohd-Yusof (1997) and also applied by Fadlun et al. (2000). In this method, the N-S equations are employed to compute the force on the boundary. More recently, a boundary condition-enforced IBM was developed by Wu and Shu (2009). In the previous force calculation schemes, the restoring force is pre-calculated and there is no mechanism to enforce the no-slip boundary condition. In contrast, Wu and Shu's IBM considers the restoring force as unknown and it is determined in a way that the no-slip boundary condition is enforced. In this manner, flow penetration that is observed in the previous IBM simulation is proved to be effectively eliminated. In addition to the advances in algorithms, application of IBM for structure-fluid interactions has also been extended to a broad range. The application of IBM includes particulate flow (Fogelson and Peskin 1988, Feng and Michaelides 2004, Wu and Shu 2009), flexible filament (Zhu and Peskin 2002), structure-turbulent flow interactions (Balaras 2004) to name a few. An elegant review of kindred topics is provided by Mittal and Iaccarino (2005). It can be seen that tremendous effort has been devoted to refine IBM. However, most works are restricted to the Dirichlet boundary condition over decades. To the best of our knowledge, research that aims at extending the

IBM to depict the Neumann boundary condition is very limited. This remarkably restricts the application of IBM in CFD since physical phenomena associated with Neumann boundary conditions are extremely diverse. One of the instances is the solid-multiphase flow interactions. To study these problems in the phase-field framework, the no-slip boundary condition is still utilized. Additionally, two Neumann boundary conditions are used to govern the variation of composition on a solid boundary (Jacqmin 2000). Although many works have been done by the phase-field method, most reported works investigate three-phase (two fluids with solid) interaction on smooth surface or, at most, grooved surface with simple geometries represented by straight lines. This is mainly caused by tedious implementation of Neumann boundary conditions on a curved geometry. To overcome this difficulty, an IBM-based algorithm that can handle Neumann boundary conditions will be instrumental.

1.4 Objectives of the Thesis

Based on the previous literature review, to establish an efficient numerical framework to study the solid-multiphase flow interactions, there are four major objectives in this work. Concerning multiphase flow simulation, there are two objectives. One is to develop a stencil adaptive phase-field LBM to balance accuracy and efficiency. The other is to develop a phase-field LBM for multiphase flow with density contrast. On other hand, with respect to boundary condition implementation, the third major objective of this thesis is to develop an IBM for Neumann boundary conditions and to create a breakthrough in the long existing limitation that IBM can only handle Dirichlet boundary conditions for various solid-fluid interactions. Last but not least, application of the developed method to simulate solid-multiphase flow interactions will also be demonstrated. These objectives are illustrated further in the following context:

(1) To develop a stencil adaptive phase-field lattice Boltzmann solver for two-dimensional (2D) incompressible multiphase flows. In order to achieve high resolution of interface within affordable computational consumption, the stencil adaptive technique will be implemented in phase-field LBM simulation. Attributed to the consistency between stencil grid-structure and D2Q9 lattice model, the developed method is expected to be freed from complicated spatial and temporal interpolation. Both the accuracy and efficiency of the proposed method will be studied through simulation of several multiphase flow problems.

(2) To develop a phase-field LBM for multiphase flow with density contrast. A novel phase-field LBM will be developed to improve Z-S-C model (Zheng et al. 2005) for correct consideration of density contrast. To correctly consider the effect of local density variation in the momentum equation, the particle distribution function in the LBE is initially used to measure the local density and momentum. Then, to improve numerical stability, a transformation which is similar to that used in the work of He et al. (1999) will be introduced to change the particle distribution function for the local density and momentum into that for the mean density and momentum. As a consequence, the present model, on one hand, enjoys the good property of using the particle distribution function for mean density and momentum, and on the other hand, can correctly consider the effect of density contrast in the momentum equation. The proposed method will be verified in detail through simulation of 2D/3D steady and unsteady multiphase flow problems.

(3) To develop an immersed boundary method for Neumann boundary conditions for solid-fluid interactions. In this work, we will make the first endeavour to extend the

application of IBM with Neumann boundary condition. To achieve this, we will start from the physical conservation law, and view the Neumann boundary condition as contribution of flux from the boundary to a dependent variable in a control volume. The flux contribution from the boundary can be directly linked to the correction of dependent variable. The developed IBM for Neumann boundary conditions will be used consistently with the boundary condition-enforced IBM for Dirichlet boundary conditions. The solid-fluid interactions involving Dirichlet and/or Neumann boundary conditions will be presented.

(4) To apply the immersed boundary-phase field-lattice Boltzmann method to study solid-multiphase flow interactions. The developed IBM (for both Dirichlet and Neumann boundary conditions) will be used together with the phase-field lattice Boltzmann method to treat two distinct types of interfaces. To be concrete, the IBM will be used to implement boundary conditions for solid surface. Concurrently, the phase-field lattice Boltzmann method will be used to capturing the liquid-liquid interface. The application of the developed method for steady and unsteady solid-multiphase flow interactions will be presented.

1.5 Organization of the Thesis

The rest of thesis is organized as follows:

To establish the groundwork of this thesis, Chapter 2 will first introduce the free energy and phase-field theory. Subsequently, the phase-field model in both Navier-Stokes description

and lattice Boltzmann framework will be illustrated. Furthermore, wetting boundary conditions for solid-multiphase flow interactions in the phase-field framework will also be presented. Finally, a brief conclusion will be given at the end of this Chapter. To validate the current code, numerical examples including rotation of a Zalesak's disk, deformation of a circular interface and droplet deformation in the shear flow are presented. The obtained numerical results are compared with the theoretical results and data in the literature.

Chapter 3 presents the development of a stencil adaptive phase-field lattice Boltzmann method for two-dimensional multiphase flow simulation. First, the stencil adaptive algorithm will be illustrated. Thereafter, a detailed description of stencil adaptive algorithm for phase-field lattice Boltzmann equations and evaluation of relevant spatial derivatives will be provided. The proposed algorithm will be verified with respect to accuracy and efficiency through simulation of stationary bubble, bubble rising in quiescent fluid and droplet spreading in the partial wetting regime.

In Chapter 4, development of a phase-field lattice Boltzmann method for simulation of multiphase flow with density contrast will be presented. In this Chapter, the Z-S-C model and the incompressible transformation will be reviewed in the first place. It is then followed by demonstration of a newly developed phase-field LBM for multiphase flow with density contrast. The proposed algorithm will be verified through 2/3D steady and unsteady numerical examples including: viscous coupling, Rayleigh-Taylor instability, droplet splash, droplet collision and droplet impact on solid considering dynamic contact angle.

Chapter 5 demonstrates the development of an immersed boundary method for solid-fluid interactions involveing Dirichlet and/or Neumann boundary conditions. First, a brief introduction of immersed boundary method is presented. Secondly, a boundary condition-enforced IBM for Dirichlet boundary condition will be illustrated. Thirdly, the following subsection is devoted to elaborate the idea to implement Neumann boundary condition in IBM in detail. Thereafter, the application of IBM for various solid-fluid interaction problems will be demonstrated. The numerical examples include: solid-single phase flow interactions such as flow over a circular cylinder, fish motion at high Reynolds number and flow over a sphere as well as solid-multiphase flow interaction problems such as a transition layer formed on solid surface.

Chapter 6 presents application of immersed boundary phase-field lattice Boltzmann method to study solid-multiphase flow interactions. An introduction of solid-multiphase flow interactions will be provided in the first place. Secondly, the simulation procedures will be summarized. Subsequently, numerical examples will be presented. The method is first applied to simulate dynamics cases including de-wetting process and droplet spreading on a smooth surface in the partial wetting regime for validation. Moreover, simulation of droplet spreading on a curved surface will also be performed. Additionally, the ability of the current algorithm to handle complex geometries will be demonstrated by simulation of the contact line dynamics on single and two alongside circular cylinders as well as impulsive motion of a submerged cylinder. Furthermore, extension of the developed method to simulate 3D moving contact line problems will also be presented.

Lastly, a conclusion of the present work and recommendation for future studies will be presented in Chapter 7 to end this thesis.

Chapter 2

Free Energy-Based Phase-Field Method

The works in this thesis are based on the phase-field lattice Boltzmann method. Thus, to establish the groundwork, Chapter 2 is devoted to introducing free energy theory and fundamental governing equations in both Navier-Stokes formulation and lattice Boltzmann framework. Moreover, the boundary conditions in the phase-field method for solid-multiphase flow interactions will also be presented. The ability of the phase-field LBM introduced in this Chapter to simulate multiphase flow problems are demonstrated through several numerical cases including: rotation of a Zalesak's disk, deformation of a circular interface and three-dimensional droplet deformation in shear flow.

2.1 Free Energy Theory

Before presenting the governing equations, it would be helpful to introduce free energy theory. In the phase-field method, an order parameter ϕ (Anderson et al. 1998), is introduced to characterize the phases and interface. It holds a constant value ($\pm\phi_{Bulk}$) in the bulk regions (where the change of density is negligible) while changes smoothly across the interface. Considering a system of two incompressible immiscible fluids, the Helmholtz free energy functional of a system can be written as

$$\Im = \int_V \left[A\Psi(\phi) + \frac{\kappa}{2}(\nabla\phi)^2 \right] dV \tag{2.1}$$

The above equation means that the total free energy $\Im$ (over the flow domain V) consists of bulk free energy density $A\Psi(\phi)$ and interface energy $\frac{\kappa}{2}(\nabla\phi)^2$. For the bulk free energy density, a commonly used double-well form is used. It takes the form of

$$\Psi(\phi) = (\phi - \phi_{Bulk})^2 (\phi + \phi_{Bulk})^2 \tag{2.2}$$

In Eqs. (2.1) and (2.2), there are two coefficients κ and A. These two coefficients are related to interface width w and surface tension σ in such a way that the interface width is proportional to $\sqrt{\kappa/A}$ and the surface tension is proportional to $\sqrt{\kappa A}$ (Jacqmin 1999, Papatzacos 2002). In numerical simulation, interface width and surface tension are usually given so that κ and A can be evaluated based on them. To be specific, the coefficients κ and A can be evaluated through

$$w = \frac{\sqrt{2\kappa/A}}{\phi_{Bulk}} \tag{2.3}$$

$$\sigma = \frac{4\sqrt{2\kappa A}}{3}\phi_{Bulk}^3 \tag{2.4}$$

Additionally, in the free energy framework, the chemical potential μ_ϕ of the composition variable ϕ is defined as the rate of change of free energy with respect to the phase concentration. It can be written as

$$\mu_\phi = \frac{\partial\Im}{\partial\phi} - \nabla\cdot\frac{\partial\Im}{\partial\nabla\phi} = 4A\phi(\phi^2 - \phi_{Bulk}^2) - \kappa\nabla^2\phi \tag{2.5}$$

2.2 Governing Equations in Navier-Stokes Formulation

Coupled with the free energy theory, the governing equations of an incompressible viscous fluid system can be written as

$$\nabla \cdot \boldsymbol{u} = 0 \tag{2.6}$$

$$\frac{\partial(\rho \boldsymbol{u})}{\partial t} + \nabla \cdot (\rho \boldsymbol{u}\boldsymbol{u}) = -\nabla p + \nabla \cdot \left[\mu \left(\nabla \boldsymbol{u} + \nabla \boldsymbol{u}^T \right) \right] + \boldsymbol{F}_b \tag{2.7}$$

where $\boldsymbol{u}$ is the velocity vector, μ is the dynamic viscosity and p is pressure which will be defined later. In addition, $\boldsymbol{F}_b$ is the body force and the exact expression depends on the physical problem studied. For example, in a bubble rise case, $\boldsymbol{F}_b$ can be buoyancy $g\Delta\rho$ (g is gravity acceleration and $\Delta\rho$ is the density difference between two fluids). Different from governing equations for single phase fluid, the surface tension can be incorporated in term ∇p. It takes the form of

$$\nabla p = \phi \nabla \mu_\phi + \nabla p_0 \tag{2.8}$$

This equation can be rearranged as

$$\nabla p = \nabla \left(\phi \mu_\phi + p_0 \right) - \mu_\phi \nabla \phi \tag{2.9}$$

Substituting Eq. (2.9) into Eq. (2.7), the momentum equation for a binary fluid system can also be written as

$$\frac{\partial(\rho \boldsymbol{u})}{\partial t} + \nabla \cdot (\rho \boldsymbol{u}\boldsymbol{u}) = -\nabla \left(\phi \mu_\phi + p_0 \right) + \mu_\phi \nabla \phi + \nabla \cdot \left[\mu \left(\nabla \boldsymbol{u} + \nabla \boldsymbol{u}^T \right) \right] + \boldsymbol{F}_b \tag{2.10}$$

In addition to the flow field, the change of the phase-field is governed by the Cahn-Hilliard equation

$$\frac{\partial \phi}{\partial t} + (\boldsymbol{u} \cdot \nabla)\phi = M\nabla^2 \mu_\phi \tag{2.11}$$

where M is a parameter named as mobility. It can be seen from Eq. (2.11) that the phase-field is not only influenced by convection but also by diffusion caused by the gradient of chemical potential μ_ϕ.

2.3 Governing Equations in Lattice Boltzmann Framework

The free energy-based phase-field theory is an interface capturing method which can be used together with different flow field solvers. The preceding section gives the governing equations in the Navier-Stokes formulation. Besides N-S solver, an alternative lattice Boltzmann method (LBM) has attracted much interest for multiphase flow simulation recently. It enjoys advantages such as easy programming and suitable for parallel computation as introduced in Chapter 1. Therefore, the phase-field LBM will be used for multiphase flow simulation in this work. Considering two immiscible incompressible fluids, the lattice Boltzmann equation (LBE) for the flow field can be written as

$$f_\alpha(\boldsymbol{x} + \boldsymbol{e}_\alpha \delta t, t + \delta t) = f_\alpha(\boldsymbol{x}, t) + \Omega_\alpha \tag{2.12}$$

Here, f_α is the density distribution function, δt is the time step and $\boldsymbol{e}_\alpha$ is the lattice velocity. The collision term Ω_α with additional force terms reads as

$$\Omega_\alpha = \frac{f_\alpha^{eq}(\boldsymbol{x}, t) - f_\alpha(\boldsymbol{x}, t)}{\tau} + \frac{w_\alpha}{c_s^2}\left(1 - \frac{1}{2\tau}\right)\left[(\boldsymbol{e}_\alpha - \boldsymbol{u}) + \frac{(\boldsymbol{e}_\alpha \cdot \boldsymbol{u})}{c_s^2}\boldsymbol{e}_\alpha\right](\mu_\phi \nabla \phi + \boldsymbol{F}_b)\delta t \tag{2.13}$$

with

$$\upsilon = \left(\tau - 0.5\right)c_s^2 \delta t \tag{2.14}$$

In Eqs. (2.12) and (2.13), w_α is a coefficient, $\boldsymbol{e}_\alpha$ is the lattice velocity and c_s is the speed of sound in LBM. Their values depend on lattice velocity model chosen. The most commonly used lattice model including D2Q9, D3Q15 and D3Q19 (denoted as DnQm, where *n* indicates space dimension and *m* indicates the speed model) as sketched in Fig. 2.1. The main parameters of these lattice velocity models are listed in Table 2.1. In addition, τ is the relaxation parameter, and υ in Eq. (2.14) is the kinematic viscosity of fluid. The equilibrium distribution function that satisfies the conservation laws takes the form of

$$f_\alpha^{eq} = w_\alpha A_\alpha + w_\alpha \rho \left(\frac{\boldsymbol{e}_\alpha \cdot \boldsymbol{u}}{c_s^2} + \frac{\left(\boldsymbol{e}_\alpha \cdot \boldsymbol{u}\right)^2 - c_s^2 \left|\boldsymbol{u}\right|^2}{2c_s^4} \right) \tag{2.15}$$

The coefficients for D2Q9 and D3Q15 models are

$$\begin{cases} A_0 = 9\rho/4 - 5\left(\phi\mu_\phi + \rho c_s^2/3\right)/\left(4c_s^2\right) \\ A_{1-\alpha} = \left(\phi\mu_\phi + \rho c_s^2\right)/c_s^2 \end{cases} \tag{2.16}$$

where α equals 8 and 14 for D2Q9 and D3Q15 model, respectively. Moreover, the macroscopic variables can be evaluated through the conservation laws

$$\rho = \sum_\alpha f_\alpha \tag{2.17}$$

$$\rho \boldsymbol{u} = \sum_\alpha f_\alpha \boldsymbol{e}_\alpha + \frac{1}{2}\left(\mu_\phi \nabla\phi + \boldsymbol{F}_b\right)\delta t \tag{2.18}$$

In addition to the flow field, the other set of LBE is used to capture the interface change (Zheng et al. 2005, 2008). It is formed by the distribution function g_α

$$g_\alpha\left(\boldsymbol{x}+\boldsymbol{e}_\alpha\delta t,t+\delta t\right)=g_\alpha\left(\boldsymbol{x},t\right)+\left(1-q\right)\left[g_\alpha\left(\boldsymbol{x}+\boldsymbol{e}_\alpha\delta t,t\right)-g_\alpha\left(\boldsymbol{x},t\right)\right]+\Omega_\alpha \tag{2.19}$$

where Ω_α represents the collision term and it reads as

$$\Omega_\alpha=\frac{g_\alpha^{eq}(\boldsymbol{x},t)-g_\alpha(\boldsymbol{x},t)}{\tau_\phi} \tag{2.20}$$

Here, g_α^{eq} represents the equilibrium distribution function and τ_ϕ is the relaxation parameter for ϕ field. The equilibrium distribution function g_α^{eq} satisfies the following conservation laws

$$\phi=\sum_\alpha g_\alpha^{eq} \tag{2.21}$$

The mobility parameter is

$$M=q\left(\tau_\phi q-0.5\right)\delta t\Gamma \tag{2.22}$$

Here, $q=1/\left(\tau_\phi+0.5\right)$ and Γ is the characteristic mobility. Furthermore, the equilibrium distribution function takes the form of

$$g_\alpha^{eq}=A_\alpha+B_\alpha\phi+C_\alpha\phi\boldsymbol{e}_\alpha\cdot\boldsymbol{u} \tag{2.23}$$

Moreover, the relevant coefficients for g_α^{eq} are

$$A_\alpha=\begin{cases}-D\Gamma\mu_\phi, & \alpha=0\\ \dfrac{1}{2}\Gamma\mu_\phi, & \alpha\neq0\end{cases},\qquad B_\alpha=\begin{cases}1, & \alpha=0\\ 0, & \alpha\neq0\end{cases},\qquad C_\alpha=\frac{1}{2q} \tag{2.24}$$

where D is the dimension. The D2Q5 and D3Q7 lattice velocity models are used for interface capturing LBE in two and three-dimensional simulations, respectively. The above

introduced LBE can recover Cahn-Hilliard equation with second order accuracy (Zheng et al. 2005).

2.4 Wetting Boundary Conditions

A general phase-field framework for multiphase flow without considering the presence of a solid boundary has been introduced previously. In this subsection, modeling of a partial wetting surface will be addressed. When a solid surface interacts with multiphase flows, the surface may be neutral or partially favored to be wetted by one fluid. This surface characteristic is referred to as wettability. In the phase-field method, wettability can be represented by a wall free energy in the total free energy functional

$$\Im = \int_V \left[A\Psi(\phi) + \frac{\kappa}{2}(\nabla\phi)^2 \right] dV + \int_S \Psi_s(\phi_s)\, dS \tag{2.25}$$

where S denotes the solid surface, ϕ_s is the order parameter on the wall and $\Psi_s(\phi_s)$ is the wall free energy density that takes the form of

$$\Psi_s(\phi_s) = -\tilde{\omega}\phi_s \tag{2.26}$$

where $\tilde{\omega}$ describes the essential feature of a solid surface and it is called as wetting potential. Minimizing the total free energy functional gives the boundary condition

$$\kappa \boldsymbol{n} \cdot (\nabla\phi) = \Psi_s'(\phi_s) = -\tilde{\omega} \tag{2.27}$$

where $\boldsymbol{n}$ indicates the local unit outward normal on a solid surface. It can be seen that it is a Neumann boundary condition for the order parameter. Moreover, four equilibrium solutions of the order parameter on the wall are (Papatzacos 2002)

$$\begin{cases} \phi_{s1} = -\phi_{Bulk}\sqrt{1+|\omega|} \\ \phi_{s2} = -\phi_{Bulk}\sqrt{1-|\omega|} \\ \phi_{s3} = \phi_{Bulk}\sqrt{1-|\omega|} \\ \phi_{s4} = \phi_{Bulk}\sqrt{1+|\omega|} \end{cases} \tag{2.28}$$

with the non-dimensional wetting potential ω defined as

$$\omega = \frac{\tilde{\omega}}{\phi_{Bulk}^2\sqrt{2\kappa A}} \tag{2.29}$$

The relation between ω and the equilibrium contact angle reads

$$\cos\theta_{eq} = \frac{1}{2}\left[(1+\omega)^{\frac{3}{2}} - (1-\omega)^{\frac{3}{2}}\right] \tag{2.30}$$

Based on the monotonically decreasing relationship (as shown in Fig. 2.2) established by Eq. (2.30), the value of ω can be uniquely determined with a given equilibrium contact angle. Thereafter $\tilde{\omega}$ can also be calculated in a straightforward way. In addition to the boundary condition expressed by Eq. (2.27), a zero mass flux condition of the chemical potential μ_ϕ is applied

$$\boldsymbol{n}\cdot\left(\nabla\mu_\phi\right)_s = 0 \tag{2.31}$$

It is a Neumann boundary condition for the chemical potential. To sum up, the boundary conditions that should be enforced on a solid surface are

$$\boldsymbol{u}_s = 0 \tag{2.32}$$

$$\left(\frac{\partial\phi}{\partial\boldsymbol{n}}\right)_s = -\frac{\tilde{\omega}}{\kappa} \tag{2.33}$$

$$\left(\frac{\partial \mu_\phi}{\partial \boldsymbol{n}}\right)_s = 0 \tag{2.34}$$

2.5 Numerical Validations

In this subsection, several multiphase flow problems were simulated to validate the models and the codes. The numerical examples include: rotation of a Zalesak's disk, deformation of a circular interface and 3D droplet deformation in shear flow.

2.5.1 Rotation of a Zalesak's disk

A benchmark case, rotation of Zalesak's disk (Zheng et al. 2005), is simulated to examine the accuracy of interface capturing of the current codes. A disk with radius of $0.4L$ attached with a slot of $0.075L$ width is centered at $(0.5L, 0.5L)$ in a flow field of $L \times L$ ($L = 120$ lattice units). The order parameter is set as 1 inside the disk and -1 outside the disk. Periodic boundary condition is applied on all boundaries. In this case, the velocity field is symmetric and takes form of

$$u = -U_0 \pi (x/L - 0.5) \tag{2.35}$$

$$v = U_0 \pi (y/L - 0.5) \tag{2.36}$$

where U_0 is set as 0.01 in the current simulation. The rotation of a Zalesak's disk is shown in Fig. 2.3 at 0, 0.25T, 0.5T, 0.75T and T of rotation (from top to bottom, left to right). It can be seen that during the rotation of the disk, shape of both the circle and slot is captured well.

Additionally, Table 2.2 compares the absolute area loss ($\left|Area_{Theoretical} - Area_{Numerical}\right|$) as well as the relative area loss ($\left|Area_{Theoretical} - Area_{Numerical}\right| / Area_{Theoretical}$) for Zalesak's disk rotation on grids 121×121 and 241×241. It can be seen that the area loss is very small. It is 0.065 even with course grids 121×121.

2.5.2 Deformation of a circular interface

In addition to rotation of a complex topology, a more challenging case that involves topology change of interface is simulated in this subsection. In this case, a circle with radius of $0.2L$ is initially centered at $(0.5L, 0.3L)$ in a computational domain of $L\times L$ ($L=120$ lattice units). The velocity field is given by (Rudman 1997, Zheng et al. 2005)

$$u = -U_0\pi\cos\left[\pi\left(x/L-0.5\right)\right]\sin\left[\pi\left(y/L-0.5\right)\right] \tag{2.37}$$

$$v = U_0\pi\sin\left[\pi\left(x/L-0.5\right)\right]\cos\left[\pi\left(y/L-0.5\right)\right] \tag{2.38}$$

This velocity field is imposed on the whole field when $0\le t\le T$ while for $T<t\le 2T$, the sign of u and v are reversed. The interface deformation during $0\le t\le 2T$ is shown in Fig 2.4. It can be seen from Fig. 2.4(a) to 2.4(c) that the circle is rotated anticlockwise and deformed during $0\le t\le T$. When $T\le t\le 2T$ (Fig. 2.4(d) and (e)), the deformed circle is rotated back and returned to its original shape. To demonstrate the superior ability of interface capturing by the present method, a result by VOF method (Zheng et al. 2005) was also shown in Fig. 2.5. More information about VOF methods' simulation of this problem can be found in the work of Rudman (1997). It can be seen that the circular shape caputred by the present method has little distortion and very smooth interface.

2.5.3 Droplet deformation in shear flow

Apart from the preceding 2D cases, 3D problems will be demonstrated hereafter. In this subsection, simulation of a 3D droplet in shear flow was performed.

In this case, a droplet is deformed between two parallel moving walls. A droplet with initial radius *R* is centered in the computational domain. The distance between upper and lower walls is denoted as *H* and the walls are moving with velocity U_{upper} and U_{lower}. In this context, the shear rate $\dot{\gamma}$ and Capillary number are defined as $\dot{\gamma} = \left(U_{upper} - U_{lower}\right)/H$ and $Ca = \eta_1 \dot{\gamma} R/\sigma$ (the subscripts 1 and 2 indicate properties of droplet and surrounding fluid, respectively). To perform validation, the parameters are first set the same as those in the literature (van der Graaf et al. 2006, Huang 2009). To be specific, $r_\rho = \rho_1/\rho_2 = 1$, Ca took the value from 0.05 to 0.3 with spacing of 0.05. The droplet of radius 15 is initially centered in a domain of $120 \times 30 \times 60$. Owing to the symmetry of this problem (symmetric to x-z plane), only half of the domain is considered. The droplet deformation parameter (defined as $D_f = \left(R_L - R_B\right)/\left(R_L + R_B\right)$ where R_L and R_B are major and minor axis of ellipse) is compared with data in the literature in Fig. 2.6. The important parameters are summarized in Table 2.3. The theoretical result is given by $D_f = 35Ca/32$ (Huang 2009), which is based on small Capillary number assumption. From Fig. 2.6, it can be seen that the present results show good comparison with the theoretical prediction at low Capillary number ($Ca < 0.2$). However, when the Capillary number increases, the numerical results show nonlinear deviation from the theoretical results, which is the same as that obtained by Huang (2009). In addition, it also can be seen that compared with Huang's result, the present result better

approximates the theoretical result. This is because larger computational domain and higher resolution are used in the present simulation. Moreover, the droplet shape under different Capillary number is presented in Fig. 2.7. It can be seen clearly that the droplet undergoes obvious deformation when the Capillary number is equal to 0.3.

2.6 Concluding Remarks

The phase-field framework was introduced in this Chapter to provide a background for subsequent Chapters. In summary, the free energy theory was introduced in the first place. Thereafter, the governing equations of phase-field method in both Navier-Stokes formulation and lattice Boltzmann framework were described. Additionally, considering the interest of this thesis, wetting boundary conditions were also elaborated in this Chapter. Moreover, the introduced phase-field LBM was validated through simulation of rotation of a Zalesak's disk, deformation of a circular interface and 3D droplet deformation in shear flow. The current results demonstrate good comparison with theoretical and numerical results in the literature.

Table 2.1 Parameters of DnQm lattice models (n indicates space dimension and m means the speed model)

Model	Lattice vector $\boldsymbol{e}_\alpha$	Weight ω_α	c_s^2
D2Q9	$(0,0)$ $(\pm1,0),\ (0,\pm1)$ $(\pm1,\pm1)$	4/9 1/9 1/36	1/3
D3Q15	$(0,0,0)$ $(\pm1,0,0),\ (0,\pm1,0),\ (0,0,\pm1)$ $(\pm1,\pm1,\pm1)$	16/72 8/72 1/72	1/3
D3Q19	$(0,0,0)$ $(\pm1,0,0),\ (0,\pm1,0),\ (0,0,\pm1)$ $(\pm1,\pm1,0),\ (\pm1,0,\pm1),\ (0,\pm1,\pm1)$	12/36 2/36 1/36	1/3

Table 2.2 Area loss for the Zalesak's disk rotation

	Exact area	Numerical area	Absolute area loss	Relative area loss
Grids 121×121	4150.01	3879.49	270.52	0.065
Grids 241×241	16860.30	16349	511.31	0.03

Table 2.3 Important parameters in droplet deformation

Definition	Expression
Shear rate	$\dot{\gamma} = \left(U_{upper} - U_{lower}\right)/H$
Capillary number	$Ca = \eta_1 \dot{\gamma} R/\sigma$
Droplet deformation parameter	$D_f = \left(R_L - R_B\right)/\left(R_L + R_B\right)$

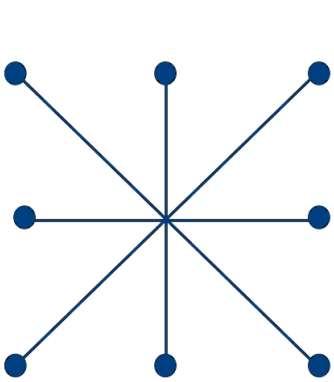

(a) D2Q9

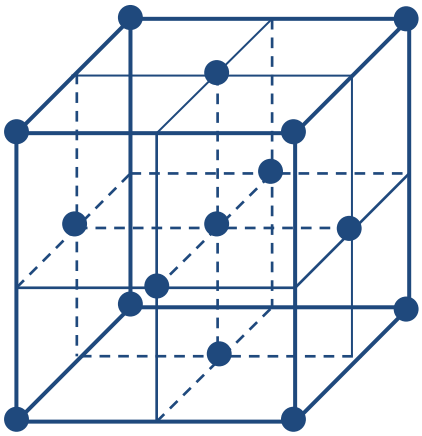

(b) D3Q15

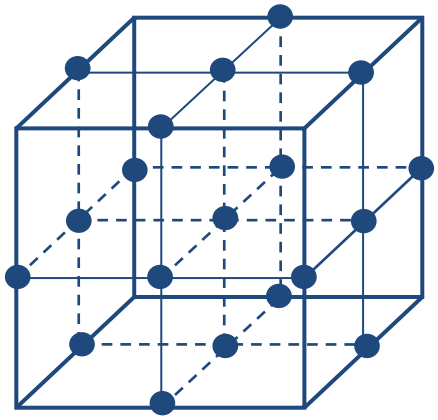

(c) D3Q19

Fig. 2.1 Sketches of some DnQm lattice velocity models

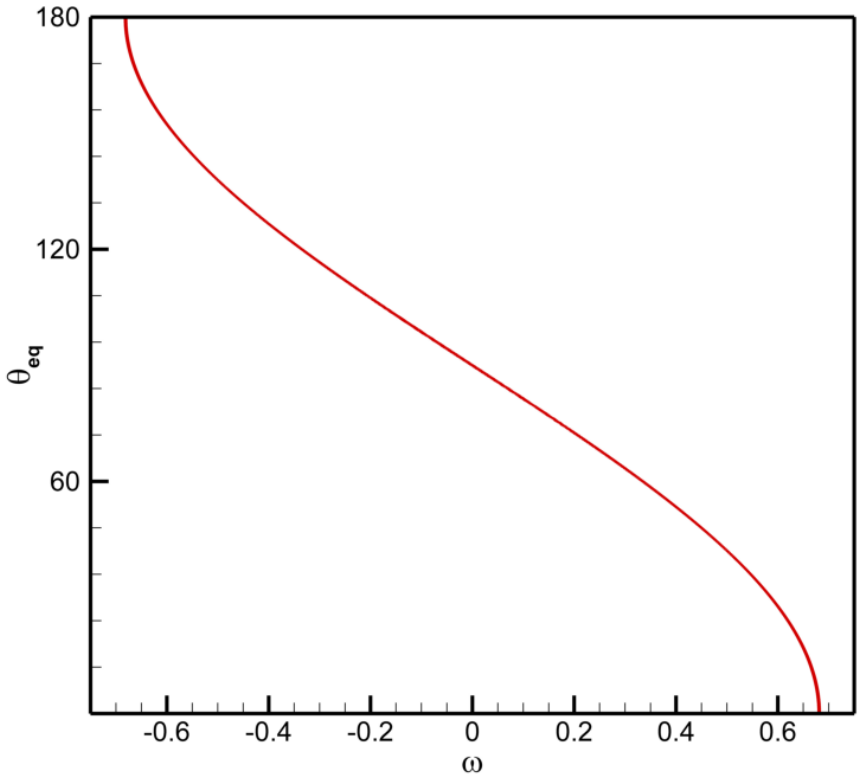

Fig. 2.2 The non-dimensional wetting potential versus the equilibrium contact angle

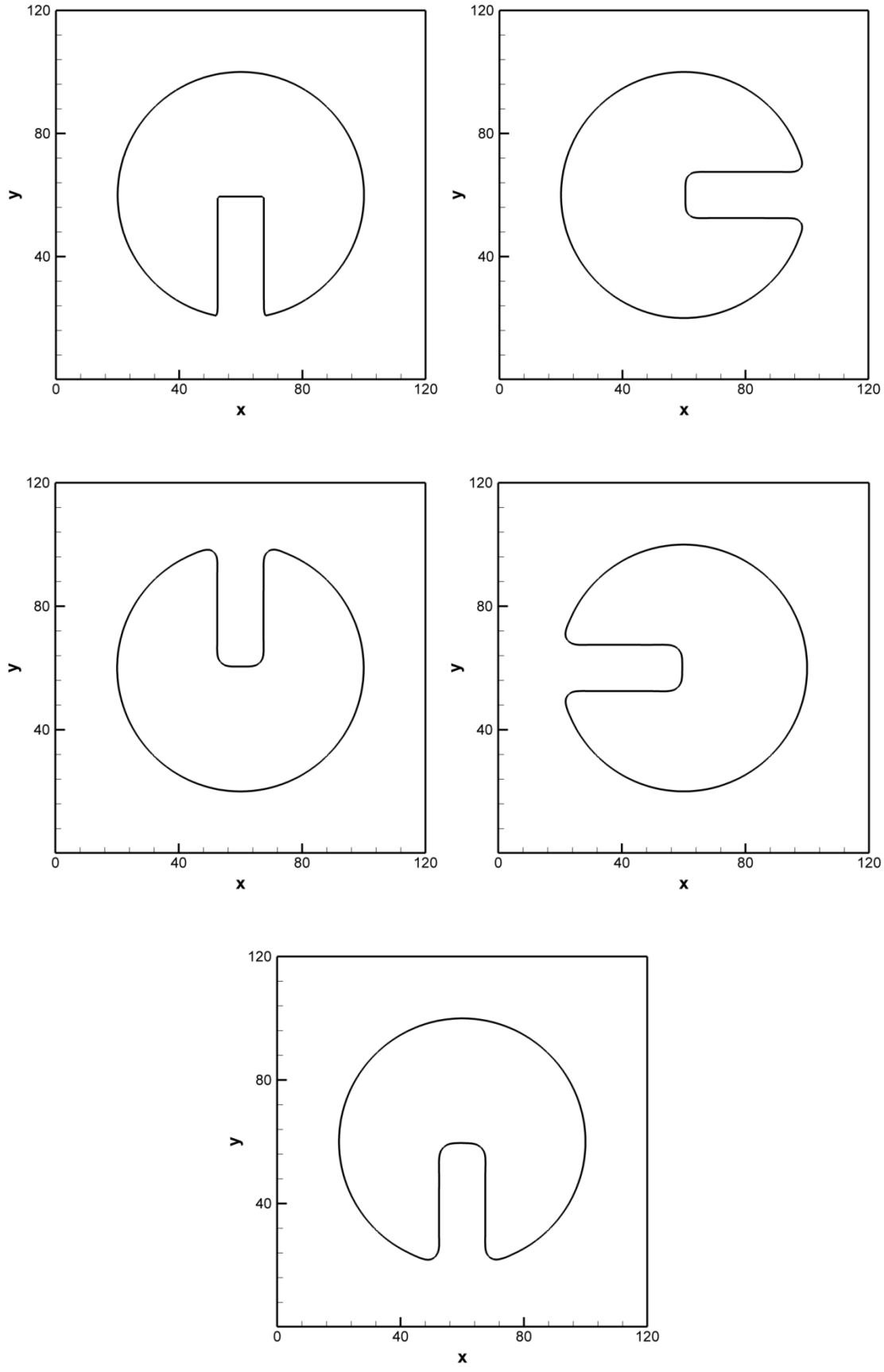

Fig. 2.3 Zalesak's disk at time 0, 0.25T, 0.5T, 0.75T and T

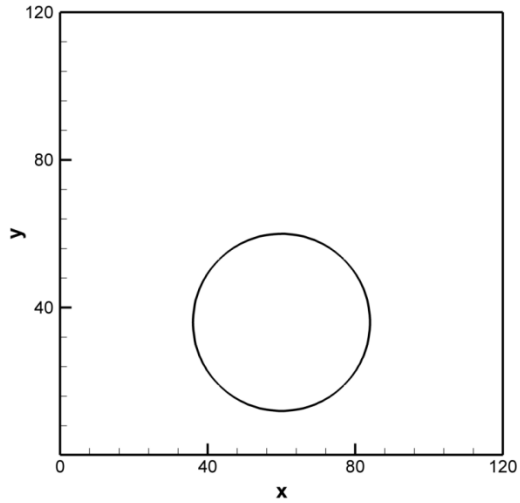

(a) t=0

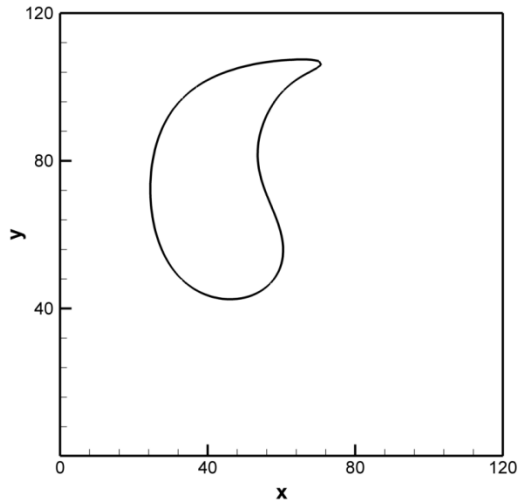

(b) t=T/2

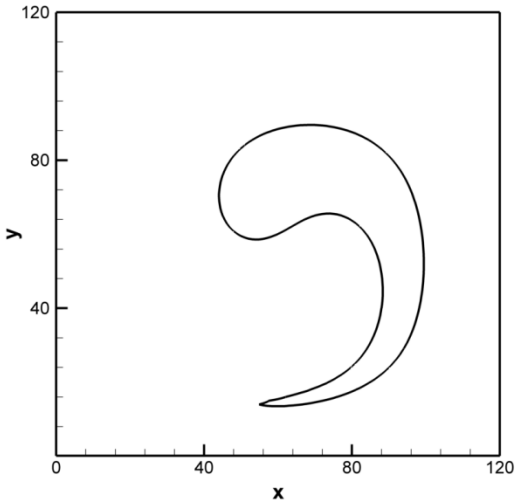

(c) t=T

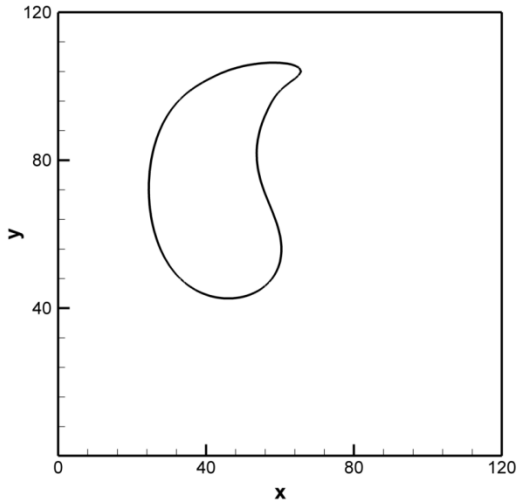

(d) t=3T/2

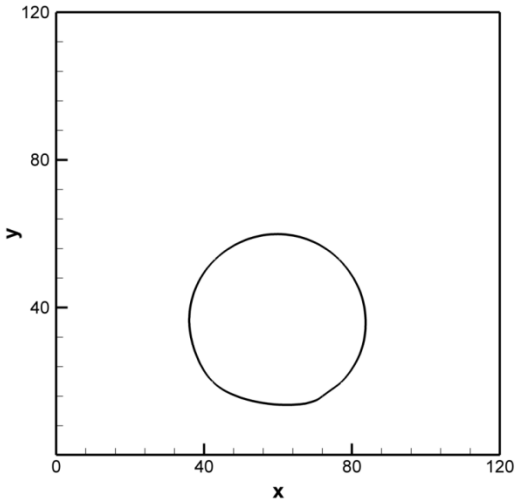

(e) t=2T

Fig. 2.4 Interface deformation in shear flow

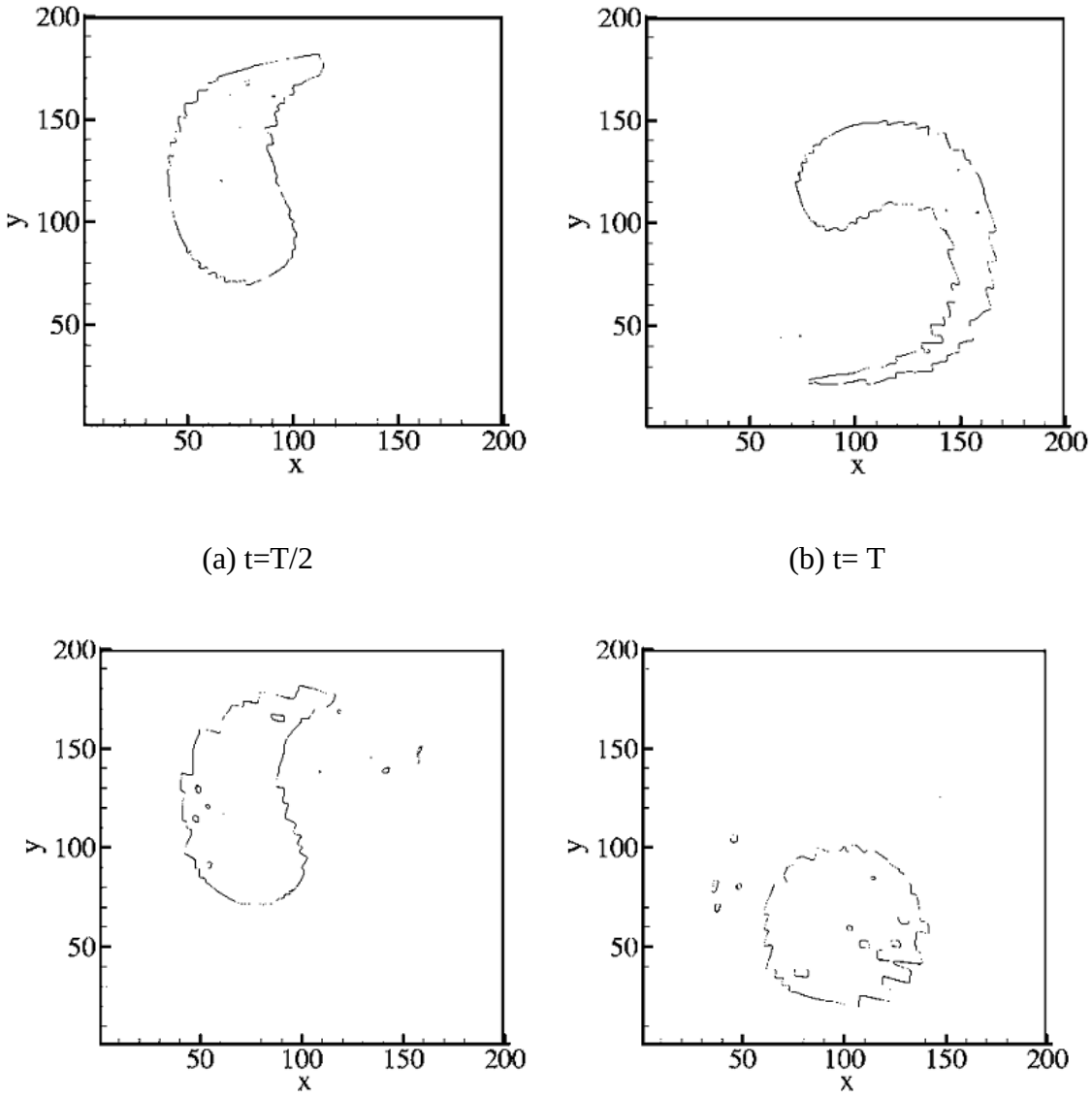

(a) t=T/2 (b) t= T

(c) t=3T/2 (d) t=2T

Fig. 2.5 Interface deformation in shear flow by VOF method

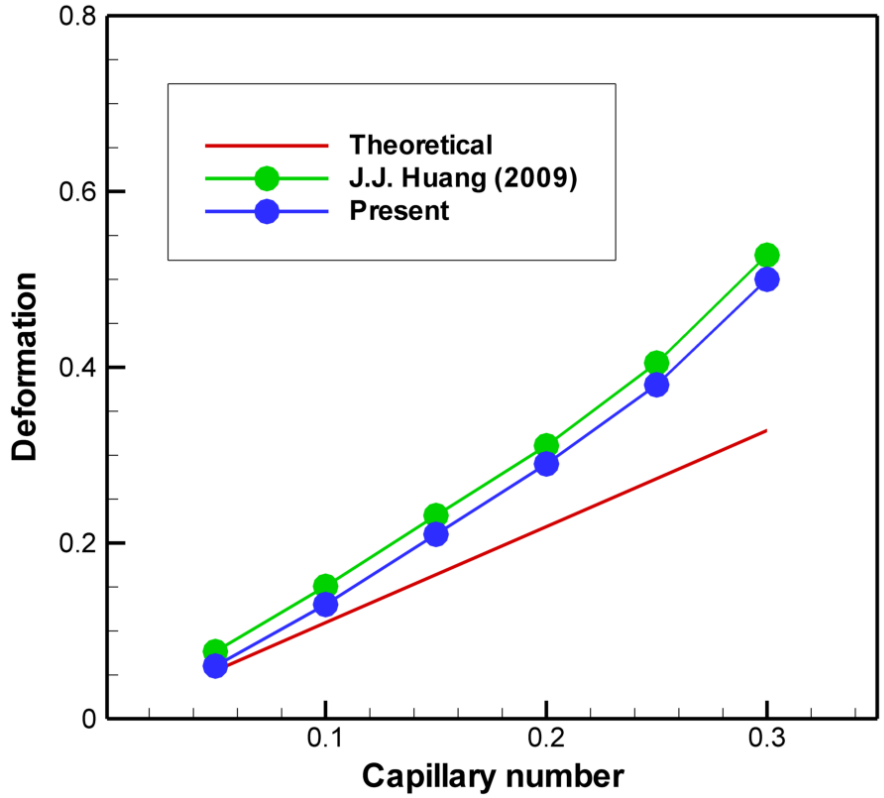

Fig. 2.6 Comparison of deformation parameter at different capillary numbers

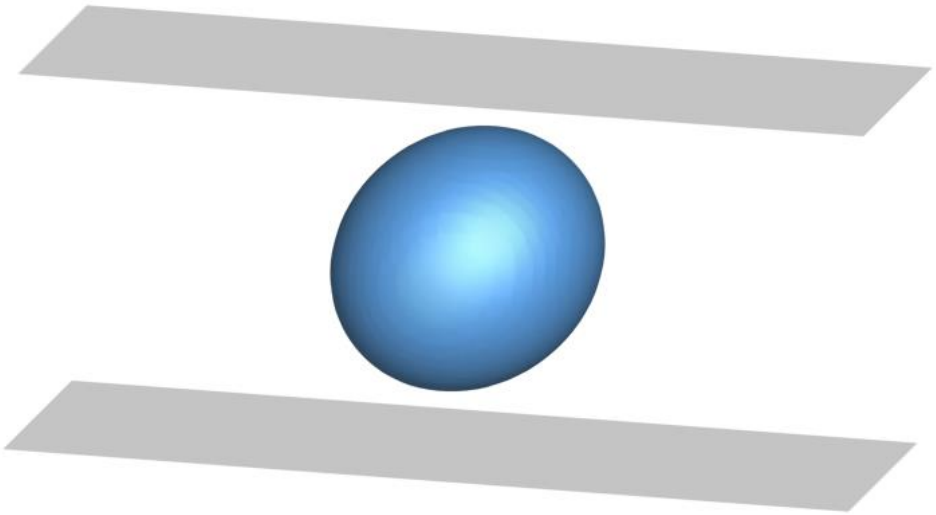

(a) *Ca*=0.05

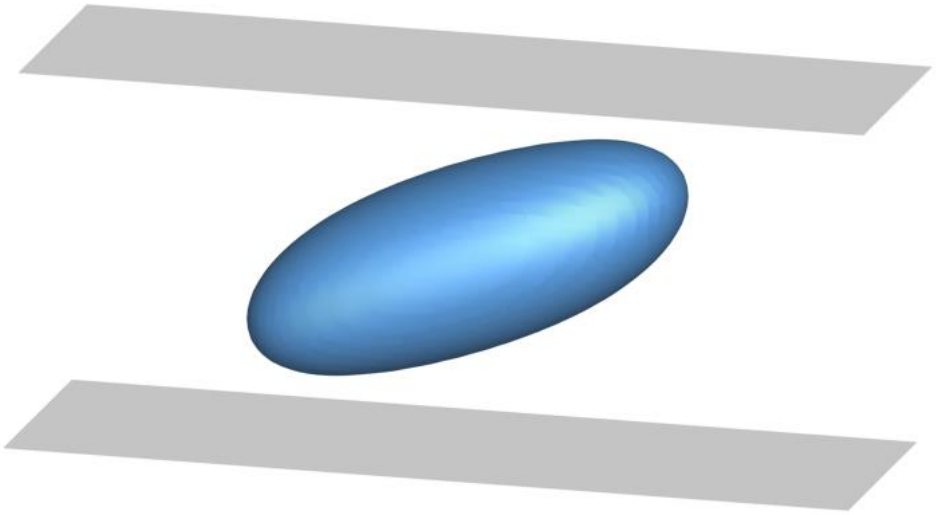

(b) *Ca*=0.3

Fig. 2.7 Droplet shape with different Capillary numbers

Chapter 3[1]

Development of a Stencil Adaptive Phase-Field Lattice Boltzmann Method for Two-Dimensional Incompressible Multiphase Flows

As introduced in Chapter 1, there are two major challenges faced by the phase-field lattice Boltzmann method for multiphase flow simulations. One difficulty is to incorporate the solution adaptive technique to gain flexibility in grid arrangement and achieve high computational efficiency. The other is the difficulty in simulating multiphase flow with density contrast. This Chapter will be devoted to addressing the first issue. It presents a stencil adaptive phase-field lattice Boltzmann method (LBM) for simulation of two-dimensional (2D) multiphase flows.

It is known that a major challenge faced by the phase-field model is to approach sharp interface limit within affordable computational loads. A natural solution is to supplement phase-field model with adaptive mesh refinement (AMR). Although much effort has been devoted to apply AMR with Navier-Stokes (N-S) (Kan et al. 1998) solvers, only a few works can be found in the framework of LBM. To enable high-efficiency multiphase flow simulation, this Chapter will develop a stencil adaptive (Ding and Shu 2006, Wu and Shu 2011) phase-field LBM. The proposed method enables high resolution of interface with considerable saving in grid points. Additionally, owing to the symmetric structure of two

[1] The material in this Chapter has been partially published in
J. Y. Shao, C. Shu, J. Wu and Y. T. Chew, "A stencil adaptive phase-field lattice Boltzmann method for two dimensional incompressible multiphase flows." International Journal for Numerical Methods in Fluids: Publish on line.

stencils used, the present adaptive phase-field LBM avoids complex spatial and temporal interpolation that are required in previously developed adaptive LBMs (Crouse et al. 2003, Toolke et al. 2006). The accuracy and efficiency of the proposed method will be demonstrated through simulation of both steady and unsteady problems including stationary bubble, bubble rising in quiescent flow as well as spreading droplet in the partial wetting regimes.

The rest of this Chapter is organized as follows: Section 3.1 briefly introduces the stencil adaptive algorithm in the first place. Section 3.2 is then devoted to describing in detail the stencil adaptive phase-field lattice Boltzmann method for two-dimensional incompressible multiphase flow problems. The numerical examples will be presented in Section 3.3. Lastly, concluding remarks are drawn in Section 3.4.

3.1 Stencil Adaptive Algorithm

It is known that adaptive mesh refinement is a well-developed technique for conventional N-S solvers. For 2D AMR N-S solvers, the quad-tree structured grid is commonly applied. In this kind of methods, the physical parameters are usually defined at the cell center. During the refinement process, the cell can be simply divided into four sub-cells. This technique is suitable for finite volume-based algorithms. On the other hand, it should be indicated that this technique may not be easy to approximate gradients of flow variables with high order accuracy. This is because for each cell, the flow variables are defined at the cell center and each cell only has 4 neighbouring cells. In this case, the information provided by a reference cell's immediate neighbours is not sufficient to approximate spatial derivatives of flow variables with high order accuracy. When the quad-tree technique is applied to solve the

lattice Boltzmann equation, the situation will be even worse. To be concrete, considering the D2Q9 lattice model in LBM, the streaming process involves the reference node itself and 8 neighbouring points. Obviously, the quad-tree grid does not have complete 9-point structure to perform streaming. Thus, to carry out streaming with quad-tree grid, complex interpolation procedures are necessary. In contrast, the stencil adaptive algorithm utilizes two types of symmetric 5-point stencils, the orthogonal stencil and the diagonal stencil (they are denoted as "+" and "×", respectively) as shown in Fig. 3.1. They are alternately inserted into the mesh as the mesh is refined level by level. Every point in a flow field is then identified by a unique global index and also by either of these two structures. It is found (Wu and Shu 2011) that the combination of these two stencil structures could construct a structure similar to the D2Q9 model so that the streaming process can be effectively performed. In this subsection, the stencil refinement technique will be introduced in the first place. It is followed by description of coarsening technique, action indicator and initialization of physical parameters for a newly inserted point.

In the stencil adaptive method, a uniform Cartesian mesh is generated initially. It is regarded as the background mesh and labeled as level 0. For an interior mesh point i, two types of stencils are alternatively added for a target point (the grid point where refinement or coarsening happens). Concurrently, the configuration of the refined stencil is changed from orthogonal to diagonal or contrary. Fig. 3.2 shows the stencil of a reference node i changed from orthogonal to diagonal after insertion of four new points i_1^1, i_2^1, i_3^1 and i_4^1. Meanwhile, the stencil type and resolution level of newly added points keep the same as those of the reference node i. The coordinates of four newly inserted nodes can be evaluated through

$$\boldsymbol{x}_1^1 = \frac{\boldsymbol{x}_1^0 + \boldsymbol{x}_2^0}{2},\ \boldsymbol{x}_2^1 = \frac{\boldsymbol{x}_2^0 + \boldsymbol{x}_3^0}{2},\ \boldsymbol{x}_3^1 = \frac{\boldsymbol{x}_3^0 + \boldsymbol{x}_4^0}{2},\ \boldsymbol{x}_4^1 = \frac{\boldsymbol{x}_4^0 + \boldsymbol{x}_1^0}{2} \tag{3.1}$$

To further refine the mesh around the reference point i, four new points are inserted and the resolution level will be advanced from level 1 to level 2. The stencil type of this reference node will transfer to orthogonal after the second refinement. Through this stencil refinement process and definition of resolution level, it can be concluded that the stencil with even resolution level has the orthogonal configuration and the stencil with odd resolution level has the diagonal configuration. In order to simplify the refinement process and ensure stability, there are two constraints for stencil refinement process as pointed out by Ding and Shu (2006):

- Constraint 1: The resolution level of the stencil at the supporting node cannot be coarser than that of the target stencil (the stencil of a target point) at the reference node.
- Constraint 2: The maximum difference of resolution level in one stencil cannot be greater than a certain value, for example, one or two.

The aim of adaptive technique is to apply the finest mesh around the region needed to be highly resolved while using coarse mesh for the rest. In interfacial dynamics, both the position and shape of interface change from time to time. Thus it is desirable to keep the finest mesh around the interface while removing the unnecessary nodes when solution at some points is not so sensitive. This can be done by the coarsening process. Compared to the refinement process, the coarsening process is relatively easier. In correspondence to the refinement constraints, there are two constraints for the stencil coarsening process:

- Constraint 3: When the resolution level of the target stencil reaches the original level where the background node is generated, the stencil coarsening stops.

- Constraint 4: the resolution level of the stencil at the supporting nodes cannot be finer than that of the target stencil.

In addition to the refinement and coarsening algorithms, an action indicator is required to control the dynamic adaptive process. Generally, two kinds of indicators can be used. They are absolute difference and relative difference of any parameter of interest.

$$\text{Absolute difference: } \Delta_1 = \max\left(\phi_i\right) - \min\left(\phi_i\right) \tag{3.2}$$

$$\text{Relative difference: } \Delta_2 = \frac{\max\left(\phi_i\right) - \min\left(\phi_i\right)}{\max\left|\phi_i\right|} \tag{3.3}$$

where ϕ_i indicates the value of ϕ (the order parameter in the phase-field model, which is chosen to be the indicator in the present study) on the supporting nodes of a stencil. The subscript i varies from 1 to 4 and denotes four supporting nodes in a stencil. In addition, the upper and lower thresholds must be set to control refinement and coarsening region. The value of upper and lower thresholds will be addressed in Section 3.3 for each case.

Furthermore, besides a smooth transition among grid with different resolution levels, an accurate initialization of flow variables at the newly inserted point is also essential to obtain a stable solution. A high order initialization scheme proposed by Ding and Shu (2006) is adopted in the present study. The equation takes the form of

$$\left(\cdot\right) = \frac{1}{4}\sum_{\gamma=1}^{4}\left(\cdot\right)_{\gamma}^{m} - \frac{h_m^2}{4}\Delta\left(\cdot\right) + O\left(h_m^4\right) \tag{3.4}$$

In Eq. (3.4), $\left(\cdot\right)$ indicates any parameter of interest of a newly added point, while Δ is the Laplacian operator and it is approximated by the central difference scheme. The superscript *m*

is the resolution level of a point and the subscript γ is the index of supporting nodes in the stencil of the newly inserted point that runs from 1 to 4. Moreover, h_m is the characteristic length of a stencil, which is defined as the distance between a supporting node and its reference node. For instance, take node *k* in Fig. 3.3 as a reference node, h_m is the distance between node *i* and *k*. In this manner, the macroscopic variables can be initialized. In the lattice Boltzmann framework, the density distribution function at the newly added point is initialized by its equilibrium distribution function evaluated through macroscopic variables.

3.2 Stencil Adaptive Phase-field Lattice Boltzmann Method

Since the collision is simply a local process in LBM, this part will focus on the implementation of streaming process, evaluation of spatial derivatives in interface capturing LBE and refinement of stencil near the boundary.

3.2.1 Implementation of streaming process

In the present study, D2Q9 lattice velocity model is used for simulating flow field and interface capturing. To provide a complete demonstration of streaming process, implementation of the lattice Boltzmann equation for flow field $f_\alpha\left(\boldsymbol{x}+\boldsymbol{e}_\alpha\delta t,t+\delta t\right)=f_\alpha\left(\boldsymbol{x},t\right)+\Omega_\alpha$ is illustrated. Following the procedures in the work of Wu and Shu (2011), the governing equation for flow field can be rearranged as

$$f_\alpha\left(\boldsymbol{x},t+\delta t\right)=l_\alpha\left(\boldsymbol{x}-\boldsymbol{e}_\alpha\delta t,t\right) \tag{3.5}$$

$$l_\alpha\left(\boldsymbol{x}-\boldsymbol{e}_\alpha\delta t,t\right)=f_\alpha\left(\boldsymbol{x}-\boldsymbol{e}_\alpha\delta t,t\right)+\Omega_\alpha \tag{3.6}$$

In the above equations, $l_\alpha\left(\boldsymbol{x}-\boldsymbol{e}_\alpha\delta t,t\right)$ is the post-collision state of density distribution function. When a non-uniform grid is used, an interpolation technique developed by Wu and Shu (2010) is adopted to evaluate $l_\alpha\left(\boldsymbol{x}-\boldsymbol{e}_\alpha\delta t,t\right)$ with assistant of the surrounding points. Since the interpolation is applied at the same time level, the time *t* in function l_α is omitted in following description. Take a Diagonal (current stencil structure)-Orthogonal (parent stencil structure) configuration as an example. As shown in Fig. 3.4, the solid circle indicates reference node, the open circle indicates existing supporting point and the solid square represents the intermediate streaming position of which the density distribution function must be interpolated based on the information on the stencil. To evaluate the distribution functions at position from $l1$ to $l8$, a second order local interpolation is utilized. First, take the position $l1$ for instance. It is on the horizontal line of $y=y_i$. In this case, only three points: i_3^{m-1}, i and i_1^{m-1} contribute to interpolation of the density distribution function at position $l1$ as shown in Fig. 3.5. The algebraic interpolation form reads as

$$l_1(\boldsymbol{x}-\boldsymbol{e}_1\delta t)=a_1 l_1\left(\boldsymbol{x}_3^{m-1}\right)+a_2 l_1\left(\boldsymbol{x}_i\right)+a_3 l_1\left(\boldsymbol{x}_1^{m-1}\right) \tag{3.7}$$

In the above equation, $\boldsymbol{x}_3^{m-1}$, $\boldsymbol{x}_i$ and $\boldsymbol{x}_1^{m-1}$ are the coordinates of points i_3^{m-1}, i, and i_1^{m-1}, respectively. Additionally, a_{1-3} are interpolation coefficients which can be expressed as

$$\begin{cases} a_1=\dfrac{\left(x_{l1}-x_i\right)\left(x_{l1}-x_1^{m-1}\right)}{\left(x_3^{m-1}-x_i\right)\left(x_3^{m-1}-x_1^{m-1}\right)} \\ a_2=\dfrac{\left(x_{l1}-x_3^{m-1}\right)\left(x_{l1}-x_1^{m-1}\right)}{\left(x_i-x_3^{m-1}\right)\left(x_i-x_1^{m-1}\right)} \\ a_3=\dfrac{\left(x_{l1}-x_3^{m-1}\right)\left(x_{l1}-x_i\right)}{\left(x_1^{m-1}-x_3^{m-1}\right)\left(x_1^{m-1}-x_i\right)} \end{cases} \tag{3.8}$$

In Eq. (3.8), $x_{l1} - x_i = -\delta x = -\delta t \cdot c$. Moreover, if we use the characteristic stencil length h_m as defined previously, Eq. (3.8) can be simplified as

$$\begin{cases} a_1 = \dfrac{\delta x(h_{m-1} + \delta x)}{2h_{m-1}^2} \\ a_2 = \dfrac{(h_{m-1} - \delta x)(h_{m-1} + \delta x)}{h_{m-1}^2} \\ a_3 = \dfrac{-\delta x\left(h_{m-1} - \delta x\right)}{2h_{m-1}^2} \end{cases} \tag{3.9}$$

In this manner, l_1 can be obtained through Eqs. (3.7) and (3.9). Following the same procedure, l_3 can be evaluated using the density distribution function at three points: i_4^{m-1}, i and i_2^{m-1} along the vertical line. Besides the positions $l1, l3, l5, l7$ that fall on a line parallel either with x or y direction, the density distribution functions at other positions $l2, l4, l6, l8$ can also be evaluated in a similar way. Take the density distribution function at position $l2$ for example. Instead of performing interpolation along x and y direction, the value at position $l2$ is evaluated based on i_3^m, i and i_1^m along a diagonal line. The corresponding equation reads

$$l_2(\boldsymbol{x} - \boldsymbol{e}_2\delta t) = b_1 l_2\left(\boldsymbol{x}_3^m\right) + b_2 l_2\left(\boldsymbol{x}_i\right) + b_3 l_2\left(\boldsymbol{x}_1^m\right) \tag{3.10}$$

And the corresponding coefficients are

$$\begin{cases} b_1 = \dfrac{\delta x\left(h_m/\sqrt{2} + \delta x\right)}{h_m^2} \\ b_2 = \dfrac{2\left(h_m/\sqrt{2} - \delta x\right)\left(h_m/\sqrt{2} + \delta x\right)}{h_m^2} \\ b_3 = \dfrac{-\delta x\left(h_m/\sqrt{2} - \delta x\right)}{h_m^2} \end{cases} \tag{3.11}$$

The above procedure is performed in the Diagonal-Orthogonal type stencil. The same approach can be applied to the Orthogonal-Diagonal type stencil. Furthermore, it can be found that the interpolation coefficients are only related to the stencil configurations and lattice velocities. It should be indicated that an identical δx which is equal to or smaller than the finest grid length and an identical $\delta t = \delta x / c$ is used in the numerical simulation. Therefore, only the spatial interpolation is required. Once l_α is obtained, the streaming process can be carried out in a straightforward manner along different lattice velocity directions. Similarly, the streaming process for interface capturing lattice Boltzmann equation could also be completed following the same procedure.

3.2.2 Approximation of spatial derivatives in interface capturing LBE

An accurate evaluation of distribution function is a crucial issue in the adaptive lattice Boltzmann method. On the other hand, since the order parameter varies sharply in the interfacial region, a stable discretization of spatial derivatives also has remarkable effect on the simulation of interfacial dynamics. In this part, we will show how to use a 9-point isotropic structure (Swift et al. 1996, Tiribocchi et al. 2009, Guo et al. 2011) to discretize spatial derivatives in the interface capturing LBE. We will take the Diagonal-Orthogonal (D-O) stencil as an example to demonstrate discretization of both the first and the second order derivatives of order parameter. As shown in Fig. 3.6, a point with D-O type structure is taken as the reference node, which has the stencil size of h_m (distance from point 2 to point 0). Its supporting nodes are denoted from 1 to 8 for simplicity. One forward way to construct partial derivatives using the reference node and the surrounding 8 points is to apply Taylor series expansion. For instance, to evaluate the first order derivative of ϕ along x direction, one

could apply Taylor series expansion to three pairs of nodes: points 2 and 4, points 1 and 5 as well as points 6 and 8.

$$\left.\frac{\partial \phi}{\partial x}\right|_{upper} = \frac{\phi_2 - \phi_4}{2\left(h_m/\sqrt{2}\right)} \tag{3.12}$$

$$\left.\frac{\partial \phi}{\partial x}\right|_{middle} = \frac{\phi_1 - \phi_5}{2\sqrt{2}h_m} \tag{3.13}$$

$$\left.\frac{\partial \phi}{\partial x}\right|_{lower} = \frac{\phi_8 - \phi_6}{2\left(h_m/\sqrt{2}\right)} \tag{3.14}$$

Thereafter, $\frac{\partial \phi}{\partial x}$ at the reference point could be evaluated through

$$\frac{\partial \phi}{\partial x} = \frac{1}{3}\left(\left.\frac{\partial \phi}{\partial x}\right|_{upper} + \left.\frac{\partial \phi}{\partial x}\right|_{middle} + \left.\frac{\partial \phi}{\partial x}\right|_{lower}\right) \tag{3.15}$$

Similarly, the second order derivative along *x* direction could be evaluated by

$$\frac{\partial^2 \phi}{\partial x^2} = \frac{1}{6h_m^2}\left(\phi_1 + \phi_5\right) + \frac{1}{3h_m^2}\left(\phi_2 + \phi_4 + \phi_6 + \phi_8\right) - \frac{5}{3h_m^2}\phi \tag{3.16}$$

3.2.3 Refinement of the stencil near boundary

In certain multiphase flow problems such as contact line dynamics, accurate implementation of the involved Neumann boundary condition is crucial. To achieve a stable and accurate solution, the finest mesh should be assigned and preserved along the boundary during the simulation when Neumann boundary condition is needed. Hence, once a new boundary node is inserted, its type and relationship with the surrounding points must be identified correctly.

Fig. 3.7(a) demonstrates grid points along the lower boundary. In this figure, the grid near the boundary is refined to level 2. The open circle indicates point of level 0, the solid circle is point of level 1, the open diamond indicates point of level 2 and the solid square is the boundary point. It could be seen that the stencil structure of a boundary point is incomplete and different from that for interior nodes. To be specific, it can be seen in Fig. 3.7(b) that the stencil of a point on the lower boundary takes the form of "$\perp$" rather than a complete "+" structure, which is one type of symmetric stencil as shown in Fig. 3.1. Therefore, specific attention should be paid to establish connection for a boundary node. First, all initial points are categorized into several categories: interior points, boundary points and corner points. Moreover, the four boundaries and four corner points are also distinguished. Consider the following situation: a stencil near the boundary is refined and a point such as i_4^2 in Fig. 3.7(a) is inserted into the boundary. First, track back to its parent structure and the nodes i_3^1 and i_4^1. If both of them are on the same boundary, then the newly added node i_4^2 must be on the same boundary. Thereafter, points i, i_4^2, i_3^1 and i_4^1 construct a lower boundary stencil "$\perp$". One may ask how to manipulate the corner that is missed from the complete "+". In the present work, this corner is viewed as pointing to the reference node itself. It could also be left as null in the data structure. In this manner, the grid could be refined to the finest level near the boundary and enable high resolution for the Neumann boundary condition.

3.3 Results and Discussions

In this subsection, the accuracy and efficiency of the developed stencil adaptive phase-field lattice Boltzmann method will be validated through several numerical tests including the stationary bubble case, bubble rising under buoyancy and the contact line problem-spreading

of a droplet in the partial wetting regimes. It should be stressed that only the results of grid independency were shown hereafter for convergence study. This is because there is a relation: $\delta x/\delta t = c$ (c usually takes value of 1) in LBM. With this relation, grid independency also implies time step size independency.

3.3.1 Stationary bubble

As a classical validation case, the simulation of a stationary bubble is performed in this subsection. First, the effect of interface thickness is studied. Then, the convergence of phase-field model to sharp interface limit is investigated. These numerical experiments serve to provide a guidance to select appropriate numerical parameters and demonstrate the characteristics of stencil adaptive phase-field lattice Boltzmann method. The validation of Laplace law is also shown at the end of this subsection.

3.3.1.1 Effect of interface width

In this case, a bubble initially represented by many line segments will eventually return to its equilibrium state and show a smooth circular shape. The flow domain is represented by a background uniform grid of 121×121 with the finest region of 4 resolution levels locating in the vicinity of the interface. The finest grid spacing $\Delta x_{\min}$ is set as 1. The radius of this bubble is set as 25 background grid length. Moreover, the densities (kg/m^3) of two kinds of fluids are set as $\rho_H = 1.2$ and $\rho_L = 1$. The order parameter is set to be $-\phi_0$ inside the bubble and ϕ_0 (defined by $\phi_0 = \dfrac{\rho_H - \rho_L}{2\rho_{unit}}$ with ρ_{unit} indicates unit mass density) elsewhere. In

addition, the other physical parameters are set as $\sigma = 0.1(mN/m)$, $\tau = 0.875$ and $\tau_\phi = 0.7$. For a 2D problem, the Laplace law reads as

$$\sigma = \Delta p \times R \tag{3.17}$$

where Δp is the pressure jump across the interface and R is the radius of the bubble. In order to provide a guidance to choose an appropriate interface thickness in the stencil adaptive phase-field LBM, the effect of interface width with a fixed radius and resolution level is investigated first.

The width of interface layer is taken from 2.0 to 6.0. Figure 3.8 plots both theoretical and numerical surface tension force versus interface width. It is shown that the accuracy of numerical surface tension increases with the interface width. When the interface width is equal to 2.0, the numerical simulation only resolves approximately 60% of theoretical surface tension force. However, when the interface width gradually increases to 3.5, the numerical simulation resolves more than 90% of theoretical surface tension force. Moreover, the numerical results become stable and approach the analytical value when the interface width increases even further. This is attributed to the fact that the discretization error will decrease as the interface width increases (Lee and Lin 2005). Therefore, in order to accurately resolve the surface tension force, the interface width should be set larger than 3 grid spacing in the vicinity of interface.

3.3.1.2 Effect of stencil refinement on Cahn number, solution accuracy and computational efficiency

Based on the investigation of the influence of interface thickness, it can be seen that the interface thickness is usually selected as 3 to 5 grid spacing to accurately resolve the surface tension. On the other hand, the phase-field model will converge to sharp interface limit only when the Cahn number, which is defined as $Cn = w/L$ (where w indicates the interface thickness and L is the characteristic length of flow domain), decreases toward 0. If a uniform grid is used, the high resolution of a sharp interface will entail unnecessary fine grid all over the flow domain and thus poses strict constraint in problem size even for 2D problems. Consequently, the dynamic refinement and coarsening are crucial for the model. To demonstrate the superiority of adaptive phase-field model, the Cahn number is examined when the grid resolution level increases from 0 to 6 with radius fixed as 25 times of the background grid length and the interface thickness is set as 3.5 lattice units. Owing to the symmetry of this problem, only the right upper corner of initial order parameter contour together with grid distribution at different resolution levels is plotted in Fig. 3.9. Meanwhile, the equilibrium interface profile versus distance away from the center at different resolution levels is presented in Fig. 3.10. It can be observed that the interface thickness reduces remarkably as the resolution level increases. Compared with the result of a uniform grid (resolution level = 0), the interface profile simulated at resolution level = 6 is very sharp.

Furthermore, the Cahn number and the number of nodes used for each case are listed in Table 3.1. Supplemented by adaptive technique, the Cahn number in the phase-field model becomes one order smaller when the resolution level increases from 0 to 6. Meanwhile, it can also be found from Table 3.1 that 961×961 nodes are required for a uniform grid if Cahn number is

chosen as 0.00875. However, with adaptive technique, only 4.25% of nodes are needed. To further clarify the relationship between Cahn number and resolution level in the stencil adaptive lattice Boltzmann method, a quantificational equation is provided. The interface thickness can be expressed as

$$W_m = C\frac{\Delta x_{background}}{2^{\frac{m}{2}}} \tag{3.18}$$

In the above equation, C is the number of grid-spacing used to represent the interface thickness in the phase-field model, m indicates resolution level and $\Delta x_{background}$ is background grid spacing. Usually, C and $\Delta x_{background}$ are fixed during the simulation. For this case, when the grid is refined to m levels, the finest mesh will be $\Delta x_{background} \Big/ \left(2^{\frac{m}{2}}\right)$. Thus the interface thickness can be calculated through Eq. (3.18). Consequently, the Cahn number can be expressed as

$$Cn = \frac{1}{L}\left(C\frac{\Delta x_{background}}{2^{\frac{m}{2}}}\right) \tag{3.19}$$

Eq. (3.19) implies that the Cahn number will be $2^{\frac{m}{2}}$ times smaller when resolution level is equal to m as compared to a uniform background grid.

Besides the accuracy, the efficiency improvement is demonstrated in Table 3.2 (3×10^6 steps were run on both solvers). The absolute and percentage of number of nodes used by the adaptive LBM and the standard LBM solver with uniform grid (the uniform grid spacing is taken as the same with the minimum grid spacing in adaptive LBM) are presented in the table.

It can be seen that with increase of the refinement level, the number of nodes used by adaptive LBM can be reduced remarkably as compared to uniform grid. Furthermore, the CPU time is also compared in the table. It can be found that, when the resolution level equals zero, the time taken by the adaptive solver is double of that by uniform solver. This is due to the fact that adaptive solver utilizes a non-uniform grid, and extra time is needed for searching the neighbouring nodes of a reference node. It might not be very economical to conduct a simulation on a uniform grid using adaptive solver as expected. Nevertheless, when the resolution level is increased to 2 and 4, the time taken by adaptive solver becomes much less than uniform solver because substantial amount of unnecessary nodes is avoided in the simulation. Consequently, stencil adaptive LBM is a favorable solver when both high resolution and efficiency are desired.

3.3.1.3 Validation of Laplace law

To validate Laplace law, the simulation of a bubble with radius varying from 10 to 30 (variation of radius is chosen as 2.5) is performed. In addition, the interface width is fixed as 4 and the finest refinement level is set as 4 based on the previous investigation on accuracy and efficiency. The pressure jump as a function of curvature is presented in Fig. 3.11. As predicted by Eq. (3.17), the relationship is linear, which is well confirmed in the figure. Furthermore, the slope of the straight line is also the same as the analytical surface tension.

3.3.2 Bubble rising under buoyancy

The accuracy and convergence of the stencil adaptive LBM for multiphase flows have been testified through simulation of a stationary bubble under different situations. To further

demonstrate the ability of this method to capture moving interface, a rising bubble in a quiescent flow is simulated. The parameters are chosen the same as those in the work of Takada et al. (2001). They used the free-energy based LBM (swift et al. 1996) and included the buoyancy force in the lattice Boltzmann equation for the flow field. The simulations in their work were performed on the uniform grid. In this case, a bubble with radius of 12 lattice units is initially centered at (60, 60) in a flow domain of 80×300. A uniform grid of 41×151 is used as background mesh and the resolution level is set as 4. Different from the case of stationary bubble, the shape and position of the interface cannot be predicted in advance for this problem. Therefore, a dynamic refinement/coarsening indicator is required. In the present study, the absolute difference of the order parameter is employed as the action indicator, and the corresponding lower and upper thresholds are set as 1.5 and 3.0, respectively. The physical parameters are set as $\rho_H = 1.42$, $\rho_L = 0.58$ (kg/m^3) and $\sigma = 0.00521$ (N/m). The order parameter in this case is set as $-\phi_0$ inside the bubble and ϕ_0 elsewhere. In addition, several important dimensionless parameters including Morton number, Eötvös number as well as Reynolds number are defined below

$$Mo = \frac{g\left(\rho_H - \rho_L\right)\mu_H^4}{\rho_H^2\sigma^3} \tag{3.20}$$

$$E\ddot{o} = \frac{g\left(\rho_H - \rho_L\right)d^2}{\sigma} \tag{3.21}$$

$$\mathrm{Re} = \frac{\rho_H V_T d}{\mu_H} \tag{3.22}$$

where g is the gravity acceleration, d is the diameter of the bubble, μ is the dynamic viscosity and V_T is the terminal velocity of the rising bubble. Four cases with Eötvös number in the range of 5 to 40 are simulated. The relevant parameters are listed in Table 3.3.

For this problem, the bubble will first accelerate and then approach a terminal velocity. This trend is clearly demonstrated in Fig. 3.12, which shows the evolution of the velocity at different $Eö$. Compared with the results of Takada et al. (2001), the adaptive lattice Boltzmann method provides good results with only approximately 30% of nodes used by a uniform grid in the previous study (Takada et al. 2001) (To be precise, 7547 nodes are used in the present study while 24381 nodes are used for the uniform grid). This is because although less number of nodes is used in the present study, the adaptive technique enables the finest grid being located in the vicinity of interface where the largest gradient occurs. The exact value of terminal velocity is compared with the data in the literature in Table 3.4. It can be seen from Table 3.4 that the present terminal bubble velocity compares well with those of Takada et al. (2001) even with much lesser nodes used. Furthermore, the bubble shape represented by order parameter contour together with local grid distribution in part of the flow field is presented in Fig. 3.13. The present bubble shapes of all cases are in line with those obtained by Takada et al. (2001) and Hirt and Nichols (1981).

Additionally, the influence of mesh refinement on accuracy in this dynamic process is also investigated. Three different refinement levels are chosen to simulate cases 2 and 4. Table 3.5 compares the terminal velocities obtained through refinement level at 2, 4 and 6 with the data available in the literature. It shows that, when the background mesh is kept the same, and the finer grid is used in the vicinity of the interface, the numerical results will be more accurate. Furthermore, Fig. 3.14 shows the bubble shape and its surrounding mesh with mesh refinement level being equal to 2, 4 and 6, respectively. It could be seen that as mesh is refined level by level, the bubble will converge to a specific shape. From the grid refinement

study above, it can be inferred that the convergence as well as the accuracy of current adaptive technique for dynamic process are well validated.

3.3.3 Spreading of a droplet in the partial wetting regime

In this subsection, the droplet spreading which involves three phase interactions is simulated to demonstrate the accuracy of boundary refinement. To be specific, a two-dimensional liquid droplet spreading on a solid surface with the equilibrium contact angle varying from 45° to 135° is simulated (the variation of contact angle is chosen to be 15°). The computational domain is set as 200×100 with a droplet radius of 25 lattice units. The initial contact angle is 160°. A uniform grid of 101×51 is used as background mesh. The resolution level is set as 4, and the absolute difference of the order parameter is chosen as the action indicator with the lower and upper thresholds being selected to 1 and 3, respectively. Different from the bubbly flows, the highest resolution region in the contact line dynamics usually locates around the boundary. Therefore, besides the vicinity of the droplet interface, the finest grid is also applied on the lower wall. For the physical parameters, we take $\rho_H = 1.42$, $\rho_L = 0.58$ and the surface tension as 0.00521. In addition, the interface thickness is taken as 6 times of the finest grid spacing. Fig. 3.15 compares the numerical equilibrium contact angle and theoretical value. In this figure, the line is the theoretical value predicted by $\cos\theta = \frac{1}{2}\left[(1+\omega)^{\frac{3}{2}} - (1-\omega)^{\frac{3}{2}}\right]$, and the open circle is the numerical result of adaptive LBM. The equilibrium contact angle is calculated based on droplet height and base radius measured. It can be observed that the current results are in good agreement with theoretical values in a wide range of contact angles. Fig. 3.16 presents equilibrium profile of droplet in three

different cases (θ_{eq} equals 60°, 90° and 120°). Additionally, the spreading process together with grid distribution are plotted in Fig. 3.17 which presents the droplet profile at several typical time stages when $\theta_{eq} = 60^{\circ}$. Particularly, Figs. 3.17 (a) to (c) show the droplet deforming locally. The time here is nondimensionalized by U/D where D is initial diameter of the drop and U is given as 5×10^{-4}. It is obvious that the shape of the droplet only changes locally in vicinity of the contact line region near the lower wall. Figs. 3.17 (d) to (f) demonstrate the global spreading process. During this stage, both the height and base diameter change dramatically until the droplet approaches the equilibrium contact angle.

Furthermore, the computational efficiency of the proposed stencil adaptive phase-field LBM to simulate a dynamic process is studied through this case. The equilibrium contact angle is chosen as 60° without loss of generality. In order to compare the efficiency, the refinement levels are set as m = 2, 4 and 6, respectively and three sets of uniform grids with the grid spacing at $\Delta x_{background} \Big/ 2^{\frac{m}{2}}$ are used for comparison. First, the accuracy of the numerical simulation is verified through comparison of the numerical equilibrium contact angle with the theoretical prediction in Table 3.6. Thereafter, the efficiency improvement is presented in Table 3.7. It could be seen that if the uniform grid is adopted, the computational load quickly increases as the grid size is increased. Concurrently, the adaptive algorithm stands out of the standard LBM with regard to both computational storage and efficiency. Concretely speaking, when m = 4 and 6, approximately 30% of grid points is used in adaptive technique as compared to the standard LBM. At the same time, 50% to 60% of computational time is required. These results prove the enhanced efficiency of current scheme, which indicates that the use of adaptive approach in LBM for multiphase flow simulation is favorable.

3.4 Concluding Remarks

In this Chapter, with the help of stencil adaptive technique, a high resolution phase-field lattice Boltzmann method for the incompressible multiphase flows was developed. The two major ingredients in the current method are the phase-field lattice Boltzmann model and a stencil adaptive lattice Boltzmann algorithm. The phase-field model allows simulation of multiphase flows on an Eulerian grid regardless of topology and shape change of the interface. In addition, it can also naturally resolve the contact line problem by simply introducing the diffusion-induced motion. On the other hand, the stencil adaptive algorithm utilizes two types of symmetric stencils. These two stencils can be combined to form a similar structure as D2Q9 model in LBM. As a result, only one-dimensional interpolation with second order accuracy is performed. Therefore, the stencil adaptive LBM maintains the simplicity of the original LBM. To validate the proposed method, several multiphase flow problems have been simulated. The accuracy and convergence of the current method were first investigated through the simulation of a stationary bubble. The numerical result compared well with that predicted by Laplace law. Furthermore, to demonstrate the ability of proposed method for capturing moving interface, simulation of a rising bubble in a quiescent flow was carried out. In addition, the current method was also applied to simulate the spreading of a droplet in the partial wetting regime, which showed the capability of present method for interaction of three phases (solid and two liquid phases). For these dynamic problems, the accuracy and efficiency of current scheme were also examined. All the obtained results showed good agreement with those in the literature. In conclusion, the numerical experiments performed in this study indicate that the current stencil adaptive phase-field LBM enables a high resolution for the interfacial dynamics with greater grid distribution flexibility and considerable saving in computational effort.

Table 3.1 Comparison of Cahn number and the number of nodes used in stencil adaptive LBM

Resolution level	*Cn*	Number of nodes
0	0.07	14641
2	0.035	17461
4	0.0175	23797
6	0.00875	39289

Table 3.2 Comparison of total numbers of nodes and running time between stencil adaptive LBM and standard LBM (The computations were accomplished on Laptop with CPU specifications: Intel Core 2 Duo P8400 / 2.26 GHz.)

Solvers	Resolution level	Number of nodes	Percentage of nodes used by adaptive solver (%)	Running time (s)	Percentage of time used by adaptive solver (%)
Standard LBM	-	121×121	-	11203.81	-
Stencil adaptive LBM	0	14641	100	21630.48	193.06
Standard LBM	-	241×241	-	41578.39	-
Stencil adaptive LBM	2	17461	30.06	37949.22	91.27
Standard LBM	-	481×481	-	187540.91	-
Stencil adaptive LBM	4	23797	10.29	85124.06	45.39

Table 3.3 Parameters for the bubble rising under buoyancy

Cases	*Eö*	Mo	*w*
1	5	0.2267	1.5
2	10	0.4535	1.5
3	20	0.9070	1.2
4	40	1.8134	1.0

Table 3.4 Comparison of terminal velocity (m/s) for bubble rising under buoyancy

Cases	VOF (Hirt and Nicholas 1981)	Takada et al. (2001)	Present
1	8.28e-3	7.82e-3	7.83e-3
2	1.43e-2	1.38e-2	1.41e-2
3	2.15e-2	2.17e-2	2.16e-2
4	3.08e-2	3.11e-2	3.18e-2

Table 3.5 Terminal bubble rising velocities with different refinement levels (results of VOF by Hirt and Nichols 1981; results of Takada et al. 2001)

Cases	VOF	Takada et al. (2001)	Present (2 levels)	Present (4 levels)	Present (6 levels)
2	1.43e-2	1.38e-2	1.21e-2	1.41e-2	1.42e-2
4	3.08e-2	3.11e-2	3.3e-2	3.18e-2	3.09e-2

Table 3.6 Numerical equilibrium contact angles with different refinement levels

Refinement level	2	4	6
Numerical $\theta_{eq}(^\circ)$	58.7	59.2	59.5

Table 3.7 Efficiency comparison between standard and stencil adaptive LBM in droplet spreading

Solvers	Resolution level	Number of nodes	Percentage of nodes used by adaptive solver (%)	Running time (s)	Percentage of time used by adaptive solver (%)
Standard LBM	-	201×101	-	8218.14	-
Stencil adaptive LBM	2	9865	48.60	7620.59	92.73
Standard LBM	-	401×201	-	37442.89	-
Stencil adaptive LBM	4	22847	28.34	19200.30	51.28
Standard LBM	-	801×401	-	126153.99	-
Stencil adaptive LBM	6	90825	28.27	82994.88	65.79

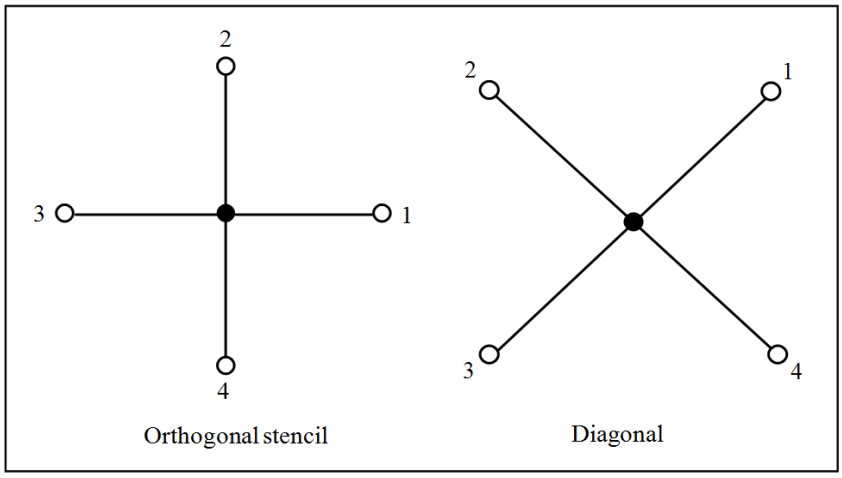

Fig. 3.1 Configuration of Orthogonal and Diagonal stencils

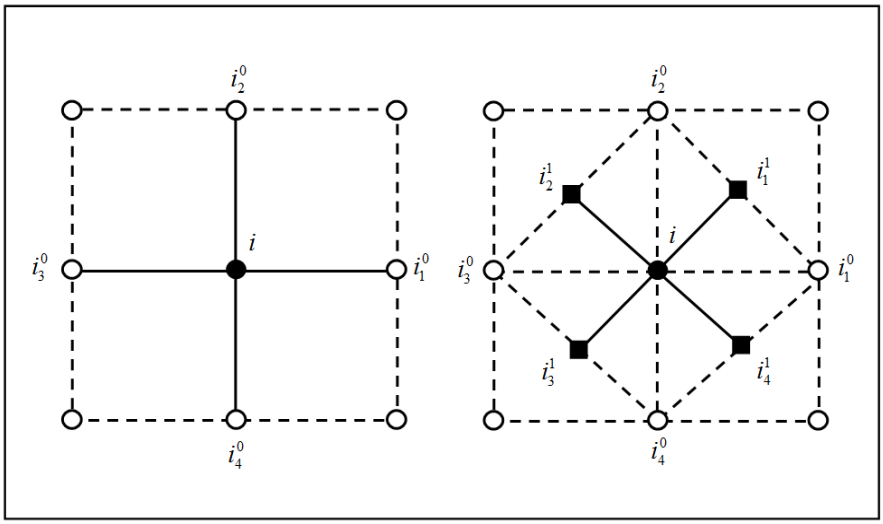

Fig. 3.2 Stencil at an arbitrary point *i* changes from level 0 (orthogonal) to level 1 (diagonal)

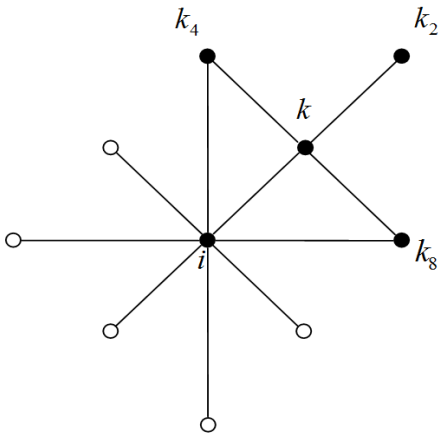

Fig. 3.3 Assistant nodes for interpolation of a newly inserted node *k*

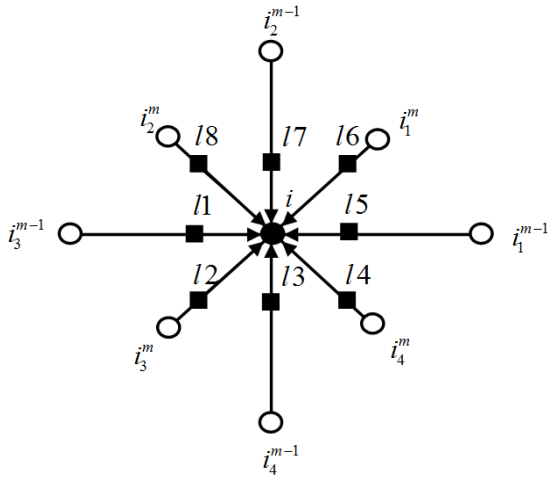

Fig. 3.4 Sketch of local interpolation for a reference node i and streaming on a diagonal-orthogonal stencil

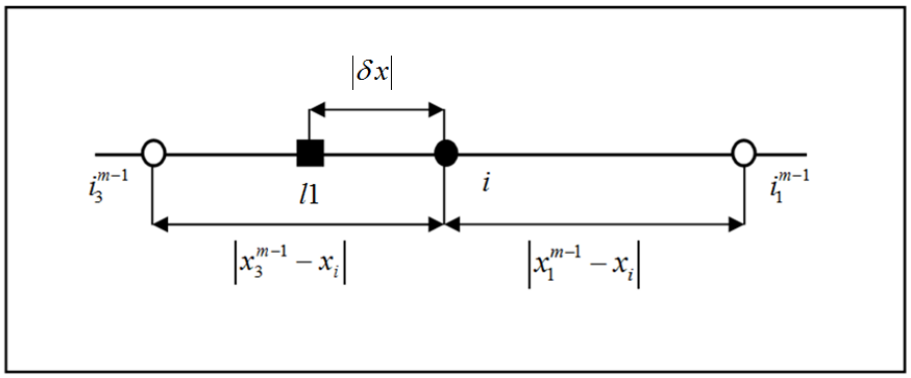

Fig. 3.5 Sketch for the interpolation of $l1$ along a horizontal line

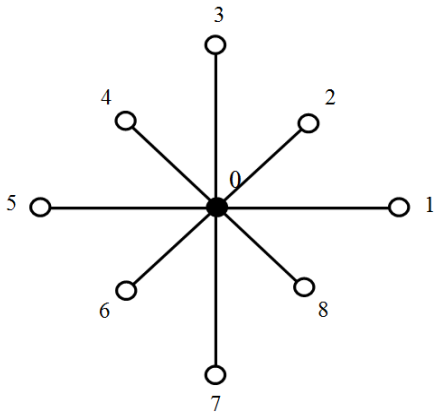

Fig. 3.6 Sketch of points used for approximation of the first and second order derivatives

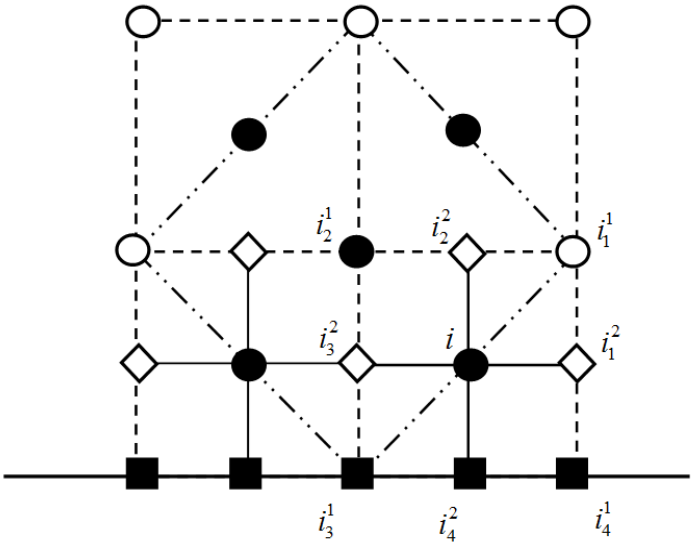

(a) Sketch of stencil refinement near a boundary

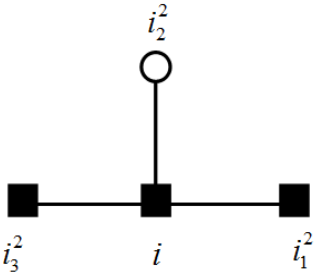

(b) The stencil structure of a reference node on a boundary

Fig. 3.7 Stencil structure on the boundary

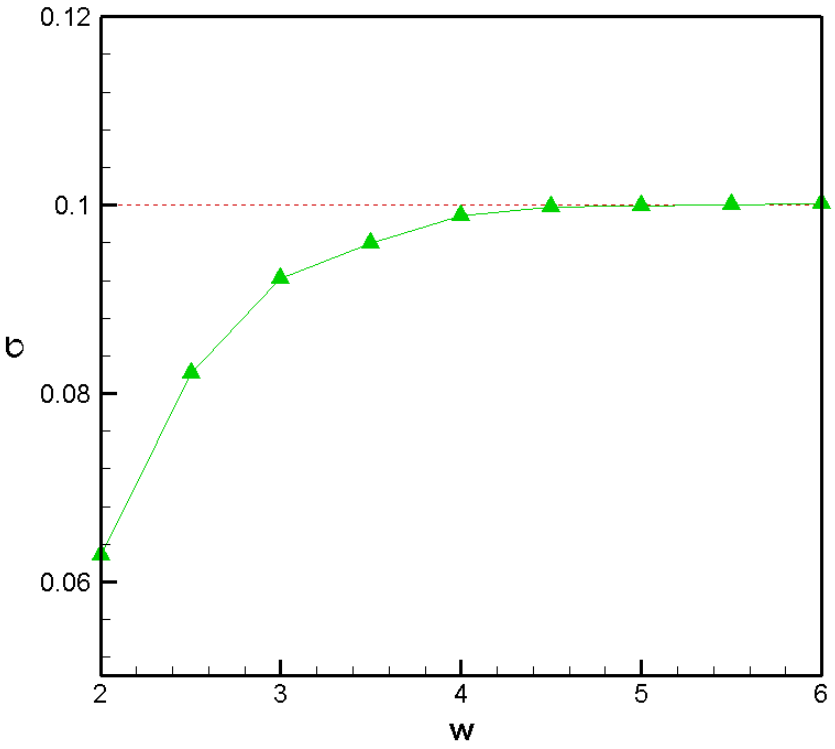

Fig. 3.8 Surface tension (mN/m) versus interface width (in lattice unit)

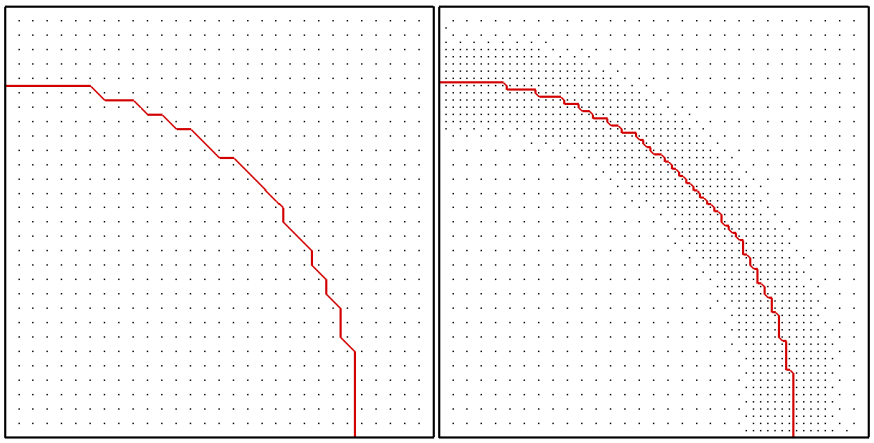

(a) Resolution level=0 (b) Resolution level=2

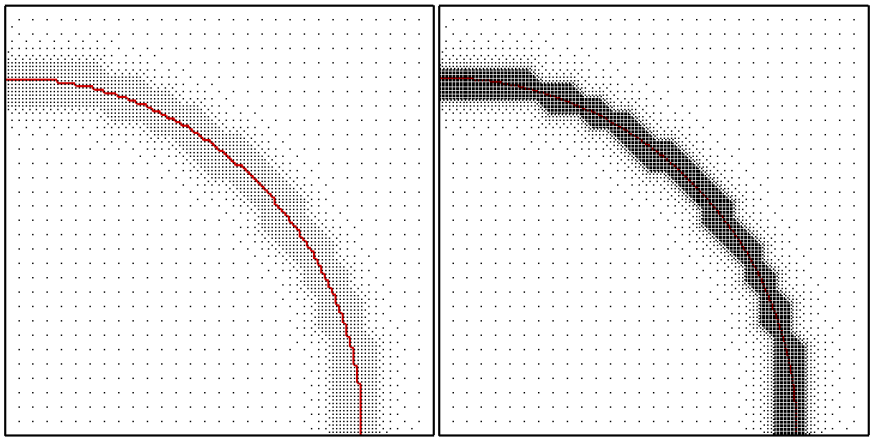

(c) Resolution level=4 (d) Resolution level=6

Fig. 3.9 Local interface profile with gird distribution and different resolution levels

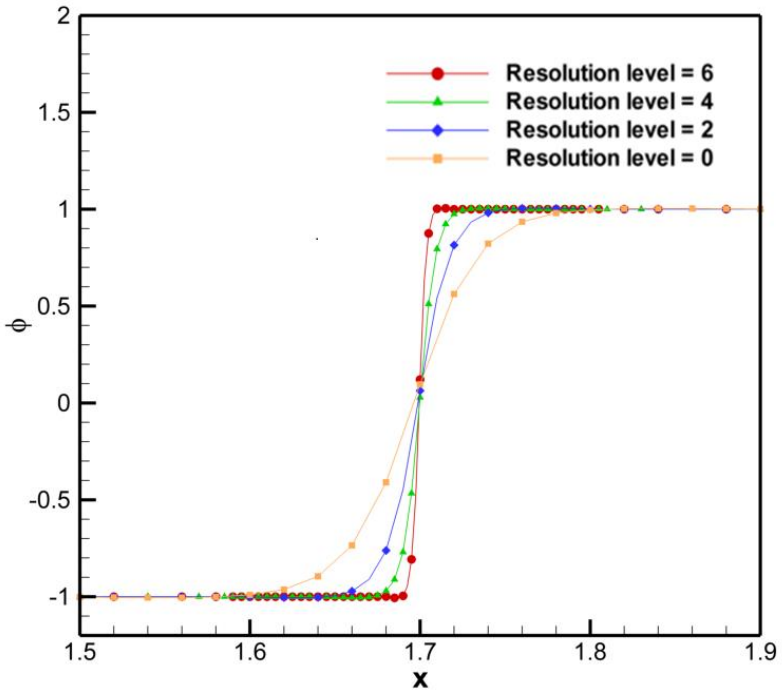

Fig. 3.10 Interface profile when resolution level increases from 0 to 6 (The length is scaled by the initial diameter of the bubble and the order parameter ϕ is an nondimensional parameter)

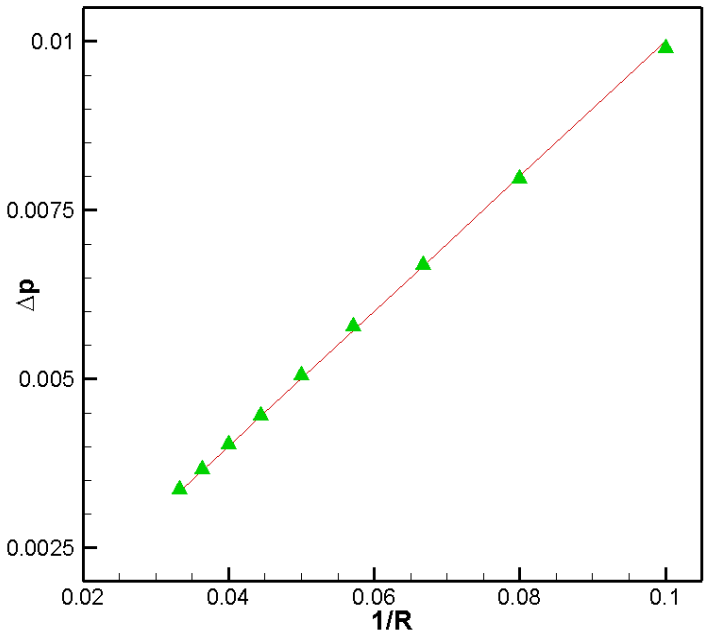

Fig. 3.11 Validation of Laplace law (R in lattice unit and $\Delta p = \sigma / R$ theoretically)

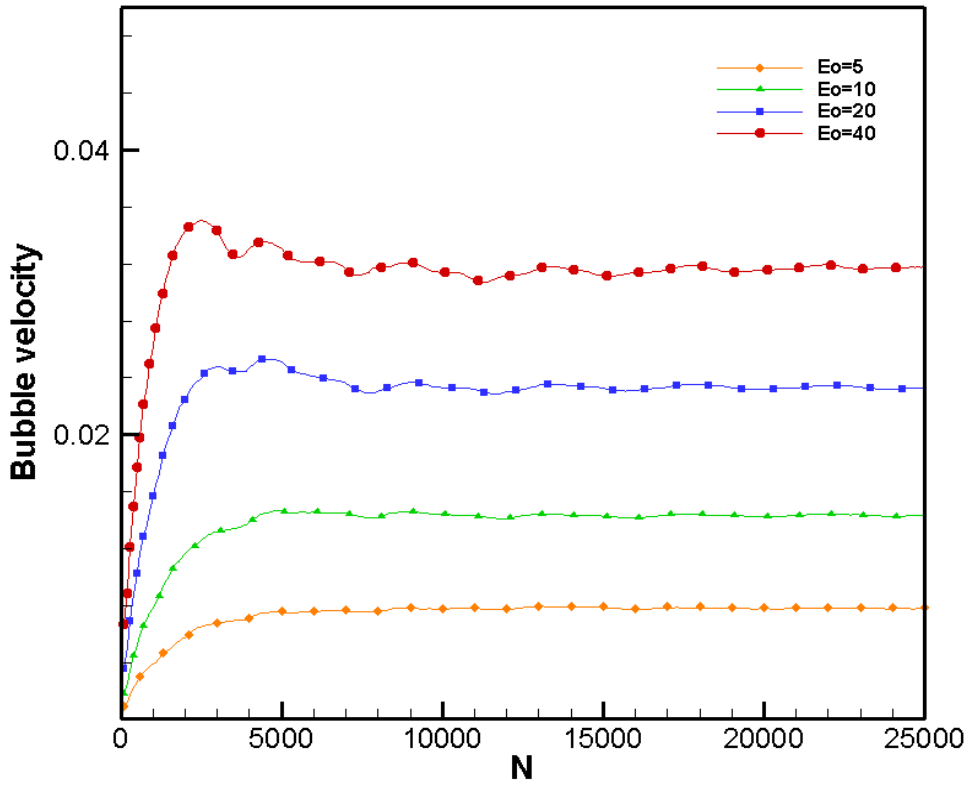

Fig. 3.12 Evolution of the bubble velocity (*m/s*) at different *Eö* (*N* is time step)

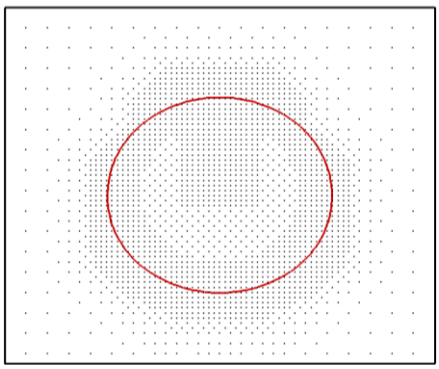

(a) $E\ddot{o} = 5$

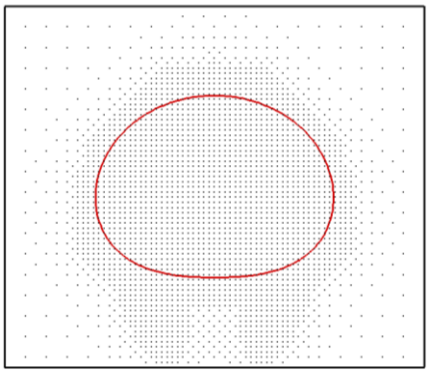

(b) $E\ddot{o} = 10$

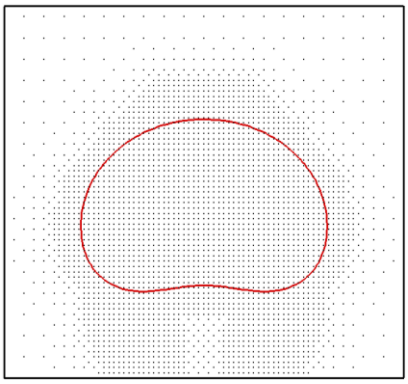

(c) $E\ddot{o} = 20$

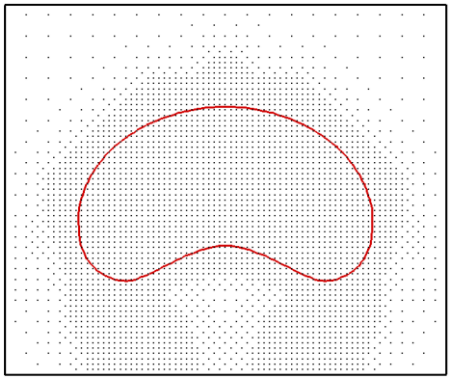

(d) $E\ddot{o} = 40$

Fig. 3.13 Shape of the bubble at different $E\ddot{o}$ with local grid distribution

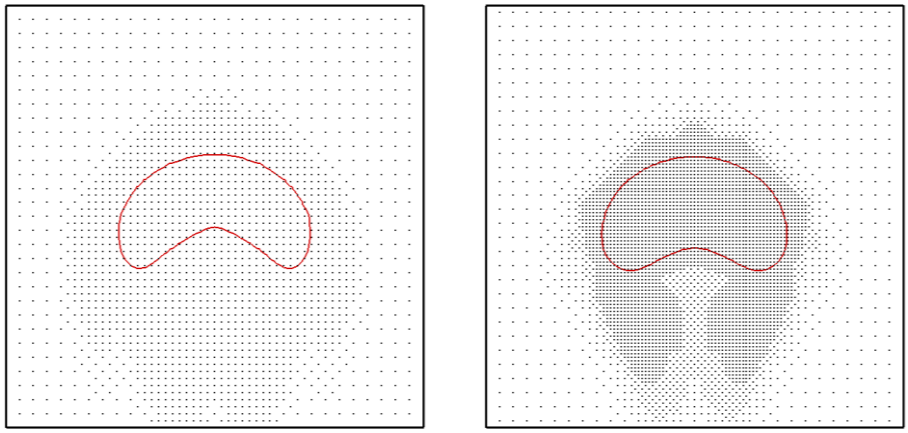

(a) Resolution level=2 (b) Resolution level=4

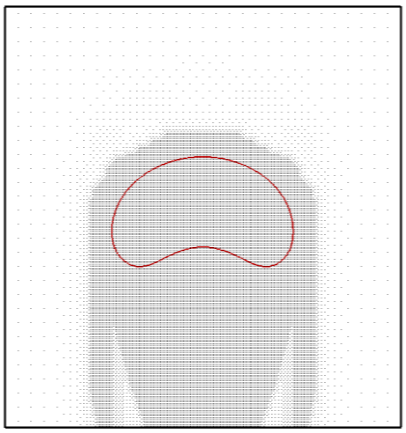

(c) Resolution level=6

Fig. 3.14 Bubble shape with different levels of refinement (Case 4)

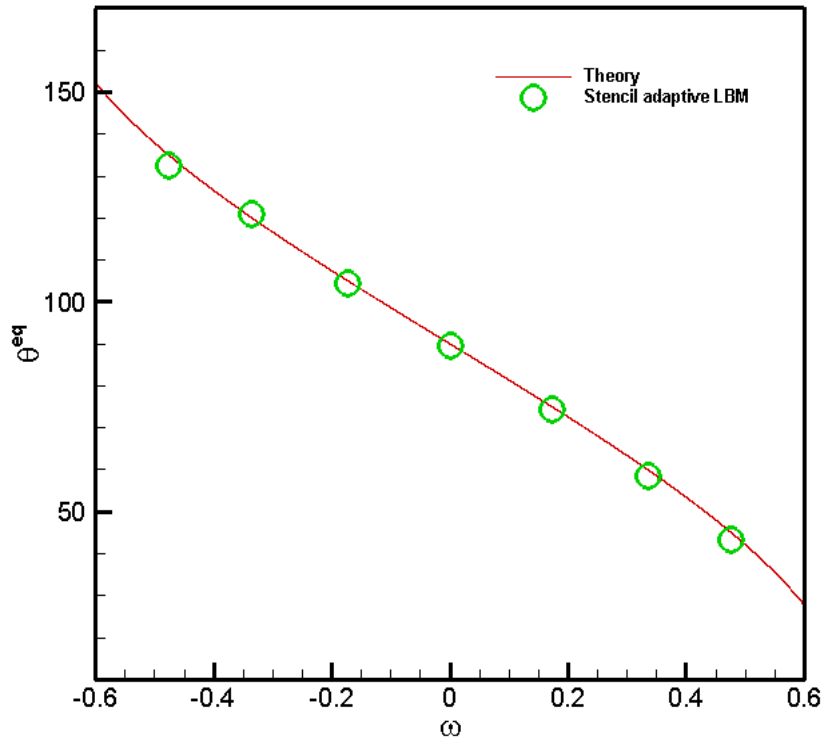

Fig. 3.15 The equilibrium contact angle (◦) versus dimensionless wetting coefficient

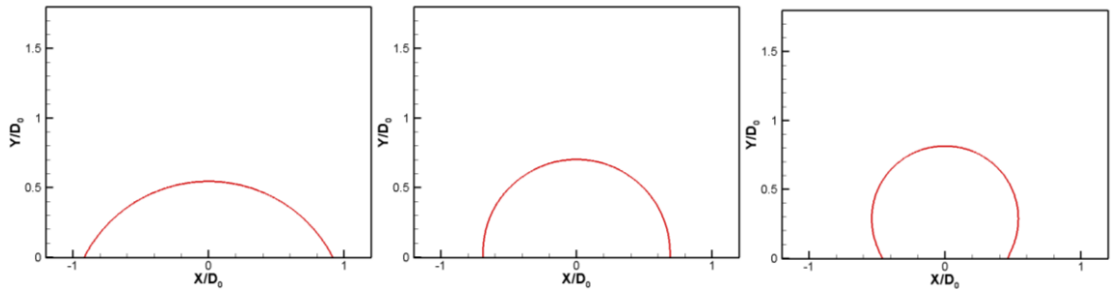

(a) $\theta^{eq} = 60^{\circ}$ (b) $\theta^{eq} = 90^{\circ}$ (c) $\theta^{eq} = 120^{\circ}$

Fig. 3.16 Droplet shapes at different equilibrium contact angles

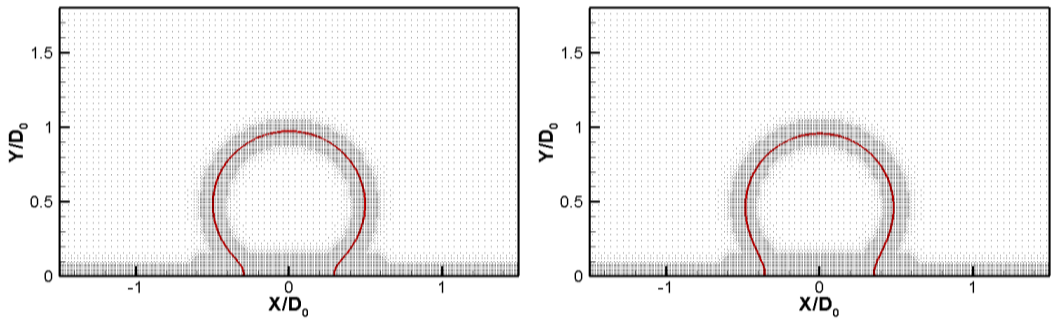

(a) T = 0.02 (b) T = 0.04

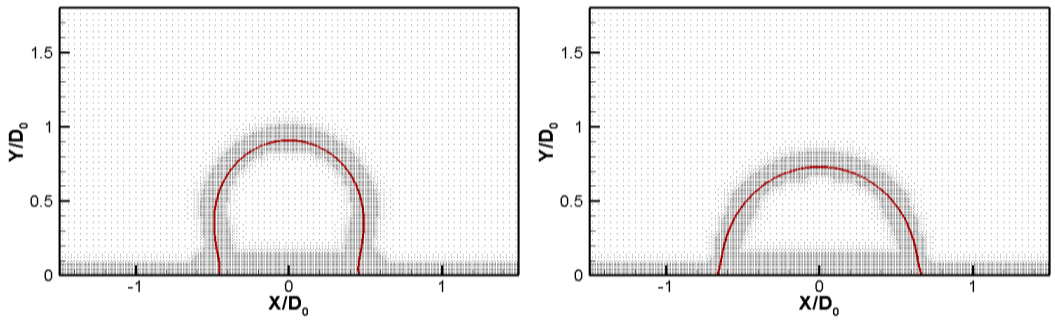

(c) T = 0.08 (d) T = 0.2

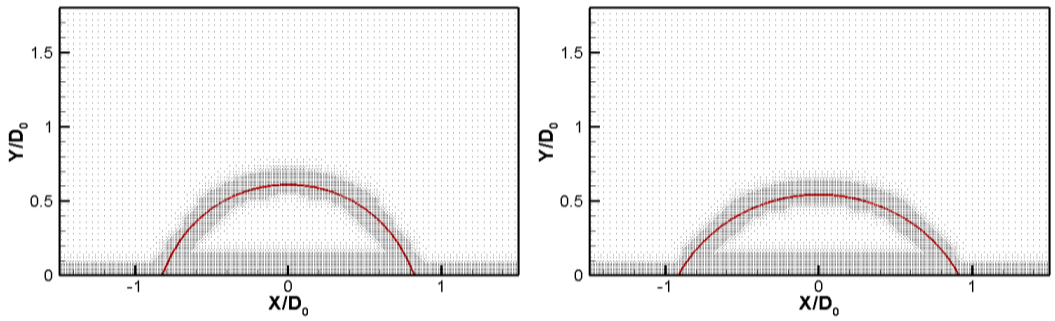

(e) T = 0.4 (f) T = 0.8

Fig. 3.17 Droplet shapes with grid distribution at different time when $\theta^{eq} = 60^{\circ}$

Chapter 4

Development of a Free Energy-Based Phase-Field Lattice Boltzmann Method for Simulation of Multiphase Flow with Density Contrast

Chapter 4 will be devoted to solve the other challenging issue in the simulation of multiphase flows by phase-field lattice Boltzmann method (LBM), that is, simulation of density contrast multiphase flow problems. It is known that the phase-field LBM has become increasingly popular for multiphase flow simulation. However, it is nontrivial to modify the density matched LBM to the density contrast cases. The present method is to improve the Z-S-C model (Zheng et al. 2006) for correct consideration of the density contrast in the momentum equation. The original Z-S-C model uses the particle distribution function in the lattice Boltzmann equation (LBE) for the mean density and momentum, which ensures a stable simulation but cannot properly consider the effect of local density variation in the momentum equation. To correctly consider it, the particle distribution function in LBE must be for the local density and momentum. However, when the LBE of such distribution function is solved, it will encounter a severe numerical instability. To overcome this difficulty, a transformation, which is similar to the one used in the works of He et al. (1999) and of Lee and Lin (2005) is introduced in this work to change the particle distribution function for the local density and momentum into that for the mean density and momentum. As a result, the present model still uses the particle distribution function for the mean density and momentum, and in the meantime, considers the effect of local density variation in the LBE as a forcing term. Numerical examples demonstrate that the present model correctly simulates multiphase flows

with density contrast, and it has an obvious improvement over the Z-S-C model in terms of solution accuracy.

The rest of this Chapter is arranged as follows: First, a brief review of Z-S-C model and incompressible transformation will be presented in Section 4.1. Thereafter, a novel free energy-based phase-field LBM will be proposed in Section 4.2 to simulate multiphase flow problems with density contrast. The proposed method will be verified in Section 4.3. The validation cases include two-dimensional (2D) viscous coupling of multiphase flows, nonlinear development of Rayleigh-Taylor instabilities and droplet splash on the wet surface. In addition, simulation of three-dimensional (3D) off-center droplet collisions and drop impact on the dry walls will also be performed. Finally, the concluding remarks will be drawn in Section 4.4.

4.1 Review of Z-S-C model and incompressible transformation

4.1.1 Z-S-C model

In Z-S-C model, the Cahn-Hilliard equation is used for the interface capturing and a Lattice Boltzmann Equation (LBE) which uses the mean density of two phases as conservative variable is used for the flow field simulation. The interface is captured via the Cahn-Hilliard equation (Zheng et al. 2005, 2006, 2008)

$$\frac{\partial \phi}{\partial t} + (\boldsymbol{u} \cdot \nabla)\phi = M \nabla^2 \mu_\phi \tag{4.1}$$

Here ϕ is the order parameter, M is the mobility and μ_ϕ is the chemical potential that is defined as $4A\phi(\phi^2-\phi_0^2)-\kappa\nabla^2\phi$ (ϕ_0 is the order parameter value in the bulk fluid region). The coefficients κ and A can be evaluated through $w=\sqrt{2\kappa/A}\big/\phi_0$ and $\sigma=4\sqrt{2\kappa A}\big/3\phi_0^3$ with w and σ being interface width and surface tension, respectively. In the lattice Boltzmann framework, the Cahn-Hilliard equation can be expressed by a Lattice Boltzmann Equation (LBE) as

$$g_\alpha\left(\boldsymbol{x}+\boldsymbol{e}_\alpha\delta t,t+\delta t\right)=g_\alpha\left(\boldsymbol{x},t\right)+\left(1-q\right)\left[g_\alpha\left(\boldsymbol{x}+\boldsymbol{e}_\alpha\delta t,t\right)-g_\alpha\left(\boldsymbol{x},t\right)\right]+\frac{g_\alpha^{eq}\left(\boldsymbol{x},t\right)-g_\alpha\left(\boldsymbol{x},t\right)}{\tau_\phi} \tag{4.2}$$

where g_α is the distribution function and used to compute the order parameter, g_α^{eq} is the equilibrium distribution function and τ_ϕ is relaxation parameter. Moreover, δt is the time step and $\boldsymbol{e}_\alpha$ is the lattice velocity (the value of which depends on the lattice velocity model chosen). For two-dimensional (2D) and three-dimensional (3D) flow problems, D2Q5 and D3Q7 lattice velocity models are used, respectively. The corresponding lattice velocity as well as equilibrium distribution function g_α^{eq} are given by

$$\boldsymbol{e}_\alpha=\begin{cases}\left(0,0\right), & \alpha=0\\ \left(\pm1,0\right), & \alpha=1,3\\ \left(0,\pm1\right), & \alpha=2,4\end{cases} \tag{4.3a}$$

$$\boldsymbol{e}_\alpha=\begin{cases}\left(0,0,0\right), & \alpha=0\\ \left(\pm1,0,0\right), & \alpha=1,4\\ \left(0,\pm1,0\right), & \alpha=2,5\\ \left(0,0,\pm1\right), & \alpha=3,6\end{cases} \tag{4.3b}$$

Eq. (4.3a) is the lattice velocities for D2Q5 model and Eq. (4.3b) is for D3Q7 lattice velocity model. In addition,

$$g_\alpha^{eq} = A_\alpha + B_\alpha \phi + C_\alpha \phi \boldsymbol{e}_\alpha \cdot \boldsymbol{u} \tag{4.4a}$$

$$A_\alpha = \begin{cases} -D\Gamma\mu_\phi, & \alpha = 0 \\ \dfrac{1}{2}\Gamma\mu_\phi, & \alpha \neq 0 \end{cases}, \quad B_\alpha = \begin{cases} 1, & \alpha = 0 \\ 0, & \alpha \neq 0 \end{cases}, \quad C_\alpha = \frac{1}{2q} \tag{4.4b}$$

where D is the dimension. $q = 1/\left(\tau_\phi + 0.5\right)$ and Γ are related to the mobility as $M = q\left(\tau_\phi q - 0.5\right)\delta t\Gamma$. Moreover, the order parameter is calculated through

$$\phi = \sum_\alpha g_\alpha \tag{4.5}$$

As introduced in Chapter 2, this LBE can recover the Cahn-Hilliard equation with second order accuracy. Apart from using the density distribution function g_α for interface capturing, another set of LBE is used for the flow field simulation (Zheng et al. 2006)

$$\begin{aligned} h_\alpha\left(\boldsymbol{x} + \boldsymbol{e}_\alpha \delta t, t + \delta t\right) &= h_\alpha\left(\boldsymbol{x}, t\right) + \frac{h_\alpha^{eq}\left(\boldsymbol{x}, t\right) - h_\alpha\left(\boldsymbol{x}, t\right)}{\tau_h} \\ &+ \left(1 - \frac{1}{2\tau_h}\right)\frac{w_\alpha \delta t}{c_s^2}\left[\left(\boldsymbol{e}_\alpha - \boldsymbol{u}\right) + \frac{\left(\boldsymbol{e}_\alpha \cdot \boldsymbol{u}\right)}{c_s^2}\boldsymbol{e}_\alpha\right]\left(\mu_\phi \nabla\phi + \boldsymbol{F}\right) \end{aligned} \tag{4.6}$$

The equilibrium distribution function is

$$h_\alpha^{eq} = w_\alpha A_\alpha + w_\alpha n\left[\frac{\boldsymbol{e}_\alpha \cdot \boldsymbol{u}}{c_s^2} + \frac{\left(\boldsymbol{e}_\alpha \cdot \boldsymbol{u}\right)^2}{2c_s^4} - \frac{\left|\boldsymbol{u}\right|^2}{2c_s^2}\right] \tag{4.7}$$

with $A_0 = (9/4)n - 15\left[\phi\mu_\phi + (1/3)n\right]/4$ and $A_{1\sim8} = 3\left[\phi\mu_\phi + (1/3)n\right]$. Moreover, the density and velocity are calculated through the following equations

$$n = \sum_\alpha h_\alpha \tag{4.8a}$$

$$n\boldsymbol{u} = \sum_\alpha \boldsymbol{e}_\alpha h_\alpha + \frac{1}{2}\left(\mu_\phi \nabla\phi + \boldsymbol{F}\right) \tag{4.8b}$$

It should be noted that in the Z-S-C model, the density of flow field is set as the mean value of two different fluids, that is, $n = \left(\rho_H + \rho_L\right)/2$ with ρ_H and ρ_L representing high and low density values. In this manner, a pressure field nc_s^2 (where c_s is the speed of sound) that subjects to small variation is generated implicitly by the streaming process in LBE. This ensures continuity of pressure across the fluid-fluid interface. However, this manipulation only is unable to consider the effect of density contrast (Fakhari and Rahimian 2010). This is because the effect of local density variation is not considered in the momentum equation. The major contribution of this work is to remove this drawback.

4.1.2 Incompressible Transformation

As indicated previously, to correctly consider the effect of density contrast in the momentum equation, the particle distribution function in LBE must be for the local density and momentum. Then, to avoid high variation of the particle distribution function which may cause numerical instability, we need to introduce a similar transformation like the incompressible transformation proposed by He et al. (1999) and applied in the work of Lee and Lin (2005). In the following, we will give a very brief description on the incompressible

transformation. By setting $g_\alpha = f_\alpha c_s^2 + \left(p - \rho c_s^2\right) w_\alpha$ and $g_\alpha^{eq} = f_\alpha^{eq} c_s^2 + \left(p - \rho c_s^2\right) w_\alpha$, one can simply transform the original particle distribution function f_α for the local density and momentum into g_α for the pressure and momentum. The resultant discrete Boltzmann equation (DBE) after transformation reads (Lee and Lin 2005)

$$\left(\frac{\partial}{\partial t} + \boldsymbol{e}_\alpha \cdot \nabla\right) g_\alpha = -\frac{1}{\lambda}\left(g_\alpha - g_\alpha^{eq}\right) + \left(\boldsymbol{e}_\alpha - \boldsymbol{u}\right) \cdot \left[\nabla \rho c_s^2 \left(\Gamma_\alpha - w_\alpha\right) - \phi \nabla \mu_\phi \Gamma_\alpha\right] \tag{4.9}$$

where $c_s^2 = 1/3$ is the sound speed in LBM. Γ_α is defined as

$$\Gamma_\alpha = \frac{f_\alpha^{eq}}{\rho} = w_\alpha \left[1 + \frac{\boldsymbol{e}_\alpha \cdot \boldsymbol{u}}{c_s^2} + \frac{\left(\boldsymbol{e}_\alpha \cdot \boldsymbol{u}\right)^2}{2c_s^4} - \frac{|\boldsymbol{u}|^2}{2c_s^2}\right] \tag{4.10}$$

By using the Chapman-Enskog expansion analysis, Eq. (4.9) can recover the pressure and momentum equations as follows (Lee and Lin 2005)

$$\frac{\partial p}{\partial t} + \rho c_s^2 \nabla \cdot \boldsymbol{u} = 0 \tag{4.11a}$$

$$\rho\left(\frac{\partial \boldsymbol{u}}{\partial t} + \boldsymbol{u} \cdot \nabla \boldsymbol{u}\right) = -\nabla p + \nabla \cdot \left[\mu\left(\nabla \boldsymbol{u} + \left(\nabla \boldsymbol{u}\right)^T\right)\right] - \phi \nabla \mu_\phi \tag{4.11b}$$

The pressure and velocity fields can be obtained from the pressure distribution functions. In addition, the local density in the above equation is calculated from the order parameter $\rho = \phi \rho_L + (1-\phi)\rho_H$ (with ϕ taking the value of 0 and 1 in two bulk regions).

4.2 New Free Energy-Based Lattice Boltzmann Model for Multiphase Flow with Density Contrast

To illustrate the present model, we will start from the following LBE with the interfacial force

$$h_\alpha\left(\boldsymbol{x}+\boldsymbol{e}_\alpha\delta t,t+\delta t\right)=h_\alpha\left(\boldsymbol{x},t\right)+\frac{h_\alpha^{eq}\left(\boldsymbol{x},t\right)-h_\alpha\left(\boldsymbol{x},t\right)}{\tau_h}+\frac{\left(\boldsymbol{e}_\alpha-\boldsymbol{u}\right)\cdot\left(-\phi\nabla\mu_\phi\right)}{c_s^2}\Gamma_\alpha\delta t \quad (4.12)$$

When the particle distribution function h_α in Eq. (4.12) is used for the mean density and velocity, the effect of the local density variation cannot be properly considered in the momentum equation. This may lead to incorrect results for multiphase flow problems with density contrast. To correctly consider the local density effect in the momentum equation, h_α has to be used for the local density and velocity. On the other hand, when $h_\alpha\left(\boldsymbol{x},t\right)$ is used for the local density, from Chapman-Enskog expansion analysis, it is known that the streaming process implicitly generates ρc_s^2 (where ρ is the local density) for the pressure. This relationship between pressure and density is valid for the incompressible single phase flow as both pressure and density are continuous and change very little in the flow domain. However, when the multiphase flow with density contrast is considered, the relationship of $p=\rho c_s^2$ will lead to unphysical solution. This is because the fluid-fluid interface is a contact discontinuity, where the pressure is continuous but the density is discontinuous. In the lattice Boltzmann framework, c_s is a constant in the chosen lattice velocity model. Obviously, the relationship of $p=\rho c_s^2$ will give a discontinuous pressure across the fluid-fluid interface. This is physically incorrect. To correctly recover N-S equation, we have to take the difference of $-\nabla(p-\rho c_s^2)$ as a forcing term (He et al. 1999) in LBE. It is shown in the Z-S-C model

(Zheng et al. 2006) that the pressure field can be computed by $p=\rho_0 c_s^2$, where ρ_0 is the mean density. Thus, to simulate multiphase flows with density contrast, the LBE should be changed to

$$h_\alpha\left(\boldsymbol{x}+\boldsymbol{e}_\alpha\delta t,t+\delta t\right)=h_\alpha\left(\boldsymbol{x},t\right)+\frac{h_\alpha^{eq}\left(\boldsymbol{x},t\right)-h_\alpha\left(\boldsymbol{x},t\right)}{\tau_h}+\frac{\left(\boldsymbol{e}_\alpha-\boldsymbol{u}\right)\cdot\left(-\phi\nabla\mu_\phi\right)}{c_s^2}\Gamma_\alpha\delta t+\left(\boldsymbol{e}_\alpha-\boldsymbol{u}\right)\cdot\left[-\nabla(\rho_0-\rho)\right]\Gamma_\alpha\delta t \tag{4.13}$$

When the density contrast increases, the calculation will become very unstable due to the presence of large density gradient and resultant drastic velocity oscillation. It is very likely to violate the low Mach number limit as $O\left(\boldsymbol{u}\right)=O\left(Ma\right)$. To solve this problem, we follow the idea of incompressible transformation and introduce the following transformation to change the particle distribution function for the local density and velocity into that for the mean density and velocity,

$$\overline{f}_\alpha=h_\alpha+\left(\rho_0-\rho\right)w_\alpha \tag{4.14}$$

where h_α is used for the local density and $\overline{f}_\alpha$ is utilized for the mean density. The corresponding equilibrium distribution function is

$$\overline{f}_\alpha^{eq}=h_\alpha^{eq}+\left(\rho_0-\rho\right)w_\alpha=w_\alpha\left[\rho_0+\rho\left(\frac{\left(\boldsymbol{e}_\alpha\cdot\boldsymbol{u}\right)}{c_s^2}+\frac{\left(\boldsymbol{e}_\alpha\cdot\boldsymbol{u}\right)^2}{2c_s^4}-\frac{\left|\boldsymbol{u}\right|^2}{2c_s^2}\right)\right] \tag{4.15}$$

where ρ_0 is defined as the mean density of multiphase flow, $\rho_0=\left(\rho_H+\rho_L\right)/2$ which is subjected to small variation and ρ is the local density which varies across the fluid interface. By using Eqs. (4.13) and (4.14), we can derive the following expression

$$\overline{f}_\alpha\left(\boldsymbol{x}+\boldsymbol{e}_\alpha\delta t,t+\delta t\right)-\overline{f}_\alpha\left(\boldsymbol{x},t\right)=h_\alpha\left(\boldsymbol{x}+\boldsymbol{e}_\alpha\delta t,t+\delta t\right)-h_\alpha\left(\boldsymbol{x},t\right)+\left[\left(\frac{\partial}{\partial t}+\boldsymbol{e}_\alpha\cdot\nabla\right)\delta t\right]\left(\rho_0-\rho\right)w_\alpha \tag{4.16}$$

With incompressible condition of $\left(\frac{\partial}{\partial t}+\boldsymbol{u}\cdot\nabla\right)\rho_0=0$ and $\left(\frac{\partial}{\partial t}+\boldsymbol{u}\cdot\nabla\right)\rho=0$, the above equation can be rewritten as

$$\overline{f}_\alpha\left(\boldsymbol{x}+\boldsymbol{e}_\alpha\delta t,t+\delta t\right)-\overline{f}_\alpha\left(\boldsymbol{x},t\right)=h_\alpha\left(\boldsymbol{x}+\boldsymbol{e}_\alpha\delta t,t+\delta t\right)-h_\alpha\left(\boldsymbol{x},t\right)+\delta t w_\alpha(\boldsymbol{e}_\alpha-\boldsymbol{u})\cdot\nabla\left(\rho_0-\rho\right) \tag{4.17}$$

Substituting Eq. (4.17) into Eq. (4.13), the following equation can be obtained

$$\overline{f}_\alpha\left(\boldsymbol{x}+\boldsymbol{e}_\alpha\delta t,t+\delta t\right)-\overline{f}_\alpha\left(\boldsymbol{x},t\right)=\frac{h_\alpha^{eq}\left(\boldsymbol{x},t\right)-h_\alpha\left(\boldsymbol{x},t\right)}{\tau_h}+\frac{\left(\boldsymbol{e}_\alpha-\boldsymbol{u}\right)\cdot\left(-\phi\nabla\mu_\phi\right)}{c_s^2}\Gamma_\alpha\delta t-\left(\boldsymbol{e}_\alpha-\boldsymbol{u}\right)\cdot\nabla(\rho_0-\rho)\delta t(\Gamma_\alpha-w_\alpha) \tag{4.18}$$

For the incompressible flow $\nabla\rho_0\sim O(Ma^2)$ and $(\Gamma_\alpha-w_\alpha)\sim O(Ma)$, thus $(\Gamma_\alpha-w_\alpha)\nabla\rho_0\sim O(Ma^3)$ which can be omitted. Moreover, to recover the N-S equation more accurately, the forcing term are modified and the LBE for the flow field are written as (Guo et al. 2011)

$$f_\alpha\left(\boldsymbol{x}+\boldsymbol{e}_\alpha\delta t,t+\delta t\right)=f_\alpha\left(\boldsymbol{x},t\right)-\frac{1}{\tau_f}\left[f_\alpha\left(\boldsymbol{x},t\right)-f_\alpha^{eq}\left(\boldsymbol{x},t\right)\right]+\left(1-\frac{1}{2\tau_f}\right)\delta t\frac{\left(\boldsymbol{e}_\alpha-\boldsymbol{u}\right)}{c_s^2}\cdot\left[\nabla\rho c_s^2\left(\Gamma_\alpha-w_\alpha\right)-\phi\nabla\mu_\phi\Gamma_\alpha\right] \tag{4.19}$$

where $\tau_f=\tau_h$ and $\overline{f}_\alpha$ is written as f_α for convenience. The macroscopic variables are computed by

$$\rho_0 = \sum_\alpha f_\alpha + \frac{1}{2}\boldsymbol{u}\cdot\nabla\rho\delta t\,, \quad \rho\boldsymbol{u} = \sum_\alpha f_\alpha \boldsymbol{e}_\alpha - \frac{1}{2}\phi\nabla\mu_\phi\delta t \tag{4.20}$$

The corresponding equilibrium distribution function is $f_\alpha^{eq} = \overline{f}_\alpha^{eq}$. In the following, the Chapman-Enskog expansion analysis is applied to Eq. (4.19). Define $f_\alpha = f_\alpha^{(0)} + \varepsilon f_\alpha^{(1)} + \varepsilon^2 f_\alpha^{(2)}$, $\partial_t = \varepsilon\partial_{t^0} + \varepsilon^2\partial_{t^1}$, $\nabla = \varepsilon\nabla_1$, and $G_\alpha = \varepsilon G_\alpha^{(1)}$, where ε is a small expansion parameter. The following relations can be established

$$f_\alpha^{(0)} = f_\alpha^{eq} \tag{4.21a}$$

$$\left(\partial_{t^0} + \boldsymbol{e}_\alpha\cdot\nabla_1\right) f_\alpha^{(0)} = -\frac{1}{\tau_f\delta t} f_\alpha^{(1)} + G_\alpha^{(1)} \tag{4.21b}$$

$$\partial_{t^1} f_\alpha^{(0)} + \left(1-\frac{1}{2\tau_f}\right)\left(\partial_{t^0} + \boldsymbol{e}_\alpha\cdot\nabla_1\right) f_\alpha^{(1)} = -\frac{1}{\tau_f\delta t} f_\alpha^{(2)} - \frac{\delta t}{2}\left(\partial_{t^0} + \boldsymbol{e}_\alpha\cdot\nabla_1\right) G_\alpha^{(1)} \tag{4.21c}$$

with $G_\alpha = \left(1-\frac{1}{2\tau_f}\right)\frac{(\boldsymbol{e}_\alpha - \boldsymbol{u})}{c_s^2}\cdot\left[\nabla\rho c_s^2\left(\Gamma_\alpha - w_\alpha\right) - \phi\nabla\mu_\phi\Gamma_\alpha\right]$. Additionally, the relations $\sum_\alpha f_\alpha^{(1)} = -\frac{1}{2}\boldsymbol{u}\cdot\nabla_1\rho\delta t$, $\sum_\alpha f_\alpha^{(1)}\boldsymbol{e}_\alpha = \frac{1}{2}\phi\nabla_1\mu_\phi\delta t$, $\sum_\alpha f_\alpha^{(2)} = 0$, $\sum_\alpha f_\alpha^{(2)}\boldsymbol{e}_\alpha = 0$, $\sum_\alpha G_\alpha^{(1)} = \left(1-\frac{1}{2\tau_f}\right)\boldsymbol{u}\cdot\nabla_1\rho$, and $\sum_\alpha G_\alpha^{(1)}\boldsymbol{e}_\alpha = \left(1-\frac{1}{2\tau_f}\right)\left(-\phi\nabla_1\mu_\phi\right)$ could also be established. With these relations, the zeroth moments of Eq. (4.21b) and (4.21c) give

$$\begin{aligned}&\partial_{t^0}\rho_0 + \nabla_1\left(\rho\boldsymbol{u}\right) = -\frac{1}{\tau_f\delta t}\left(-\frac{1}{2}\boldsymbol{u}\cdot\nabla_1\rho\delta t\right) + \left(1-\frac{1}{2\tau_f}\right)\boldsymbol{u}\cdot\nabla_1\rho = \boldsymbol{u}\cdot\nabla_1\rho \\ &\Rightarrow \partial_{t^0}\rho_0 + \rho\nabla_1\cdot\boldsymbol{u} = 0\end{aligned} \tag{4.22a}$$

$$\begin{aligned}
&\partial_{t^1}\rho_0+\left(1-\frac{1}{2\tau_f}\right)\left[\partial_{t^0}\left(-\frac{1}{2}\boldsymbol{u}\cdot\nabla_1\rho\delta t\right)+\nabla_1\left(\frac{1}{2}\phi\nabla_1\mu_\phi\delta t\right)\right]=\\
&\qquad -\frac{1}{2}\left(1-\frac{1}{2\tau_f}\right)\delta t\left[\partial_{t^0}\left(\boldsymbol{u}\cdot\nabla_1\rho\right)+\nabla_1\left(-\phi\nabla_1\mu_\phi\right)\right]\\
&\Rightarrow \partial_{t^1}\rho_0=0
\end{aligned}\tag{4.22b}$$

Moreover, the first moments of Eq. (4.21b) and (4.21c) are

$$\begin{aligned}
&\partial_{t^0}\left(\rho\boldsymbol{u}\right)+\nabla_1\left(\rho\boldsymbol{u}\otimes\boldsymbol{u}+\rho_0c_s^2\right)=-\frac{1}{\tau_f\delta t}\left(\frac{1}{2}\phi\nabla_1\mu_\phi\delta t\right)+\left(1-\frac{1}{2\tau_f}\right)\left(-\phi\nabla_1\mu_\phi\right)\\
&\Rightarrow \partial_{t^0}\left(\rho\boldsymbol{u}\right)+\nabla_1\left(\rho\boldsymbol{u}\otimes\boldsymbol{u}+\rho_0c_s^2\right)=-\phi\nabla_1\mu_\phi
\end{aligned}\tag{4.23a}$$

$$\begin{aligned}
&\partial_{t^1}\left(\rho\boldsymbol{u}\right)+\left(1-\frac{1}{2\tau_f}\right)\left[\partial_{t^0}\left(\frac{1}{2}\phi\nabla_1\mu_\phi\delta t\right)+\nabla_1\left(\sum f_\alpha^{(1)}\boldsymbol{e}_\alpha\boldsymbol{e}_\beta\right)\right]=\\
&\qquad -\frac{1}{2}\delta t\left[\left(1-\frac{1}{2\tau_f}\right)\partial_{t^0}\left(-\phi\nabla_1\mu_\phi\right)+\nabla_1\left(\sum G_\alpha^{(1)}\boldsymbol{e}_\alpha\boldsymbol{e}_\beta\right)\right]\\
&\Rightarrow \partial_{t^1}\left(\rho\boldsymbol{u}\right)=\nabla_1\left[\rho\left(\tau_f-0.5\right)c_s^2\delta t\left(\nabla_1\boldsymbol{u}+\left(\nabla_1\boldsymbol{u}\right)^T\right)\right]
\end{aligned}\tag{4.23b}$$

To sum up, the macroscopic equations recovered are

$$\frac{\partial\rho_0}{\partial t}+\rho\nabla\cdot\boldsymbol{u}=0\tag{4.24a}$$

$$\frac{\partial\left(\rho\boldsymbol{u}\right)}{\partial t}+\nabla\cdot\left(\rho\boldsymbol{u}\otimes\boldsymbol{u}\right)=-\nabla p+\nabla\cdot\left[\mu\left(\nabla\boldsymbol{u}+\left(\nabla\boldsymbol{u}\right)^T\right)\right]-\phi\nabla\mu_\phi\tag{4.24b}$$

where $p=\rho_0c_s^2$. It can be seen that Eq. (4.19) can correctly reflect the influence of density contrast and it will be used for simulation of the flow field. D2Q9 and D3Q15 lattice velocity models are used for this LBE for 2D and 3D problems respectively. From the density distribution function, the mean density and velocity of the flow field can be calculated. Meanwhile, the local density can be computed from the order parameter by

$\rho = \rho_L + \left[\left(\phi + \phi_0\right)/2\phi_0\right]\left(\rho_H - \rho_L\right)$ where $\phi_0 = \left(\rho_H - \rho_L\right)/2$ is in the high density phase ($-\phi_0$ in the other phase). It can be seen that in this way, the conservation variable of the distribution function can be kept away from large oscillation and thus enable a stable simulation. Concurrently, the influence of density gradient is incorporated into the governing equation as a forcing term. Besides the LBE for the flow field, one also needs a governing equation for evolution of the order parameter. In the current work, the LBE in Z-S-C model is adopted because D2Q5 (for 2D cases) and D3Q7 (for 3D cases) models used in Z-S-C interface capturing LBE are more computationally effective.

In conclusion, a new free energy-based lattice Boltzmann model has been proposed in this subsection. This work mainly improves the lattice Boltzmann equation for simulation of the flow field used in the work of Zheng et al. (2006). To correctly account for the density contrast in the multiphase flow simulation, the particle distribution function should be used for the local density. Then, to improve numerical stability, a transformation is introduced to change the particle distribution function for the local density into that for the mean density.

4.3 Results and Discussions

In this Section, the proposed free energy based LBM is validated through both stationary and dynamic problems. There are 2D cases including viscous coupling of multiphase flow in a plane channel, nonlinear development of Rayleigh-Taylor instability and droplet splash on a wet surface as well as 3D cases including off-center droplet collision and droplet splash on a surface considering dynamic contact angle.

4.3.1 Viscous coupling in a 2D Channel

Viscous coupling of immiscible multiphase flows is a fundamental problem in porous media (Huang and Lu 2009). In this subsection, we study viscous coupling in a 2D channel as sketched in Fig. 4.1. The computational domain is set as 100×200. The periodic boundary condition is applied on the left and right boundaries. Meanwhile, the no slip boundary condition is used on the upper and lower boundaries. A body force of $G=1.5\times10^{-8}$ is applied only on fluid 1. It can be seen from Fig. 4.1 that one phase moves along the solid surface in the region of $a<|y|<b$ and the other flows in the region of $0<|y|<a$. The dynamic viscosity ratio between the two phases is defined as $R_\mu=\mu_1/\mu_2$. To examine the ability of the proposed method to account for density contrast, the kinematic viscosity is set as the same for both fluids. Hence, $R_\mu=\rho_1\nu/\rho_2\nu$ takes the same value as $R_\rho=\rho_1/\rho_2$. The analytical velocity profile can be expressed as $u_1=A_1y^2+C_1$ and $u_2=B_2y+C_2$, where $A_1=-G/2\rho_1\nu$, $B_2=2R_\mu A_1a$, $C_1=-A_1a^2-B_2(b-a)$ and $C_2=-B_2b$. A detailed derivation can be found in Huang and Lu (2009). The numerical results are plotted together with those of Z-S-C model and theoretical prediction in Fig. 4.2, in which the density contrasts are $R_\rho=\rho_1/\rho_2=1/18$ (Fig. 4.2(a)) and $R_\rho=1/50$ (Fig. 4.2(b)), respectively. It can be seen that the results obtained by Z-S-C model are smooth parabola and different from the analytical solutions. On the other hand, the present numerical results agree well with the corresponding analytical solutions. A small difference is that the turning point at lattice unit (±50) is not as sharp as the analytical solution. This is expected since a diffuse interface method is used where the fluid-fluid interface spreads over several mesh intervals. Conversely, this effect is not considered in the analytical solutions. In conclusion, the results demonstrate that the proposed method can successfully resolve the stationary multiphase flow problems with density contrast.

4.3.2 Rayleigh-Taylor instability

In this subsection, a dynamic problem, Rayleigh-Taylor instability, is simulated. When a heavier fluid is placed on the top of another lighter fluid and the system is subject to gravitational field, any perturbation along the interface can grow nonlinearly. This is the Rayleigh-Taylor instability (Sharp 1984, Tryggvason 1988, He et al. 1999). It is characterized by the Atwood number $At = \left(\rho_H - \rho_L\right)/\left(\rho_H + \rho_L\right)$ which represents the density difference of two fluids and the Reynolds number $Re = \sqrt{L^3 g}/\nu$ (L is the characteristic length which is taken as the width of the domain, g is gravity acceleration and ν is the kinematic viscosity). The high nonlinearity and density difference-dependent characteristics of the problem make it a challenging and suitable dynamic validation case for the proposed LBM to simulate multiphase flows with density contrast.

To verify the proposed model, the same computational parameters are applied as in He et al. (1999). The Atwood number is set as 0.5, the Reynolds number is taken as 256 and the viscosity contrast is not considered. The computational domain is $L \times 4L$ and an interface is initialized at $y = 2L + 0.1L\cos\left(2\pi x/L\right)$, which indicates a planer interface perturbed by a wave with amplitude of $0.1L$ and wave number of $k = 1$. Three sets of mesh sizes: 64×256, 128×512 and 256×1024, are used to examine the grid dependency. Fig. 4.3 compares the time evolution of bubble/spike position on three different grids with that of He et al (1999). In this figure, the time was non-dimensionalized by $\sqrt{L/g}$. The numerical results show that the present solver provides satisfactory results on all three sets of grids. It could be found that the results on grids of 128×512 and 256×1024 are almost identical to each other. As

demonstrated in Fig. 4.4, at the initial stage of Rayleigh-Taylor instability, two symmetric rotating vortices are formed around the evolving interface subject to gravity. The vortices are elongated as the initial perturbation grows, and are finally broken up into two pairs of small vortices. Fig. 4.5 shows the interface contours represented by $\phi = 0$ at five non-dimensional time levels from 1 to 5. It could be seen that as time progresses, the initial perturbation first grows downwards following the direction of gravity (Time=1.0). The spike of heavier fluid then rolls up and two secondary side-spikes are generated (Time=2.0 and 3.0). Thereafter, the main spike keeps moving downwards while two second side-spikes evolve upwards driven by the up-moving lighter fluid (Time=4.0). After that, the extended side-spike would break up into several small droplets (Time=5.0). The present interface patterns at different time states compare well with those of He et al (1999) as shown in Fig. 4.6. The differences of interface structures at Time=5.0 are attribute to the fact that different numbers/values of contour levels were plotted.

4.3.3 Droplet splash on a wet surface

To further verify the proposed model, the droplet splash on a wet surface is simulated. Both the time evolution of droplet radius and the droplet shape at different time levels are compared with results in the literature (Fakhari and Rahimian 2010). Fakhari and Rahimian (2010) used a phase field-based LBM coupled with multiple relaxation time (MRT) technique to simulate drop impact on a wet surface. The applied phase field-based LBM is similar to that proposed by He et al. (1999). To improve the numerical stability for high viscosity contrast or high Reynolds number problems, the MRT technique is introduced into their method. Two important non-dimensional parameters of this problem are Reynolds and Weber numbers defined by

$$Re = \frac{U_0 D}{\nu_L} \tag{4.25}$$

$$We = \frac{\rho_L U_0^2 D}{\sigma} \tag{4.26}$$

where U_0 is the initial impact velocity, D is the initial droplet diameter, ν_L and ρ_L are the liquid kinematic viscosity and density, respectively. The problem set-up is sketched in Fig. 4.7. The mesh size of 1201×401 is used. The wall boundary condition at the bottom and slip boundary condition at the top were applied. At the same time, the periodic boundary condition is used at the left and right sides. The initial droplet radius is set as 100 and the impact velocity was $U_0 = 0.05$. The densities of droplet and ambient fluid are $\rho_L = 5$ and $\rho_G = 1$, respectively. The height of the wet surface is taken as $H_{wet} = H/10$, where H is the height of computational domain. Moreover, the Weber number was kept as 5000 in all simulations for this case. Same as the situation in Fakhari and Rahimian (2010), three different Reynolds numbers, 50, 200 and 1000, are considered (for high Reynolds number such as 1000, Multiple-Relaxation-Time collision operator was used). The time evolution of the dimensionless droplet radius (the dimensionless time is defined as $T = tU_0 / D$ and the dimensionless droplet radius is defined as $R = r / D$) is compared with the results in the literature in Fig. 4.8. Agreement can be observed at different Reynolds numbers. Furthermore, Fig. 4.9 compares the shape of droplet and thin liquid layer (the interface is represented by $\phi = 0$ contour) during splash with that given by Fakhari and Rahimian (2010) at several time stages. At low Reynolds number of 50, after the initial impact with relatively low impact velocity, the droplet gently spreads on the thin liquid film, then gradually bridges the gas gap between the droplet and the film and generates a liquid jet at later time stage. Additionally, it can also be seen that during this process, a surface wave is also generated and propagates

along the surface. On the other hand, different flow phenomenon could be observed at higher Reynolds number (Re=200). As can be seen from Fig. 4.9, a liquid jet is formed immediately after the impact (Time=0.4). As the droplet spreads on the film, the liquid jet also grows into a corolla and rolls up (from Time=0.6 to Time=4.0). When time evolves, the rim of the corolla is elongated and finally breaks up into several small droplets (Time=5.0). It is shown that the proposed model also provides satisfactory results in terms of droplet shapes at different Reynolds numbers.

4.3.4 Off-center droplet collision

To further explore the capability of the present model, the 3D off-center droplet collisions with complex topological interface change were simulated in this subsection. In this case, two droplets with the same radius (12 lattice units) are placed in the flow domain as shown in Fig. 4.10. The density contrast of liquid droplet and the ambient fluid is set as $R_\rho = \rho_1/\rho_2 = 4$, the dynamic viscosity contrast is $R_\mu = \mu_1/\mu_2 = 4$. The dimensionless parameters are the Weber number $We = 2\rho_1 RU^2/\sigma$, (where R is the droplet radius and $D = 2R$ is diameter, U is the relative impact velocity between two droplets and σ is the surface tension. We is fixed as 60 in the following simulations), $Re = \rho_1 DU/\mu_1$ (Re is fixed as 200 in the following simulations) and $B = H/D$ which is a geometrical impact parameter. It is shown that different interface patterns can be observed with varying We and B (Ashgriz and Poo 1990, Qian and Law 1997, Inamuro et al. 2004, Premnath and Abraham 2005). One half of the flow domain is discretized with a mesh size of $111\times51\times91$. Symmetric boundary condition is applied on the z-x plane while periodic boundary condition is used on other boundaries. The two droplets are separated by 6 lattice units in the *x* direction. Cases with B = 0.27, 0.36,

0.82 and 0.91 are simulated. Figure 4.11 shows evolution (time is nondimensionalized by U/D) of droplet shape during collision at B = 0.27. With relative low value of B, large portion of droplet coalesces at the initial stage of collision as shown in Fig. 4.11(b). After the initial coalesce, the un-coalesced portion of two droplets will continuously move along with their initial impact velocity direction. Moreover, due to asymmetry of the droplet movements, the coalescent droplet rotates clockwise as can be observed in Fig. 4.11 (c-f). In this low B value case, the two droplets will not separate after initial coalesce and this regime is termed as "coalescence regime" (Ashgriz and Poo 1990). Besides the coalescence regime, the stretching separation regime was also captured in the current simulation as shown in Fig. 4.12 with B=0.91. Separation regime is always observed with large impact parameter B (Ashgriz and Poo 1990, Qian and Law 1997), in which only small portion of the droplets is in contact during the initial impact as shown in Fig. 4.12(c) and 4.12(d). The same as in the coalescence regime, after initial collision, the coalescent droplet rotates clockwise due to asymmetry of the velocity field. At the latter stages in separation regime, the neck of the coalescent droplet will be continuously stretched as shown in Fig. 4.12(e) and (f) and finally breakup (Fig. 4.12(g) and (h)). In the simulation, it is found that when B equals 0.27 and 0.36, the droplet collision falls into the coalescence regime while the droplet collision falls into the separation regime when B equals 0.82 and 0.91. The droplet movement and the obtained droplet collision regimes are consistent with the experimental (Ashgriz and Poo 1990, Qian and Law 1997) and numerical (Premnath and Abraham 2005) results in the literature.

4.3.5 Drop impact on dry walls

In this subsection, 3D drop impacts on dry walls while considering the dynamic contact angle is simulated by the proposed phase-field LBM. It is known that the surface wettability can be

represented by an equilibrium contact angle θ_{eq}. Nevertheless, when a contact line moves, the dynamic contact angle θ_d can be different from θ_{eq} (Blake 2006). In this subsection, the influence of dynamic contact on droplet impingement is considered. The setup of this problem is sketched in Fig. 4.13. As showed in this figure, a droplet with radius of $R_0 = 35$ lattice units is initialized close to the *x*-*y* plane with impact velocity U_0. The wall boundary condition and the dynamic contact angle are applied on the lower wall. The open boundary conditions are applied on the other boundaries. Owing to the symmetry of this problem, only a quarter of the whole domain is simulated. The simulated computational domain is $140\times140\times105$. The density and viscosity ratios of two fluids are defined as $r_\rho = \rho_L/\rho_G$ and $r_\mu = \mu_L/\mu_G$, respectively. Moreover, the major non-dimensional parameters are: the Weber number $We = \left(\rho_L D_0 U_0^2\right)/\sigma$, the Reynolds number $Re = \left(\rho_L D_0 U_0\right)/\mu_L$, the Ohnesorge number $Oh = \mu_L/\sqrt{\rho_L D_0 \sigma}$, the contact line capillary number $Ca_{cl} = \left(\rho_L \upsilon_L U_{cl}\right)/\sigma$. Additionally, the time is nondimensionalized by U_0/D. In this context, the dynamic contact angle θ_d can be evaluated through an empirical relation employed by Mukherjee and Abraham (2007) as well as Sikalo et al. (2005). It takes the form of

$$\theta_d = f_H\left[Ca_{cl} + f_H^{-1}(\theta_{eq})\right] \tag{4.27}$$

where f_H^{-1} is the inverse of the Hoffman function which is defined as

$$f_H(x) = \arccos\left\{1 - 2\tanh\left[5.16\left(\frac{x}{1+1.31x^{0.99}}\right)^{0.706}\right]\right\} \tag{4.28}$$

To validate the implementation of dynamic contact angle, the computational parameters are set the same as that of Mukherjee and Abraham (2007). They used a MRT version of Lee and

Lin (2005)'s LBM model to simulate the drop impact on a wet surface. Lee and Lin (2005)'s method starts from discrete Boltzmann equation and solve the resultant lattice Boltzmann equation in three steps: pre-streaming collision, streaming and post-streaming collision. In addition, a second-order mixed difference approach was employed by Lee and Lin (2005), which is helpful for high density ratio simulation. In this case, the density and viscosity ratios are set as $r_\rho = 10$ and $r_\mu = 10$. Moreover, the Weber number is set as 30 and Ohnesorge numbers is set as 0.026. The equilibrium contact angle is set as $\theta_{eq} = 87.4^\circ$. Fig. 4.14 compares the evolution of spread factor ($R^* = R_{Drop} / R_0$) with data in the literature. It can be seen that good agreement is achieved. Moreover, droplet deformation at different time stages is also plotted in Fig. 4.15. The current droplet patterns at different time steps also compare well with those in Mukherjee and Abraham (2007). Moreover, the influence of Ohnesorge number on impact process is examined. Fig. 4.16 presents the evolution of spread factor at different Ohnesorge numbers. It can be seen that increase of Ohnesorge number can greatly restrict the drop motion. This is expected since Ohnesorge number expresses the ratio of viscous to surface tension force. Besides, effect of the gravitational force was also studied. Simulations with Bond number, $Bo = \Delta\rho g D^2 / \sigma$ equals 10, 30, 50 were performed. Evolutions of the spread factor were plotted in Fig. 4.17. It can be seen that the drop impact was enhanced by the gravitational force with increasing Bond number. Moreover, the interface patterns during impact with the Bond number 10, and 50 were shown in Fig. 4.18 and Fig. 4.19, respectively. The influence of gravitational force can be observed more directly from these figures.

4.4 Concluding Remarks

In the original Z-S-C model (Zheng et al. 2006), two sets of LBEs are used. One set of LBE is used for interface capturing, which can recover the Cahn-Hilliard equation with the second order of accuracy. The other set of LBE is for simulation of the flow field, where the particle distribution function is directly used for the mean density and momentum. The use of mean density in the Z-S-C model can well capture the pressure field and its numerical computation is very stable and efficient. However, when a multiphase flow with density contrast is considered, it may not give the correct solution since the density contrast is not properly considered in the momentum equation. To overcome the drawback of Z-S-C model, a new set of LBE for simulation of the flow field is presented in this work. In the meantime, the set of LBE in the Z-S-C model for interface capturing is still used in the present work. To correctly consider the effect of density contrast in the momentum equation, we start with a LBE, where the particle distribution function is for the local density and momentum. Then, to improve numerical stability, a transformation which is similar to the one used in the works of He et al. (1999) and Lee and Lin (2005) is introduced to change the particle distribution function for the local density and momentum into that for the mean density and momentum. Through this way, the LBE for flow field in the present model can correctly consider the effect of density contrast in the momentum equation. In the meantime, it enjoys good properties of particle distribution function for the mean density. The proposed model was validated through simulations of viscous coupling in a plane channel, nonlinear Rayleigh-Taylor instability, droplet splash on a wet surface, three-dimensional off-center droplet collisions and drop impact with dynamic contact angle. Numerical results showed that the current model successfully embodies influence of density contrast and correctly simulates both steady and dynamic multiphase flow problems.

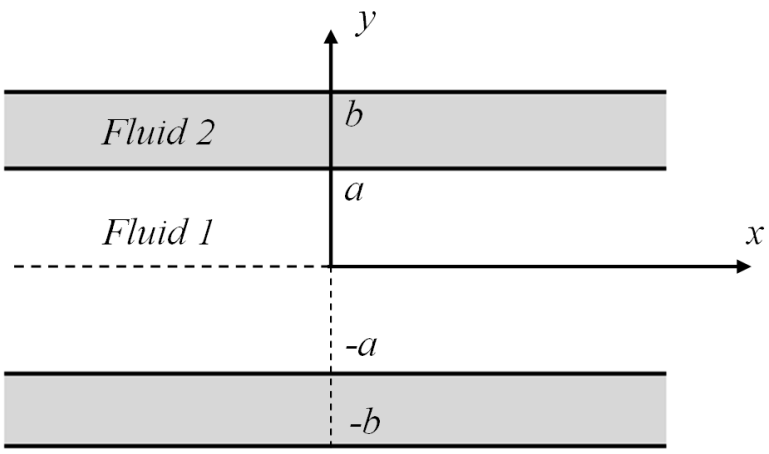

Fig. 4.1 Sketch of viscous coupling in a 2D channel

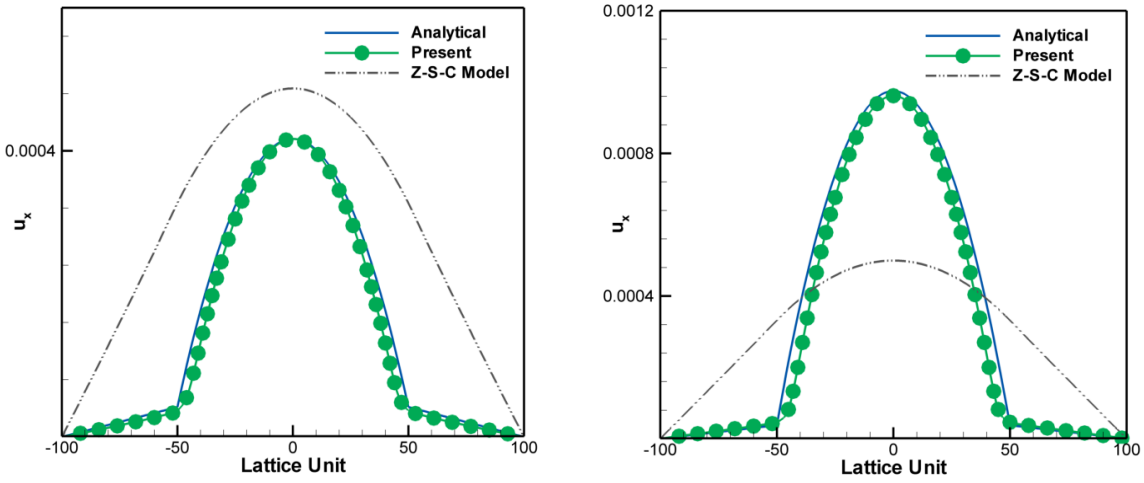

(a) $R_\rho = 1/18$ (b) $R_\rho = 1/50$

Fig. 4.2 Profile of u_x in the middle of a channel

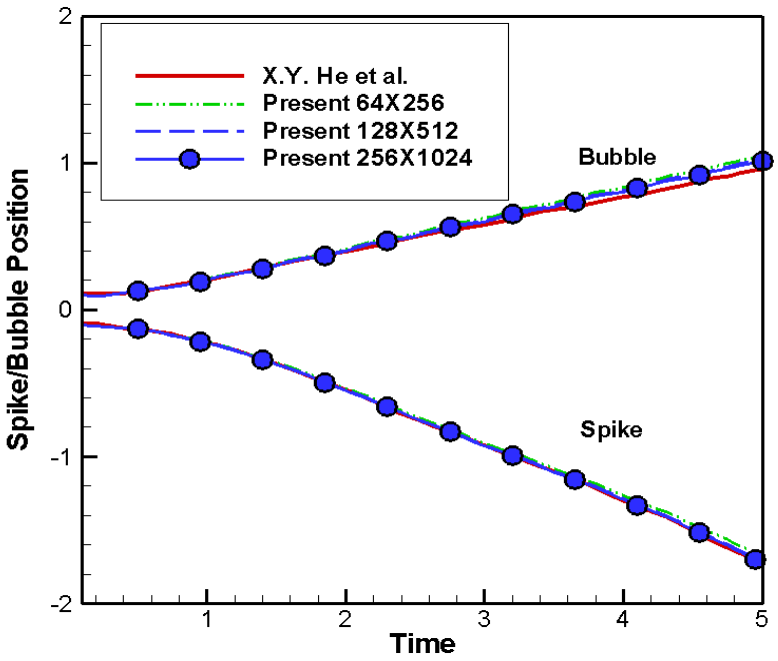

Fig. 4.3 Time evolution of spike and bubble position

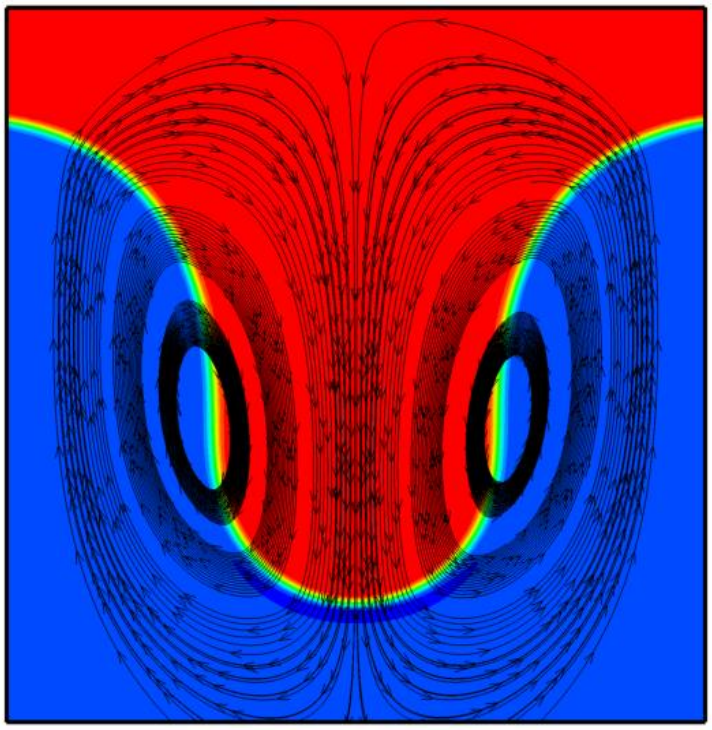

Fig. 4.4 Interface shape with streamline at Time 1.5

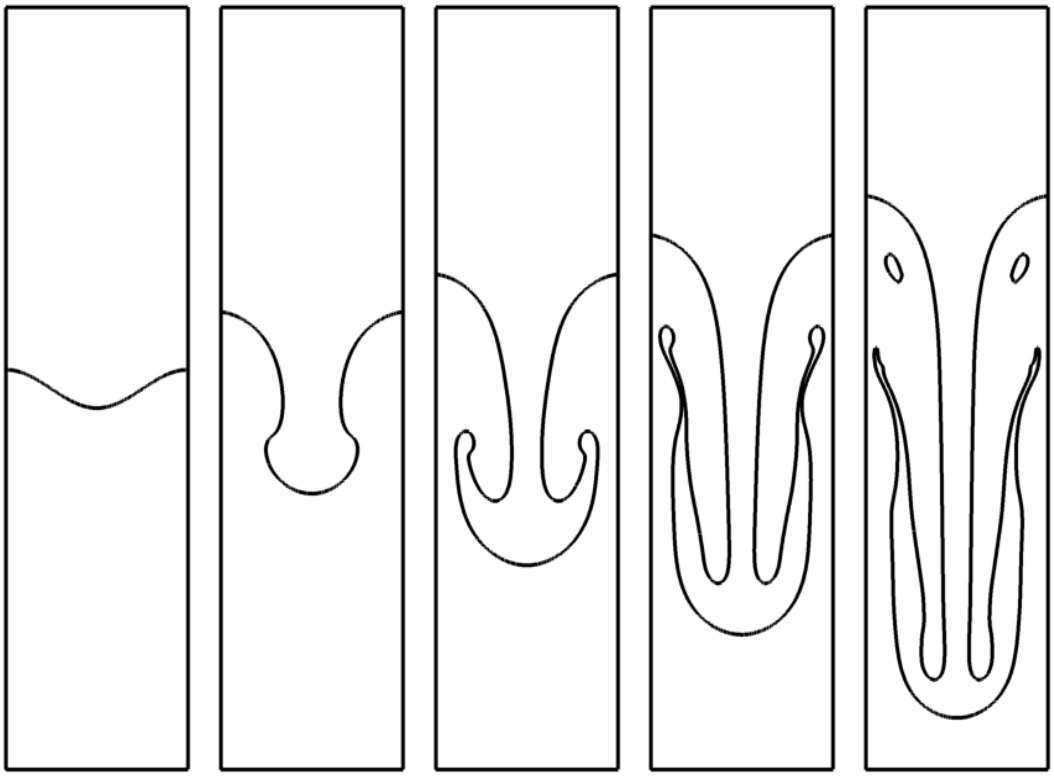

(a) Time = 1.0 (b) Time = 2.0 (c) Time = 3.0 (d) Time = 4.0 (e) Time = 5.0

Fig. 4.5 Fluid interface evolution of Rayleight Taylor instability at Re = 256

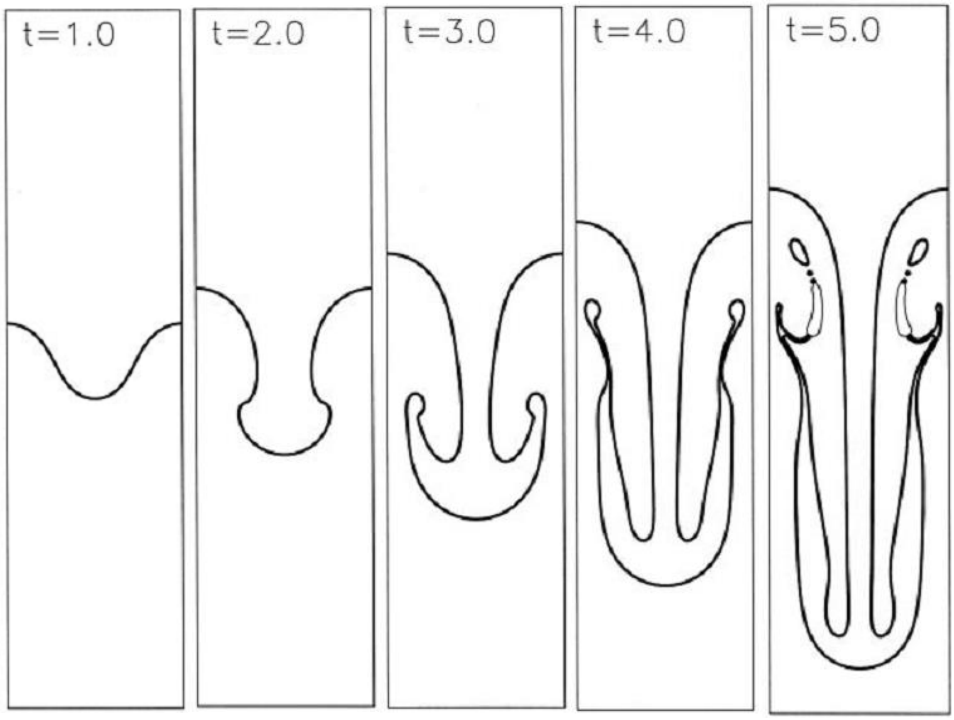

Fig. 4.6 Rayleight Taylor instability at Re = 256 (He et al. 1999)

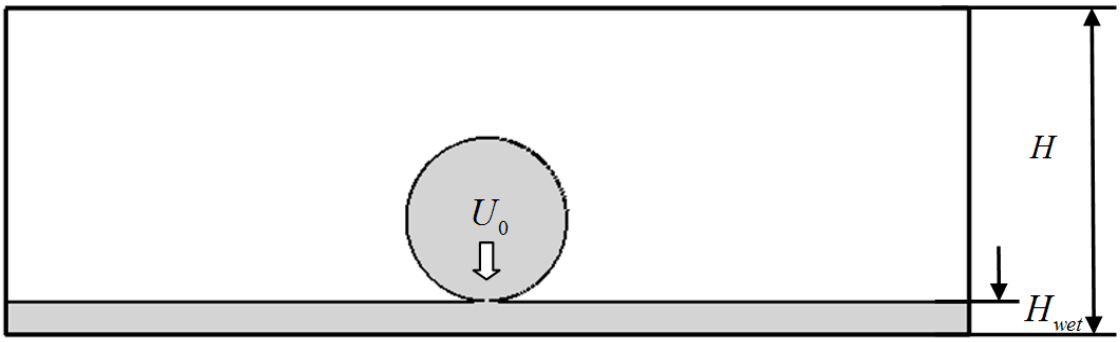

Fig. 4.7 Problem setup of droplet splash on wet surface

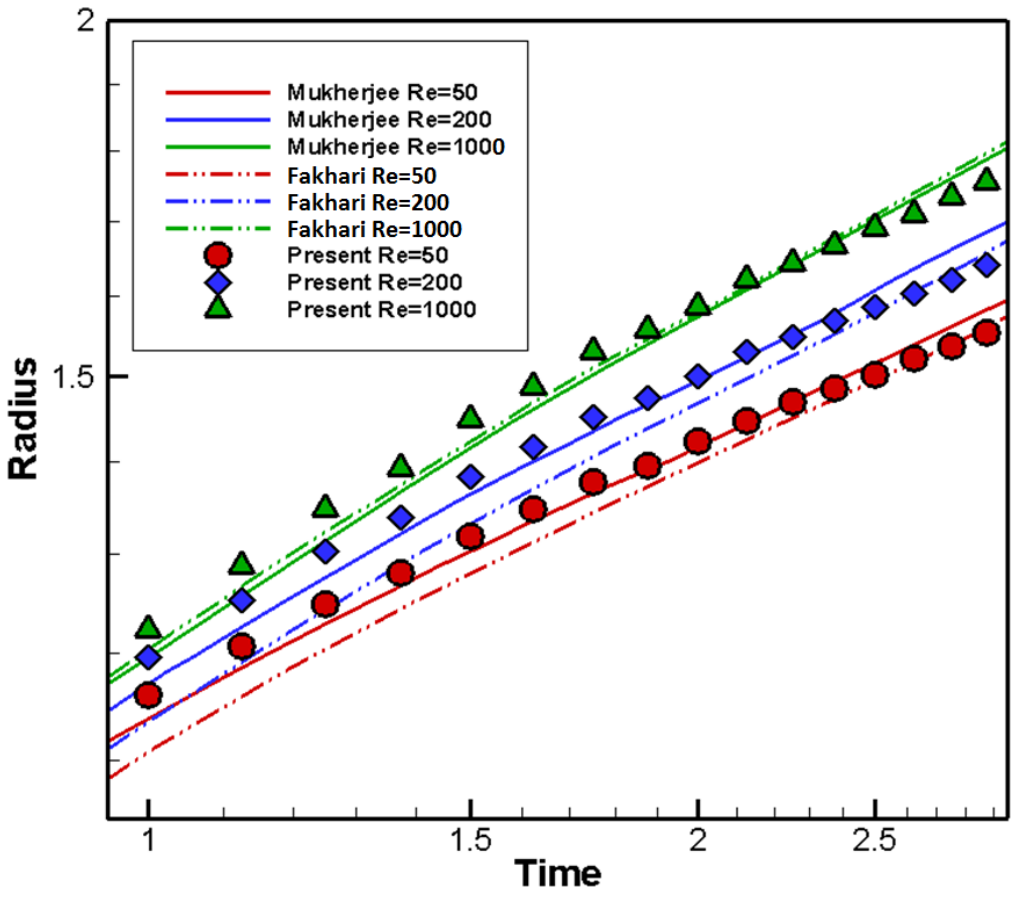

Fig. 4.8 Time evolution of droplet splashing radius

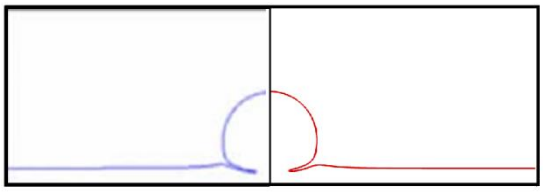

(a) Re=50, Time=0.2

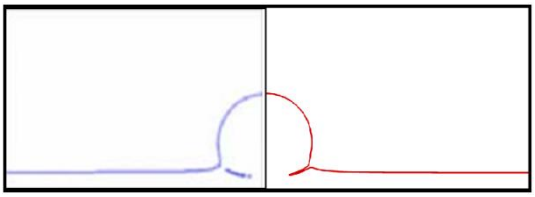

(b) Re=200, Time=0.2

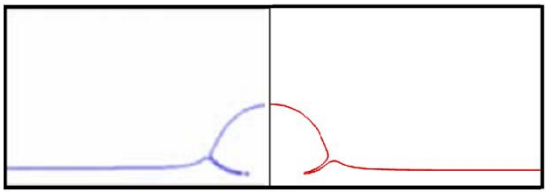

(c) Re=50, Time=0.4

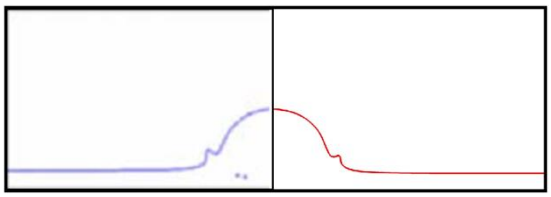

(d) Re=200, Time=0.4

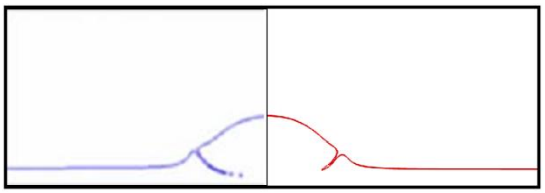

(e) Re=50, Time=0.6

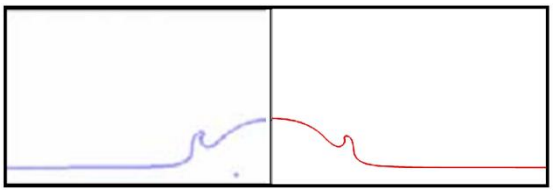

(f) Re=200, Time=0.6

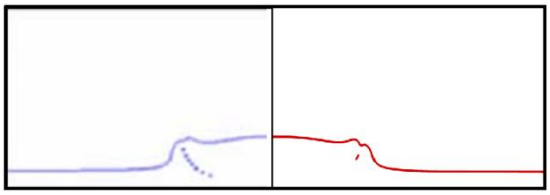

(g) Re=50, Time=1.0

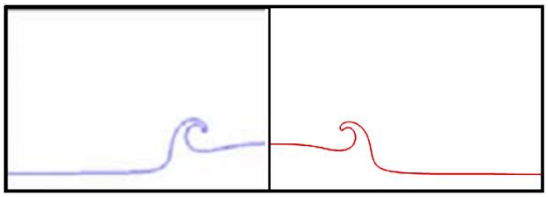

(h) Re=200, Time=1.0

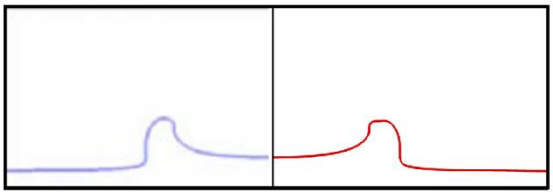

(i) Re=50, Time=2.0

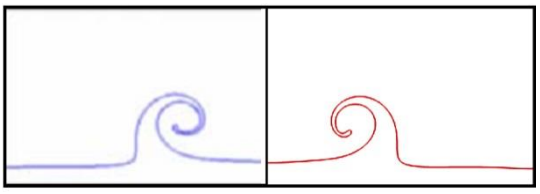

(j) Re=200, Time=2.0

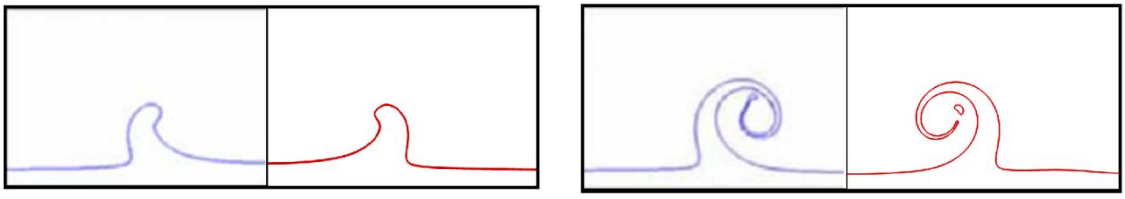

(k) Re=50, Time=3.0 (l) Re=200, Time=3.0

Fig. 4.9 Droplet splashing process at Reynolds numbers of 50 and 200. The left column shows results at Re=50 and the right column shows results at Re=200. In each frame, the present results (right panel) are compared with those of Fakhari and Rahimian (2010) (left panel)

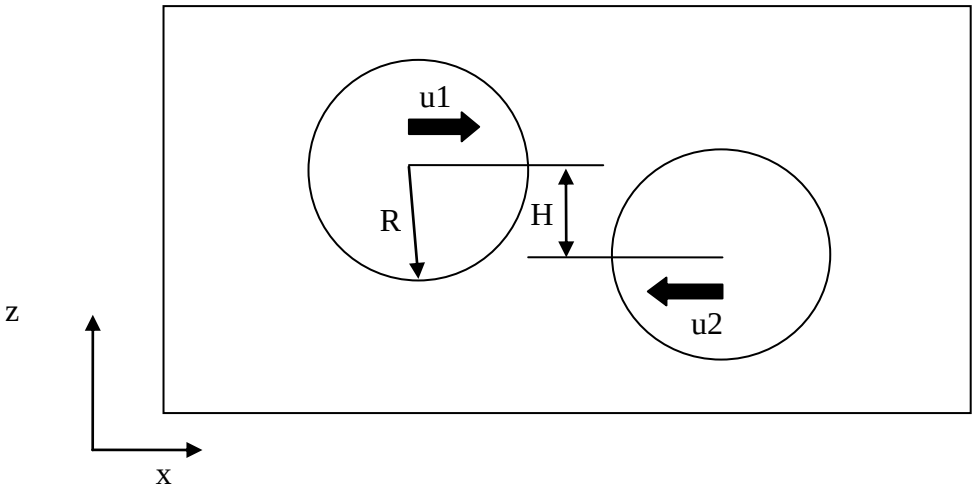

Fig. 4.10 Problem setup of two-droplets collision

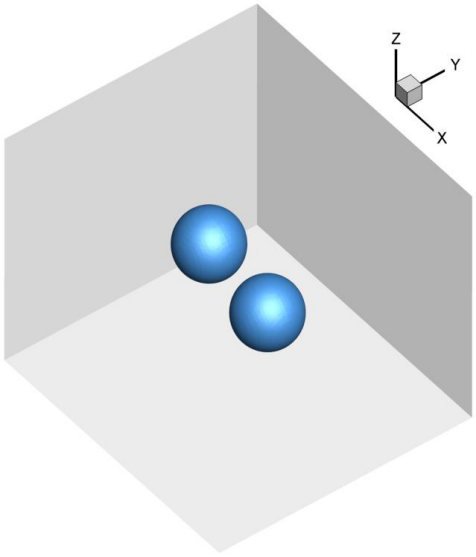

(a) T=0

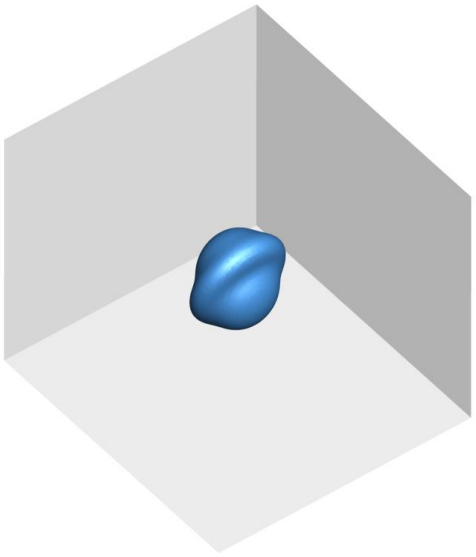

(b) T=1.83

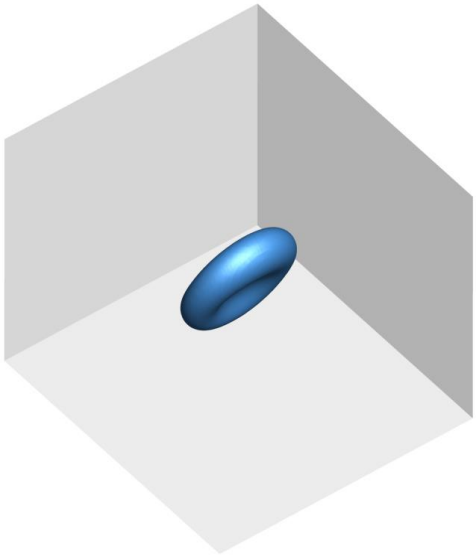

(c) T=3.67

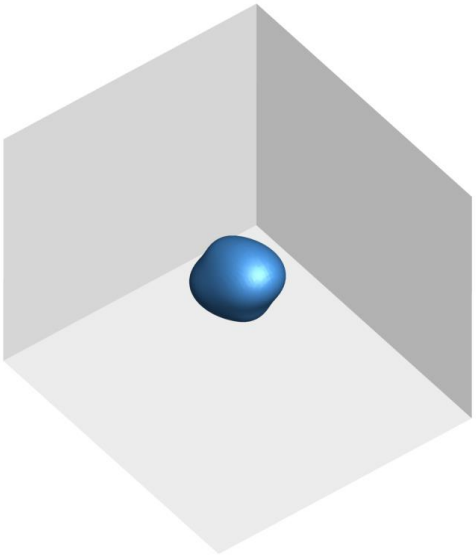

(d) T=6.41

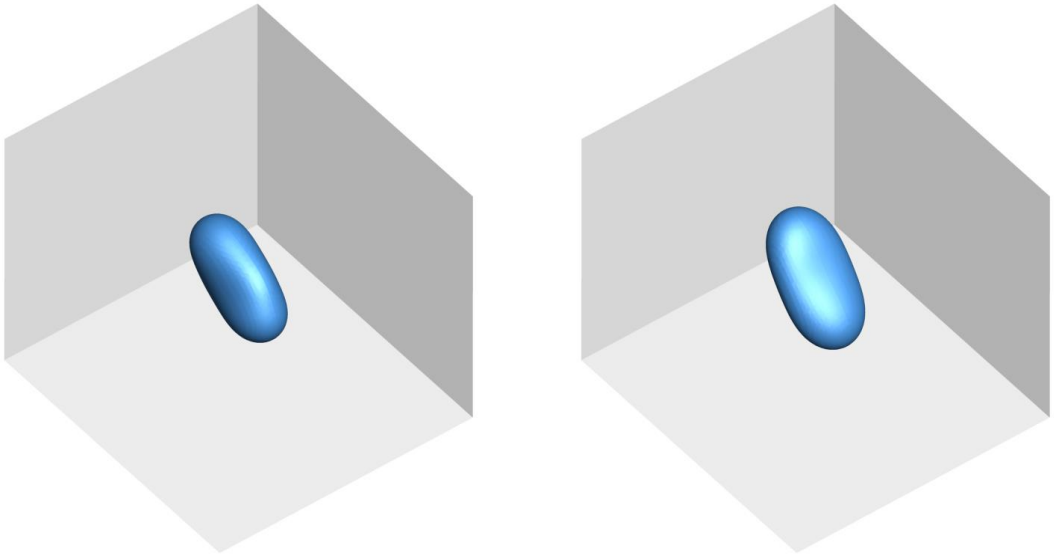

(e) T=8.25 (f) T=11

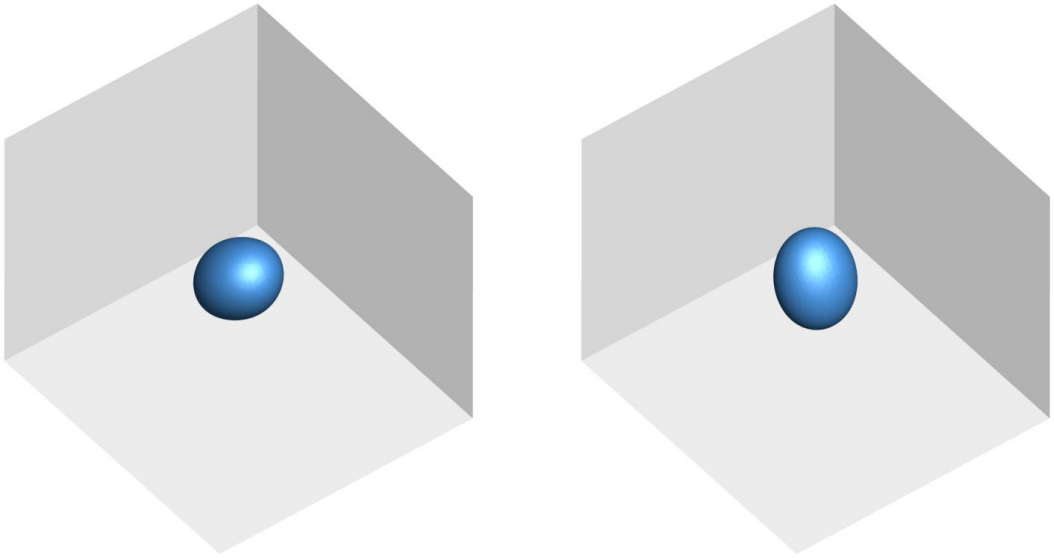

(g) T=14.67 (h) T=22.93

Fig. 4.11 Interface evolution during droplet collision at We = 60, B = 0.27

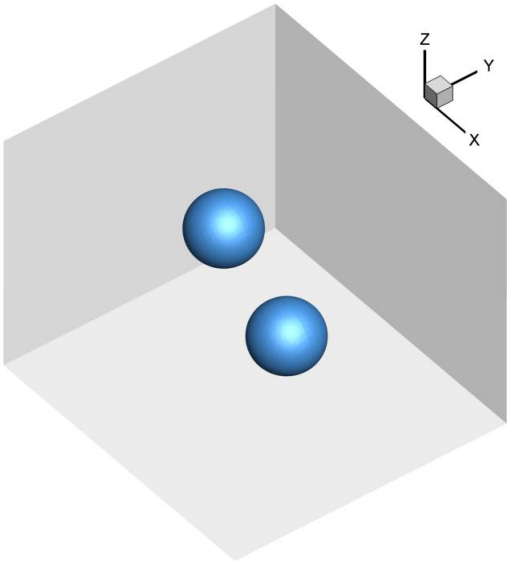

(a) T=0

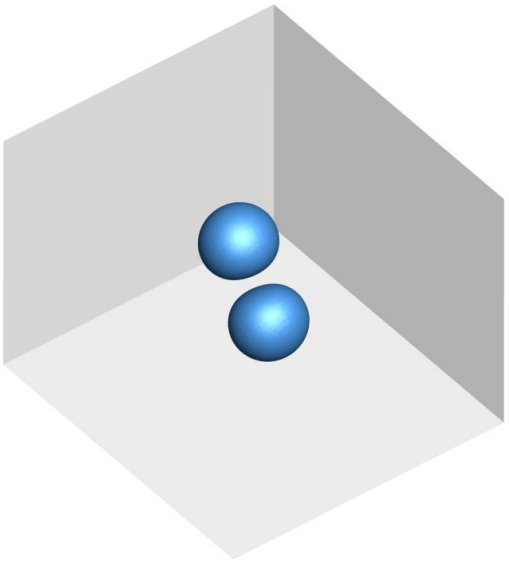

(b) T=1.83

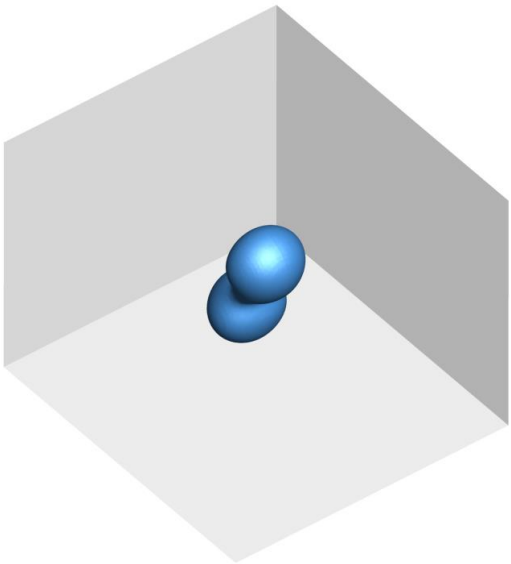

(c) T=2.75

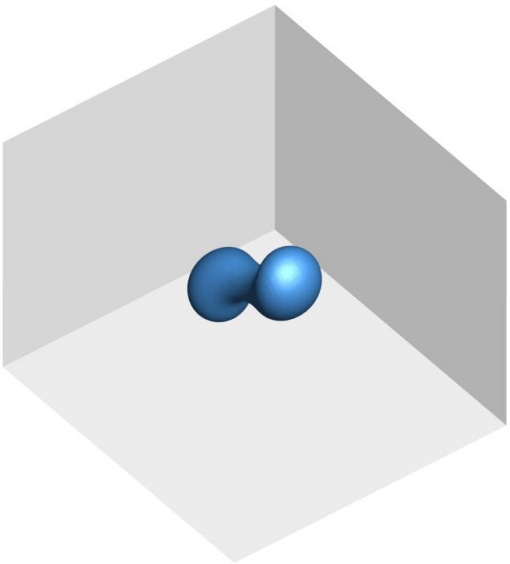

(d) T=4.59

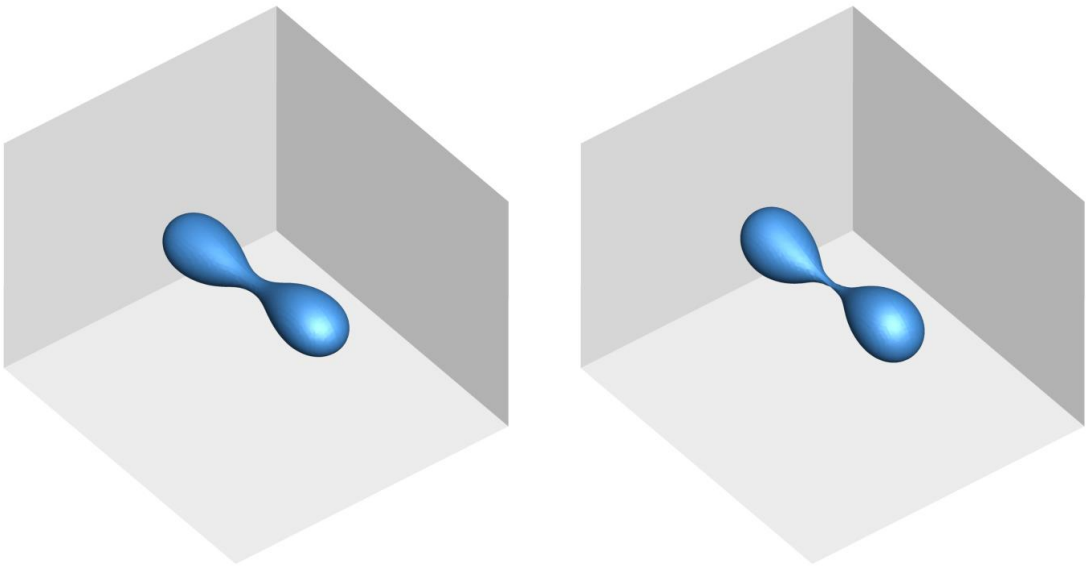

(e) T=9.2 (f) T=10.1

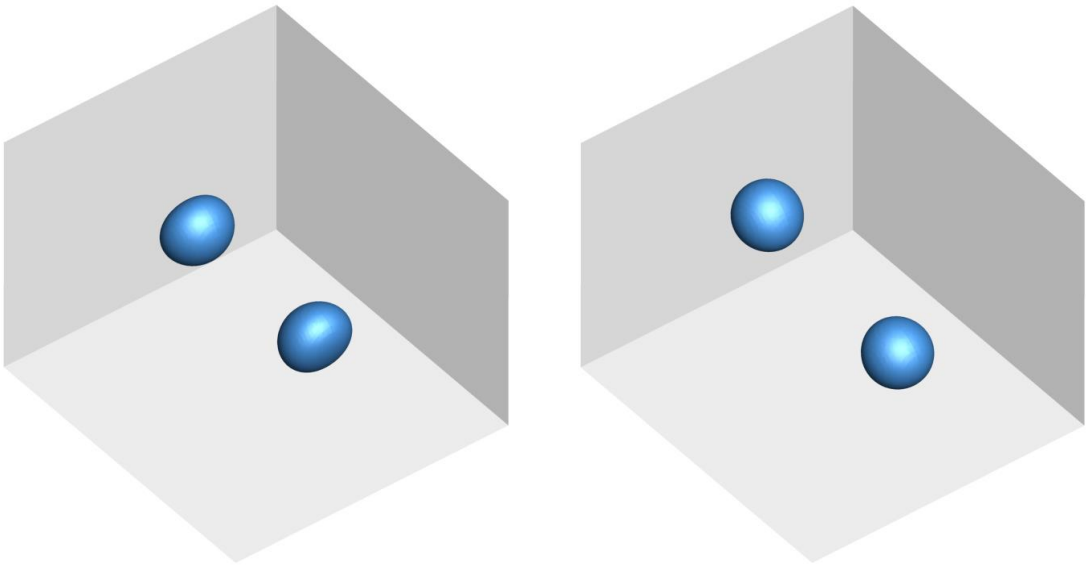

(g) T=13.8 (h) T=18.3

Fig. 4.12 Interface evolution during droplet collision at We = 60, B = 0.91

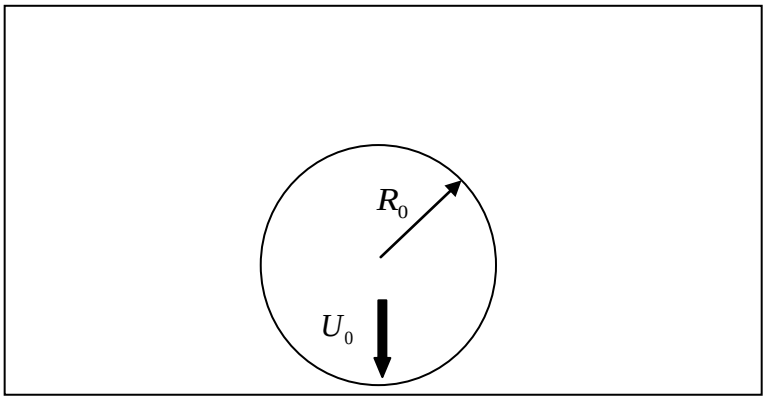

Fig. 4.13 Sketch of drop impact problem

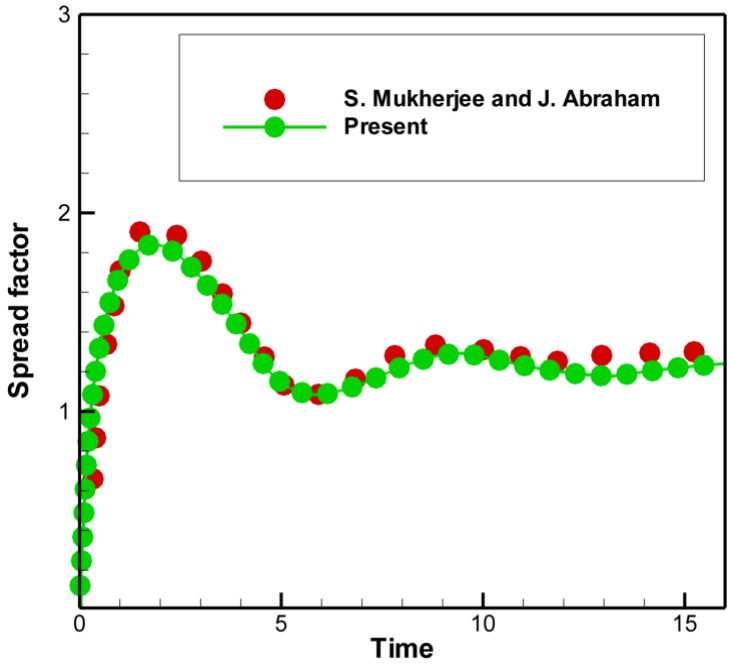

Fig. 4.14 Time evolution of spread factor

(a) T = 0.12 (b) T = 0.54

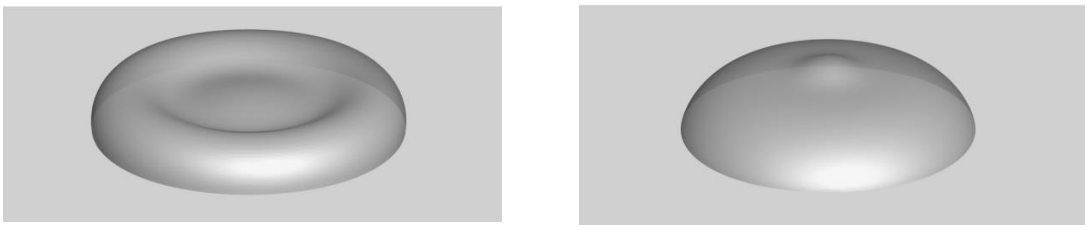

(c) T = 1.38 (d) T = 3.06

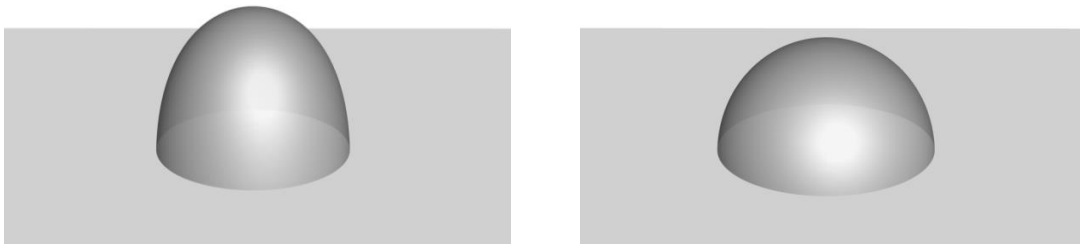

(e) T = 5.58 (f) T = 15.87

Fig. 4.15 Droplet deformation at different time stages

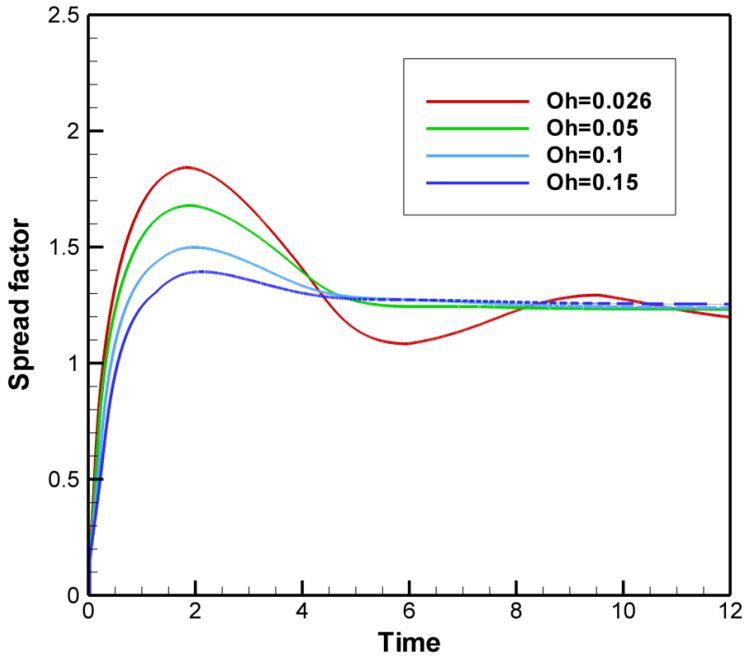

Fig. 4.16 Evolution of spread factor with different Ohnesorge numbers

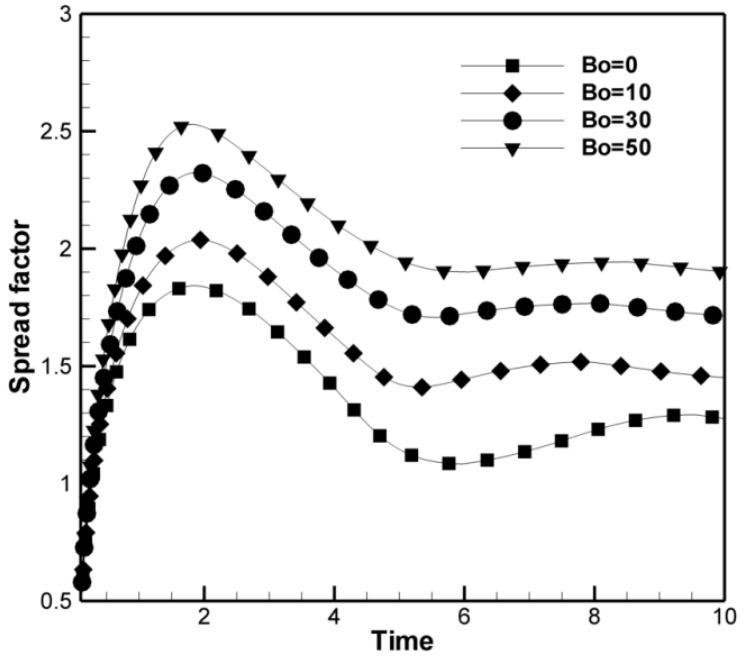

Fig. 4.17 Evolution of spread factor for drop impact on a dry wall

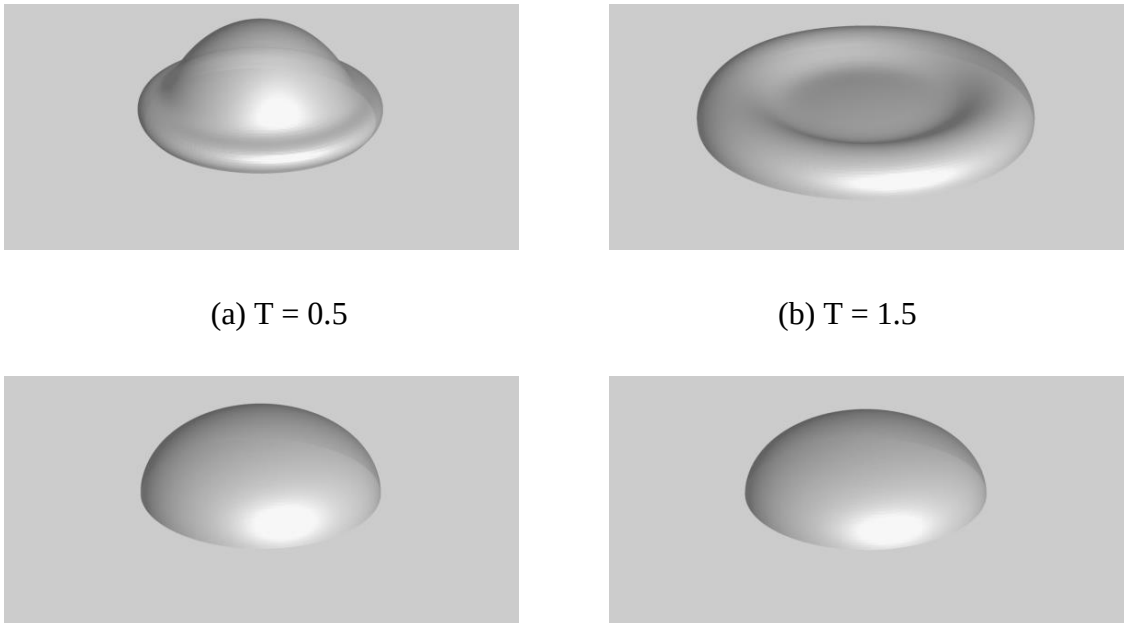

(a) T = 0.5 (b) T = 1.5

(c) T = 5.6 (d) T = 18

Fig. 4.18 Droplet deformation with Bond number 10

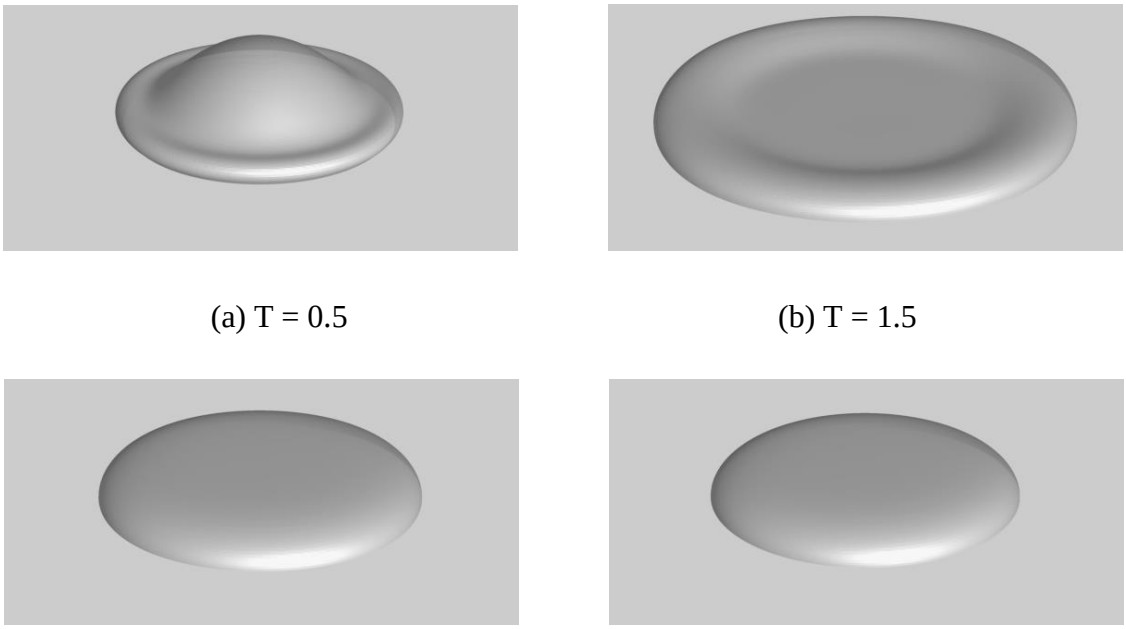

(a) T = 0.5 (b) T = 1.5

(c) T = 5.6 (d) T = 18

Fig. 4.19 Droplet deformation with Bond number 50

Chapter 5[2]

Development of an Immersed Boundary Method to Simulate Solid-Fluid Interactions

In Computational Fluid Dynamics (CFD), solid-fluid (single/multi-phase flows) interactions are prevalent and have received sustained academic and industrial interests. To simulate such a problem, a central issue is to implement boundary conditions, such as Dirichlet and Neumann boundary conditions, on solid bodies. Among various methods to implement boundary conditions as introduced in Chapter 1, Immersed Boundary Method (IBM) is famous for its efficiency and robustness. Since being developed by Peskin (1972, 1977), extensive works have been undertaken to improve IBM for Dirichlet boundary conditions (Mittal and Iaccarino 2005, Wu 2010). In particular, the boundary condition-enforced IBM (Wu and Shu 2009) adopts an implicit velocity correction approach and ensures satisfaction of Dirichlet boundary condition. Besides refinement of the algorithm, the application of IBM has also been extended to a very broad range (Mittal and Iaccarino 2005, Wu 2010). Nevertheless, they are mainly restricted to problems such as solid-single phase flow interactions, which only involve Dirichlet boundary conditions. The difficulty is attributed to the fact that implementation of Neumann boundary condition is not as straightforward as that of Dirichlet boundary condition. This disadvantage greatly limits the application of IBM because many problems may also involve Neumann boundary condition such as solid-

[2] The material in this Chapter has been partially published in
J. Y. Shao, C. Shu and Y. T. Chew (2013), "Development of an immersed boundary-phase field-lattice Boltzmann method for Neumann boundary condition to study contact line dynamics," Journal of Computational Physics **243**:8-32.

multiphase flow interactions. In this Chapter, we will initiate the first endeavour to implement Neumann boundary conditions in IBM. Additionally, within this work, both Dirichlet and Neumann boundary conditions will be implemented consistently through IBM for various solid-fluid interaction problems.

This Chapter is organized as follows: Section 5.1 brifely introduces the immersed boundary method in the first place. Section 5.2 introduces IBM for Dirichlet boundary condition in the lattice Boltzmann framework, considering the interest of present work. It is then followed by Section 5.3 to elaborate the idea to implement Neumann boundary conditions in IBM. Thereafter, numerical examples of solid-fluid problems involving Dirichlet and/or Neumann boundary conditions simulated by IBM will be demonstrated in Section 5.4. Finally, conclusions will be drawn in Section 5.5.

5.1 Immersed Boundary Method

Since being introduced by Peskin (1972, 1977), the immersed boundary method has become increasingly popular for implementing Dirichlet boundary condition to simulate solid-fluid interactions. The popularity and high efficiency of IBM is attributed to decoupling of solution of the governing equations for the flow field with implementation of the boundary conditions. The governing equations can be solved on a fixed Eulerian grid regardless of the solid geometry. Concurrently, the influence of a solid boundary is represented by a forcing term, which is first evaluated on the solid boundary and then distributed back to Eulerian grid through discrete Delta functions. A major issue in IBM, also the focus in previous IBM development, is to accurately evaluate the forcing term (Wu 2010). The original work by

Peskin (1972, 1977) is also known as the penalty method. In the penalty method, restoring force is calculated through Hooke's Law. It introduces an arbitrary spring parameter that influences force calculation. To avoid using arbitrary coefficients, direct forcing method, in which the momentum equation is used to evaluate the forcing term, is developed and widely applied (Mohd-Yusof 1997, Fadlun et al. 2000). The direct forcing method is improved with regard to forcing oscillation by Uhlmann (2005) and also combined with a nonlinear weighted approach by Luo et al. (2007). Nevertheless, in these IBMs, the forcing term is evaluated explicitly and the no-slip boundary condition is only approximately satisfied. To enforce the no-slip boundary condition, a boundary condition-enforced IBM has been proposed by Wu and Shu (2009) recently. In this method, the forcing term is calculated in an implicit manner, and it is determined in the way that the velocity at the boundary point satisfies the no-slip boundary condition. Their results show that the no-slip boundary condition is well satisfied and the streamline penetration observed in the previous works is effectively eliminated. The method has also been applied to investigate various solid-fluid interactions (Wu 2010). This method will be introduced in detail later and used in the present work for Dirichlet boundary condition.

As introduced previously, a large body of work has been done to improve treatment of Dirichlet boundary condition (Mittal and Iaccarino 2005, Wu 2010). On the hand, to the best of our knowledge, there are few works of IBM for Neumann boundary condition available in the literature since IBM was proposed in the 1970s. Absence of such an approach greatly limits the application of IBM because it is known that Neumann boundary condition is commonly encountered in solid-fluid interactions. Motivated by the numerous potential applications, we will initiate the first endeavour to implement the Neumann boundary

condition in IBM in this work, based mainly on physical interpretation. Concretely speaking, rooted in physical conservation law, the Neumann boundary condition is considered as contribution of the flux from the boundary to its relevant physical parameter in a control volume. Additionally, the link between the flux and its corresponding flow field variable is directly manipulated through the immersed boundary concept. In this way, the Neumann boundary condition can be implemented in IBM. In the following context, the IBM for Dirichlet boundary condition will be introduced first. Thereafter, Section 5.3 will be devoted to implement the Neumann boundary condition in IBM.

5.2 Immersed Boundary Method for Dirichlet Boundary Condition

To enforce the Dirichlet boundary condition, a recently developed boundary condition-enforced IB-LBM (Wu and Shu 2009) is adopted in this work. In this method, the velocity correction term is determined in a way that guarantees that the no-slip boundary condition is enforced. Recalling the lattice Boltzmann equations (LBEs) for the flow field in Chapter 2, they are rearranged as

$$f_\alpha\left(\boldsymbol{x}+\boldsymbol{e}_\alpha\delta t,t+\delta t\right)-f_\alpha\left(\boldsymbol{x},t\right)=-\frac{1}{\tau}\left[f_\alpha^{eq}\left(\boldsymbol{x},t\right)-f_\alpha\left(\boldsymbol{x},t\right)\right]+\boldsymbol{F}_\alpha\delta t \tag{5.1}$$

$$\boldsymbol{F}_\alpha=\frac{w_\alpha}{c_s^2}\left(1-\frac{1}{2\tau}\right)\left[\left(\boldsymbol{e}_\alpha-\boldsymbol{u}\right)+\frac{\left(\boldsymbol{e}_\alpha\cdot\boldsymbol{u}\right)}{c_s^2}\right]\cdot\left(\mu_\phi\nabla\phi+\boldsymbol{F}_b\right) \tag{5.2}$$

$$\rho\boldsymbol{u}=\sum_\alpha\boldsymbol{e}_\alpha f_\alpha+\frac{1}{2}\left(\mu_\phi\nabla\phi+\boldsymbol{F}_b\right)\delta t \tag{5.3}$$

As can be seen from Eq. (5.3), the velocity consists of three parts. One arises from the density distribution function. The other two are attributed to the force density $\boldsymbol{F}=\left(\mu_\phi\nabla\phi+\boldsymbol{F}_b\right)$.

There are two types of forces contributing to $\boldsymbol{F}$, namely, the interfacial force $\mu_\phi \nabla \phi$ (Jacqmin 1999) and the forcing term $\boldsymbol{F}_b$ that represents the effect of immersed boundary (without considering any other body force). Hence we can define the three velocity components as below

$$\boldsymbol{u}_\rho = \frac{1}{\rho} \sum_\alpha \boldsymbol{e}_\alpha f_\alpha \tag{5.4}$$

$$\boldsymbol{u}_\phi = \frac{1}{2\rho} \mu_\phi \nabla \phi \delta t \tag{5.5}$$

$$\delta \boldsymbol{u} = \frac{1}{2\rho} \boldsymbol{F}_b \delta t \tag{5.6}$$

With this definition, the overall velocity is

$$\boldsymbol{u} = \boldsymbol{u}_\rho + \boldsymbol{u}_\phi + \delta \boldsymbol{u} \tag{5.7}$$

where $\boldsymbol{u}$ is the overall velocity, $\boldsymbol{u}_\rho$ is from the density distribution function without considering the presence of the solid boundary, $\boldsymbol{u}_\phi$ is caused by the interfacial force and $\delta \boldsymbol{u}$ is the velocity correction term caused only by the no-slip boundary condition. Based on this analysis, an intermediate velocity $\boldsymbol{u}^*$ is defined as

$$\boldsymbol{u}^* = \boldsymbol{u}_\rho + \boldsymbol{u}_\phi \tag{5.8}$$

Therefore, the overall velocity can be rearranged as

$$\boldsymbol{u} = \boldsymbol{u}^* + \delta \boldsymbol{u} \tag{5.9}$$

In the boundary condition-enforced IB-LBM, the velocity correction term $\delta \boldsymbol{u}$ is set as an unknown and evaluated implicitly. To solve $\delta \boldsymbol{u}$ on Eulerian points, $\delta \boldsymbol{u}_B^l$ is first defined to represent the velocity correction on Lagrangian points. In this context, $\delta \boldsymbol{u}$ can be obtained by Dirac delta function

$$\delta \boldsymbol{u}(\boldsymbol{x},t) = \int_{\Gamma} \delta \boldsymbol{u}_B^l \left(\boldsymbol{X}_B^l, t \right) \delta \left(\boldsymbol{x} - \boldsymbol{X}_B^l \right) ds \tag{5.10}$$

where Γ is a closed curve defined by the boundary and $\delta\left(\boldsymbol{x} - \boldsymbol{X}_B^l \right)$ is smoothly approximated by continuous kernel distribution (Feng and Michaelides 2005)

$$D\left(\boldsymbol{x}_E - \boldsymbol{X}_B^l \right) = \frac{1}{h^2} \delta\left(x_E - x_B^l \right) \delta\left(y_E - y_B^l \right) \tag{5.11a}$$

for 2D cases. For 3D cases, it takes form of

$$D\left(\boldsymbol{x}_E - \boldsymbol{X}_B^l \right) = \frac{1}{h^3} \delta\left(x_E - x_B^l \right) \delta\left(y_E - y_B^l \right) \delta\left(z_E - z_B^l \right) \tag{5.11b}$$

Moreover,

$$\delta(r) = \begin{cases} (1/4)\left[1 + \cos\left(\pi |r| / 2 \right) \right], & |r| \le 2 \\ 0, & |r| > 2 \end{cases} \tag{5.12}$$

where r is the distance between a Eulerian point and a Lagrangian point. Using the continuous delta function, Eq. (5.10) could be written as

$$\delta u(x_E, t) = \sum_{l=1 \ldots m} \delta u_B^l \left(X_B^l, t \right) D\left(x_E - X_B^l \right) \Delta s \tag{5.13}$$

In the above equation, Δs is the arc length between two neighbouring boundary points (or surface area for 3D cases). Recalling Eq. (5.9), the corrected velocity in Eulerian domain can also be written as

$$\boldsymbol{u}\left(x_E,t\right)=\boldsymbol{u}^*\left(x_E,t\right)+\delta\boldsymbol{u}\left(x_E,t\right) \tag{5.14}$$

To satisfy the no-slip boundary condition, the interpolated fluid velocity on a boundary point must equal to the wall velocity $\boldsymbol{U}_B^l\left(\boldsymbol{X}_B^l,t\right)$ at the same place. The mathematical description is

$$\boldsymbol{U}_B^l\left(\boldsymbol{X}_B^l,t\right)=\sum\boldsymbol{u}^*\left(\boldsymbol{x}_E,t\right)D_{xy}\Delta x\Delta y+\sum\sum\delta\boldsymbol{u}_B^l(\boldsymbol{X}_B^l,t)D_{xy}\Delta s_l D_{xy}\Delta x\Delta y \tag{5.15a}$$

for 2D cases. For 3D cases, it takes form of

$$\boldsymbol{U}_B^l\left(\boldsymbol{X}_B^l,t\right)=\sum\boldsymbol{u}^*\left(\boldsymbol{x}_E,t\right)D_{xyz}\Delta x\Delta y\Delta z+\sum\sum\delta\boldsymbol{u}_B^l(\boldsymbol{X}_B^l,t)D_{xyz}\Delta s_l D_{xyz}\Delta x\Delta y\Delta z \tag{5.15b}$$

or in a matrix form

$$\boldsymbol{A}\boldsymbol{X}=\boldsymbol{B} \tag{5.16}$$

with $\boldsymbol{A}$, $\boldsymbol{B}$ and $\boldsymbol{X}$ expressed as

$$\boldsymbol{A}=\begin{pmatrix}\delta_{11}&\delta_{12}&\cdots&\delta_{1n}\\\delta_{21}&\delta_{22}&\cdots&\delta_{2n}\\\vdots&\vdots&\ddots&\vdots\\\delta_{m1}&\delta_{m2}&\cdots&\delta_{mn}\end{pmatrix}\begin{pmatrix}\delta_{11}^B&\delta_{12}^B&\cdots&\delta_{1m}^B\\\delta_{21}^B&\delta_{22}^B&\cdots&\delta_{2m}^B\\\vdots&\vdots&\ddots&\vdots\\\delta_{n1}^B&\delta_{n2}^B&\cdots&\delta_{nm}^B\end{pmatrix} \tag{5.17}$$

$$\boldsymbol{B}=\begin{pmatrix}\boldsymbol{U}_B^1\\\boldsymbol{U}_B^2\\\vdots\\\boldsymbol{U}_B^m\end{pmatrix}-\begin{pmatrix}\delta_{11}&\delta_{12}&\cdots&\delta_{1n}\\\delta_{21}&\delta_{22}&\cdots&\delta_{2n}\\\vdots&\vdots&\ddots&\vdots\\\delta_{m1}&\delta_{m2}&\cdots&\delta_{mn}\end{pmatrix}\begin{pmatrix}\boldsymbol{u}_1^*\\\boldsymbol{u}_2^*\\\vdots\\\boldsymbol{u}_n^*\end{pmatrix} \tag{5.18}$$

$$\boldsymbol{X} = \left\{ \delta \boldsymbol{u}_B^1, \quad \delta \boldsymbol{u}_B^2, \quad \cdots \quad \delta \boldsymbol{u}_B^m \right\}^T \tag{5.19}$$

where subscript m is the number of Lagrangian points; and n is the number of adjacent Eulerian points around the boundary. With $\delta \boldsymbol{u}_B^l$ determined in this system, it is then distributed back to Eulerian points and the resulting force density can be evaluated through

$$\boldsymbol{F}_b = 2\rho \delta \boldsymbol{u} / \delta t \tag{5.20}$$

With the velocity corrected in this manner, the no-slip boundary condition can be enforced and streamline penetration to the boundary, which is commonly observed in the conventional IBM, could be eliminated. This method has been applied for simulation of 2D/3D stationary as well as moving boundary problems (Wu and Shu 2009, 2010a, 2010c). Several solid-single phase fluid interactions will also be demonstrated in this Chapter for the purpose of code validation.

5.3 Immersed Boundary Method for Neumann Boundary Condition

The Dirichlet boundary condition is implemented in the previous section. However, in many solid-fluid interactions, both Dirichlet and Neumann boundary conditions are present. As introduced formerly, although numerous works have been devoted to refine the implementation of Dirichlet boundary condition in IBM, few IBM applications with Neumann boundary condition are available at present to the best of our knowledge. In this work, the Neumann boundary condition is implemented based on physical conservation laws for the first time. For clear explanation, we will first consider a linear diffusion equation with a Neumann boundary condition to illustrate the concept, which can be applied to implement Neumann boundary conditions in different physical problems. Then, more concrete examples

for application of this approach to simulate solid-multiphase flow interactions will also be demonstrated.

5.3.1 Flux contribution at the control surface to dependent variable in a control volume

To elaborate the implementation process, we consider the following diffusion equation

$$\frac{\partial \phi}{\partial t} = \alpha \nabla^2 \phi \tag{5.21}$$

with Neumann boundary condition ($\partial\phi/\partial \boldsymbol{n}$ specified). In Eq. (5.21), α is a constant, ∇^2 is the Laplacian operator. If we define a flux vector $\boldsymbol{q}$ as

$$\boldsymbol{q} = \left(q_x, \quad q_y, \quad q_z\right) = -\alpha \nabla \phi \tag{5.22}$$

then, Eq. (5.21) can be rearranged as

$$\frac{\partial \phi}{\partial t} = -\nabla \cdot \boldsymbol{q} \tag{5.23}$$

As shown in Fig. 5.1, Eq. (5.23) can be obtained by applying the physical conservation law to a control volume. There are six control surfaces for the control volume. The flux at control surface of $x = 0$ is $q_x dydz$, which is into the control volume, while the flux at control surface of $x = dx$ is $\left(q_x + dx\,\partial q_x/\partial x\right) dydz$, which is out of the control volume. The net flux into the control volume by these two surfaces is $-\left(dxdydz\right)\partial q_x/\partial x$. Overall, the net flux into the control volume by the six control surfaces is $-\left(\nabla \cdot \boldsymbol{q}\right) dxdydz$. From physical conservation law, this net flux must be equal to the rate of change of ϕ within the control volume $\left(\partial\phi/\partial t\right) dxdydz$, that is $\left(\partial\phi/\partial t\right) dxdydz = -\left(\nabla \cdot \boldsymbol{q}\right) dxdydz$. As a result, Eq. (5.23) is obtained.

From the above process, for a general control surface, which has an outward normal direction $\boldsymbol{n}=\left(n_x,\quad n_y,\quad n_z\right)$, its flux contribution to the control volume is

$$-\left(q_x n_x+q_y n_y+q_z n_z\right)dS=-q_n dS \tag{5.24}$$

where dS is the area of the control surface, and $q_n=-\alpha\,\partial\phi/\partial\boldsymbol{n}$. This means that the flux $q_n dS$ directly contributes to $\partial\phi/\partial t$ when the single control surface is considered. We will use this feature to correct for ϕ when presenting the Neumann boundary condition.

5.3.2 Implementation of Neumann boundary condition in the context of IBM

To clearly illustrate the idea, implementation of Neumann boundary condition in 2D through IBM will be presented in this subsection. The extension to 3D case is straightforward. In the context of IBM, the solution of Eq. (5.21) can be obtained by the following steps. In the first step, we solve Eq. (5.21) in the whole domain including interior and exterior of the immersed object. For simplicity, we note its solution as ϕ^*. That is, ϕ^* satisfies

$$\frac{\partial\phi^*}{\partial t}=\alpha\nabla^2\phi^* \tag{5.25}$$

and with ϕ^*, we can calculate its normal derivative at the boundary point by the following way. Using interpolation, the first order derivatives at the boundary point can be calculated by

$$\frac{\partial\phi^*}{\partial x}\left(\boldsymbol{X}_B^i,t\right)=\sum_j\frac{\partial\phi^*}{\partial x}\left(\boldsymbol{x}_j,t\right)D\left(\boldsymbol{x}_j-\boldsymbol{X}_B^i\right)h^2 \tag{5.26}$$

$$\frac{\partial \phi^*}{\partial y}\left(\boldsymbol{X}_B^i, t\right) = \sum_j \frac{\partial \phi^*}{\partial y}\left(\boldsymbol{x}_j, t\right) D\left(\boldsymbol{x}_j - \boldsymbol{X}_B^i\right) h^2 \tag{5.27}$$

where $\frac{\partial \phi^*}{\partial x}\left(\boldsymbol{X}_B^i, t\right)$ and $\frac{\partial \phi^*}{\partial y}\left(\boldsymbol{X}_B^i, t\right)$ represent the first order derivatives of ϕ^* with respect to x and y at the boundary point $\boldsymbol{X}_B^i$, while $\frac{\partial \phi^*}{\partial x}\left(\boldsymbol{x}_j, t\right)$ and $\frac{\partial \phi^*}{\partial y}\left(\boldsymbol{x}_j, t\right)$ are the first order derivatives of ϕ^* with respect to x and y at Eulerian point $\boldsymbol{x}_j$. Note that the derivatives at Eulerian points are obtained by the second order central difference schemes. Finally, the normal derivative at the boundary point is calculated by

$$\frac{\partial \phi^*}{\partial n}\left(X_B^i, t\right) = \frac{\partial \phi^*}{\partial x}\left(X_B^i, t\right) n_{xi} + \frac{\partial \phi^*}{\partial y}\left(X_B^i, t\right) n_{yi} \tag{5.28}$$

For the general case, the computed $\partial \phi^* / \partial \boldsymbol{n}$ is not equal to the given $\partial \phi / \partial \boldsymbol{n}$ at boundary points. As discussed in Section 5.3.1, their difference will contribute as a surface flux to correct ϕ value at the surrounding Eulerian points. In the context of IBM, the whole domain including interior and exterior of the immersed object is used as the computational domain. Thus, at a boundary point, there are two normal directions. One is to point to the flow domain while the other is to direct into the inside of the immersed object. The surface fluxes from two directions will affect the ϕ field at the surrounding Eulerian points. As shown in Fig. 5.2, due to the feature of Dirac delta function interpolation, the surface flux on a small area dS will only affect its surrounding Eulerian points in the box of $\left|\boldsymbol{x} - \boldsymbol{X}_B\right| \le 2h$. In fact, for any Eulerian point in the box, its control volume must enclose the small surface area dS. For this case, the surface fluxes from two opposite directions of dS will both contribute positively to ϕ in the control volume. Thus, due to non-satisfying of Neumann boundary condition (offset of normal derivative), the surface flux from dS can be written as

$$\delta q_n\left(\boldsymbol{X}_B^i,t\right)=-2\alpha\left(\left.\frac{\partial\phi}{\partial n}\right|_{Specified}-\frac{\partial\phi^*}{\partial n}\right) \tag{5.29}$$

The flux δq_n in Eq. (5.29) will be used to correct for ϕ at Eulerian points in the box. Suppose that the correction is noted as $\delta\phi$. Following the concept of IBM for distributing the surface force (flux) at a boundary segment to its surrounding Eulerian points by the delta function (the effect of the boundary to the surrounding Eulerian points is decreased as the distance of a Eulerian point from the boundary is increased) (Peskin 1972, Mittal and Iaccarino 2005), we can have

$$\frac{\delta\phi\left(\boldsymbol{x}_j,t\right)}{\delta t}=\sum_i\delta q_n\left(\boldsymbol{X}_B^i,t\right)D_{ij}\left(\boldsymbol{x}_j-\boldsymbol{X}_B^i\right)\Delta s_i \tag{5.30}$$

The above process is similar to the velocity correction. Once $\delta\phi\left(\boldsymbol{x}_j,t\right)$ is obtained by Eq. (5.30), we can correct for the ϕ field by

$$\phi\left(\boldsymbol{x}_j,t\right)=\phi^*\left(\boldsymbol{x}_j,t\right)+\delta\phi\left(\boldsymbol{x}_j,t\right) \tag{5.31}$$

Eq. (5.30) is applied for the time-dependent diffusion equation (5.21). For this case, IBM uses an explicit approach to update the solution in time due to the effect of the boundary. For a time-independent problem, an iterative process can be taken first before IBM is applied. To illustrate the iterative process, we consider the following time-independent equation

$$\phi=\alpha\nabla^2\phi \tag{5.32}$$

with Neumann boundary condition. After numerical discretization, the resultant equation system of Eq. (5.32) can be solved by a direct method. It can also be solved by an iterative method. One of the iterative processes can be written as

$$\phi^{m+1} = \alpha \nabla^2 \phi^m \tag{5.33}$$

where *m* is the iteration number. To start the iterations, we need to give an initial guess of ϕ. Then from Eq. (5.33), we can get ϕ^*. Like the time-dependent case, the computed $\partial \phi^* / \partial \boldsymbol{n}$ is in general not equal to the given $\partial \phi / \partial \boldsymbol{n}$ at the boundary point. Then we can follow the same procedure as for the time-dependent problem to compute δq_n by using Eq. (5.29). With δq_n, the correction $\delta \phi$ can be calculated by

$$\delta \phi \left(\boldsymbol{x}_j \right) = \sum_i \delta q_n \left(\boldsymbol{X}_B^i \right) D_{ij} \left(\boldsymbol{x} - \boldsymbol{X}_B^i \right) \Delta s_i \tag{5.34}$$

Eq. (5.34) is used to determine $\delta \phi \left(\boldsymbol{x}_j \right)$ and it is the same as Eq. (5.30) if one takes δt as 1. Next, ϕ is updated through Eq. (5.31) at Eulerian points around the immersed boundary. After that, we move to the next iteration. With updated ϕ value given by Eq. (5.31), we can get a new ϕ^* from Eq. (5.33) (updated ϕ value is applied to the right side of Eq. (5.33)). This iteration process is carried on until the convergence criterion is satisfied.

5.3.3 Application to solid-multiphase flow interactions

In this subsection, the approach illustrated above will be used to simulate solid-multiphase flow interactions. It should be stressed that although the solid-multiphase flow interactions are taken as an example to further illustrate the implementation process, the developed IBM for Neumann boundary condition can be generally applied to different physical problems. In solid-multiphase flow interactions, two Neumann boundary conditions of $\partial \phi / \partial \boldsymbol{n} = -\tilde{\omega} / \kappa$ and $\partial \mu_\phi / \partial \boldsymbol{n} = 0$ need to be implemented. They are related to the expression of Cahn-Hilliard

equation and chemical potential as introduced in Chapter 2. For demonstration purpose, we rewrite them to the following two forms

$$\frac{\partial \phi}{\partial t} + \boldsymbol{u} \cdot \nabla \phi = -\nabla \cdot \boldsymbol{q}_{\phi} \tag{5.35}$$

$$\mu_{\phi} = 4\left(\phi^3 - \phi_0^2 \phi\right) - \nabla \cdot \boldsymbol{q}_{\mu} \tag{5.36}$$

where

$$\boldsymbol{q}_{\phi} = -M \nabla \mu_{\phi}, \qquad \boldsymbol{q}_{\mu} = \kappa \nabla \phi \tag{5.37}$$

Following the procedure in Section 5.3.2, we first solve Eqs. (5.35) and (5.36) in the whole domain without consideration of the boundary conditions to obtain ϕ^* and μ_{ϕ}^*. In this case, ϕ^* and μ_{ϕ}^* satisfy the following equations

$$\frac{\partial \phi}{\partial t} + \boldsymbol{u} \cdot \nabla \phi^* = -\nabla \cdot \boldsymbol{q}_{\phi}^* \tag{5.38}$$

$$\mu_{\phi}^* = 4\left(\phi^{*3} - \phi_0^2 \phi^*\right) - \nabla \cdot \boldsymbol{q}_{\mu}^* \tag{5.39}$$

Following the steps in Eqs. (5.26-5.28), with obtained ϕ^* and μ_{ϕ}^*, we can easily compute $\partial \phi^* / \partial n$ and $\partial \mu_{\phi}^* / \partial n$. In general, the calculated $\partial \phi^* / \partial n$ and $\partial \mu_{\phi}^* / \partial n$ are not equal to the given Neumann boundary conditions. Their differences will generate the surface fluxes $\delta q_{\phi n}$ and $\delta q_{\mu n}$. According to Eqs. (5.29) and (5.37), $\delta q_{\phi n}$ and $\delta q_{\mu n}$ can be expressed as

$$\delta q_{\phi n}\left(\boldsymbol{X}_B^i, t\right) = -2M \left(\left. \frac{\partial \mu_{\phi}}{\partial n} \right|_{Specified} - \frac{\partial \mu_{\phi}^*}{\partial n} \right) \tag{5.40}$$

$$\delta q_{\mu n}\left(\boldsymbol{X}_B^i,t\right)=2\kappa\left(\left.\frac{\partial\phi}{\partial n}\right|_{Specified}-\frac{\partial\phi^*}{\partial n}\right) \tag{5.41}$$

Note that $\delta q_{\phi n}$ is to correct $\partial\phi/\partial t$ in Eq. (5.35), while $\delta q_{\mu n}$ is to correct μ_ϕ in Eq. (5.36). If we set correction of ϕ as $\delta\phi$ and correction of μ_ϕ as $\delta\mu_\phi$, following Eqs. (5.30) and (5.34), we have

$$\frac{\delta\phi\left(\boldsymbol{x}_j,t\right)}{\delta t}=\sum_i\delta q_{\phi n}\left(\boldsymbol{X}_B^i,t\right)D\left(\boldsymbol{x}_j-\boldsymbol{X}_B^i\right)\Delta s_i \tag{5.42}$$

$$\delta\mu_\phi\left(\boldsymbol{x}_j,t\right)=\sum_i\delta q_{\mu n}\left(\boldsymbol{X}_B^i,t\right)D\left(\boldsymbol{x}_j-\boldsymbol{X}_B^i\right)\Delta s_i \tag{5.43}$$

where Δs_i is the arc length of Lagrangian grid in 2D case and surface area in 3D case. After obtaining $\delta\phi$ and $\delta\mu_\phi$, the corrected ϕ and μ_ϕ at Eulerian points can be computed by

$$\phi\left(\boldsymbol{x}_j,t\right)=\phi^*\left(\boldsymbol{x}_j,t\right)+\delta\phi\left(\boldsymbol{x}_j,t\right) \tag{5.44}$$

$$\mu_\phi\left(\boldsymbol{x}_j,t\right)=\mu_\phi^*\left(\boldsymbol{x}_j,t\right)+\delta\mu_\phi\left(\boldsymbol{x}_j,t\right) \tag{5.45}$$

At present, the updated μ_ϕ and ϕ have included the influence of the solid boundary. Thereafter, they are readily adopted to evaluate the resulting forcing and velocity terms in Eqs. (5.2) and (5.3). In this manner, the Neumann boundary conditions are implemented in the framework of immersed boundary method.

5.4 Some Test Examples

In this section, numerical examples of solid-fluid interactions will be presented. The problems consist of solid-single phase flow interactions that involve Dirichlet boundary conditions as well as solid-multiphase flow interactions that involve both Dirichlet and Neumann boundary conditions. The solid-single phase flow interactions will be presented in the first place. For single phase flow problems, the interfacial force is zero and the lattice Boltzmann equation for interface capturing is not solved. Thereafter, simulation of solid-multiphase flow interactions will be briefly demonstrated. The detailed application of the developed method for solving solid-multiphase flow interactions will be shown in the next chapter.

5.4.1 Flow over a circular cylinder

Wake flows around two-dimensional bluff bodies such as circular cylinders have been extensively studied. With increase of Reynolds number (defined as $\mathrm{Re} = \frac{U_\infty D}{\upsilon}$, where D is the diameter of the cylinder, U_∞ is the free stream velocity and υ is the kinematic viscosity), the wake becomes unsteady and then asymmetric when the flow passes over a circular cylinder (Sheard et al. 2003). The initial transition for the cylinder wake occurs with the separation of flow from the rear of the cylinder. When Reynolds number is in range of $5 < \mathrm{Re} < 47$, the recirculation zone remains steady and symmetrical about the centerline of the flow. A transition to periodic flow occurs when Reynolds number is larger than 47.1, which was found by Dusek et al. (1994) through numerical simulation and also validated by Sheard et al. (2001). The wake transition shape and the corresponding Reynolds number are

listed in Table 5.1. Besides the transition in wake patterns, the drag force coefficient as defined in Eq. (5.46) also changes with variation of Re.

$$C_d = \frac{F_D}{(1/2)\rho U_\infty^2 D} \tag{5.46}$$

where F_D is total drag force which is calculated by

$$F_D = -\int_\Omega f_x d\mathbf{x} \tag{5.47}$$

and f_x is the *x*-component of the force density. When the Reynolds number increases, the wake becomes unsteady, and a lift force appears. Following the same way, the lift force coefficient can be evaluated by

$$C_l = \frac{F_L}{(1/2)\rho U_\infty^2 D} \tag{5.48}$$

where F_L is the lift force

$$F_L = -\int_\Omega f_y d\mathbf{x} \tag{5.49}$$

and f_y is the *y*-component of the force density. In the current work, the fluid density is set as $\rho = 1.0$ and the free stream velocity is $U_\infty = 0.1$. This velocity is also used as the initial velocity of the flow field. According to the wake transition type, four different Reynolds numbers of 20, 40, 100 and 200 are chosen. First, steady flow at Re = 20 and 40 is simulated. To accurately simulate the influence of the circular cylinder and reduce the computational resources required, a non-uniform Cartesian grid is used. In the present simulation, a circular

cylinder with diameter of 1.0 represented by 120 Lagrangian points is put in a rectangular domain of $60D \times 50D$ with 397×337 grid points. The fine grid region around the cylinder is $1.2D \times 1.2D$ with 97×97 grid points. The center of this cylinder is located at (20.6D, 25.6D). Simulations have been performed on three computational domains: $45D \times 37.5D$, $60D \times 50D$, and $90D \times 75D$. The results show that the computational domain $60D \times 50D$ is large enough to obtain accurate results. Figures 5.3 and 5.4 show the global geometry and local mesh around the circular cylinder, respectively. For the steady case, the simulation is performed until the nondimensional time 50.0 (nondimensionalized by U_∞ / D with $D = 1$). The streamlines around the cylinder are presented in Figs. 5.5 and 5.6. The results obtained by the boundary condition-enforced IBM are compared with those of conventional direct forcing IBM. It can be seen that, in the present results, the streamlines inside the circular cylinder are closed. This means that there is no mass transfer across the cylinder. Conversely, the streamline penetration is very obvious in the results obtained by the conventional direct forcing IBM. This is mainly due to the fact that no-slip boundary condition is accurately enforced by the boundary condition-enforced IBM. Nevertheless, this condition is only approximately satisfied in the traditional IBMs. Additionally, the drag force coefficient C_d and recirculation length L at Re = 20 and 40 obtained by the boundary condition-enforced IBM are compared with data in the literature in Table 5.2. It shows that the present results quantitatively compare well with those in the literature (Dennis and Chang 1970, He and Doolen 1997). Furthermore, simulations of the unsteady shedding wakes at *Re* = 100 and *Re* = 200 are performed. The simulation was performed until nondimensional time equals 200. The time-averaged drag coefficients at Re = 100 are compared with results in the literature in Table 5.3. It can be seen that good agreement is achieved. In addition, the streamlines around the cylinder and instantaneous positive-negative vortex shedding at Re = 100 and Re = 200 are plotted in Fig. 5.7 and Fig. 5.8. They show typical vortex shedding patterns after the flow

field lost symmetry. The Karman vortex street can be clearly observed. Furthermore, Fig. 5.9 shows the time evolution of the drag and lift coefficients for the circular cylinder at Re = 100 and Re = 200. The periodic variation of the drag and lift coefficients can be seen clearly from the figures.

5.4.2 Fish motion

Besides simulation of flow around a stationary object in the previous subsection, the boundary condition-enforced IBM will also be applied to simulate a moving boundary flow problem, that is, fish motion at high Reynolds numbers. Investigation of fish motion has been an area of active interest in different fields for decades. Many efforts have been made to model the kinetics of fish (Lighthill 1960, Koochesfahani 1989, Liu and Kawachi 1999, Sfakiotakis et al. 1999, Colgate and Lynch 2004). Among them, a kinematics model for undulatory motion of a swimming fish was proposed by Wassersug and Hoff (1985). They also plotted the specific amplitude from tip to tail of a larvae and cod. Additionally, by using Fourier terms, Videler (1993) provided a formula to describe lateral motion of a swimming fish. According to Videler (1993), the undulatory fish swimming motion can be accurately expressed by the equation that describes harmonic motion in physics. The lateral motion that expressed by the first three, odd Fourier terms reads (Videler 1993)

$$y_m(x,t) = \sum_{i=1,3,5} [a_i(x)\cos(i2\pi f_i t) + b_i(x)\sin(i2\pi f_i t)] \tag{5.50}$$

in this equations, $y_m(x,t)$ is the coordinate of the center line in the *y* direction. Moreover, $a_i(x)$ and $b_i(x)$ are Fourier coefficients, f_i is the phase speed of the travelling wave, *t* is the

time and x is the coordinate. By dropping the less effective terms, the fifth frequency terms, one can derive the expression (Videler 1993)

$$y_m(x,t) = a_1(x)\cos(2\pi ft) + b_1(x)\sin(2\pi ft) \tag{5.51}$$

together with

$$\begin{cases} a_1(x) = a_m(x)\cos(2\pi x/\lambda) \\ b_1(x) = b_m(x)\sin(2\pi x/\lambda) \end{cases} \tag{5.52}$$

where, $a_m(x)$ is the undulatory amplitude, λ is the wavelength and f is the frequency. Eq. (5.51) can also be simplified as

$$y_m(x,t) = a_m(x)\cos(2\pi x/\lambda - 2\pi ft) \tag{5.53}$$

The amplitude of undulation wave varies for different swimming species. According to the plot of the specific amplitude along the body (Wassersug and Hoff 1985), the amplitude function can be determined. Studying several types of third and fourth-order polynomials, Liu and Kawachi (1999) found that a polynomial denoted by "am3" results in bigger propulsion with the same snout and tail amplitude. They also concluded that this might be due to the smooth line of mode "am3", and this enables production of equilibrium vortex generation. The third-order polynomial (Liu and Kawachi 1999) can be written as

$$a_m(x) = C_0 + C_1x + C_2x^2 + C_3x^3 \tag{5.54}$$

Coefficients from C_0 to C_3 are calculated from the curve plotted by Wassersug and Hoff (1985) through Chebyshev Curve Fitting method. The exact values of these coefficients are listed in Table 5.4. The amplitude approximated by this third-order polynomial is also plotted

in Fig. 5.10. In the present analysis, NACA0012 airfoil expressed by Eq. (5.55) is used as the contour of the fish body

$$y(x) = \frac{0.12}{0.2}(0.2969\sqrt{x} - 0.126x - 0.3516x^2 + 0.2843x^3 - 0.1015x^4) \qquad (5.55)$$

where x varies from 0.0 to 1.0. The flow field is 30×24 with non-uniform grid represented by 821×601 points. The finest grid is 1.1×0.6 with mesh spacing of 1/200 around the fish body. The mesh with NACA0012-shaped fish contour is illustrated in Fig.5.11. The fish is represented by 181 boundary points and located at (10.0, 12.0) initially. The fluid density is $\rho = 1.0$, the free stream velocity is $U_\infty = 0.1$ and Reynolds number is 7200. Three cases with different frequencies of 1.3, 1.7 and 2.0 are simulated. The instantaneous streamlines and alternately positive-negative vorticity shedding after the drag/lift coefficient demonstrates periodic characteristic are shown in Fig. 5.12 and 5.13. It is known that the propulsive force is generated by the momentum transferred to the surrounding fluid during fish motion. When an undulation wave is passed across the fish, fluid is displaced around a fish and reaction forces arise. By integration of the force density along the fish surface, one can obtain the net force and moment generated by the fish. The total force includes contribution from the lift and drag forces. Lift is defined as the force acting perpendicular to the direction of motion, while drag acts parallel to the direction of motion. Table 5.5 compares the maximum and minimum drag coefficients in a period at f = 1.3, f = 1.7 and f = 2.0 with data in the literature (Shu et al. 2007). It can be seen that the present results show satisfactory comparison with data in the literature. Moreover, Fig. 5.14 shows drag coefficient at different undulation frequency. Negative drag coefficient implies propulsion force, which is generated by undulatory fish motion. The drag coefficient at different frequencies shown in Fig. 5.14 reveals that the frequency has remarkable influence on the propulsive force generated. It can

be seen that when frequency equals to 1.3, the average drag coefficient in a period is nearly zero. When frequency is up to 1.7, the propelling force almost lasts for the entire period. Moreover, the propelling force rises remarkably when the frequency increases further to 2.0.

5.4.3 Flow over a sphere

A three-dimensional problem, flow over a sphere, is presented in this subsection. In this case, Reynolds number is defined as $\mathrm{Re} = \frac{U_\infty D}{\nu}$, where U_∞ is the free stream velocity taken as 0.1 and D is the sphere diameter. According to Sheard et al. (2003), the flow around a sphere could be classified into three different regimes: steady axisymmetric flow ($\mathrm{Re} \le 200$), steady non-axisymmetric flow ($210 \le \mathrm{Re} \le 270$) and unsteady non-axisymmetric flow ($280 \le \mathrm{Re} < 375$). Steady flow at Re = 100 and 200, non-axisymmetric flow at Re = 250 are simulated in this study. The flow domain is a rectangular box with size of $30D \times 20D \times 20D$ in x, y and z directions respectively as shown in Fig. 5.15. It is represented by non-uniform mesh with $155 \times 146 \times 146$ nodes. The center of the sphere is located at $(10D, 10D, 10D)$ in the flow domain. The finest mesh region is arranged around the sphere with dimension of $1.3D \times 1.3D \times 1.3D$ represented by $52 \times 52 \times 52$ nodes as shown in Fig. 5.16. Since the flow is axisymmetric when Re = 100 (Fig.5.17) and 200 (Fig.5.18), only the streamlines at the x-y plane of symmetry are plotted. The symmetric recirculation region can be seen clearly from the figures. It can also be seen that the recirculation length increases with Reynolds number. The drag coefficient at Re = 100 and 200 are compared with the benchmark data in Table 5.6. The convergence criteria was set as the difference of the drag force between two iteration steps less than 10^{-5}. The present results agree well with the previous numerical (Johnson and Tezduyar 1994) and experimental results (White 1974). Moreover, for axisymmetric flow, the

simulations at Re = 250 are also performed. When Reynolds number goes up to 250, the non-axisymmetric recirculation region can be seen clearly from Fig. 5.19 and Fig. 5.20. It shows that the streamlines in the x-y plane is still symmetric. However, the symmetry is lost at the x-z plane. In this case, the flow is being considered as planar symmetric. This result is in good agreement with previous finding (Johnson and Tezduyar 1994).

5.4.4 Transition layers on hydrophilic and hydrophobic walls

The previous subsections demonstrate interactions between solid and single phase flows that involve Dirichlet boundary conditions. In the following subsections, problems with immersed solid in the multiphase flows, in which both Dirichlet and Neumann boundary conditions are present, will be discussed. The transition layer generated when a solid object is immersed in multiphase flows is presented in this subsection.

When a solid wall is immersed in a multiphase flow and the surface wettability is not neutral, that is, $\left(\partial\phi/\partial\boldsymbol{n}\right)_s$ has non-zero value, the value of the order parameter on the wall will deviate from that in the bulk region (Papatzacos 2002) and a transition layer can be formed along the solid surface. In this case, analytical solutions exist for the order parameter on the solid surface. Hence it is adopted to test the performance of the proposed algorithm. The problem considered in this section is a square domain with a circular cylinder located in the center of the domain. The cylinder radius is chosen as the reference length, that is, the non-dimensional radius is 1, and the non-dimensional length of the computational domain is taken as 3.5. To ensure that the computation is consistent between the physical system and the lattice Boltzmann system, the non-dimensional radius and the length of computational domain in the

lattice Boltzmann system are kept as 1 and 3.5, respectively. For the present LBM calculation, δx is set as 1 for simplicity. Thus in the lattice Boltzmann system, the number of mesh points for the radius, N_{radius}, is the radius of the cylinder, and the number of mesh points used in each direction, *N*, is actually the length of the domain. Since the cylinder radius N_{radius} is taken as the reference length, in the lattice Boltzmann system, the non-dimensional radius of the cylinder is $N_{radius} / N_{radius} = 1$, and the non-dimensional length of the square computational domain should be $N / N_{radius} = 3.5$. This general rule must be obeyed when different mesh size and radius of cylinder are used in the lattice Boltzmann system. Hereafter, all the computational parameters are given in the lattice Boltzmann system unless stated otherwise.

5.4.4.1 Effect of transition layer thickness

A solid circular cylinder with radius of 40 represented by 148 Lagrangian points is centered at (70, 70) in a 140×140 computational domain. The flow domain is initialized as follows. $\rho = 1$ for both fluids, ϕ_0 is set as 1 in the bulk region, $\sigma = 0.001$, τ and τ_ϕ take the same value as 0.75. (These physical parameters will be used for the cases hereafter unless otherwise stated). In this case, the gradient of the order parameter is fixed as $\omega = 0.334933$ which corresponds to static contact angle of 60°, and the transition layer thickness (*w* in Chapter 2, Eq. (2.3)) varies from 4.0 to 6.0 with increment of 0.5. Moreover, neutral boundary conditions are applied on the outer boundaries. To be concrete, for density distribution functions: $f_\alpha\big|_{Boundary} = f_\alpha^{eq}\big|_{Boundary}$ and $g_\alpha\big|_{Boundary} = g_\alpha^{eq}\big|_{Boundary}$ with α running over 0 to 8 lattice directions. For the macroscopic variables, natural boundary conditions (or neutral wetting boundary conditions) are applied. To be concrete: $\boldsymbol{u}\big|_{Boundary} = \boldsymbol{0}$, $\rho\big|_{Boundary} = 1$,

$\phi|_{Boundary}=1$, $\nabla\phi|_{Boundary}=0$ and $\nabla\mu_{\phi}|_{Boundary}=0$. In addition, the convergence criterion is set as $\left|\phi_s^{n+1}-\phi_s^n\right|/\phi_s^n<10^{-5}$ hereafter for this case. Figure 5.21 displays the initial flow field where ϕ takes the same value in the whole flow domain. Figure 5.22 demonstrates the flow domain after applying the boundary condition through IBM when the transition layer thickness is set as 4.0. The transition layer attached to the solid boundary can be seen clearly in this figure. Moreover, Table 5.7 compares ϕ on the boundary obtained through numerical simulation with the analytical solution when the surface thickness varies from 4.0 to 6.0. The relative error is defined as

$$E_{Relative}=\frac{\left|\phi_{Theoretical}-\phi_{Numerical}\right|}{\phi_{Theoretical}} \tag{5.56}$$

It can be found in Table 5.7 that the present results agree well with the theoretical prediction.

Moreover, on account of the circular cylinder being a central-symmetric geometry, the solution of this problem should also be isotropic. Hence, it is natural to raise a question, that is, whether ϕ obtained on the solid boundary demonstrates isotropy. To examine this issue, one can first look at Fig. 5.22. No oscillation can be observed in the flow domain. To be more precise, quantitative comparison is made in Table 5.8. It lists the maximum error between the local and the average numerical ϕ value. It shows that the maximum errors are less than 6×10^{-4} and the errors monotonously decrease as the thickness increases. The above comparisons demonstrate good isotropy of the obtained numerical results. In addition, the influence of grid size on numerical solution is examined. The interface width is chosen as 7 and other computational parameters except for grid size are set to be the same. Three sets of grids (141×141, 211×211 and 281×281) are tested and listed together with results in Table

5.9. It can be seen that the numerical results steadily approach theoretical solution as grid size is refined from 141×141 to 281×281. Note that for the three sets of grids, the non-dimensional length of the domain is kept as 3.5.

5.4.4.2 Effect of $(\partial\phi/\partial\boldsymbol{n})_s$

The previous subsection simulates the case with a fixed Neumann boundary condition that is equivalent to contact angle of 60°. This subsection demonstrates the capacity of the present method to handle different $(\partial\phi/\partial\boldsymbol{n})_s$ (corresponding to $5^\circ < \theta_{eq} < 175^\circ$). The surface thickness is taken as 9.0. The computation is carried out on a 251×251 mesh size and the radius of the cylinder is represented by 65 grid points. Fig. 5.23 compares the numerical results with the theoretical values corresponding to different wetting potentials. The data are listed in Table 5.10. It can be seen that the numerical results compare well with theoretical values when contact angle varies from 5° to 135°. It can also be found that both the absolute and relative errors increase from zero when θ_{eq} deviates from 90°. This may be attributed to the nature of this problem. According to the relationship provided by $\cos\theta_{eq} = \frac{1}{2}\left[(1+\omega)^{\frac{3}{2}} - (1-\omega)^{\frac{3}{2}}\right]$ which is also shown in Fig. 2.2 in Chapter 2, it can be seen that when the equilibrium contact angle is close to 0° or 180°, the curve becomes very sharp. This indicates that in the region near 0° or 180°, the equilibrium contact angle is very sensitive to the ω value. That is, when ω is changed a little bit, the equilibrium contact angle will change a lot. So, in the region near 0° or 180°, a small numerical error for ω would cause a large numerical error for the equilibrium contact angle. To further study this issue, the same problem is simulated by direct implementation of the boundary conditions. It is found that the numerical results given by

direct implementation of the boundary conditions also give larger errors when the contact angle is close to 0° or 180°, but are more accurate than the IBM results. This means that the present solver may not be very efficient to resolve the problem when the contact angle is close to 0° or 180°. It would need a very fine mesh to solve the problem in order to get an accurate solution.

5.5 Concluding Remarks

In this Chapter, both Dirichlet and Neumann boundary conditions were implemented consistently in IBM for simulation of various solid-fluid interactions. The IBM for Dirichlet boundary condition was briefly discussed. More importantly, for the first time, an IBM to implement Neumann boundary condition was developed in this work. The primary concept of the current method is to utilize the physical mechanism and interpret Neumann boundary condition as contribution of the flux from the surface to its relevant physical parameters over a control volume. Using the concept of IBM, the flux is directly related to the correction of the flow variables at Eulerian points. Several numerical experiments were performed to demonstrate the ability of IBM for simulation of solid-fluid interactions. First, simulation of steady and unsteady problems of solid-single phase flow interactions that involve Dirichlet boundary condition was performed. The numerical cases included flow over a circular cylinder, fish motion at high Reynolds number and flow over a sphere. The present numerical results compared well with data in the literature. Additionally, the developed immersed boundary method for Neumann boundary condition was applied together with the boundary condition-enforced IBM for Dirichlet boundary condition to simulate solid-multiphase flow interactions. The developed method was examined in detail through simulation of transition

layers on both hydrophilic and hydrophobic walls. The results show that the Neumann boundary condition can be implemented accurately. This work releases IBM from the long standing restriction that it can only handle Dirichlet boundary condition and sheds light on the implementation of IBM to ubiquitous fluid-solid interactions defined by Neumann boundary conditions.

Table 5.1 Transition Reynolds numbers for the wake around a circular cylinder (Sheard et al. 2001)

Circular cylinder transition type	Reynolds number
Boundary –layer separation	4 to 5
Unsteady wake	47

Table 5.2 Comparison of the drag force coefficient C_d and recirculation length L for steady flow over a circular cylinder at Re = 20 and 40

Reynolds number	References	C_d	L
Re = 20	Dennis and Chang (1970)	2.045	1.88
	He and Doolen (1997)	2.152	1.842
	Present	2.044	1.88
Re = 40	Dennis and Chang (1970)	1.522	4.96
	He and Doolen (1997)	1.499	4.49
	Present	1.529	4.63

Table 5.3 Comparison of the drag coefficient for flow over a cylinder at Re = 100

Method	C_d
Liu et al. (1998)	1.35
Linnick and Fasel (2005)	1.34
Present	1.349

Table 5.4 The polynomial coefficients for fish motion

Coefficients	C_0	C_1	C_2	C_3
Value	0.055306	0.22649	0.29446	-0.32656

Table 5.5 Maximum and minimum drag coefficients for fish motion at Re = 7200

Frequency	Reference	Maximum	Minimum
f = 1.3	Shu et al. (2007)	0.0963	-0.0469
	Present	0.1162	-0.0439
f = 1.7	Shu et al. (2007)	0.0008	-0.3383
	Present	0.0038	-0.3261
f = 2.0	Shu et al. (2007)	-0.1117	-0.6120
	Present	-0.1129	-0.6200

Table 5.6 Comparison of the drag coefficient for flow over a sphere at Re = 100 and 200

Reynolds number	Reference	Results
100	Johnson and Patel (1999)	1.112
	White (1974)	1.8
	Present	1.126
200	Johnson and Patel (1999)	0.79
	White (1974)	0.81
	Present	0.79

Table 5.7 Comparison of ϕ on the cylinder surface with theoretical prediction

$\phi_{Theoretical} = 1.155$		
Interface thickness	$\phi_{Numerical}$	Relative error
4.0	1.091	5.5%
4.5	1.095	5.1%
5.0	1.098	4.9%
5.5	1.101	4.6%
6.0	1.104	4.4%

Table 5.8 Maximum error on the boundary

Interface thickness	4.0	4.5	5.0	5.5	6.0
$\left\|\phi-\phi_{average}\right\|_{\max}$	5.634×10^{-4}	5.573×10^{-4}	5.543×10^{-4}	5.403×10^{-4}	5.336×10^{-4}

Table 5.9 Influence of grid size on ϕ value on the boundary

$\phi_{Theoretical}=1.155$		
Mesh Size	$\phi_{numerical}$	Relative error
141×141	1.114	3.54%
211×211	1.122	2.86%
281×281	1.127	2.42%

Table 5.10 Comparison of ϕ value on the boundary

$\theta_{eq}(^\circ)$	ω	$\phi_{theoretical}$	ϕ_{IBM}	$E_{absolute}$	$E_{relative}$ (%)
5	0.679	1.295	1.23	0.065	5.062
30	0.586	1.259	1.202	0.057	4.566
45	0.476	1.214	1.168	0.046	3.789
60	0.335	1.155	1.122	0.033	2.857
75	0.173	1.083	1.065	0.018	1.662
90	0	1.0	1.0	0.0	0.0
105	-0.173	0.91	0.928	0.018	1.978
120	-0.335	0.816	0.853	0.037	4.534
135	-0.476	0.724	0.779	0.055	7.597
150	-0.586	0.643	0.716	0.073	11.331
175	-0.679	0.567	0.652	0.085	14.996

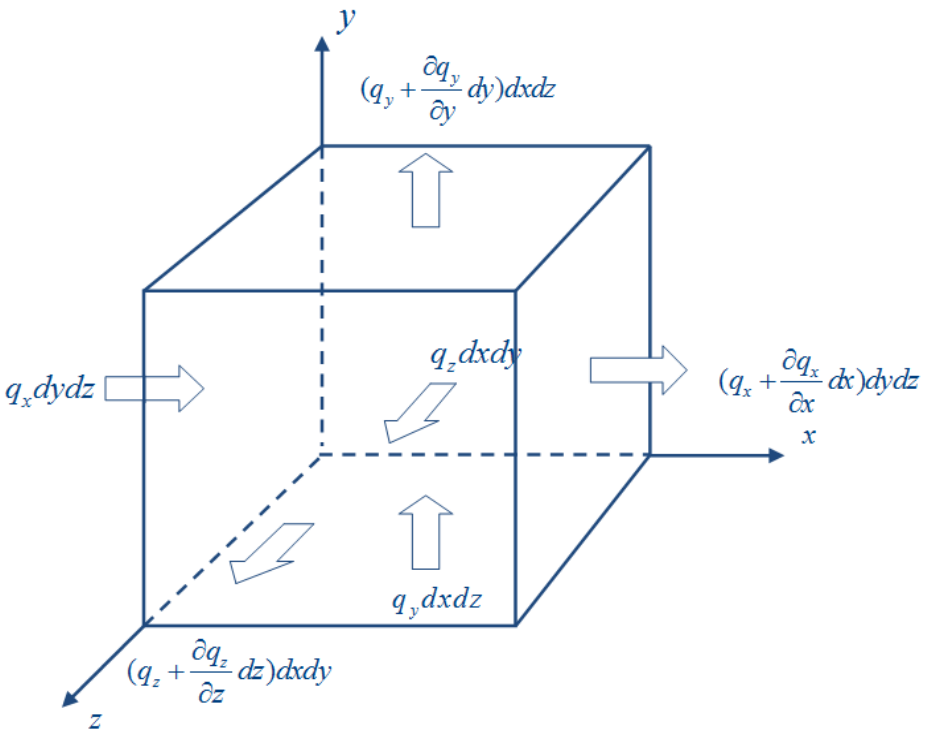

Fig. 5.1 Sketch of a control volume with flux

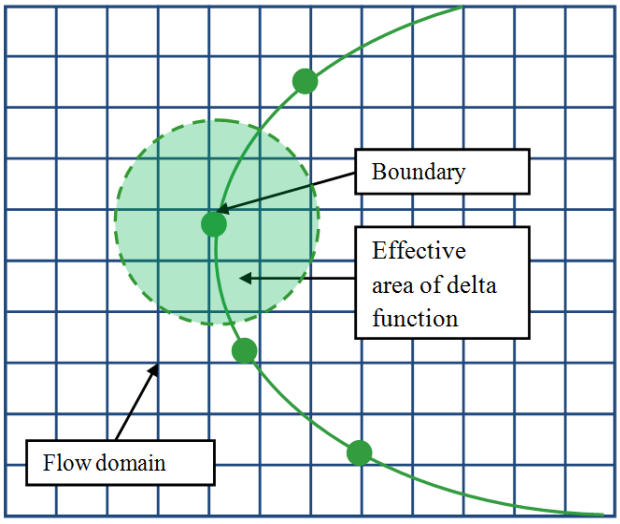

Fig. 5.2 Illustration of flow domain, immersed boundary points and influence region of boundary points to surrounding fluids

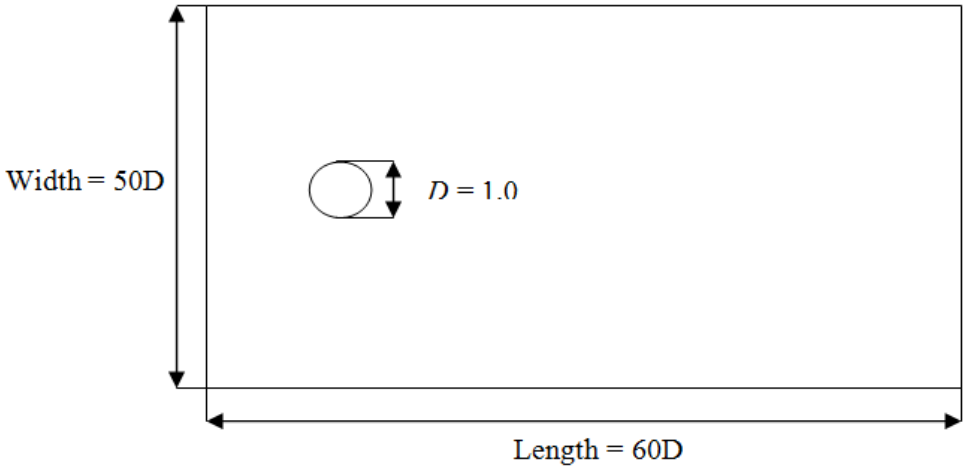

Fig. 5.3 Geometry of the flow domain and the circular cylinder

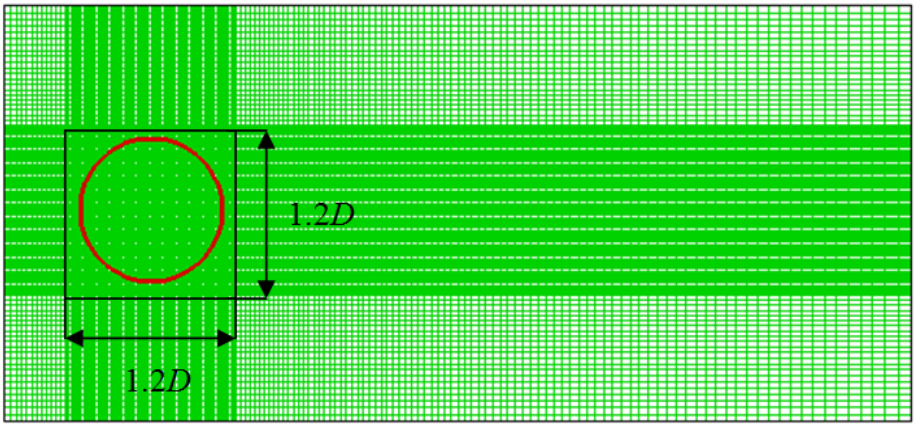

Fig. 5.4 Local mesh around the cylinder

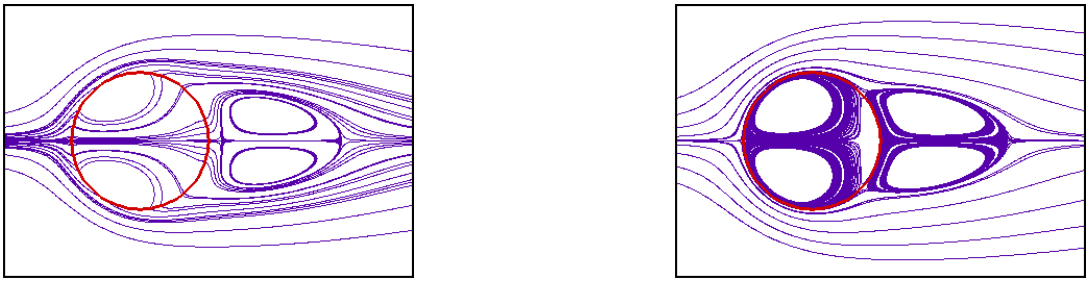

(a) Direct forcing IBM (b) Boundary condition-enforced IBM

Fig. 5.5 Streamlines around the cylinder at Re = 20 simulated by the conventional IBM and boundary condition-enforced IBM

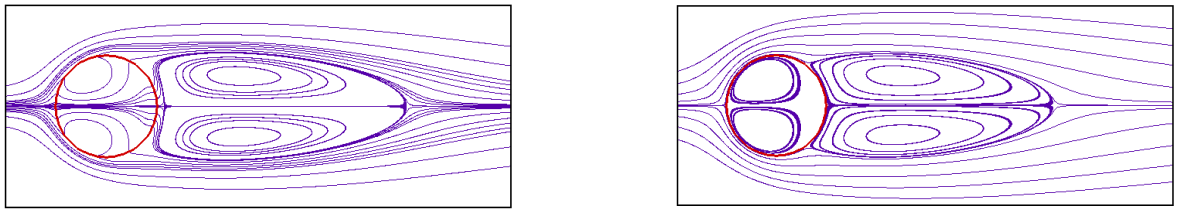

(a) Direct forcing IBM (b) Boundary condition enforced IBM

Fig. 5.6 Streamlines around the cylinder at Re = 40 simulated by the conventional IBM and boundary condition-enforced IBM

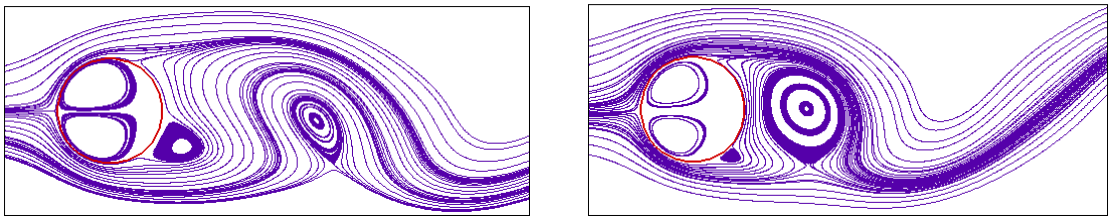

(a) Re = 100 (b) Re = 200

Fig. 5.7 Streamlines around the cylinder

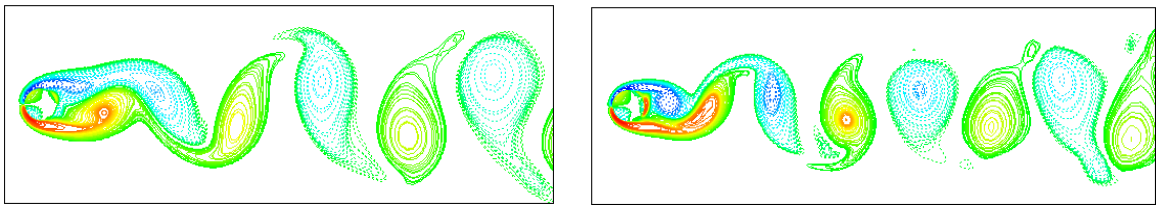

(a) Re = 100 (b) Re = 200

Fig. 5.8 Instantaneous positive-negative vorticity around the cylinder

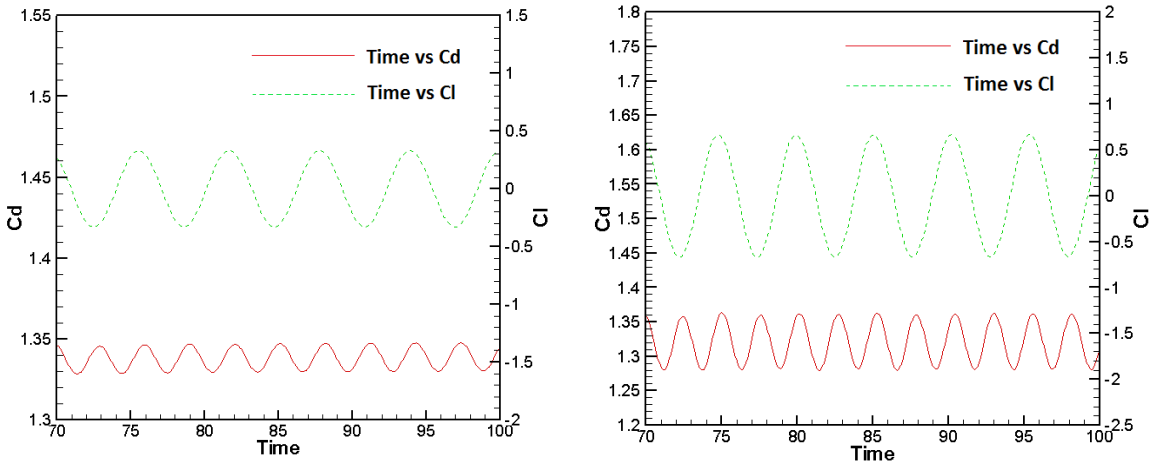

(a) Re = 100 (b) Re = 200

Fig. 5.9 Time evolution of the drag and lift coefficients

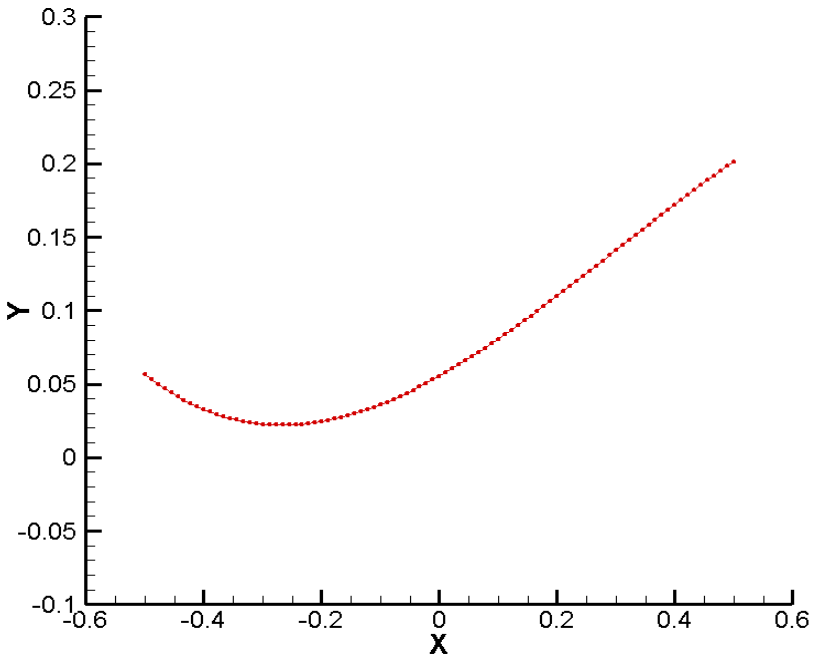

Fig. 5.10 The amplitude of fish undulation approximated by third order polynomial

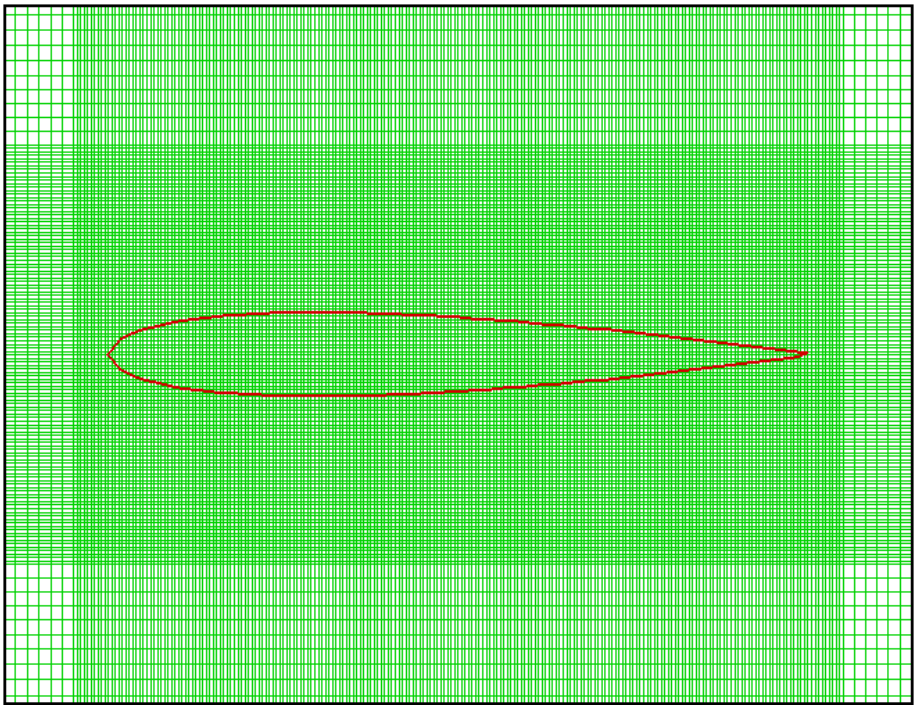

Fig. 5.11 Local non-uniform mesh around NACA0012-shaped fish contour

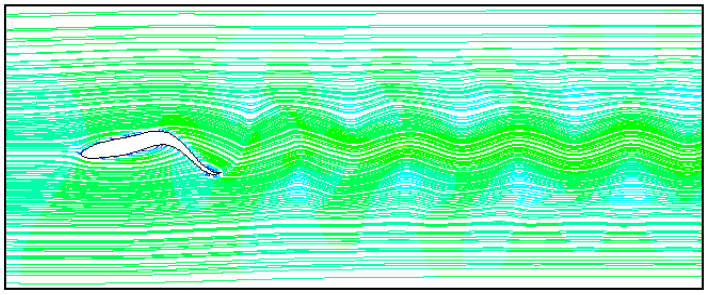

(a) Undulation frequency equals to 1.3, *Re* = 7200

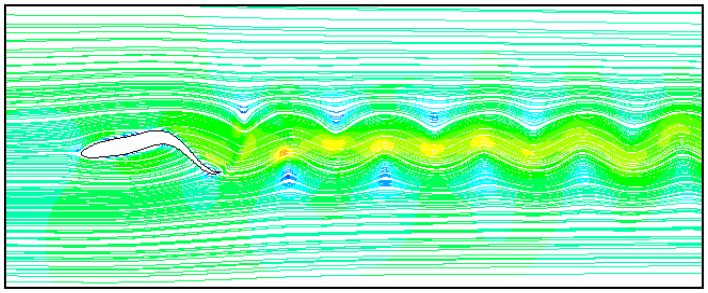

(b) Undulation frequency equals to 1.7, *Re* = 7200

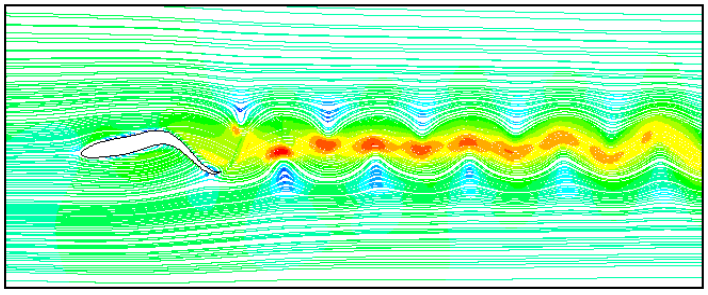

(c) Undulation frequency equals to 2.0, *Re* = 7200

Fig. 5.12 Streamlines around the swimming fish

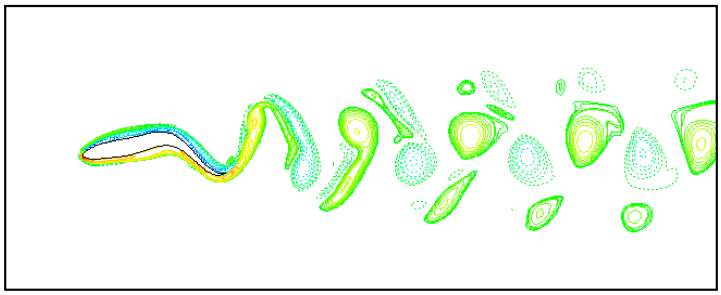

(a) Undulation frequency equals to 1.3, *Re* = 7200

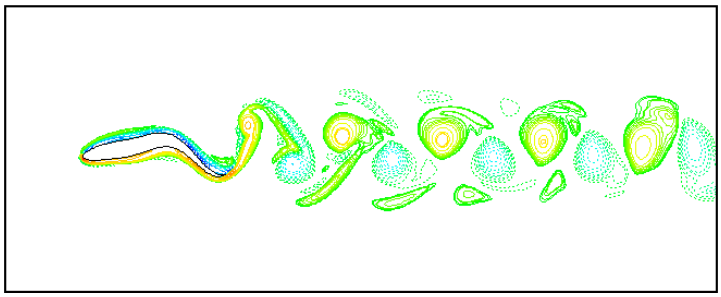

(b) Undulation frequency equals to 1.7, *Re* = 7200

(c) Undulation frequency equals to 2.0, *Re* = 7200

Fig. 5.13 Vorticity contour around the swimming fish

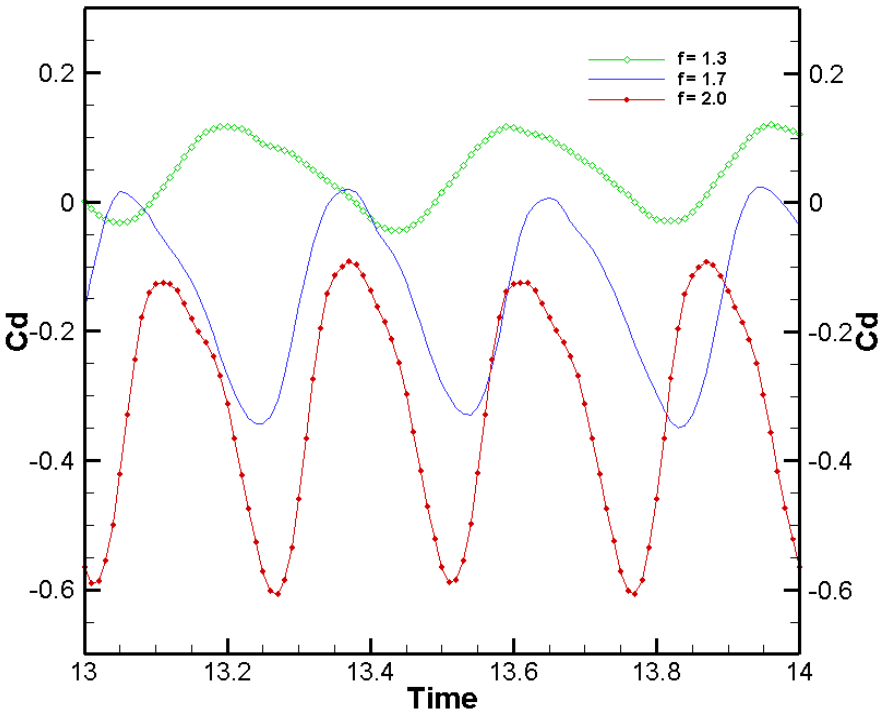

Fig. 5.14 The drag coefficient of fish swimming for different frequencies at Re = 7200

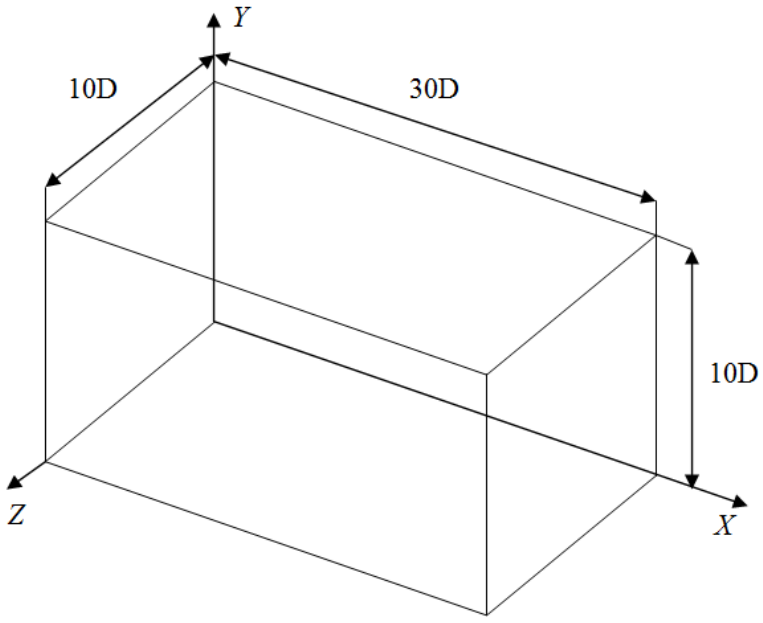

Fig. 5.15 Sketch of a rectangular flow domain

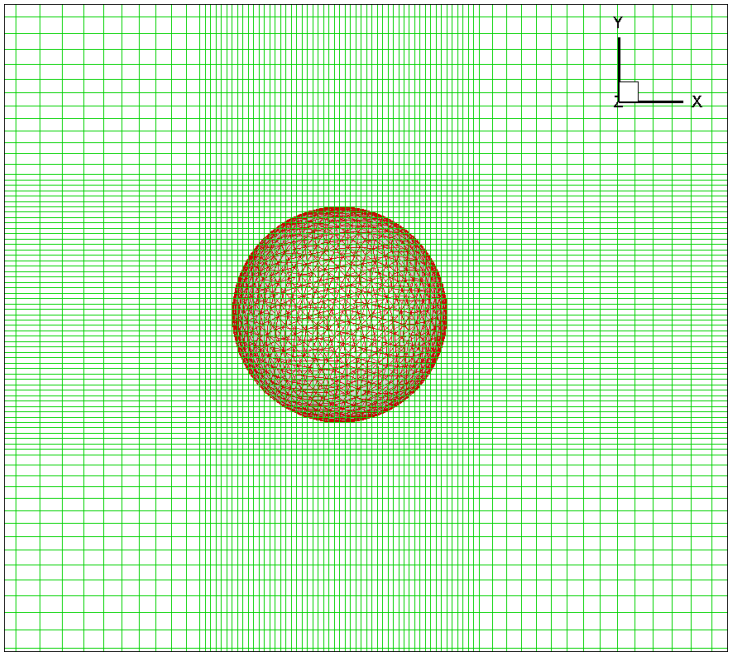

Fig. 5.16 Local mesh around the sphere

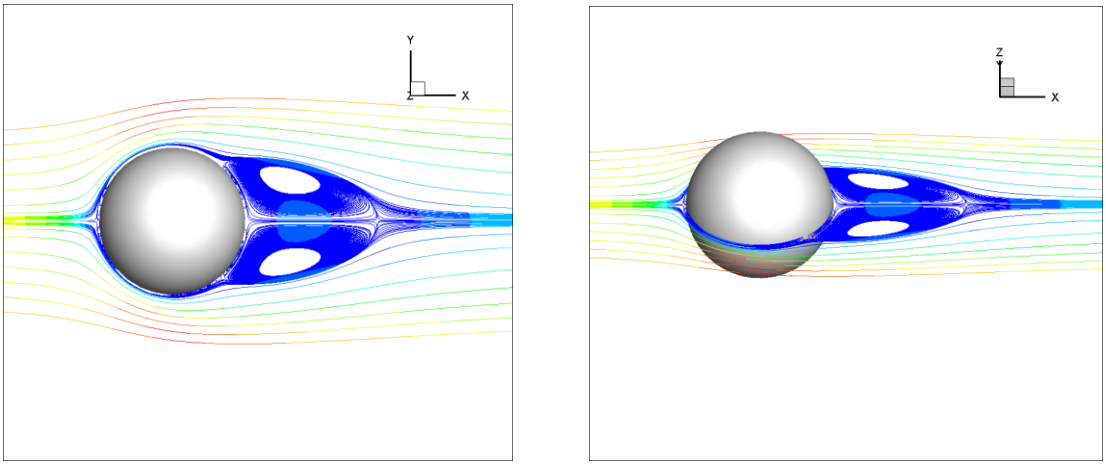

(a) (b)

Fig. 5.17 Streamlines of steady axisymmetric flows at Re = 100

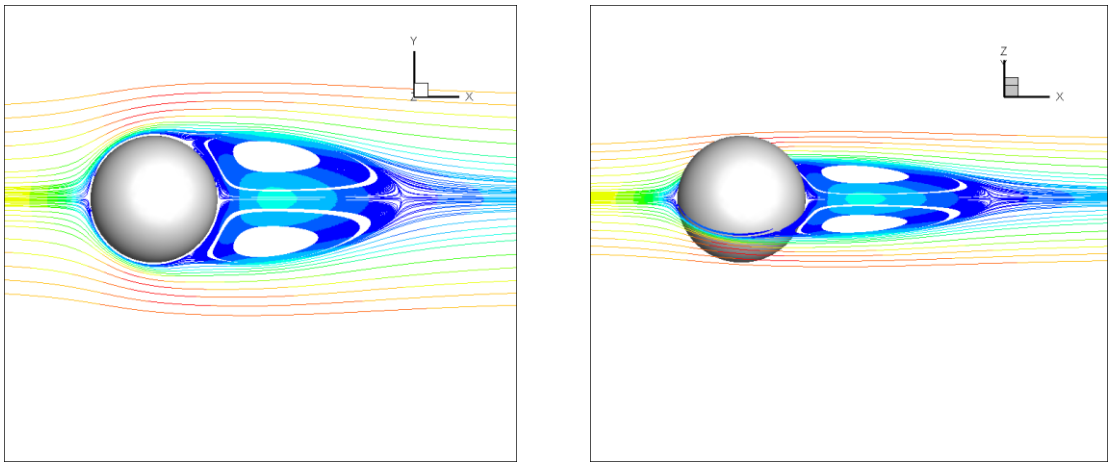

(a) (b)

Fig. 5.18 Streamlines of steady axisymmetric flows at Re = 200

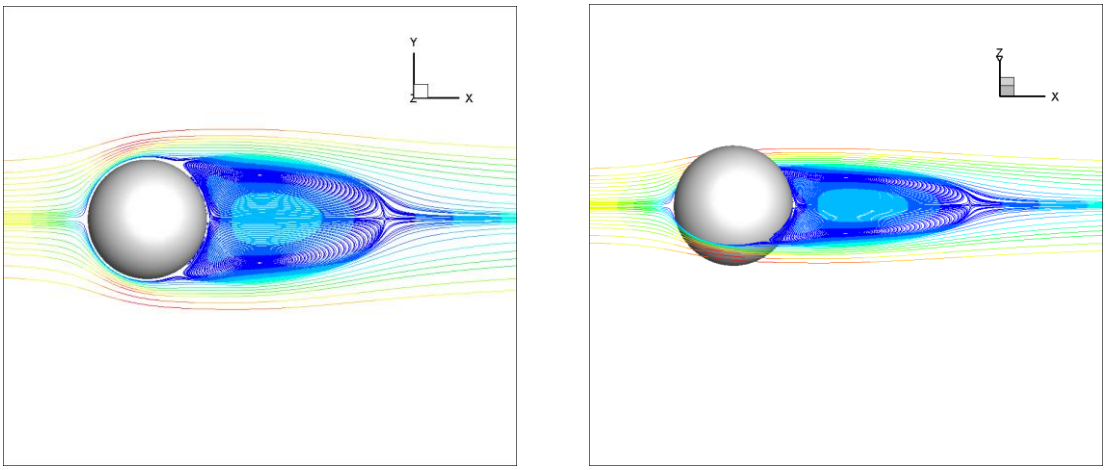

(a) (b)

Fig. 5.19 Streamlines of steady non-axisymmetric flows on x-y plane at Re = 250

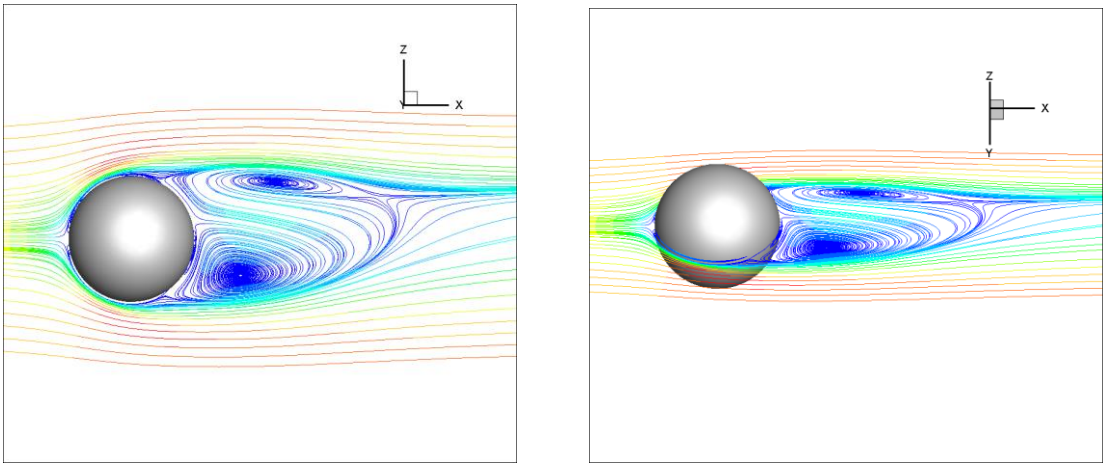

(a) (b)

Fig 5.20 Streamlines of steady non-axisymmetric flows on x-z plane at Re = 250

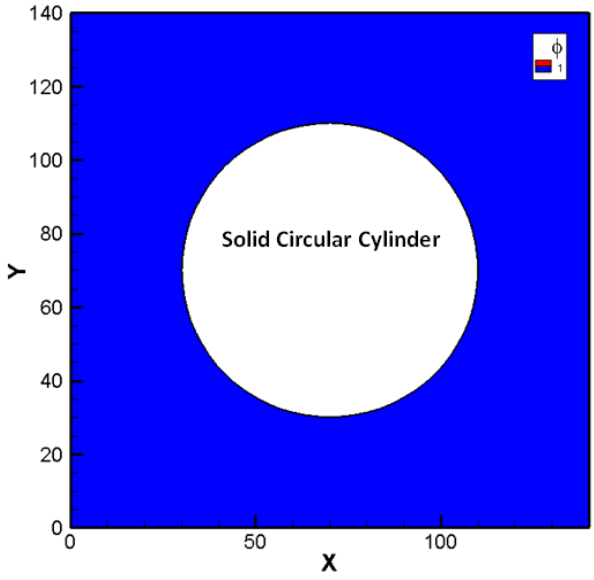

Fig. 5.21 Initial flow field with solid cylinder located at the center

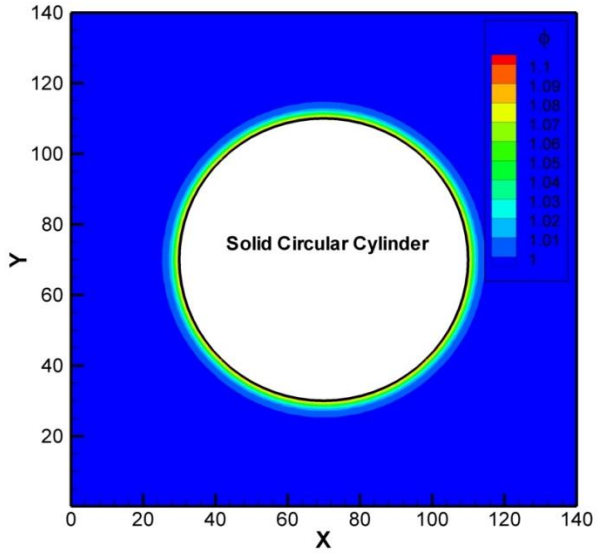

Fig. 5.22 Transition layer generated along the solid surface due to implementation of wetting boundary conditions through immersed boundary method

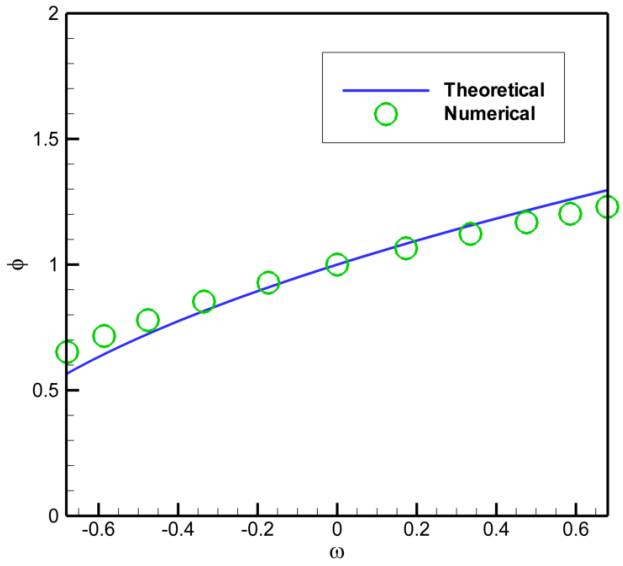

Fig. 5.23 Theoretical and numerical ϕ values on the boundary versus the non-dimensional wetting potential ω

Chapter 6[3]

Application of Immersed Boundary-Phase Field-Lattice Boltzmann Method for Solid-Multiphase Flow Interactions

In this Chapter, the numerical methods developed in previous chapters will be applied to simulate solid-multiphase flow interaction, which is still one of the most challenging problems in Computational Fluid Dynamics (CFD). The numerical challenges are mainly brought by the complexities involved. There are two distinct types of interfaces that must be treated simultaneously, that is, the liquid-liquid interface and the immersed solid boundaries. Additionally, the problem becomes much thornier when the solid is complex or allowed to move. So far, feasible and efficient solutions to this problem are still limited. In this work, we will tackle this problem through the developed Immersed Boundary-Phase Field-Lattice Boltzmann Method. In this framework, the phase-field lattice Boltzmann method is used to update the flow field and capture the fluid-fluid interface. It is a diffuse interface method that permits the fluid interface moving freely, regardless of topology change, on a fixed Eulerian grid. On the other hand, the newly developed Immersed Boundary Method (IBM) for Neumann boundary conditions is applied together with IBM for Dirichlet boundary condition to treat the solid boundary. Both two and three dimensional cases will be studied by the method developed.

[3] The material in this Chapter has been partially published in
J. Y. Shao, C. Shu and Y. T. Chew (2013), "Development of an immersed boundary-phase field-lattice Boltzmann method for Neumann boundary condition to study contact line dynamics," Journal of Computational Physics **243**:8-32.

This Chapter is organized as follows: Section 6.1 provides a brief introduction to problems of interaction between solid and multiphase flow. It is followed by a overall simulation procedure in Section 6.2. The numerical examples will be demonstrated in Section 6.3. Considering additional difficulties caused by simulation of density contrast cases (the numerical instabilities are caused by shockwave like interface, across which the density profile changes sharply and drastically), we only demonstrate application of immersed boundary phase-field LBM for small density/viscosity contrast cases. Finally, concluding remarks will be provided in Section 6.4 at the end of this Chapter.

6.1 Solid-Multiphase Flow Interactions

Solid-multiphase flow interactions encompass a wide range of natural phenomena and industrial practice, such as a raindrop impact on ground (Yarin 2006), drop sitting on lotus leaf (Quere 2008), water striders walking on fluid surface (Gao and Feng 2011) that can be observed in daily life, particle suspensions (Joseph et al. 2003, Singh and Joseph 2005, Singh et al. 2010) and wave-structure interactions (Lin and Chen 2013) in industrial applications, just to name a few. A unique characteristic that distinguishes solid-multiphase flow interaction from solid-single phase flow interaction is the contact line of three phases. It is the area where liquid interface intersects with the solid boundary. If we consider a two dimensional (2D) problem, it is actually represented by a point, and a line for a three dimensional (3D) problem (picture a drop on a leaf). The motion of three phase contact line plays a fundamental role in solid-multiphase flow interaction problems. However, the physical mechanism of a moving contact is still on debate (Dussan 1976, Dussan 1979, Blake 2006, Snoeijer and Andreotti 2013) due to the widely disparate spatial and temporal scales rooted in this problem. Based on interpretation at difference scales, the numerical modeling

of this problem also varies. From macroscopic and mesoscopic points of view, the contact line dynamics can be modeled by a slip boundary condition in sharp interface methods (Dussan and Davis 1974, Dussan 1979, Zhou and Sheng 1990, Bussmann et al. 1999, Bussmann et al. 2000, Renardy et al. 2001, Spelt 2005) or Robin boundary conditions in the phase-field method (Rowlinson and Widom 1982, Seppecher 1996, Jacqmin 2000, Yue et al. 2010). In the macroscopic sharp interface approach, the contact line is considered as a sharp discontinuity where singularity occurs (Seppecher 1996, Bonn et al. 2009). The singularity attributes to conflict between movement of contact line and the no-slip boundary condition that should be enforced for incompressible viscous flows. In contrast, the diffuse interface method (mesoscopic method) assumes that the interface has a thin thickness where the change of phase or flow parameters is smooth and gradual. Thus, the singularity encountered in the sharp interface method can be naturally resolved (Antanovskii 1995, Anderson et al. 1998, Jacqmin 2000, Ding and Spelt 2007, Ding et al. 2007). Due to this advantage, the phase-field method, as a diffuse interface method, has gained increasing popularity in simulation of contact line dynamics. As introduced in Chapter 2, to simulate contact line dynamics in phase-field method, the no-slip boundary condition is still utilized. Additionally, two Neumann boundary conditions ($\partial\phi/\partial\boldsymbol{n} = -\tilde{\omega}/\kappa$ for the order parameter ϕ and $\partial\mu_\phi/\partial\boldsymbol{n} = 0$ for chemical potential μ_ϕ) are used to govern the variation of composition on a solid boundary. However, owing to the intricacies caused by direct implementation of Neumann boundary condition on a body conformal grid for a complex geometry, most studies of contact line dynamics focus on perfectly smooth surface or grooved surface represented by straight lines. To overcome this problem, it is desirable that the boundary conditions can be applied through a non-body conformal manner. To approach this aim, an immersed boundary method that treats both the Dirichlet and Neumann boundary conditions

consistently is developed in the previous Chapter. The simulation procedures and numerical examples will be presented in the following context.

6.2 Simulation Procedures

To simulate solid-multiphase flow interactions, the methods developed in the previous Chapters are integrated together and the simulation procedures are summarized here. The phase-field LBM is adopted for flow field and interface capturing. Simultaneously, the Dirichlet and Neumann boundary conditions on solid boundaries are treated through IBM. To be concrete, the Dirichlet boundary condition is treated by a boundary condition-enforced IBM (Wu and Shu 2009) and the Neumann boundary condition is embodied analogous to the way that a flux affects its relevant physical parameter in a control volume. To provide an outline of the algorithm, the simulation procedures are summarized in the following context:

(1) Set the initial flow fields; Compute the coefficient matrix $\boldsymbol{A}$ in $\boldsymbol{AX}=\boldsymbol{B}$ (Eq. 5.16) and evaluate $\boldsymbol{A}^{-1}$;

(2) Using the lattice Boltzmann equation $f_\alpha\left(\boldsymbol{x}+\boldsymbol{e}_\alpha\delta t,t+\delta t\right)=f_\alpha\left(\boldsymbol{x},t\right)+\Omega_\alpha$ and $g_\beta\left(\boldsymbol{x}+\boldsymbol{e}_\beta\delta t,t+\delta t\right)=g_\beta\left(\boldsymbol{x},t\right)+\Omega_\beta$ to obtain the distribution functions at time level $t=t^n$ (with initial values of $\delta\boldsymbol{u}$, $\delta\mu_\phi$ and $\delta\phi$ being zero) and compute the macroscopic variables;

(3) Solve equation system $\boldsymbol{AX}=\boldsymbol{B}$ (Eq. 5.16) to determine the velocity correction term $\delta\boldsymbol{u}$ at boundary points and distribute them to Eulerian points;

(4) Apply Eq. (5.41) to evaluate $\delta q_{\mu n}$ on the boundary and Eq. (5.43) to compute $\delta \mu_\phi$ on Eulerian points. Update μ_ϕ using Eq. (5.45);

(5) Obtain $\delta q_{\phi n}$ through Eq. (5.40), compute $\partial \phi / \partial t$ on the Eulerian points using Eq. (5.42) and update the overall ϕ according to Eq. (5.44);

(6) Evaluate force density in Eq. (5.2), update velocity in Eq. (5.3) and compute the equilibrium distribution function;

(7) Repeat steps (2) to (6) until a convergence criterion is reached.

6.3 Results and Discussion

In this section, applications of immersed boundary phase-field lattice Boltzmann method will be presented. The method is first validated in detail through simulating a dewetting problem. It is then applied to simulate droplet spreading on a flat surface over a wide range of partial wetting regimes. Moreover, spreading on a curved plate is also simulated. Furthermore, the ability of the present method to handle Neumann boundary condition on complex geometries, probably the most desirable feature of proposed IBM, is demonstrated through simulation of the contact line dynamics on circular cylinder(s). Additionally, a moving boundary problem, a cylinder cross over a liquid interface is also presented. Besides 2D simulations, 3D examples including droplet on both flat and curved surface are presented. In this Section, the length is given in lattice units (one lattice unit represents $10^{-5} \sim 10^{-3}$ m). The density of both fluids will be set as 1 (can be correlated with kg/m^3 in physical units), and the surface tension is 10^{-3} (can be correlated with N/m in physical units) if otherwise stated. Moreover,

most cases considered here are with small droplets have diameter around tens of micrometers and the gravitational effect can be neglected.

6.3.1 Droplet dewetting

A solid-multiphase flow interaction problem, droplet dewetting, is used to test the numerical behavior of current method for dynamic problems. Both accuracy and grid-independency are examined in the first place. Thereafter, comparison between results of direct implementation of boundary conditions and those of immersed boundary method are carried out for different surface wettabilities.

In dewetting problems, a droplet is initialized with a relatively small contact angle (60° for instance), while the plate where the droplet is placed is set as neutral wetting or hydrophobic (with large equilibrium contact angle equal or larger than 90°). Consequently, there is an initial contact angle difference $\Delta\theta = \theta_{equilibirum} - \theta_{initial}$. In this case, the droplet will move upward due to this initial difference. This situation is similar to electrowetting experiments in which a voltage is suddenly applied. The speed of droplet motion depends on parameters such as the initial difference. To quantitatively characterize the droplet motion, two quantities are defined in the first place. They are averaged Y-position and Y-velocity component of the droplet:

$$Y_{Drop} = \frac{\sum y_{ij}\phi_{ij}}{\sum \phi_{ij}} \tag{6.1a}$$

$$V_{Drop} = \frac{\sum v_{ij}\phi_{ij}}{\sum \phi_{ij}} \tag{6.1b}$$

First, the accuracy and grid-independency for this dynamic case are verified by changing both Eulerian and Lagrangian grids. Then dewetting on solid boundary with different wettability is also examined. In these cases, the time evolutions of droplet height and velocity are compared with the results by direct implementation of boundary conditions.

6.3.1.1 Grid-independency test

Lagrangian grid-independency test

To verify the grid-independency of Lagrangian grid, three different sets of Lagrangian grid (enumerated in Table 6.1) are tested. The computational domain is set as 300×210 lattice units with a smooth plate (length equals 200 lattice units) centered at (150, 30). Concurrently, a body-conformal domain of 200×150 with a plate centered at (100, 0) is used for direct implementation of boundary conditions. Moreover, a droplet of radius 60 lattice units is centered on the plate with initial contact angle of 60°. Meanwhile, the equilibrium contact angle of the plate is set as 120°. Neutral boundary conditions are applied on upper and lower walls, while periodic boundary conditions are used for the left and right boundaries. Furthermore, τ is fixed as 0.65 (corresponding to kinematic viscosity of 0.05) hereafter unless mentioned otherwise. The time evolution of Y_{Drop} obtained by immersed boundary method on three sets of Lagrangian grid are compared with that by direct implementation of boundary conditions in Fig. 6.1. It can be seen that the dynamic processes provided by IBM are almost identical when Lagrangian grid size varies in a wide range (normally, the value of $\Delta L/\Delta E$ is larger than 1.0 and less than 2.0 in IBM). Furthermore, all the results of IBM are compared well with those given by direct implementation of boundary conditions. This

shows that the Lagrangian resolution in this study is adequate. Thus, the value of $\Delta L/\Delta E$ is chosen around 1.5 in the following numerical tests.

Eulerian grid-independency test

The grid-independency of Eulerian grid is also examined. In this part, numerical simulation is performed on three Eulerian grids. The evolution of Y_{Drop} in three cases is compared with that by direct implementation of boundary conditions in Fig. 6.2. It can be seen that the change in Eulerian grid size also has little influence on the dynamic process obtained and all the numerical results by IBM show good comparison with those by direct implementation of boundary conditions. This study also shows that the Eulerian grid size used in this work is fine enough to get accurate numerical results.

6.3.1.2 Influence of surface wettability

Besides examining the accuracy and grid-independency of the proposed algorithm to simulate dynamic process, the surface wettability is varied in this part and droplet velocity obtained by IBM is compared with that by direct implementation of boundary conditions. As demonstrated previously, Eulerian grid of 301×211 with $\Delta L/\Delta E$ varying from 1.2 to 1.8 can provide stable and accurate solution. The surface wettability is set as contact angle of 90°, 120° and 150° respectively. Figure 6.3 compares IBM results of these three different cases with those by direct implementation of boundary conditions. It can be observed that the time evolution of V_{Drop} provided by IBM basically compares well with that on the body conformal

grid even when the surface demonstrates super-hydrophobicity (i.e. $\theta_{eq} = 120^{\circ}$ and $\theta_{eq} = 150^{\circ}$).

6.3.2 Droplet spreading on a plate in partial wetting regime

We now apply the proposed method to simulate another problem: Droplet spreading in the partial wetting regime. In this case, the numerical contact angles are compared with theoretical predictions. Moreover, the time evolution of resolved droplet height and base diameter are compared with that obtained by direct implementation of the wetting boundary conditions.

In this case, a flat plate with length of 400 is centered at (250, 50) in a computational domain of 500×230. A droplet with radius of 45 is initialized above a plate with contact angle of 160°. The boundary conditions corresponding to the equilibrium contact angle θ_{eq} from 30° to 150° are tested. The interface thickness is set as 4.5. The non-dimensional time is defined as $t = Nh\sigma / D\rho\upsilon$ (Khatavkar et al. 2007), in which N indicates time steps, h means the Eulerian mesh spacing and D is the diameter of the droplet. Figures 6.4(a) to (e) display the equilibrium status of the spreading droplet with different θ_{eq}. To identify droplet contact angle, two ways are available. One way is to use a protractor and directly measure it on a phase-field contour (only one contour line $\phi = 0$ that represents the interface will be used) after the droplet evolves to its equilibrium state, as shown in Fig. 6.5(a), in which τ_{cl} is tangent line of level curve $\phi = 0$ on the wall. The other way is based on the fact that the droplet takes an arc shape to minimize the free energy after it approaches equilibrium on a

smooth surface. It is the way adopted to calculate θ_{eq} in this work. As sketched in Fig. 6.5(b) when $\theta_{eq} < 90^{\circ}$, we denote radius of droplet, height of droplet and radius of the circle as R_{Drop}, H_{Drop} and R respectively. It can be derived that the contact angle is $\theta = \pi - \cos^{-1}\left(\frac{1-k_r^2}{1+k_r^2}\right)$ with $k_r = R_{Drop} / H_{Drop}$. To be specific, it can be found that $\cos\theta_{eq} = \frac{R - H_{Drop}}{R}$. Moreover, $\left(R - H_{Drop}\right)^2 + R_{Drop}^2 = R^2$ which gives $R = \frac{H_{Drop}^2 + R_{Drop}^2}{2H_{Drop}}$. Substituting this relation into $\cos\theta_{eq} = \frac{R - H_{Drop}}{R}$, we can have $\theta_{eq} = \pi - \cos^{-1}\left(\frac{H_{Drop}^2 - R_{Drop}^2}{H_{Drop}^2 + R_{Drop}^2}\right)$. If we denote $k_r = R_{Drop} / H_{Drop}$, it can be simplified as $\theta = \pi - \cos^{-1}\left(\frac{1-k_r^2}{1+k_r^2}\right)$. Following this procedure, the same equation can be derived when $\theta_{eq} \geq 90^{\circ}$. (In this work, the values of R_{Drop} and H_{Drop} are tracked in the code based on the contour line of $\phi = 0$). Figure 6.6 compares the numerical results of the current method with the analytical solution. The numerical equilibrium contact angle was obtained after the difference of it between two iteration steps was less than 10^{-3}. This criterion was applied for the equilibrium status of spreading cases hereafter if otherwise stated. It demonstrates that the numerical results agree well with theoretical values over a wide range, especially when the contact angle is less than 135°. This may be due to the reason that for a droplet with a fixed volume, the base radius decreases for larger contact angle and hence the accuracy is negatively affected. This tendency is also observed when the boundary condition is directly implemented. In addition, quantitative comparisons are made in Table 6.2 between theoretical values and those obtained by direct implementation of the wetting boundary conditions (the computational domain is adjusted to

400×180). It can be seen that the numerical results obtained by IBM are almost identical with those by direct implementation of the wetting boundary conditions.

Besides comparison of the equilibrium contact angle, the time evolution of the droplet height and base diameter (normalized by the initial droplet diameter) by IBM is also compared with that by direct implementation of the wetting boundary conditions on a body-conformal grid in Fig. 6.7. It can be found that dynamics provided by IBM is also in good agreement with that obtained by direct application of the boundary conditions. Figure 6.7 also demonstrates overall behavior of a spreading droplet. To be specific, initially the base diameter undergoes dramatic changes while the droplet height stays almost the same when $t < 1$. Subsequently, the development of both the droplet height and diameter can be observed until the droplet relaxes to its equilibrium status (Khatavkar et al. 2007). This process can be seen more directly in Fig. 6.8. In addition, the level curves for the phase variable with velocity vector field at two time stages are plotted together with those by direct implementation of boundary conditions in Fig. 6.9. It can be seen that the flow field provided by IBM matches very well with that by direct implementation of boundary conditions. To further validate the numerical results, the spreading rate of this process is evaluated. Fitting the curves in Fig. 6.7 between $10^0 < t < 10^1$ gives $r \propto t^n$ where n = 0.351. This value compares reasonably well with that reported in Khatavkar et al. (2007) which is n = 0.34. These results demonstrate that the present algorithm can not only reproduce the equilibrium results, but also can correctly predict dynamic process of the moving contact line phenomenon.

6.3.3 Droplet spreading on a curved surface

In this case, simulation of a 2D droplet evolution on convex surface is performed. Initially, a droplet with radius of 40 is centered at (0, -30) in domain of 240×120. The center of original droplet is located in the center of computational domain (Bao et al. 2012). The reference length in the current simulation is set as 200, and the other parameters are set the same as those in the work of Bao et al. (2012) To be specific, the radius of the curved surface is 300 and the center of the curved surface is at (0, -330). Wall boundary conditions are directly applied on the upper and lower walls while the wetting boundary condition is applied through IBM on the curved surface. Cases with static contact angles of 60° and 120° are studied. Fig. 6.10 presents the equilibrium droplet shape with different static contact angles. The droplet shape resembles well with that shown in the literature. Moreover, the geometrical characteristics of the droplet ratio between H_{Drop} and R_{Drop} (defined in Figure 6.10(a)) is measured and compared in Table 6.3 with results in the literature (Bao et al. 2012). It can be seen that good agreement has been achieved.

6.3.4 Contact line dynamics on a single and two alongside circular cylinders

Most of the cases examined previously only consider the simple smooth surface in order to compare the results with those by direct implementation of the boundary conditions. This subsection is devoted to demonstrate ability of the proposed algorithm to handle problems with curved boundary. First, the contact line dynamics on a single circular cylinder is simulated. Then, contact line around two alongside cylinders is studied with different surface wettabilities.

6.3.4.1 Single cylinder

In this case, a circular cylinder with radius of 40 is fixed at the center of computational domain of 200×200. Periodic boundary condition is applied at the left and right sides and neutral wetting boundary condition is used for the upper and lower walls. The fluid-fluid interface is initialized as a flat surface located at the middle of the computational domain. The lower region is set as liquid phase with $\phi=1$ and the ambient fluid is set as $\phi=-1$ (the order parameter in the cylinder is set the same as the ambient fluid).

Figures 6.11(a) to (c) show the equilibrium statuses when theoretical contact angles are set as 60°, 90° and 120°. It can be seen that the fluid-fluid interface evolves along the solid boundary. For the hydrophilic surface, the fluid-fluid interface will rise above the initial horizontal line. On the contrary, the fluid-fluid interface is lowered below the initial horizontal line for the hydrophobic surface. In this case, the numerical contact angle is measured directly based on the obtained flow field (contour line $\phi=0$). The definition of the equilibrium contact angle (Singh and Joseph 2005) is shown in Fig. 6.12. In this figure, $\boldsymbol{n}_b$ is the outward normal of the circular cylinder and $\boldsymbol{\tau}_b$ is the tangential direction at the same position. These two directions are plotted at the three-phase contact line (contact point in this figure). Table 6.4 compares the numerical equilibrium contact angles with theoretical values. It is validated that the current numerical algorithm can accurately produce equilibrium contact angle when curved boundary is involved in the multiphase flow-solid interactions.

6.3.4.2 Two alongside cylinders

To further unfold the robustness of the present algorithm to manipulate arbitrary number and shape of complex solid boundaries, the cases with two alongside circular cylinders having the same as well as different wettabilities are simulated. The two circular cylinders with radius of 40 are fixed at (150, 50) and (250, 50) respectively in an expanded computational domain of 400×200.

Figure 6.13 shows the equilibrium flow field. The two cylinders in Fig. 6.13(a) have the same wettability with equilibrium contact angle of 60°. Meanwhile, the two cylinders in Fig. 6.13(b) have the same equilibrium contact angle of 120°. It can be found in these figures that, for each cylinder, the fluid-fluid interface deformation is asymmetric. At two ends far away from the interval between two cylinders (the left and right free ends), the fluid-fluid interface relaxes to the prescribed θ_{eq}. However, the fluid-fluid interface in the interval is raised ($\theta_{eq} = 60^\circ$) or lowered ($\theta_{eq} = 120^\circ$) as compared with initial horizontal line. This is due to the fact that when two cylinders are located close enough, a capillary interaction in the interval is generated in response to the overlap of perturbations in the meniscus shape (Kralchevsky and Nagayama 1994). Additionally, another case with two cylinders having different wettability has also been simulated. As shown in Fig. 6.13(c), the left one has $\theta_{eq} = 60^\circ$ and the right one is $\theta_{eq} = 120^\circ$. In this case, the fluid-fluid interface also relaxes to the prescribed θ_{eq} at two free ends. However, different from two cylinders with the same wettability, the interface is raised near the hydrophilic cylinder and lowered in the vicinity of the hydrophobic cylinder. In this case, the two cylinders, if they are allowed to move freely, will be pushed away from each other due to the repulsive long-range force generated. In-depth investigation

(Kralchevsky and Nagayama 1994, Kralchevsky and Nagayama 2000, Singh and Joseph 2005, Millett and Wang 2011) of these phenomena is beyond the scope of present work and interesting readers can refer to the literature listed above and references therein. In summary, numerical examples in this subsection demonstrate that, the present algorithm can easily be adapted to contact line problems with curved boundaries as well as surfaces with chemical inhomogeneous characteristics. Hence, it can serve as an efficient approach to study the multiphase fluid-solid interaction problems.

6.3.5 Impulsive motion of a submerged circular cylinder

A stationary circular cylinder interacting with free interface is simulated in the preceding subsections. In this subsection, a moving boundary problem, the impulsively started moving of an immersed cylinder is presented. A sketch of this problem is provided in Fig. 6.14. A circular cylinder is initially emerged slightly below the free interface of two fluids with density 1.1 and 1 respectively. It will move with a fixed velocity U either upwards or downwards. The radius of cylinder is set as 1.0 and the computational domain is 400×240. The interface is located in the half length of H. The distance between the center of cylinder and interface is 1.25. The non-dimensional number is $Fr = U/\sqrt{gh}$ and is fixed as 0.39 in the simulation. The computational domain is set as 400×240, the characteristic velocity is set as 0.0325, liquid kinematic viscosity is 0.15, and the wettability of cylinder is set as 90°. The free surface shape at $T=Ut/h=0.4$ is compared with result in the literature (Tyvand and Miloh 1995, Greenhow and Moyo 1997) in Fig. 6.15. It can be seen that the present disturbance of the free interface caused by motion of the cylinder shows good comparison with that in the literature. Moreover, interactions of the cylinder with the free interface at latter time stages are also shown in Fig. 6.16.

6.3.6 3D droplet spreading on a smooth surface

Beside 2D cases, 3D simulation of immersed boundary-phase field LBM for moving contact line problems is also carried out. To validate the 3D simulation, a standard case, droplet spreading on smooth surface is performed in the first place. In this case, the computational domain is set as $100\times100\times80$ with a smooth plate of 90×90 centered at (50, 50, 20). The droplet radius is set as 22.5. The 3D droplet shape when equilibrium contact angle equals 60°, 90° and 120° is demonstrated in Fig. 6.17. The numerical equilibrium contact angles are 62°, 91° and 123° respectively. It can be seen that the current numerical results well approach theoretical equilibrium contact angles.

6.3.7 3D droplet on a curved surface

After validation of the 3D code, this subsection will study 3D droplet evolution on both convex and concave shaped surfaces. In this case, the computational domain is $100\times100\times80$. A sketch of the concave case in *x*-*z* plane is shown in Fig. 6.18 (The surface only has curvature in *x*-*z* plane). As shown in the figure, the center point of chord A is fixed at (50, 50, 20) and the chord length L_{chord} is fixed as 90. Moreover, θ_{arc} as defined in Fig. 6.18 is set as 15°. For the convex case, the setting is the same except that the center of curved surface is in negative *z* direction. Fig. 6.19 compares the droplet wetted distance on surface between the plane surface and concave surface in *x*-*z* plane. It should be noted that for a flat plane, the wetted distance is the same at each direction. However, on the concave plane the distance will be different. In Fig. 6.19, the wetted distance of a drop on the concave surface is the arc length of the wetted area in middle *x*-*z* plane of the computational domain. It can be seen that the wetted distance on the concave surface is larger than that on flat surface. In contrast to the

concave surfaces, we also found that the wetted distance is smaller on the convex surface. Moreover, the droplet shapes on the curved surface are also plotted. Figs. 6.20 and 6.21 present droplet shapes with different static contact angles on both the concave and convex surfaces respectively. Through these numerical examples, the ability of the developed algorithm to investigate 3D contact line problems involving complex or curved surface such as surface wave interaction with pipes is demonstrated.

6.4 Concluding Remarks

The application of immersed boundary-phase field lattice Boltzmann method to simulate solid-multiphase flow interaction was demonstrated in this Chapter. For solid-multiphase flow interactions, two types of interfaces: the fluid-fluid interface and the solid boundary must be treated at the same time. In the present work, phase-field lattice Boltzmann method is used to capture the fluid-fluid interface. Simultaneously, the developed immersed boundary method is applied to treat both Dirichlet and Neumann boundary conditions for solid boundary. The method has been validated in details through several numerical cases. The equilibrium results and dynamic processes of solid-multiphase flow interactions were compared with theoretical predictions or data in the literature. Additionally, its capacity to be adapted to geometrical and/or chemical patterned surface was also demonstrated.

Table 6.1 Three sets of Lagrangian grid and ratio of Lagrangian grid spacing over Eulerian grid spacing ($\Delta L/\Delta E$)

Number of Lagrangian grid points	168	126	112
$\Delta L/\Delta E$	1.2	1.6	1.8

Table 6.2 Comparison of equilibrium contact angle on flat plate

Theoretical value	IBM	Direct implementation of wetting BCs
60°	60.6°	60.4°
90°	90°	90°
120°	120.5°	120°

Table 6.3 Comparison of droplet shape on curved surface

	Bao et al. 2012	Present
R_{Drop}/H_{Drop} , $\theta_{eq}=60^\circ$	1.62	1.64
R_{Drop}/H_{Drop} , $\theta_{eq}=120^\circ$	0.53	0.52

Table 6.4 Comparison of equilibrium contact angle on circular cylinder

Theoretical value	60°	90°	120°
IBM	$61^\circ \pm 1^\circ$	$90^\circ \pm 1^\circ$	$120^\circ \pm 1^\circ$

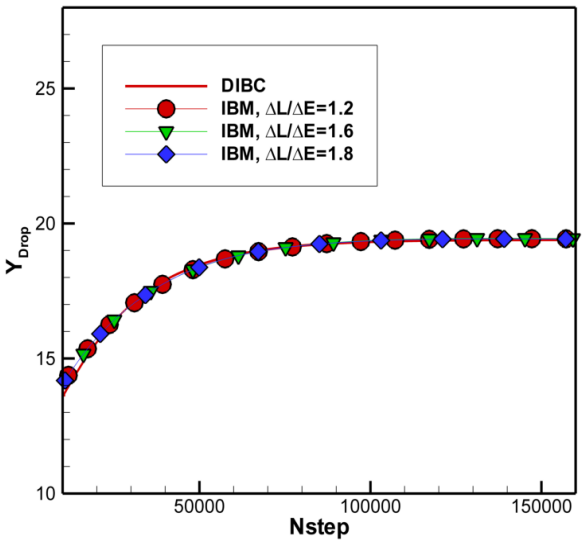

Fig. 6.1 Evolution of Y_{Drop} (Nstep is time step. Eulerian grid: 300×210; DIBC: Direct implementation of the boundary conditions; $\Delta L/\Delta E$: Mesh spacing ratio between Lagrangian and Eulerian grid)

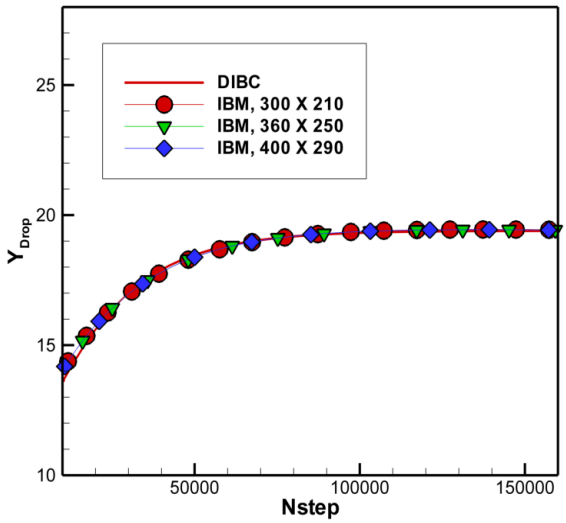

Fig. 6.2 Evolution of Y_{Drop} (Nstep is time step. Three different Eulerian grids: 301×211, 361×251 and 401×291, are used; $\Delta L/\Delta E=1.5$. DIBC: Direct implementation of the boundary conditions)

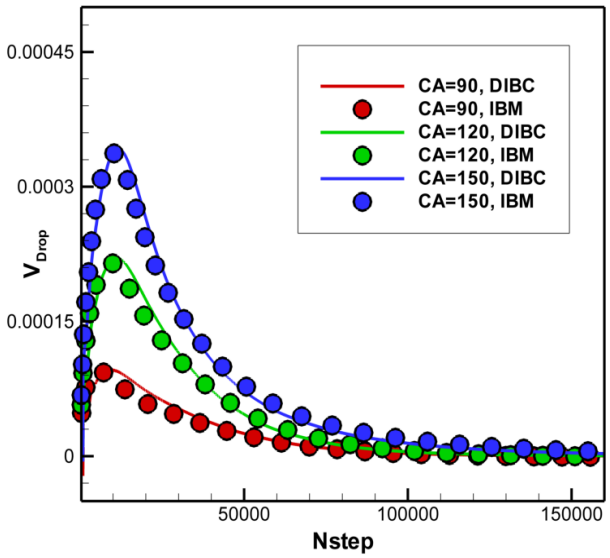

Fig. 6.3 Evolution of droplet V_{Drop} (Nstep is time step. DIBC: Direct implementation of the boundary conditions; IBM: Immersed Boundary Method)

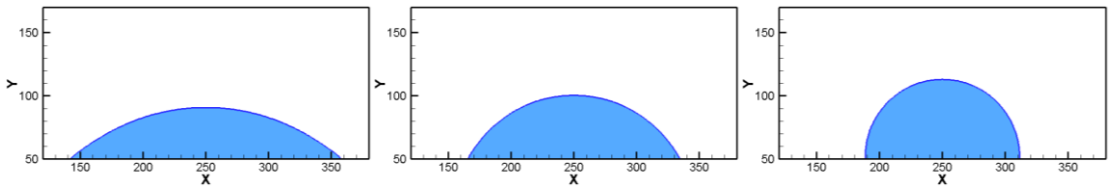

(a) $\theta_{eq} = 30^{\circ}$ (b) $\theta_{eq} = 60^{\circ}$ (c) $\theta_{eq} = 90^{\circ}$

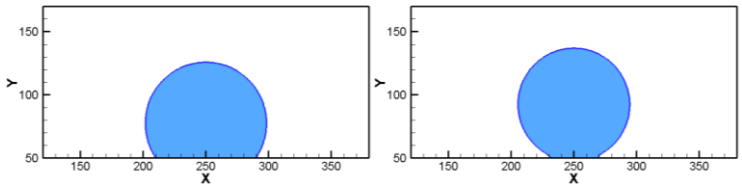

(d) $\theta_{eq} = 120^{\circ}$ (e) $\theta_{eq} = 150^{\circ}$

Fig. 6.4 Equilibrium statuses of the spreading droplet on a flat plate

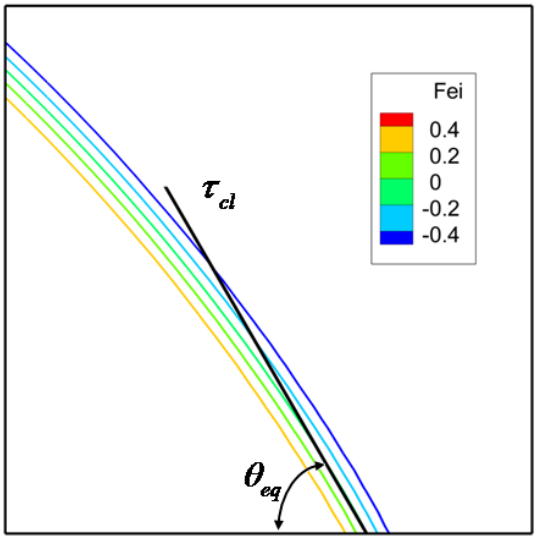

(a) Local ϕ level contours when the droplet approaches $\theta_{eq} = 60^{\circ}$

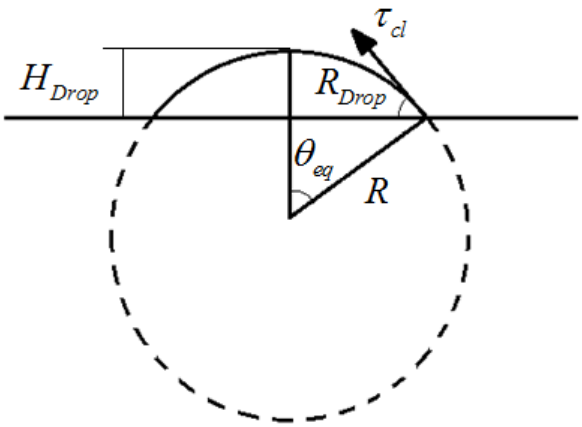

(b) Sketch of arc shape of an equilibrium droplet

Fig. 6.5 Two ways to calculate equilibrium contact angle for droplet spreading on smooth surface

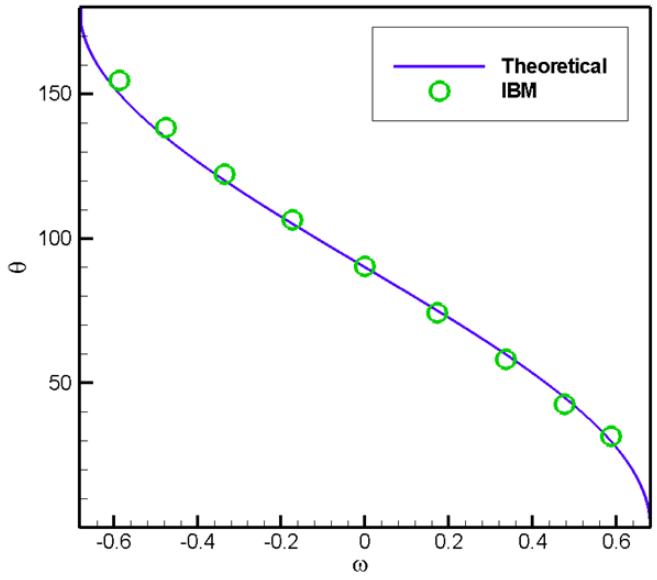

Fig. 6.6 The non-dimensional wetting potential versus the theoretical and numerical equilibrium contact angle

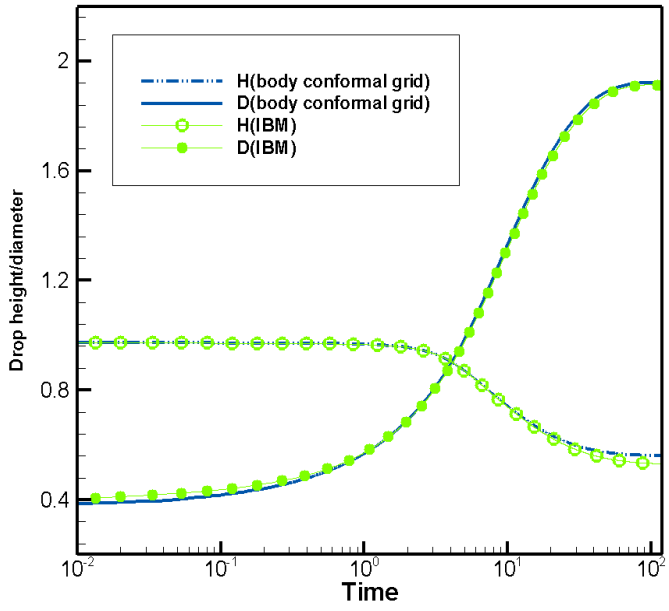

Fig. 6.7 The time evolution of non-dimensional droplet height and diameter (normalized by the initial droplet diameter) when $\theta_{eq} = 60^{\circ}$

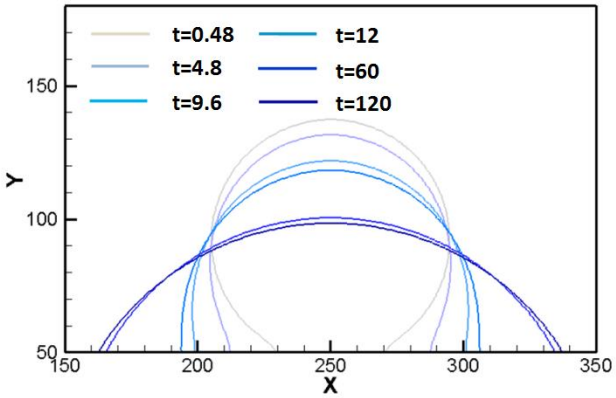

(a) $\theta_{eq} = 60^{\circ}$

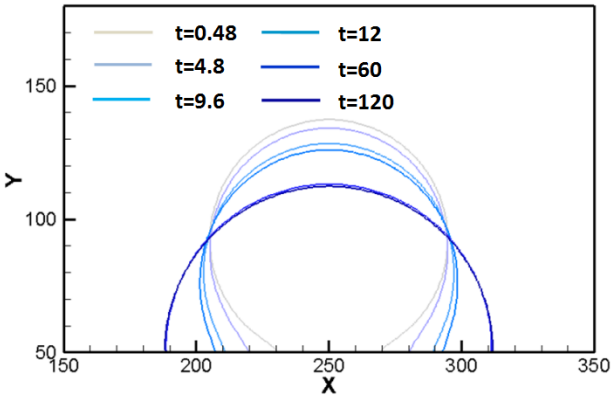

(b) $\theta_{eq} = 90^{\circ}$

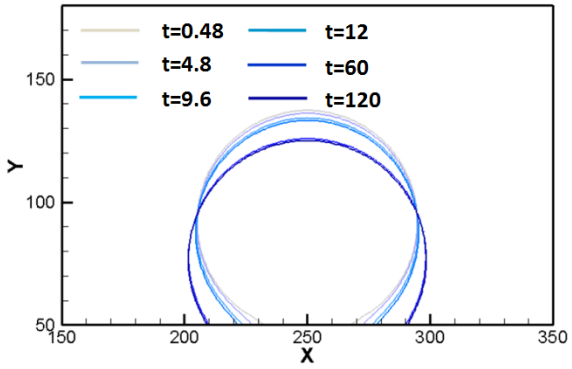

(c) $\theta_{eq} = 120^{\circ}$

Fig. 6.8 Spreading process of a droplet with three different equilibrium contact angles

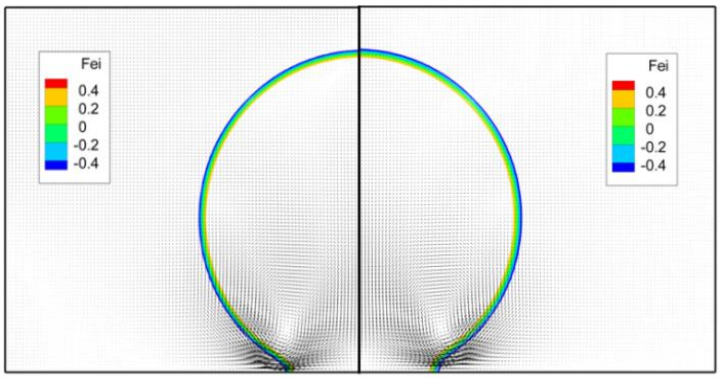

(a) Nstep = 2000

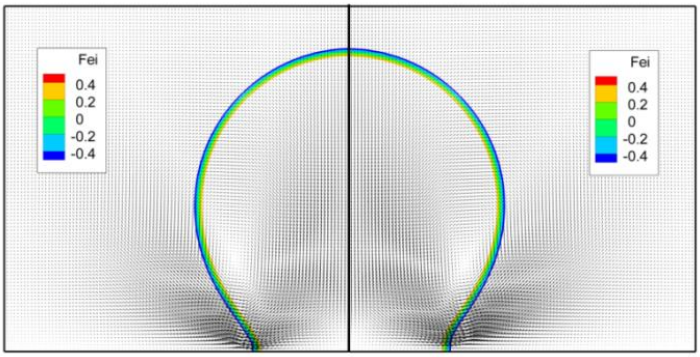

(b) Nstep = 10000

Fig. 6.9 Level curves of order parameter together with velocity vector field during spreading process. The left panel is the result by direct implementation of the boundary conditions and the right panel is result by IBM ($\theta_{eq} = 60^{\circ}$)

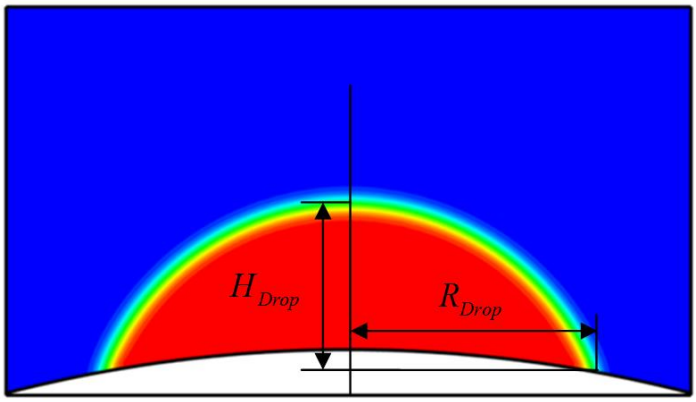

(a) $\theta_{eq} = 60^{\circ}$

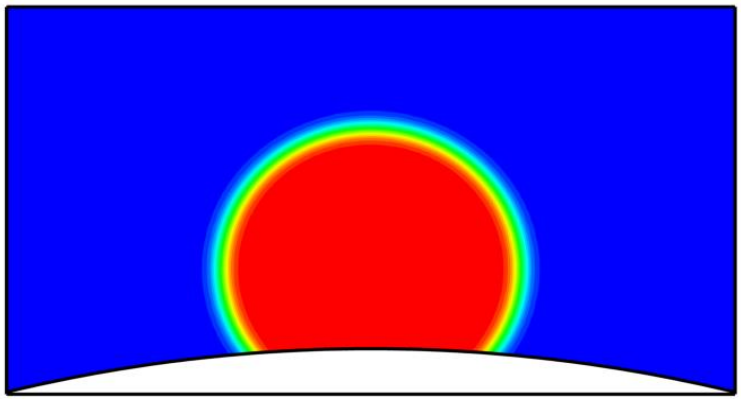

(b) $\theta_{eq} = 120^{\circ}$

Fig. 6.10 The results of contact lines on the curved surface with different equilibrium contact angles

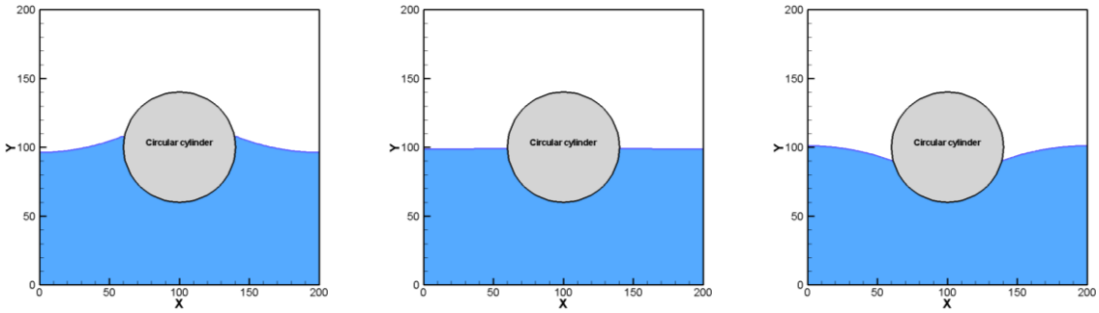

(a) $\theta_{eq} = 60^{\circ}$ (b) $\theta_{eq} = 90^{\circ}$ (c) $\theta_{eq} = 120^{\circ}$

Fig. 6.11 Contact line on a single circular cylinder

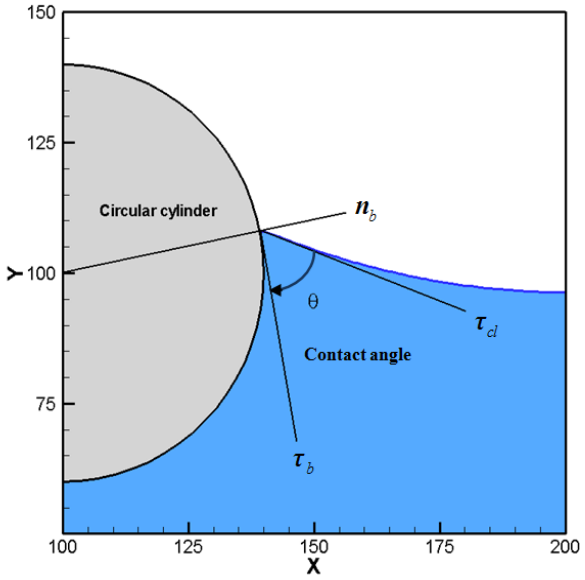

Fig. 6.12 Schematic depiction of contact angle definition on a circular cylinder

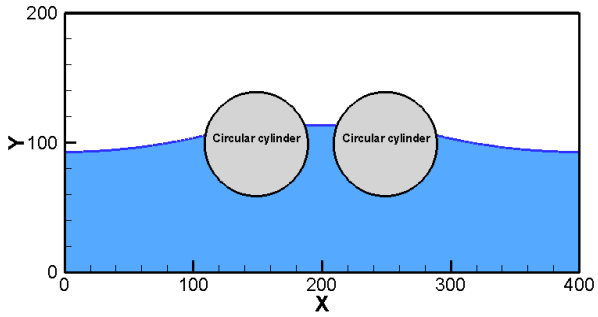

(a) Both cylinders with the same surface wettability of $\theta_{eq} = 60^{\circ}$

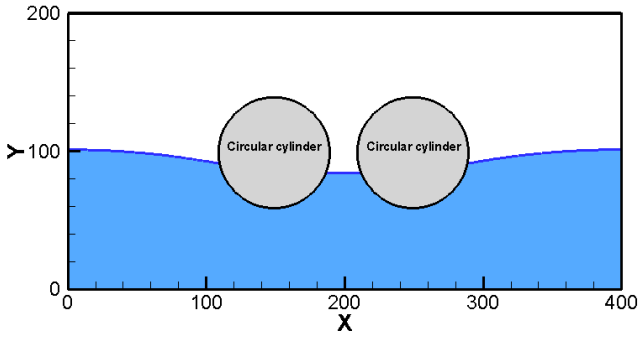

(b) Both cylinders with the same surface wettability of $\theta_{eq} = 120^{\circ}$

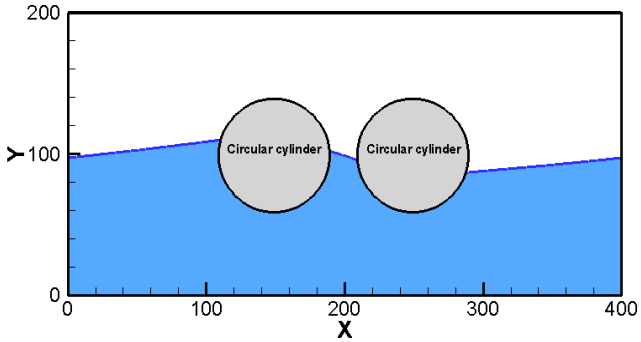

(c) The left cylinder with surface wettability of $\theta_{eq} = 60^{\circ}$ and the right one with $\theta_{eq} = 120^{\circ}$

Fig. 6.13 Contact line on two alongside cylinders with the same as well as different surface wettability

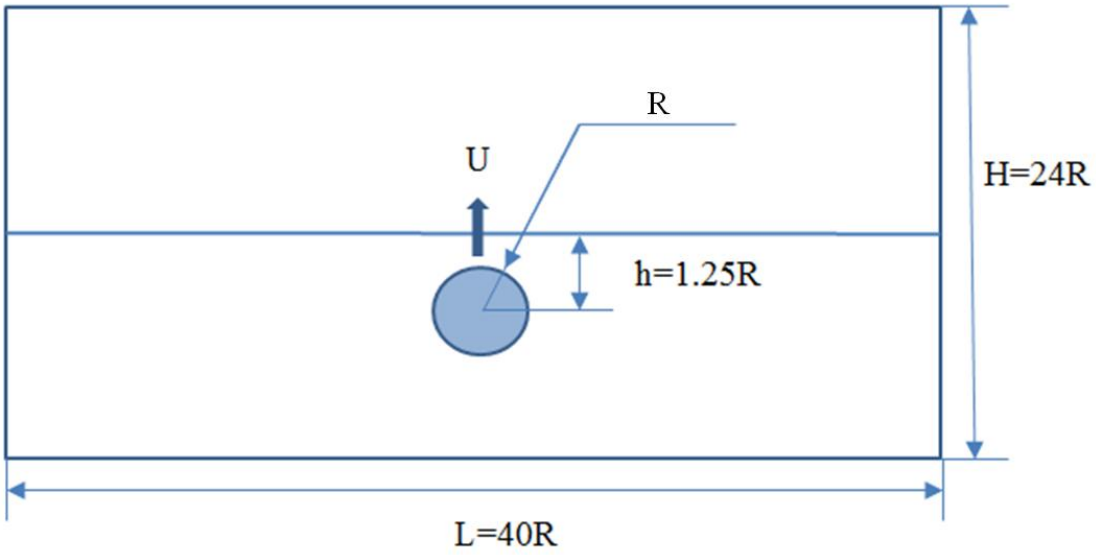

Fig. 6.14 A sketch of motion of an immersed cylinder

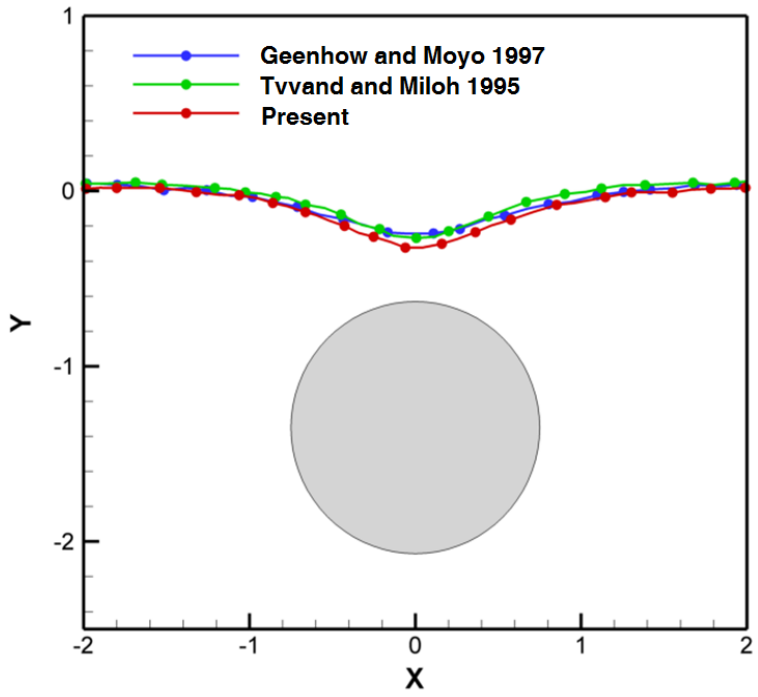

(a) Submerged cylinder impulsively moving downward

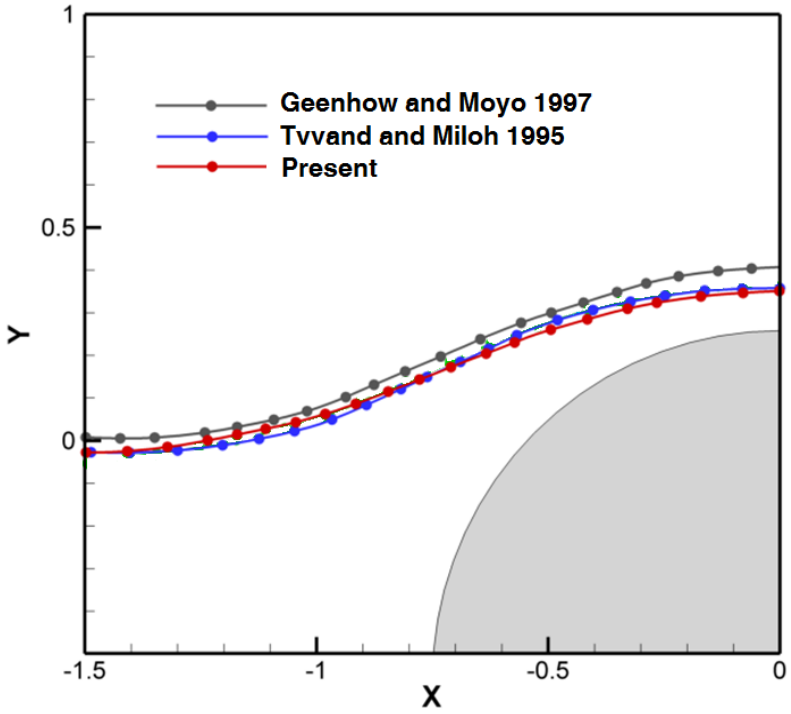

(b) Submerged cylinder impulsively moving upward

Fig. 6.15 Interface disturbance caused by impulsively started motion of cylinder

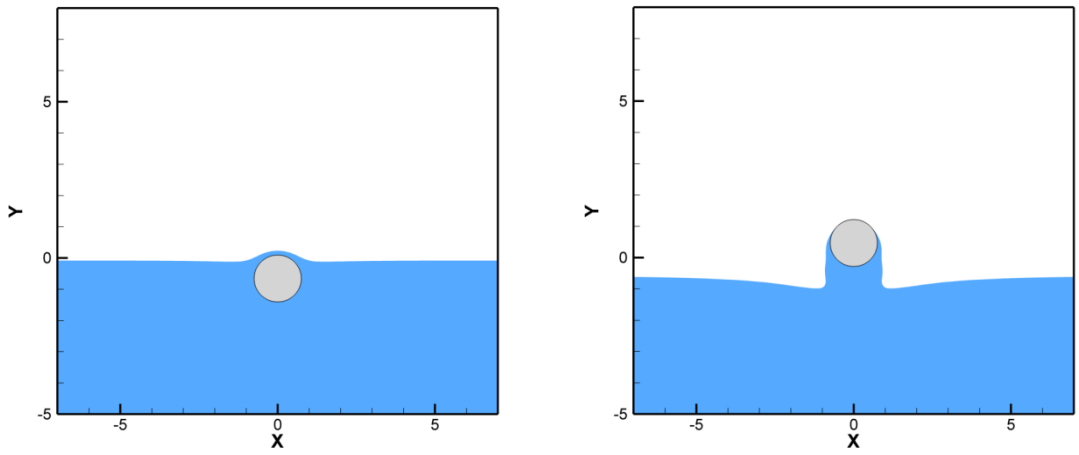

(a) T=0.3

(b) T=1.5

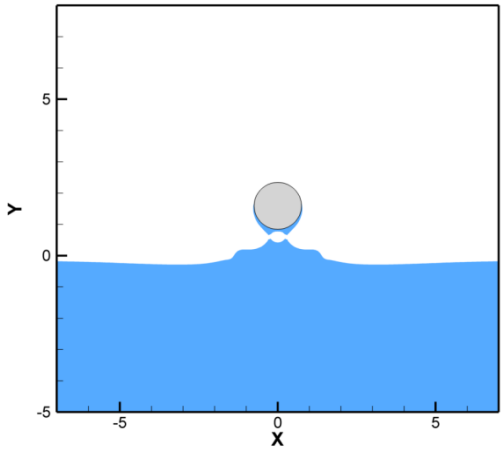

(c) T=2.7

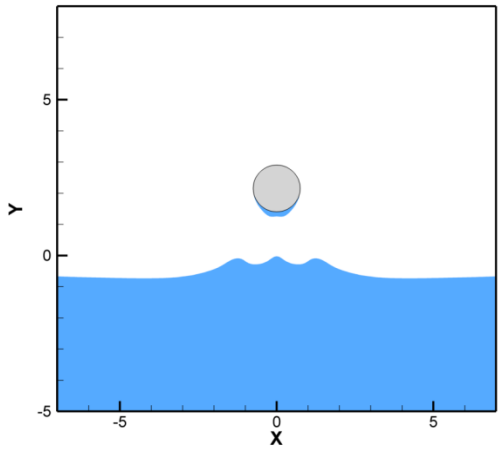

(d) T=3.3

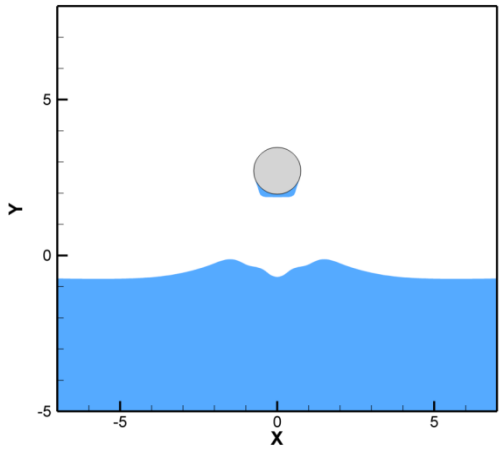

(e) T=3.9

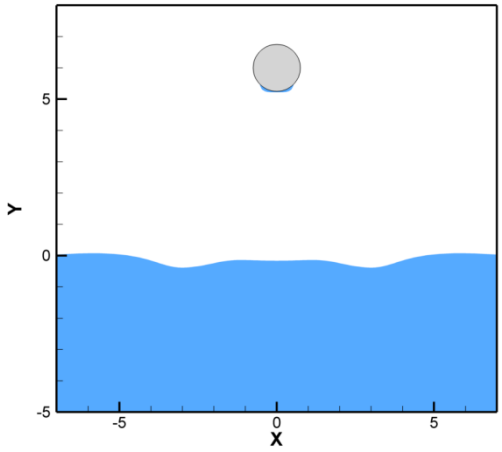

(f) T=7.5

Fig. 6.16 Interaction of a moving cylinder with the free surface

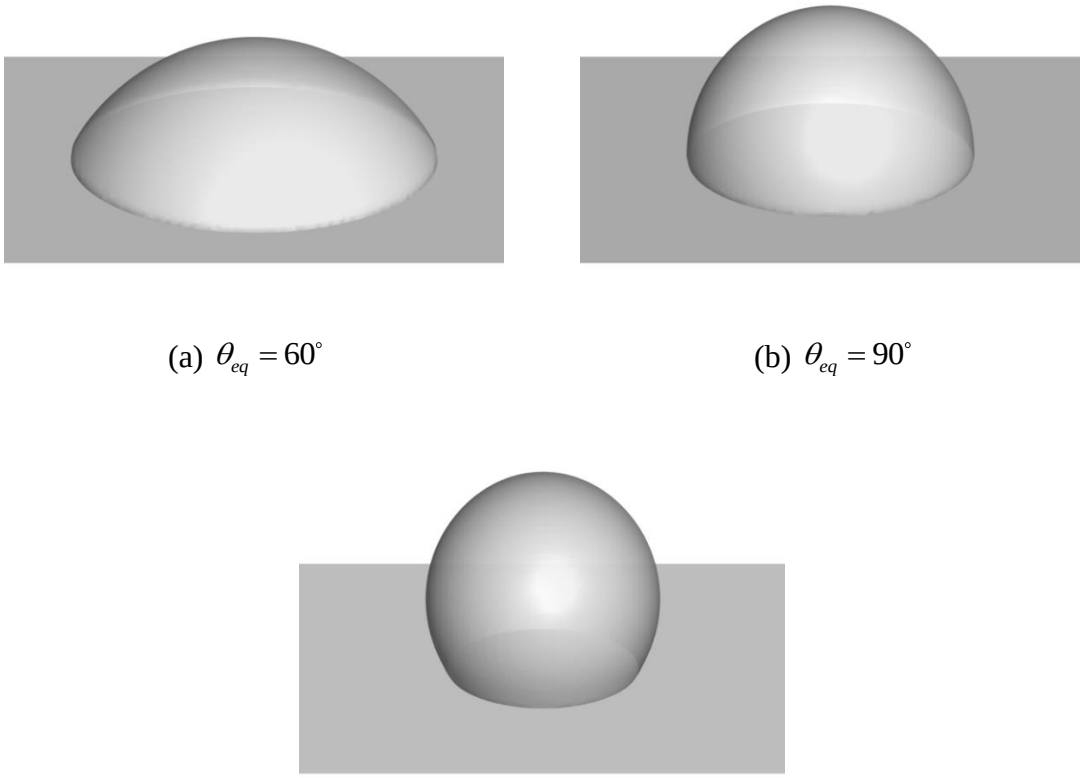

(a) $\theta_{eq} = 60^{\circ}$ (b) $\theta_{eq} = 90^{\circ}$

(c) $\theta_{eq} = 120^{\circ}$

Fig. 6.17 3D droplet spreading on the smooth plate

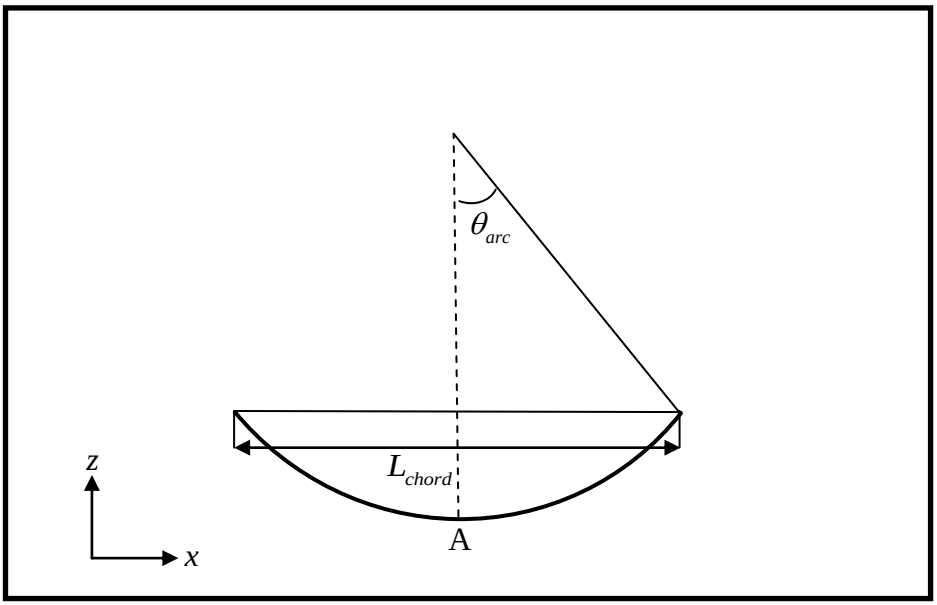

Fig. 6.18 A sketch of concave surface in computational domain

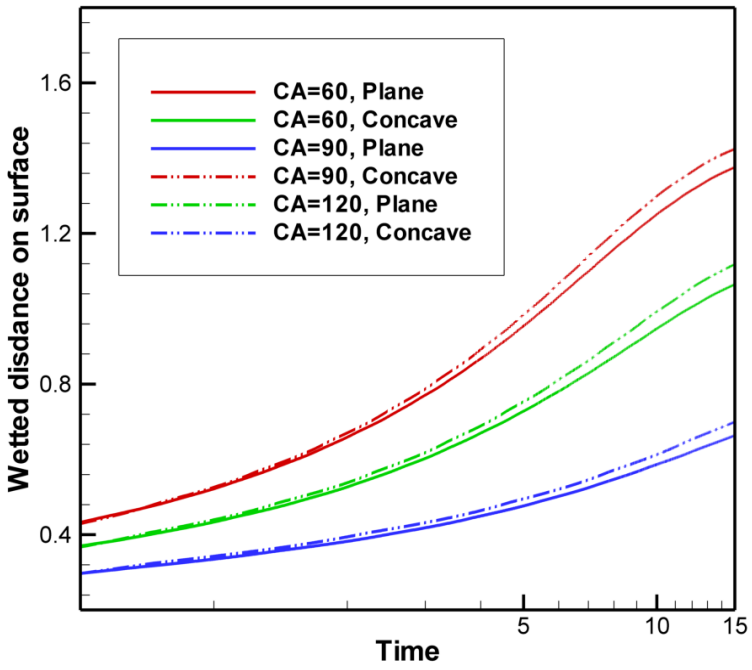

Fig. 6.19 Comparison of the droplet wetted distance on surface between plane surface and concave surface in *x*-*z* plane

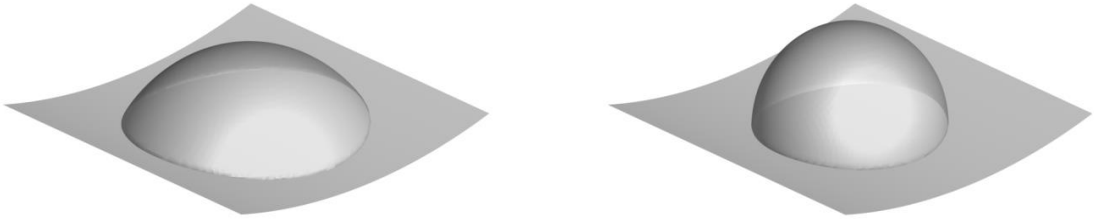

(a) $\theta_{eq} = 60^{\circ}$ (b) $\theta_{eq} = 90^{\circ}$

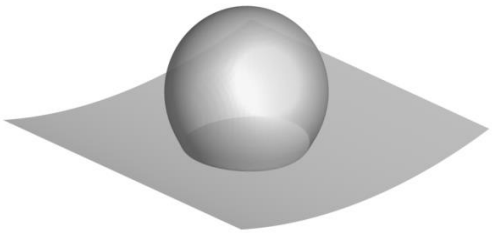

(c) $\theta_{eq} = 120^{\circ}$

Fig. 6.20 3D droplet shape on the concave surface

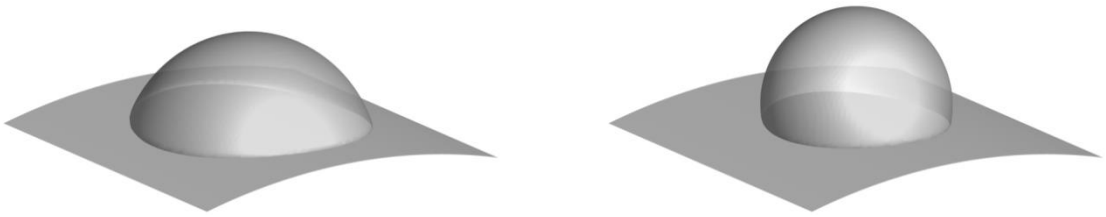

(a) $\theta_{eq} = 60^{\circ}$ (b) $\theta_{eq} = 90^{\circ}$

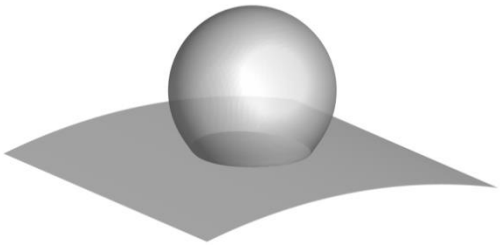

(c) $\theta_{eq} = 120^{\circ}$

Fig. 6.21 3D droplet shape on the convex surface

Chapter 7

Conclusions and Recommendations

In this Chapter, a conclusion of the present work will be provided in the first place. Thereafter, recommendations for future studies will be presented to end this Chapter.

7.1 Conclusions

In this thesis, three algorithms have been developed for simulation of solid-multiphase flow interactions. With respect to multiphase flow simulation, a stencil adaptive phase field-lattice Boltzmann method (LBM) has been proposed to balance the accuracy and computational efficiency. Moreover, a free energy-based phase-field LBM has been developed for simulation of the multiphase flow with density contrast. On the other hand, concerning boundary condition implementation, an immersed boundary method (IBM) for Neumann boundary condition has been purposed. It breaks through the long existed limitation that IBM can only treat Dirichlet boundary conditions and allows IBM to simulate more generous solid-fluid interactions. Moreover, the developed IBM was applied to study solid-multiphase flow interaction problems, which involve both Dirichlet and Neumann boundary conditions, in the phase-field framework. A more detailed summary will be provided in the following context according to the three developed algorithms respectively.

In respect of multiphase flow simulation, a stencil adaptive phase-field LBM has been developed to achieve high resolution of interface and concurrently reduce computational

resources required. The phase-field LBM has attracted much interest for the multiphase flow simulation owing to the advantages such as high efficiency in the interface capturing, natural resolving of contact line singularity and simple simulation procedure. However, as a diffuse interface method, a significant challenge for the phase-field LBM is to obtain a thin interface within affordable computational storage and time. To solve this problem, several solution-adaptive LBMs have been proposed. Nevertheless, due to the application of grid-structure that is not consistent with the lattice velocity model, these algorithms either involve complex spatial and temporal interpolation or partial loss of simplicity of LBM. To avoid complex interpolations and maintain simplicity of LBM, a stencil adaptive phase-field LBM has been developed in the present work. In the stencil adaptive algorithm, two types of symmetric stencils were alternatively inserted during the adaptive process. It was interesting to note that the combination of two types of stencil forms a structure very similar to the D2Q9 lattice model. Thanks to this similarity, the second order of accuracy can be achieved with only one-dimensional interpolation. The simplicity of LBM was also maintained. The accuracy and efficiency of the developed method has been examined through simulation of several multiphase flow problems. To be specific, the numerical behaviour of the present method was first investigated through the simulation of a stationary bubble. The Laplace law has been validated in this case. Moreover, the improvement in interface resolution was also demonstrated. Additionally, the simulation of a rising bubble was performed to demonstrate the ability of the present method to capture the moving interface. Furthermore, it was applied to simulate a contact line problem-droplet spreading on a solid surface with different wettability. All the obtained results showed good agreement with theoretical predictions and/or results in the literature. Besides accuracy, efficiency improvement was also demonstrated in stationary as well as dynamic cases. In conclusion, the numerical experiments performed verified that the developed stencil adaptive phase-field LBM enables

a high resolution for interfacial dynamics with greater grid distribution flexibility and considerable saving in computational effort.

Secondly, a novel phase-field LBM has been proposed to improve Z-S-C (Zheng et al. 2006) model for correct consideration of density contrast. In Z-S-C model, there are two sets of LBEs. One is for simulation of the flow field and the other is to recover C-H equation for the interface capturing. In the LBE for the flow field simulation, mean density is used as conservative variable. This ensures a stable and efficient simulation. However, the effect of local density variation is not properly considered. To correctly consider the effect of density contrast in the momentum equation, we start with a LBE, where the particle distribution function is for the local density and momentum. Then, to improve numerical stability, a transformation which is similar to the one used in the works of He et al. (1999) and Lee and Lin (2005) is introduced to change the particle distribution function for the local density and momentum into that for the mean density and momentum. Through this way, the LBE for the flow field in the present model can correctly consider the effect of density contrast in the momentum equation. In the meantime, it enjoys good properties of the particle distribution function for the mean density. The developed method has been validated through several numerical examples. It was first validated through simulations of viscous coupling of immiscible multiphase flow in a two-dimensional (2D) channel. The results were found to compare well with the theoretical solutions. Moreover, 2D nonlinear development of Rayleigh-Taylor instability and droplet splash on a wet surface were also simulated. Besides the 2D cases, three-dimensional (3D) simulations of drop impact on a dry surface considering the dynamic contact angle and 3D droplet collisions were performed and compared with the results in the literature as well. It is shown that the developed free energy-based LBM

successfully accounts for density contrast and can be used as an efficient tool to simulate both 2D and 3D multiphase flow problems.

Thirdly, an immersed boundary method was developed to implement Neumann boundary conditions that present in various solid-fluid interaction problems, on the complex solid surfaces. IBM is known as an efficient and robust algorithm to perform simulation of solid-fluid interactions. It has undergone continuous refinement for decades. Nevertheless, most works are limited to implementation of the Dirichlet boundary conditions. In this work, we initiate the first endeavour to apply IBM for the Neumann boundary conditions for more flexible solid-fluid interactions. The primary concept of the present method is to utilize Neumann boundary condition's physical interpretation. To be specific, Neumann boundary condition can be interpreted as contribution of the flux from the surface to its relevant physical parameters in a control volume. Using the concept of IBM, the flux can be directly related to the correction of the flow variables at Eulerian points. The application of IBM for several solid-fluid interaction problems were demonstrated in this work. First, the solid-single phase interactions such as flow over a circular cylinder, fish motion at high Reynolds number and flow over a sphere were presented. Subsequently, solid-multiphase flow interaction and transition layer formed on a solid surface were also simulated. The significance of this work is that it has extended the application of IBM to a boarder range and shed light on the implementation of IBM to ubiquitous fluid-solid interaction problems that involve the Neumann boundary conditions.

Last but not the least, the application of immersed boundary phase-field lattice Boltzmann method to study several solid-multiphase flow interactions was illustrated. Simulation of

solid-multiphase flow interactions might be one of the most challenging topics in computational fluid dynamic recently. It is because two different types of interface must be treated simultaneously in the simulation. One is the fluid-fluid interface and the other is the solid boundary. In this work, combination of the developed IBM for solid-fluid interaction and the phase-field lattice Boltzmann method provides us an efficient tool to tackle this problem. The performance of immersed boundary phase-field LBM has been testified through droplet dewetting and droplet spreading. Both equilibrium results and dynamic process were verified in details. Numerical results showed that the method can accurately reproduce equilibrium status and dynamic processes as compared to direct implementation of the same boundary conditions. The simulation of a droplet spread on a curved surface was also performed. Additionally, its capacity to simulate geometrical and/or chemical patterned surface was also demonstrated through simulation of the stationary and moving immersed cylinder(s) interaction with the free surface. Furthermore, the developed IBM for Neumann boundary condition was also extended to study the 3D moving problems on complex geometries as well.

7.2 Recommendations

This thesis has established an immersed boundary phase-field LBM framework for simulation of solid-multiphase flow interactions. Nevertheless, there is still a scope for improvement and application of these algorithms can also be further extended. Recommendations of the future works are presented in the following context.

First, the current stencil adaptive method is developed for 2D multiphase flows. It is known that for 3D simulation, the conflict between high resolution and computational effort might

be more serious. However, the 3D adaptive LBM is still less developed due to the complex structure of 3D lattice model. Thus, 3D adaptive LBM can be studied in the future work. Secondly, although the newly developed phase-field LBM has been successfully applied to both 2D and 3D multiphase flow problems have density ratio within the range of 10^2, it is still unable to handle large density contrast (in the order of 10^3). This is attributed to the fact that when a flow field is exposed to large density gradient, the physical diffusion in Cahn-Hilliard equation is not adequate to ensure a stable simulation. In this situation, it would be useful to apply more sophisticated numerical schemes and introduce artificial diffusion. To achieve this aim, the lattice Boltzmann equation for flow field can be directly coupled with the macroscopic Cahn-Hilliard equation supplemented by upwind schemes. In this manner, the phase-field LBM can be extended to problems with large density contrast in the future. In addition, the application of the developed immersed boundary phase-field lattice Boltzmann method in areas of: (1) solid interaction with multiphase flow with large density contrast and (2) moving boundary interactions with multiphase flow can be further extended.

References

C. K. Aidun and J. R. Clausen (2010). Lattice-Boltzmann Method for Complex Flows. Annual Review of Fluid Mechanics. 42: 439-472.

D. M. Anderson, G. B. McFadden and A. A. Wheeler (1998). "Diffuse-interface methods in fluid mechanics." Annual Review of Fluid Mechanics 30: 139-165.

A. Anderson, X. M. Zheng and V. Cristini (2005). "Adaptive unstructured volume remeshing I: The method." Journal of Computational Physics 208(2): 616-625.

D. M. Anderson, G. B. McFadden and A. A. Wheeler (1998). "Diffuse-interface methods in fluid mechanics." Annual Review of Fluid Mechanics 30: 139-165.

L. K. Antanovskii (1995). "A phase field model of capillarity." Physics of Fluids 7(4): 747-753.

N. Ashgriz and J. Y. Poo (1990). "Coalescence and separation in binary collisions of liquid-drops." Journal of Fluid Mechanics 221: 183-204.

N. Ashgriz and J. Y. Poo (1991). "Flair-flux line-segment model for advection and interface reconstruction." Journal of Computational Physics 93(2): 449-468.

E. Balaras (2004). "Modeling complex boundaries using an external force field on fixed Cartesian grids in large-eddy simulations." Computers & Fluids 33(3): 375-404.

K. Bao, Y. Shi, S. Y. Sun and X. P. Wang (2012). "A finite element method for the numerical solution of the coupled Cahn-Hilliard and Navier-Stokes system for moving contact line problems." Journal of Computational Physics 231(24): 8083-8099.

T. D. Blake (2006). "The physics of moving wetting lines." Journal of Colloid and Interface Science 299(1): 1-13.

D. Bonn, J. Eggers, J. Indekeu, J. Meunier and E. Rolley (2009). "Wetting and spreading." Reviews of Modern Physics 81(2): 739-805

E. Burman, A. Jacot and M. Picasso (2004). "Adaptive finite elements with high aspect ratio for the computation of coalescence using a phase-field model." Journal of Computational Physics 195(1): 153-174.

M. Bussmann, S. Chandra and J. Mostaghimi (2000). "Modeling the splash of a droplet impacting a solid surface." Physics of Fluids 12(12): 3121-3132.

M. Bussmann, J. Mostaghimi and S. Chandra (1999). "On a three-dimensional volume tracking model of droplet impact." Physics of Fluids 11(6): 1406-1417.

J.W. Cahn and J.E. Hilliard (1958). “Free energy of a nonuniform system.1. Interfacial free energy.” Journal of Chemical Physics 28: 258-267.

H. D. Ceniceros, R. L. Nos and A. M. Roma (2010). "Three-dimensional, fully adaptive simulations of phase-field fluid models." Journal of Computational Physics 229(17): 6135-6155.

S. Chen and G. D. Doolen (1998). "Lattice Boltzmann method for fluid flows." Annual Review of Fluid Mechanics 30: 329-364.

J. E. Colgate and K. M. Lynch (2004). "Mechanics and control of swimming: a review." Oceanic Engineering, IEEE Journal of 29(3): 660-673.

B. Crouse, E. Rank, M. Krafczyk and J. Tolke (2003). "A LB-based approach for adaptive flow simulations." International Journal of Modern Physics B 17(1-2): 109-112.

V. Cristini, J. Blawzdziewicz and M. Loewenberg (1998). "Drop breakup in three-dimensional viscous flows." Physics of Fluids 10(8): 1781-1783.

B. Crouse, E. Rank, M. Krafczyk and J. Tolke (2003). "A LB-based approach for adaptive flow simulations." International Journal of Modern Physics B 17(1-2): 109-112.

B. Cuenot, J. Magnaudet and B. Spennato (1997). "The effects of slightly soluble surfactants on the flow around a spherical bubble." Journal of Fluid Mechanics 339: 25-53.

D. S. Dandy and L. G. Leal (1989). "Buoyance-driven motion of a deformable drop through quiescent liquid at intermediate Reynolds numbers." Journal of Fluid Mechanics 208: 161-192.

S. Dennis and G.-Z. Chang (1970). "Numerical solutions for steady flow past a circular cylinder at Reynolds numbers up to 100." J. Fluid Mech 42(3): 471-489.

H. Ding and C. Shu (2006). "A stencil adaptive algorithm for finite difference solution of incompressible viscous flows." Journal of Computational Physics 214(1): 397-420.

H. Ding, P. D. M. Spelt and C. Shu (2007). "Diffuse interface model for incompressible two-phase flows with large density ratios." Journal of Computational Physics 226(2): 2078-2095.

H. Ding and P. D. M. Spelt (2007). "Wetting condition in diffuse interface simulations of contact line motion." Physical Review E 75(4): 046708.

J. Dušek, P. L. Gal and P. Fraunié (1994). "A numerical and theoretical study of the first Hopf bifurcation in a cylinder wake." Journal of Fluid Mechanics 264: 59-80.

E. B. Dussan and S. H. Davis (1974). "Motion of a fluid-fluid interface along a solid-surface." Journal of Fluid Mechanics 65(AUG12): 71-95.

E. B. V. Dussan (1976). "The moving contact line: the slip boundary condition." Journal of Fluid Mechanics 77(OCT22): 665-684.

E. B. V. Dussan (1979). "Spreading of liquids on solid surfaces: static and dynamic contact lines." Annual Review of Fluid Mechanics 11: 371-400.

E. A. Fadlun, R. Verzicco, P. Orlandi and J. Mohd-Yusof (2000). "Combined immersed-boundary finite-difference methods for three-dimensional complex flow simulations." Journal of Computational Physics 161(1): 35-60.

A. Fakhari and M. H. Rahimian (2010). "Phase-field modeling by the method of lattice Boltzmann equations." Physical Review E 81(3): 036707.

R. P. Fedkiw, T. Aslam, B. Merriman and S. Osher (1999). "A non-oscillatory Eulerian approach to interfaces in multimaterial flows (the ghost fluid method)." Journal of Computational Physics 152(2): 457-492.

Z. G. Feng and E. E. Michaelides (2004). "The immersed boundary-lattice Boltzmann method for solving fluid-particles interaction problems." Journal of Computational Physics 195(2): 602-628.

Z. G. Feng and E. E. Michaelides (2005). "Proteus: a direct forcing method in the simulation of particulate flows." Journal of Computational Physics 202(1): 20-51.

A. L. Fogelson and C. S. Peskin (1988). "A fast numerical method for solving the three-dimensional Stokes equations in the presence of suspended particles." Journal of Computational Physics 79: 50-69.

P. Gao and J. J. Feng (2011). "A numerical investigation of the propulsion of water walkers." Journal of Fluid Mechanics 668: 363-383.

J. W. Gibbs (1878). "On the equilibrium of heterogeneous substances." Transactions of the Connecticut Academy of Arts and Sciences 3: 108-248, 343-524.

S. van der Graaf, T. Nisisako, C. Schroen, R. G. M. van der Sman and R. M. Boom (2006). "Lattice Boltzmann simulations of droplet formation in a T-shaped microchannel." Langmuir 22(9): 4144-4152.

M. Greenhow and S. Moyo (1997). "Water entry and exit of horizontal circular cylinders." Philosophical Transactions of the Royal Society a-Mathematical Physical and Engineering Sciences 355(1724): 551-563.

A. K. Gunstensen, D. H. Rothman, S. Zaleski and G. Zanetti (1991). "Lattice Boltzmann Model of Immiscible Fluids." Physical Review A 43(8): 4320-4327.

Z. L. Guo, B. C. Shi and N. C. Wang (2000). "Lattice BGK model for incompressible Navier-Stokes equation." Journal of Computational Physics 165(1): 288-306.

Z. L. Guo, C. G. Zheng and B. C. Shi (2011). "Force imbalance in lattice Boltzmann equation for two-phase flows." Physical Review E 83(3): 036707.

F. H. Harlow and J. P. Shannon (1967). "The splash of a liquid drop." Journal of Applied Physics 38(10): 3855-3866.

F. H. Harlow and J. E. Welch (1965). "Numerical calculation of time-dependent viscous incompressible flow of fluid with free surface." Physics of Fluids 8(12): 2182-2189.

X. Y. He and G. Doolen (1997). "Lattice Boltzmann method on curvilinear coordinates system: flow around a circular cylinder." Journal of Computational Physics 134(2): 306-315.

X. Y. He, S. Y. Chen and R. Y. Zhang (1999). "A lattice Boltzmann scheme for incompressible multiphase flow and its application in simulation of Rayleigh-Taylor instability." Journal of Computational Physics 152(2): 642-663.

C. W. Hirt and B. D. Nichols (1981). "Volume of fluid (VOF) method for dynamics of free boundaries." Journal of Computational Physics 39(1): 201-225.

J. J. Huang, C. Shu and Y. T. Chew (2008). "Numerical investigation of transporting droplets by spatiotemporally controlling substrate wettability." Journal of Colloid and Interface Science 328(1): 124-133.

J. J. Huang (2009). Lattice Boltzmann Study of Near-Wall Multi-Phase and Multi-Component Flows Ph.D Thesis, National University of Singapore.

H. B. Huang and X. Y. Lu (2009). "Relative permeabilities and coupling effects in steady-state gas-liquid flow in porous media: A lattice Boltzmann study." Physics of Fluids 21(9): 092104.

T. Inamuro, T. Ogata, S. Tajima and N. Konishi (2004). "A lattice Boltzmann method for incompressible two-phase flows with large density differences." Journal of Computational Physics 198(2): 628-644.

D. Jacqmin (1999). "Calculation of two-phase Navier-Stokes flows using phase-field modeling." Journal of Computational Physics 155(1): 96-127.

D. Jacqmin (2000). "Contact-line dynamics of a diffuse fluid interface." Journal of Fluid Mechanics 402: 57-88.

T. A. Johnson and V. C. Patel (1999). “Flow past a sphere up to a Reynolds number of 300.” Journal of Fluid Mechanics 378: 19-70.A. A. Johnson and T. E. Tezduyar (1994). "Mesh

update strategies in parallel finite element computations of flow problems with moving boundaries and interfaces." Computer methods in applied mechanics and engineering 119(1): 73-94.

D. D. Joseph, J. Wang, R. Bai, B. H. Yang and H. H. Hu (2003). "Particle motion in a liquid film rimming the inside of a partially filled rotating cylinder." Journal of Fluid Mechanics 496: 139-163.

H. Kan, H. Udaykumar, W. Shyy and R. Tran-Son-Tay (1998). "Hydrodynamics of a Compound Drop with Application to Leukocyte Modeling." Physics of Fluids 10(4): 760-774.

V. V. Khatavkar, P. D. Anderson and H. E. H. Meijer (2007). "Capillary spreading of a droplet in the partially wetting regime using a diffuse-interface model." Journal of Fluid Mechanics 572: 367-387.

R. E. Khayat (2000). "Three-dimensional boundary element analysis of drop deformation in confined flow for Newtonian and viscoelastic systems." International Journal for Numerical Methods in Fluids 34(3): 241-275.

M. M. Koochesfahani (1989). "Vortical patterns in the wake of an oscillating airfoil." AIAA journal 27(9): 1200-1205.

P. A. Kralchevsky and K. Nagayama (1994). "Capillary forces between colloidal particles." Langmuir 10(1): 23-36.

P. A. Kralchevsky and K. Nagayama (2000). "Capillary interactions between particles bound to interfaces, liquid films and biomembranes." Advances in Colloid and Interface Science 85(2-3): 145-192.

B. Lafaurie, C. Nardone, R. Scardovelli, S. Zaleski and G. Zanetti (1994). "Modeling merging and fragmentation in multiphase flows with surfer." Journal of Computational Physics 113(1): 134-147.

D. V. Le, B. C. Khoo and J. Peraire (2006). "An immersed interface method for viscous incompressible flows involving rigid and flexible boundaries." Journal of Computational Physics 220(1): 109-138.

L. Lee and R. J. Leveque (2003). "An immersed interface method for incompressible Navier-Stokes equations." Siam Journal on Scientific Computing 25(3): 832-856.

T. Lee and C. L. Lin (2005). "A stable discretization of the lattice Boltzmann equation for simulation of incompressible two-phase flows at high density ratio." Journal of Computational Physics 206(1): 16-47.

T. Lee and L. Liu (2010). "Lattice Boltzmann simulations of micron-scale drop impact on dry surfaces." Journal of Computational Physics 229(20): 8045-8062.

R. J. LeVeque and Z. L. Li (1994). "The Immersed Interface Method for Elliptic Equations with Discontinuous Coefficients and Singular Sources." SIAM Journal on Numerical Analysis 31(4): 1019-1044.

Z. L. Li and M. C. Lai (2001). "The immersed interface method for the Navier-Stokes equations with singular forces." Journal of Computational Physics 171(2): 822-842.

M. Lighthill (1960). "Note on the swimming of slender fish." J. Fluid Mech 9(2): 305-317.

S. Y. Lin and Y. C. Chen (2013). "A pressure correction-volume of fluid method for simulations of fluid-particle interaction and impact problems." International Journal of Multiphase Flow 49: 31-48.

M. N. Linnick and H. F. Fasel (2005). “A high-order immersed interface method for simulating unsteady incompressible flows on irregular domians.”Journal of Computational Physics 204: 157-192.

S. V. Lishchuk, C. M. Care and I. Halliday (2003). "Lattice Boltzmann algorithm for surface tension with greatly reduced microcurrents." Physical Review E 67(3): 036701.

C. Liu, X. Zhang and C. H. Sung (1998). “Preconditioned multigrid method for unsteady incompressible flows.” Journal of Computational Physics 139: 35-57.

H. Liu and K. Kawachi (1999). "A numerical study of undulatory swimming." Journal of Computational Physics 155(2): 223-247.

J. Lopez, J. Hernandez, P. Gomez and F. Faura (2005). "An improved PLIC-VOF method for tracking thin fluid structures in incompressible two-phase flows." Journal of Computational Physics 208(1): 51-74.

J. Magnaudet, M. Rivero and J. Fabre (1995). "Accelerated flows past a rigid sphere or a spherical bubble.1.steady straining flow." Journal of Fluid Mechanics 284: 97-135.

J. C. Maxwell (1952). Capillary Action. In: Encyclopaedia Britannica. Reprinted in The Scientific Papers of James Clerk Maxwell. New York.

P. C. Millett and Y. U. Wang (2011). "Diffuse-interface field approach to modeling arbitrarily-shaped particles at fluid-fluid interfaces." Journal of Colloid and Interface Science 353(1): 46-51.

R. Mittal and G. Iaccarino (2005). "Immersed boundary methods." Annual Review of Fluid Mechanics 37: 239-261.

J. Mohd-Yusof (1997). "Combined immersed-boundary/b-spline methods for simulations of flow in complex geometries." Center for Turbulence Research Annual Research Briefs: 317-327.

S. Mukherjee and J. Abraham (2007). "Crown behavior in drop impact on wet walls." Physics of Fluids 19(5): 052103.

M. Muradoglu and S. Tasoglu (2010). "A front-tracking method for computational modeling of impact and spreading of viscous droplets on solid walls." Computers & Fluids 39(4): 615-625.

M. Muradoglu and G. Tryggvason (2008). "A front-tracking method for computation of interfacial flows with soluble surfactants." Journal of Computational Physics 227(4): 2238-2262.

R. R. Nourgaliev, T. N. Dinh, T. G. Theofanous and D. Joseph (2003). "The lattice Boltzmann equation method: theoretical interpretation, numerics and implications." International Journal of Multiphase Flow 29(1): 117-169.

S. Osher and R. P. Fedkiw (2001). "Level set methods: An overview and some recent results." Journal of Computational Physics 169(2): 463-502.

S. Osher and J. A. Sethian (1988). "Fronts propagating with curvature-dependent speed-Algorithms based on Hamiltion-Jacobi formulations." Journal of Computational Physics 79(1): 12-49.

P. Papatzacos (2002). "Macroscopic two-phase flow in porous media assuming the diffuse-interface model at pore level." Transport in Porous Media 49(2): 139-174.

M. Pasandideh-Fard, Y. M. Qiao, S. Chandra and J. Mostaghimi (1996). "Capillary effects during droplet impact on a solid surface." Physics of Fluids 8(3): 650-659.

C. S. Peskin (1972). "flow patterns around heart valves-Numerical method." Journal of Computational Physics 10(2): 252-271.

C. S. Peskin (1977). "Numerical analysis of blood flow in heart." Journal of Computational Physics 25(3): 220-252.

K. N. Premnath and J. Abraham (2005). "Simulations of binary drop collisions with a multiple-relaxation-time lattice-Boltzmann model." Physics of Fluids 17(12): 122105.

A. Prosperetti and G. Tryggvason (2003). "Appendix 3: Report of study group on computational physics." International Journal of Multiphase Flow 29(7): 1089-1099.

J. Qian and C. K. Law (1997). "Regimes of coalescence and separation in droplet collision." Journal of Fluid Mechanics 331: 59-80.

D. Quere (2008). "Wetting and roughness." Annual Review of Materials Research 38: 71-99.

L. Rayleigh (1892). "On the theory of surface forces-Compressible fluids." Pholosophical Magazine 33: 209-220.

T. Reis and T. N. Phillips (2007). "Lattice Boltzmann model for simulating immiscible two-phase flows." Journal of Physics a-Mathematical and Theoretical 40(14): 4033-4053.

M. Renardy, Y. Renardy and J. Li (2001). "Numerical simulation of moving contact line problems using a volume-of-fluid method." Journal of Computational Physics 171(1): 243-263.

M. Rohde, J. J. Derksen and H. E. A. Van den Akker (2008). "An applicability study of advanced lattice-Boltzmann techniques for moving, no-slip boundaries and local grid refinement." Computers & Fluids 37(10): 1238-1252.

J. S. Rowlinson and B. Widom (1982). Molecular Theory of Capillarity, Oxford, Oxfordshire : Clarendon Press, 1982.

M. Rudman (1997). "Volume-tracking methods for interfacial flow calculations." International Journal for Numerical Methods in Fluids 24(7): 671-691.

G. Ryskin and L. G. Leal (1984a). "Numerical solution of free-boundary problems in fluid-mechanics.1.The finite-difference technique." Journal of Fluid Mechanics 148(NOV): 1-17.

G. Ryskin and L. G. Leal (1984b). "Numerical solution of free-boundary problems in fluid-mechanics.2.Buoyancy driven motion of a gas bubble through a quiescent liquid." Journal of Fluid Mechanics 148(NOV): 19-35.

G. Ryskin and L. G. Leal (1984c). "Numerical solution of free-boundary problems in fluid-mechanics.3.Bubble deformation in an axisymmetric straining flow." Journal of Fluid Mechanics 148(NOV): 37-43.

M. Sbragaglia and X. Shan (2011). "Consistent pseudopotential interactions in lattice Boltzmann models." Physical Review E 84(3): 036703.

R. Scardovelli and S. Zaleski (1999). "Direct numerical simulation of free-surface and interfacial flow." Annual Review of Fluid Mechanics 31: 567-603.

P. Seppecher (1996). "Moving contact lines in the Cahn-Hilliard theory." International Journal of Engineering Science 34(9): 977-992.

J. A. Sethian and P. Smereka (2003). "Level set methods for fluid interfaces." Annual Review of Fluid Mechanics 35: 341-372.

M. Sfakiotakis, D. M. Lane and J. B. C. Davies (1999). "Review of fish swimming modes for aquatic locomotion." Oceanic Engineering, IEEE Journal of 24(2): 237-252.

X. W. Shan and H. D. Chen (1993). "Lattice Boltzmann Model for Simulating Flows with Multiple Phases and Components." Physical Review E 47(3): 1815-1819.

X. W. Shan and H. D. Chen (1994). "Simulaiton of Nonideal Gases and Liquid-gas Phase-Transitions by the Lattice Boltzmann-Equation." Physical Review E 49(4): 2941-2948.

D. H. Sharp (1984). "An Overview of Rayleigh-Taylor Instability." Physica D 12(1-3): 3-18.

G. J. Sheard, M. C. Thompson and K. Hourigan (2001). A numerical study of bluff ring wake stability. Proceedings of the 14th Australasian Fluid Mechanics Conference, Department of Mechanical Engineering, University of Adelaide.

G. J. Sheard, M. C. Thompson and K. Hourigan (2003). "From spheres to circular cylinders: the stability and flow structures of bluff ring wakes." Journal of Fluid Mechanics 492: 147-180.

C. Shu, N. Liu, Y. Chew and Z. Lu (2007). "Numerical simulation of fish motion by using lattice Boltzmann-Immersed Boundary Velocity Correction Method." Journal of mechanical science and technology 21(9): 1352-1358

S. Sikalo, H. D. Wilhelm, I. V. Roisman, S. Jakirlic and C. Tropea (2005). "Dynamic contact angle of spreading droplets: Experiments and simulations." Physics of Fluids 17(6): 062103.

P. Singh and D. D. Joseph (2005). "Fluid dynamics of floating particles." Journal of Fluid Mechanics 530: 31-80.

P. Singh, D. D. Joseph and N. Aubry (2010). "Dispersion and attraction of particles floating on fluid-liquid surfaces." Soft Matter 6(18): 4310-4325.

J. H. Snoeijer and B. Andreotti (2013). "Moving contact lines: Scales, regimes, and dynamical transitions." Annual review of fluid mechanics 45: 269-292.

P. D. M. Spelt (2005). "A level-set approach for simulations of flows with multiple moving contact lines with hysteresis." Journal of Computational Physics 207(2): 389-404.

M. Sussman (2005). "A parallelized, adaptive algorithm for multiphase flows in general geometries." Computers & Structures 83(6-7): 435-444.

M. Sussman, P. Smereka and S. Osher (1994). "A level set approach for computing solutions to incompressible 2-phase flow." Journal of Computational Physics 114(1): 146-159.

M. R. Swift, E. Orlandini, W. R. Osborn and J. M. Yeomans (1996). "Lattice Boltzmann simulations of liquid-gas and binary fluid systems." Physical Review E 54(5): 5041-5052.

M. R. Swift, W. R. Osborn and J. M. Yeomans (1995). "Lattice Boltzmann Simulation of Nonideal Fluids." Physical Review Letters 75(5): 830-833.

N. Takada, M. Misawa, A. Tomiyama and S. Hosokawa (2001). "Simulation of bubble motion under gravity by lattice Boltzmann method." Journal of Nuclear Science and Technology 38(5): 330-341.

A. Tiribocchi, N. Stella, G. Gonnella and A. Lamura (2009). "Hybrid lattice Boltzmann model for binary fluid mixtures." Physical Review E 80(2): 026701.

J. Toolke, S. Freudiger and M. Krafczyk (2006). "An adaptive scheme using hierarchical grids for lattice Boltzmann multi-phase flow simulations." Computers & Fluids 35(8-9): 820-830.

E. M. Toose, B. J. Geurts and J. G. M. Kuerten (1995). "A boundary integral method for 2-dimensional (non)-newtonian drops in slow viscous-flow." Journal of Non-Newtonian Fluid Mechanics 60(2-3): 129-154.

G. Tryggvason (1988). "Numerical Simulations of the Rayleigh-Taylor Instability." Journal of Computational Physics 75(2): 253-282.

G. Tryggvason, B. Bunner, A. Esmaeeli, D. Juric, N. Al-Rawahi, W. Tauber, J. Han, S. Nas and Y. J. Jan (2001). "A front-tracking method for the computations of multiphase flow." Journal of Computational Physics 169(2): 708-759.

P. A. Tyvand and T. Miloh (1995). "Free-surface flow due to impulsive motion of a submerged circular-cylinder." Journal of Fluid Mechanics 286: 67-101.

M. Uhlmann (2005). "An immersed boundary method with direct forcing for the simulation of particulate flows." Journal of Computational Physics 209(2): 448-476.

S. O. Unverdi and G. Tryggvason (1992). "A front-tracking method for viscous, incompressible. multi-fluid flows." Journal of Computational Physics 100(1): 25-37.

F. Uriel, D. Dominique, H. Brosl, L. Pierre, P. Yves and P. R. Jean (1987). "Lattice gas hydrodynamics in two and three dimensions." Complex Systems 1: 649-707.

J. J. Videler (1993). Fish swimming, Springer.

J. van der Waals (1893). "The thermodynamic theory of capillarity under the hypothesis of a continuous density variation." Transl. JS Rowlinson, 1979, Journal of Statistical Physics 20: 200-244.

R. J. Wassersug and K. Hoff (1985). "The kinematics of swimming in anuran larvae." Journal of Experimental Biology 119(1): 1-30.

F. M. White (1974). Viscous Fluid Flow 3e, Tata McGraw-Hill Education.

A. M. Worthington (1908). A study of splashes, London, New York, Bombay, Calcutta : Longmans, Green, and Co.

J. Wu and C. Shu (2009). "Implicit velocity correction-based immersed boundary-lattice Boltzmann method and its applications." Journal of Computational Physics 228(6): 1963-1979.

J. Wu (2010). Development of a novel immersed boundary-lattice Boltzmann method and its applictions. Doctor of Philosophy Ph.D Thesis, National University of Singapore.

J. Wu and C. Shu (2010). "An improved immersed boundary-lattice Boltzmann method for simulating three-dimensional incompressible flows." Journal of Computational Physics 229(13): 5022-5042.

J. Wu and C. Shu (2011). "A solution-adaptive lattice Boltzmann method for two-dimensional incompressible viscous flows." Journal of Computational Physics 230(6): 2246-2269.

J. Wu, C. Shu and Y. H. Zhang (2010). "Simulation of incompressible viscous flows around moving objects by a variant of immersed boundary-lattice Boltzmann method." International Journal for Numerical Methods in Fluids 62(3): 327-354.

S. Xu (2011). "A boundary condition capturing immersed interface method for 3D rigid objects in a flow." Journal of Computational Physics 230(19): 7176-7190.

S. Xu and Z. J. Wang (2006). "An immersed interface method for simulating the interaction of a fluid with moving boundaries." Journal of Computational Physics 216(2): 454-493.

S. Xu and Z. J. Wang (2008). "A 3D immersed interface method for fluid-solid interaction." Computer Methods in Applied Mechanics and Engineering 197(25-28): 2068-2086.

A. L. Yarin (2006). "Drop impact dynamics: Splashing, spreading, receding, bouncing." Annual Review of Fluid Mechanics 38: 159-192.

Z. Yu and L. S. Fan (2009). "An interaction potential based lattice Boltzmann method with adaptive mesh refinement (AMR) for two-phase flow simulation." Journal of Computational Physics 228(17): 6456-6478.

P. T. Yue, C. F. Zhou and J. J. Feng (2010). "Sharp-interface limit of the Cahn-Hilliard model for moving contact lines." Journal of Fluid Mechanics 645: 279-294.

H. W. Zheng, C. Shu and Y. T. Chew (2005). "Lattice Boltzmann interface capturing method for incompressible flows." Physical Review E 72(5): 056705.

H. W. Zheng, C. Shu and Y. T. Chew (2006). "A lattice Boltzmann model for multiphase flows with large density ratio." Journal of Computational Physics 218(1): 353-371.

H. W. Zheng, C. Shu, Y. T. Chew and J. H. Sun (2008). "Three-dimensional lattice Boltzmann interface capturing method for incompressible flows." International Journal for Numerical Methods in Fluids 56(9): 1653-1671.

X. M. Zheng, J. Lowengrub, A. Anderson and V. Cristini (2005). "Adaptive unstructured volume remeshing - II: Application to two- and three-dimensional level-set simulations of multiphase flow." Journal of Computational Physics 208(2): 626-650.

M. Y. Zhou and P. Sheng (1990). "Dynamics of Immiscible-Fluid Displacement in a Capillary-Tube." Physical Review Letters 64(8): 882-885.

L. D. Zhu and C. S. Peskin (2002). "Simulation of a flapping flexible filament in a flowing soap film by the immersed boundary method." Journal of Computational Physics 179(2): 452-468.